

Multi-scale approach of river morphodynamics: sediment transport, bars and meanders.

Filippo Chiodi

▶ **To cite this version:**

Filippo Chiodi. Multi-scale approach of river morphodynamics: sediment transport, bars and meanders.. Soft Condensed Matter [cond-mat.soft]. Univeristié Paris Diderot - Paris 7, 2014. English. ⟨NNT : 2014PA077047⟩. ⟨tel-01277409⟩

HAL Id: tel-01277409

https://hal.science/tel-01277409v1

Submitted on 22 Feb 2016

HAL is a multi-disciplinary open access archive for the deposit and dissemination of scientific research documents, whether they are published or not. The documents may come from teaching and research institutions in France or abroad, or from public or private research centers.

L'archive ouverte pluridisciplinaire **HAL**, est destinée au dépôt et à la diffusion de documents scientifiques de niveau recherche, publiés ou non, émanant des établissements d'enseignement et de recherche français ou étrangers, des laboratoires publics ou privés.



Distributed under a Creative Commons CC BY-NC-ND 4.0 - Attribution - Non-commercial use - No Derivative Works - International License

THÈSE DE DOCTORAT

UNIVERSITÉ PARIS DIDEROT (PARIS 7)

Spécialité

PHYSIQUE DE LA MATIÈRE MOLLE

ÉCOLE DOCTORALE: Matière Condensée et Interfaces (E.D. 518)

Présentée par

Filippo CHIODI

Approche multi-échelle à la morphodynamique des rivières: transport des sédiments, barres et méandres.

Multi-scale approach of river morphodynamics: sediment transport, bars and meanders.

À soutenir le jeudi 27 mars 2014 à 14h à l'ESPCI.

Composition du jury:

Bruno ANDREOTTI	*Co-directeur de thèse*
François CHARRU	*Examinateur*
Philippe CLAUDIN	*Co-directeur de thèse*
Pierre-Yves LAGREE	*Rapporteur*
Eric LAJEUNESSE	*Rapporteur*
Stephane RODRIGUES	*Examinateur*
Valerie VIDAL	*Examinatrice*

Cette thèse a été effectuée au sein du laboratoire de



Physique et Mécanique des Milieux Hétérogènes
(UMR 7636 CNRS/ESPCI/Paris 6/Paris 7) de l'ESPCI à Paris

Contents

Introduction **6**

I Hydrodynamics **10**

1 Flow on an inclined bed **11**
1.1 Introduction . . . 11
1.2 Dimensional analysis . . . 12
1.3 Navier-Stokes equations . . . 14
1.4 Laminar solution for the flow over a smooth inclined plane . . . 15
1.5 Turbulent flow: Reynolds decomposition . . . 17
1.6 Turbulent flow on an incline . . . 18
1.7 Depth averaged Saint Venant equations . . . 21

2 Flow in a channel **23**
2.1 Bank description . . . 23
2.2 Geometry of the base state and mode decomposition . . . 25
2.2.1 Analogy with wave guides . . . 27
2.2.2 ⟨Bra|ket⟩ formalism . . . 27
2.3 Bed and banks modulations . . . 29
2.3.1 Undulated bed . . . 29
2.3.2 Meandering banks . . . 30
2.4 The basal shear stress . . . 31
2.5 Conclusion . . . 34

3 Hydrodynamics in a channel with straight banks and an undulated bottom **35**
3.1 Laminar regime . . . 35
3.1.1 Base flow . . . 36

3.1.2 First order equations . . . 36
3.1.3 Average velocity . . . 39
3.1.4 Numerical integration . . . 40
3.1.5 Saint-Venant calculation . . . 40
3.1.6 Basal shear stress coefficients . . . 43
3.2 Turbulent flow . . . 47
3.2.1 Base flow . . . 47
3.2.2 First order equations . . . 48
3.2.3 Average velocity . . . 51
3.2.4 Numerical integration . . . 52
3.2.5 St-Venant . . . 53
3.2.6 Basal shear stress coefficients . . . 55

4 Hydrodynamics in a channel with meandering banks and a flat bottom 60
4.1 Laminar flow . . . 60
4.1.1 First order equations . . . 61
4.1.2 Average velocity . . . 62
4.1.3 Numerical integration . . . 62
4.1.4 Saint-Venant calculation . . . 63
4.1.5 Basal coefficients . . . 65
4.2 Turbulent flow . . . 70
4.2.1 First order equations . . . 70
4.2.2 Average velocity . . . 72
4.2.3 Numerical integration . . . 72
4.2.4 St-Venant . . . 73
4.2.5 Basal Coefficients . . . 75

II Transport 79

5 Sediment transport 80
5.1 Bed load and suspension . . . 80
5.2 Shields number and transport threshold . . . 81
5.2.1 Dimensional Analysis . . . 82
5.2.2 The influence of longitudinal slope . . . 84
5.3 Interface and fluxes . . . 85
5.3.1 Interface between sediment bed and fluid . . . 85
5.3.2 Flux and mass conservation . . . 85

5.4 Saturated flux . . . 87
5.4.1 Transport law . . . 88
5.4.2 Generic description of the sediment flux . . . 89
5.5 Saturation length . . . 90

6 A two phase flow model of sediment transport: transition from bed-load to suspended-load 93
6.1 Introduction . . . 93
6.2 Two-phase model . . . 94
6.2.1 Continuity equation . . . 94
6.2.2 Equations of motion . . . 95
6.2.3 Force exerted by one phase on the other . . . 96
6.2.4 Fluid constitutive relation . . . 96
6.2.5 Granular constitutive relation . . . 98
6.2.6 Diffusion . . . 99
6.3 Homogeneous steady transport . . . 100
6.3.1 Dimensional analysis . . . 100
6.3.2 Quasi-parallel flow assumption . . . 101
6.3.3 Static bed . . . 103
6.3.4 Dilute zone . . . 104
6.4 Results . . . 106
6.5 Concluding remarks . . . 110

III Bars and Meanders 113

7 The bar instability revisited 114
7.1 Linear stability analysis . . . 117
7.2 Dispersion relations . . . 118
7.2.1 Assuming a locally saturated sediment transport . . . 118
7.2.2 Introducing the saturation length . . . 119
7.3 Revisiting the bar instability . . . 121
7.3.1 Influence of the saturation parameter L_{sat}/H . . . 122
7.3.2 Influence of the ratio u_*/u_{th}^0 . . . 124
7.3.3 From alternate to multiple bars . . . 127

8 The meander instability 130
8.1 Adding bed and banks contributions . . . 130
8.1.1 Hydrodynamics . . . 131

8.1.2 Sediment transport . . . 132
8.2 Derivation of the dispersion relation . . . 132
8.2.1 Bed evolution . . . 132
8.2.2 Bank evolution . . . 136
8.2.3 Coupling the bed and the banks . . . 136
8.3 Properties of the dispersion relation . . . 137
8.3.1 Growth rate and angular velocity . . . 137
8.3.2 Influence of the parameters on the most unstable mode . . . 139
8.4 Instability mechanism . . . 144
8.4.1 Bed and banks contributions . . . 144
8.4.2 Analysis of the bed contribution . . . 146
8.4.3 The origin of the instability . . . 148
8.4.4 The Saint-Venant predictions . . . 151
8.4.5 The resonance-theory predictions . . . 154

9 Meanders in the lab **155**
9.1 Introduction . . . 155
9.2 Experimental setup . . . 156
9.2.1 Technical aspects and calibration . . . 157
9.2.2 Experimental procedure . . . 159
9.3 Experimental data . . . 166
9.3.1 Measurement of the meander evolution . . . 166
9.3.2 Geometry of the channel . . . 168
9.3.3 Velocity of the flow and hydrodynamical dimensionless numbers 173
9.4 Field data . . . 176
9.5 Dispersion relation . . . 177

Conclusion **179**

Introduction

The river meandering issue has been a central problem for people working in different scientific domains in the past century and nowadays the comprehension of the base mechanism still represents an open competition for research groups from all over the world. Although several remarkable results obtained in sediments transport, two phase flows and a huge collection of rivers data, a complete and exhaustive description of meandering phenomena is still missing. Besides, an other open challenge not yet closed is the reproduction and the control of the meanders in smaller scale, as in laboratory space. Geographers, geologists, hydraulic engineers have been ensued over the years in their attempts to provide a consistent model, often qualitatively, of river meandering: only lately physicists approach to the problem by carrying their knowledge and scientific tools to this subject in order to have a different point of view of it. For instance, A. Einstein investigated the origin of the meandering instability in 1926. Also, in the eighties, fractal theories (Rinaldo *et al.* 1993) were applied to the description of the organization of river basins (figure 1 – **b**). The branching of the river network can be reflected by the Strahler classification where all streams (main river and tributaries) are numbered in a unambiguous fashion: **(i)** any spring stream is of order one, **(ii)** the stream formed by the confluence of two streams of different orders inertiae the greater order of the two **(iii)** the stream formed by the confluence of two streams of the same order is increased by one. There are two cutoff scales in a drainage network: the large scale is set by plate tectonics, which is responsible for the uplift of mountain ranges; the small scale, which is given by the mean distance between streams, is not well understood. Nowadays, the interest is more focused on the understanding of the mechanisms responsible for the morphogenesis of the different river structures.

Rivers change their characteristics along their path from their spring in the mountains to their mouth in the plains. Rivers in mountains are steep torrents, transporting stones whose size are comparable to the water depth. Their water discharge is modest due to a limited catchment area. The cohesion of their banks is weak in the absence of a developed vegetation. Their bed typically presents step-pool sequences.

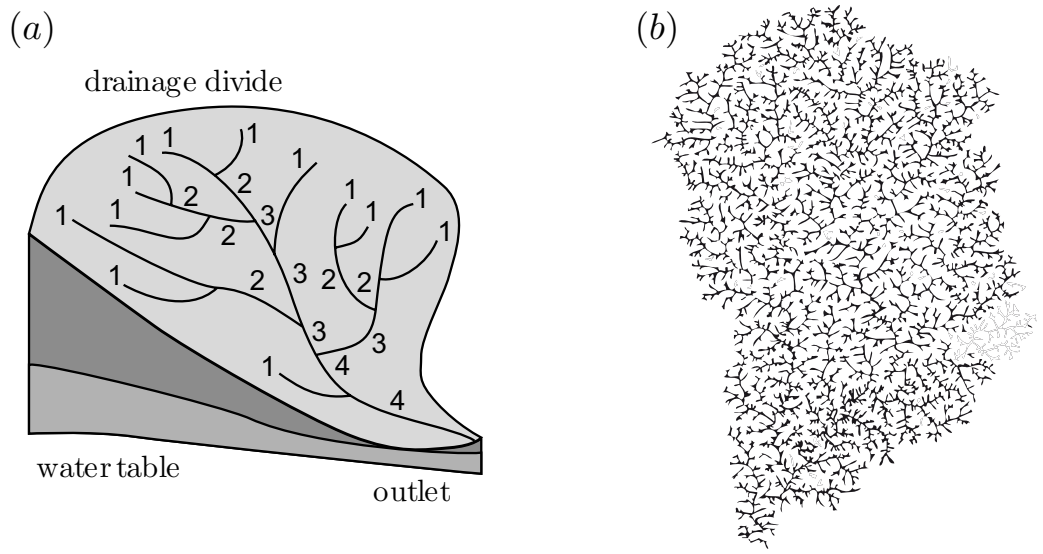


Figure 1: (a) Classification of the streams in a drainage basin (Strahler, 1957). (b) Drainage basin of the Beaver Creek (USA).

At intermediate slopes, rivers carry boulders or pebbles and can display riffle-pool sequences. In U-shaped glacial valleys, they have braided channels, with multiples bars and weekly consolidated islands. Finally, in plains, rivers flow over very small slopes and their water discharge is large (see Fig. 2 - **a**). They carry small sediments (e.g. sand). They are well channelized by cohesive banks, and can meander. Their bed presents ripples, dunes, and also sometimes (alternate) bars. This means that the four control parameters that one can think of (water discharge, slope, grain size and bank cohesion) are strongly correlated in nature. In figure 2 - **b**, the river aspect ratio is plotted as a function of the clay fraction in the banks, but it could be also effectively related to another of these quantities. It is therefore not possible to determine the dimensionless numbers that control the various instabilities and bed forms based on field measurements only, as a small part of the parameter space is available from field studies.

The general mechanisms responsible for the formation of subaqueous ripples and dunes are known (see review by Charru et al. 2013). These are transverse patterns. Ripples emerge from a linear instability of the flat bed, while dunes result from the non-linear coarsening of ripples (Fourrière et al. 2010). Antidunes are other types of transverse patterns, that form in supercritical flows, due to the resonance of the bed shape with waves a the water free surface (Raudkivi 1966, Ikeda 1983, Parker 1975, Colombini & Stocchino 2008). It has been proposed that the transition from

transverse to oblique bed forms is controlled by the ratio of the saturation length $L_{\rm sat}$, which quantifies the length scale over which the sediment flux responds to a perturbation, to the water depth H (Andreotti et al. 2011). In this thesis, we are interested in the formation of bars, which can be seen as inclined modes guided by the banks, and in particular we investigate the role of this ratio $L_{\rm sat}/H$ on the bar formation and selection.

Another focus of the thesis is the meander instability. Einstein (1926) claimed that an important hydrodynamical feature is the existence of a secondary transverse flow with respect the direction of the main flow (figure 3). This would cause an increased surface velocity at the exterior of the bend and, consequently, a greater erosion of the outside bank, while, it would reduce the flow velocity to the interior of the bend on the bottom and favour the deposition of sediments at the inside bank. The idea that the curvature of the channel drives the meander growth is at the base of the so-called bend theory (Ikeda *et al.* 1981, Parker & Andrews 1986). Another explanation proposed in the past years is that firstly formulated by Blondeaux *et al.* (1985) and successively developed by Zolezzi & Seminara (2001), Lanzoni & Seminara (2006), see review by Seminara (2006). The theory is based on the hypothesis

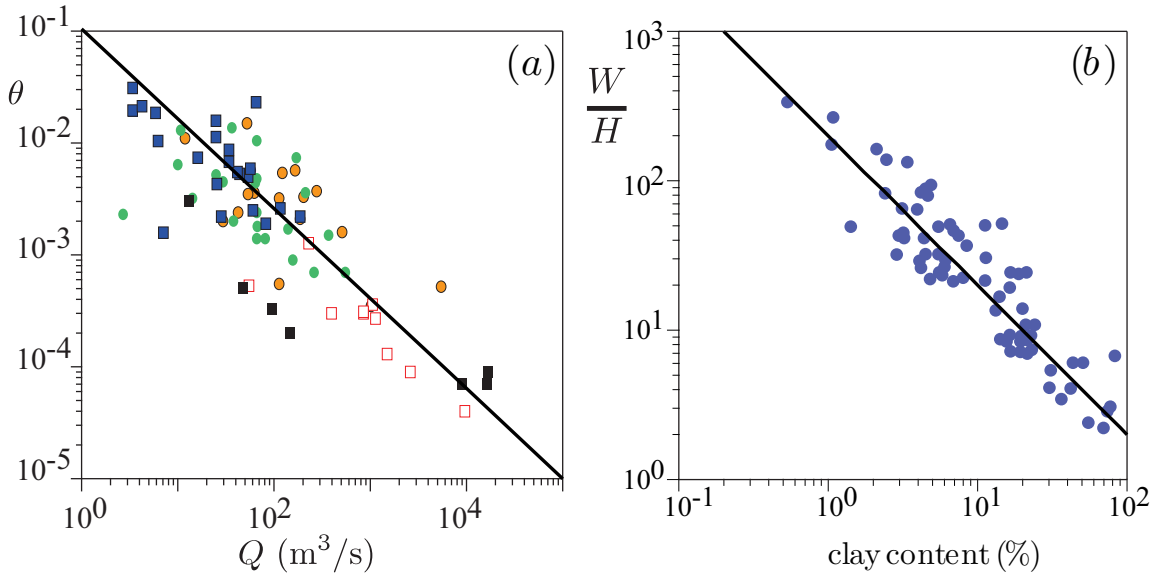


Figure 2: (*a*) Slope of natural rivers as a function of the flow rate Q in flooding conditions. (*b*) River aspect ratio as a function of the clay fraction in the banks. Data compiled by G. Parker, available online: `http://vtchl.uiuc.edu/people/parkerg/morphodynamics_e-book.htm`.

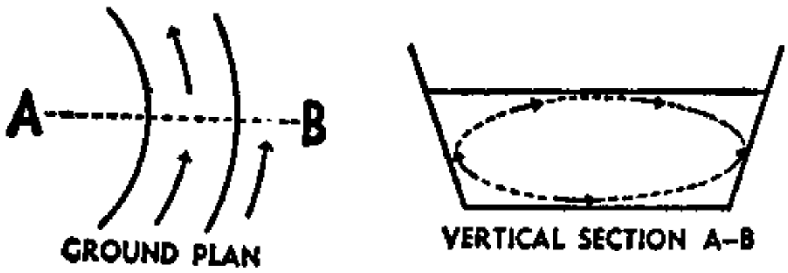


Figure 3: Einstein's model of traverse recirculation in a meandering bend.

of a *resonance* in which alternate bars with a vanishing migration velocity can trigger the bank instability. We show in this manuscript that none of these explanations are supported by our analysis.

This manuscript is organized in order to guide the reader from the base ingredients as hydrodynamics and sediment transport up to the building of a complete theory of river meandering. During this path one will face other problems as the formation of the alternate bars or the detailed study of a two phase flow. The theoretical results will be compared to experiments and field data.

Part I

Hydrodynamics

Chapter 1

Flow on an inclined bed

1.1 Introduction

Our main goal is to derive a model of river meandering, and thus to determine the dynamical mechanisms at the origin of the instability but also the wavelength selected and the propagation of meanders. Our strategy to get a clear picture of the instability is to describe hydrodynamics in a meandering channel and sediment transport separately. These two parts of the problem are obviously coupled. The bed topography and the planimetric shape of the river change the water flow. In turn, the flow transports grains. Through the erosion/deposition processes, sediment transport changes the shape of both the bed and the banks. Although this will be justified later, in the chapter devoted to the description of sediment transport, we need to hypothesize here that the river flow is not affected by transported particles in the bulk. Moreover, the time-scale of evolution of the river shape is large enough to consider that hydrodynamics is steady. We will therefore focus in chapters 2 to 4 on the hydrodynamical description of a flow channelized by static banks and over a static bed. In chapter 5, we then review the physics of sediment transport, and propose a novel description, unifying the different modes of subaqueous transport. Finally, in chapters 7 and 8, we perform the linear stability analysis of a straight and flat channel, giving rise to bar and meandering instabilities. Moreover, experiments have been performed in order to measure the growth rate of an undulated channel (chapter 9), which compares well with the model.

The hydrodynamical description of the flow in a realistic meandering channel is a remarkably difficult task. Our first step will therefore be to propose an idealization of the problem that we wish to solve. The identification of the difficulties can be

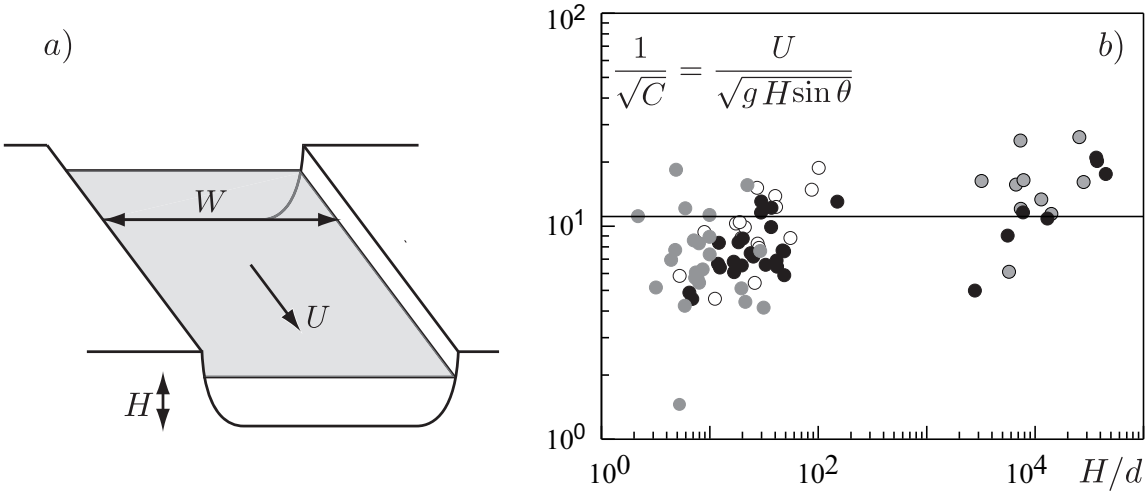


Figure 1.1: (a) Scheme of a river section and its dimensional quantities. (b) Behavior of the Chézy number as a function of the dimensionless water depth H/d where d is the grains size. The solid line is the theoretical prediction of Eq. (1.1). Data compiled by Parker.

organized in two steps. We will start by the discussion of a quite academic problem: the flow over an inclined sand bed, infinite along the transverse direction. We will identify the dimensionless numbers associated with the flow regime and with the presence of a free surface. This discussion will allow us to point out a major difficulty: as the flows in both natural rivers and small scale channels in the lab are dominated by inertial effects and turbulent fluctuations, one needs to adopt a semi-phenomenological description of the flow. We will compare the relative properties of two such frameworks: three dimensional Reynolds averaged equations with a first order closure on the one hand, and Saint-Venant depth averaged equations on the other hand. In the next chapter, we will consider further modeling problems, related to the confinement between banks.

1.2 Dimensional analysis

We first consider the central part of a river whose width W is much larger than its depth H, flowing over a regular slope. In this limit of a large aspect ratio $\beta = W/H$, the influence of the banks can be neglected. The problem can then be idealized as an homogeneous flow over a flat sand bed, infinite along the transverse direction.

The first control parameter of such a river is the angle θ of the bed with respect to the horizontal. Denoting by H the flow depth, the balance between gravity g and hydrodynamic friction selects the typical flow velocity $\bar{u}$. Comparing the driving force to the flow velocity, one builds a dimensionless number, called after Chézy, and defined by:

$$C = \frac{gH \sin\theta}{\bar{u}^2}. \tag{1.1}$$

The larger the Chézy number, the larger the friction of the flow on the bed for a given flow velocity. The Chézy number of natural rivers is found in the range $C = 0.01 \sim 0.07$ (see figure 1.1).

The Chézy number can in principle be computed from hydrodynamics. It therefore depends on the flow regime (laminar or turbulent), which is itself determined by the relative importance of inertial and viscous effects. The dimensionless number characterizing this ratio is the Reynolds number, which compare the inertial timescale U/H to the viscous diffusion time-scale ν/H^2, where ν is the kinematic viscosity:

$$R = \frac{\bar{u}H}{\nu}. \tag{1.2}$$

When the Reynolds number is much smaller than 1, the flow is dominated by viscosity. It can therefore be described with the Stokes equations. Conversely, if the Reynolds number is much larger than 1, the flow is turbulent, which means that it presents space-time fluctuations over a wide range of scales. The Reynolds number of natural rivers is always very large, however it varies depending to the nature of the river: little torrents, Seine river, Amazon have characteristic reynolds of $R \simeq 10^4$, $R \simeq 10^6$ and $R \simeq 10^8$ (Bunte *et al.* 2010). In our lab experiment (see chapter 9), however, the typical flow thickness is on the order of the millimeter scale, the velocity on the order of 10 $\mathrm{cm\,s^{-1}}$ so that the Reynolds number is typically around 10^2. This value lies in a cross-over regime between laminar and turbulent regimes. The order of magnitude clearly indicates that inertial effects are dominant over viscosity. However, in many laboratory flows over smooth surfaces, such a Reynolds number is small enough for the flow to remain laminar i.e. without any space time fluctuations. We have different indications, that will be discussed in chapter 9, that this is not the case in our centimeter scale river. This may be due to the influence of the roughness of the sand bed and/or to sediment transport. In the chapters devoted to hydrodynamics results (chapters 3 and 4), we will then develop a turbulent description of the hydrodynamics and we will systematically compare it to the laminar solutions of Navier-Stokes taken as a reference to which such results can be compared.

In the viscous regime, the Chézy and the Reynolds numbers are not independent: as shown below C goes as R^{-1}. However, this is not the case in the turbulent regime, where different surface layers (different roughnesses for instance) can induce different frictional stresses, for the very same mean velocity.

A river presents a free surface, which can propagate gravity (and capillarity) waves. In the limit of long wavelengths λ, the wave propagation speed does not depend on λ and therefore scales on $\sqrt{gH}$. The relative influence of surface waves to convective effects is characterized by the Froude number $\mathcal{F}$. It compares the flow velocity to the velocity of long gravity waves:

$$\mathcal{F} \equiv \frac{\bar{u}}{\sqrt{gH}}. \tag{1.3}$$

At Froude number smaller than 1, gravity effects are so important that the free surface essentially remains insensitive to possible disturbances coming from the bed. Conversely, at large Froude number, free surface deflections can easily be excited. The magnitude of the most of river is largely below 1, for example the Seine and Amazon rivers have Froude $0.23 \sim 0.48$ and ~ 0.09 respectively. On the contrary, in most torrents, the Froude number is of order 1 or larger. The Froude number is not independent of the other dimensionless numbers. More precisely, it can be expressed as:

$$C = \frac{\sin\theta}{\mathcal{F}^2}. \tag{1.4}$$

For natural rivers, as the Chézy number is roughly a constant, the Froude number is essentially selected by the slope.

In summary, the hydrodynamics of rivers in their central part is controlled by two principal dimensionless numbers: the Reynolds number which gives the flow regime and the Froude number which characterizes the excitability of the surface. The third dimensionless number (the Chézy number) is a subdominant parameter which is independent of $\mathcal{F}$ and R in the turbulent regime only, but does not present significant variations. We will now start the quantitative description of the flow.

1.3 Navier-Stokes equations

We first write the general laws of fluid mechanics for a incompressible fluid, known as Navier-Stokes equations. We consider the velocity field $\mathbf{u}(x, y, z, t)$ in a generic situation. It is expressed using the following coordinates: x is the overall direction of the flow, y is in-plane transverse and z is normal to the plane, oriented upwards. The

x, y, z-components of the velocity $u_i(x, y, z, t)$ are noted u, v, w respectively. Then, the momentum balance reads

$$\rho \left(\partial_t u_i + u_j \partial_j u_i\right) = \rho g_i - \partial_i P + \partial_j \sigma_{ij}, \tag{1.5}$$

where ρ is the fluid density and g_i the components of the gravity acceleration. We will consider that the velocity of sound in water ($1500\, m\, s^{-1}$) is large enough compared to the typical flow velocity to neglect compressible effects. The pressure P is then determined from the continuity equation, which expresses the conservation of mass:

$$\partial_j u_j = 0. \tag{1.6}$$

σ_{ij} stands for the viscous stress tensor which, for a Newtonian fluid, is proportional to the strain rate $\dot{\gamma}_{ij} = \partial_i u_j + \partial_j u_i$:

$$\sigma_{ij} = \rho \nu \dot{\gamma}_{ij}. \tag{1.7}$$

We recall that ν is the kinematic viscosity. It is convenient to divide Navier Stokes equations by ρ and to define a reduced pressure $p = P/\rho$ and a reduced stress tensor $\tau_{ij} = \sigma_{ij}/\rho$. In the remaining part of the manuscript, we will simply call p, the pressure and τ_{ij} the stress. We present our apologizes to the reader that would be sensitive to this abuse of language. The Navier-Stokes equation then reads:

$$\partial_t u_i + u_j \partial_j u_i = g_i - \partial_i p + \partial_j \tau_{ij}. \tag{1.8}$$

1.4 Laminar solution for the flow over a smooth inclined plane

Equations (1.6) and (1.8) simplify in the case of steady and homogeneous flows. The velocity field has then a single non-zero component $u(z)$. Projecting the momentum equation along z, one gets the hydrostatic pressure field:

$$p(z) = p_0 + g \cos\theta (H - z), \tag{1.9}$$

where p_0 is the pressure in air, above the flow. In the following, we will omit this term, which does not have any physical influence. Projecting now the dynamical equation along x, we get:

$$\tau_{xz}(z) = g \sin\theta (H - z). \tag{1.10}$$

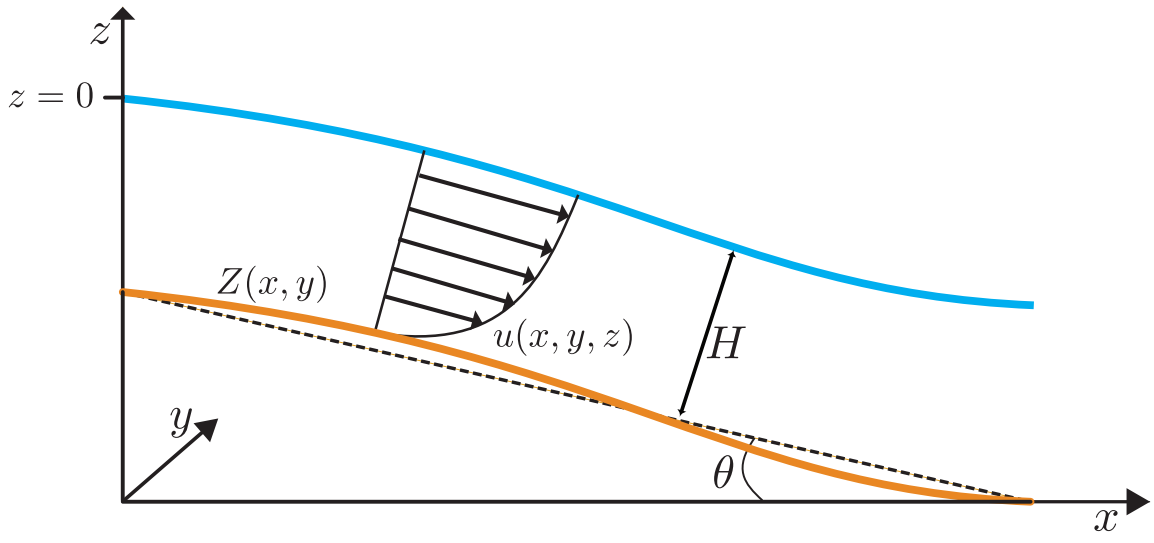


Figure 1.2: Free surface flow in the homogeneous laminar regime.

To obtain these two expressions, we have used the continuity of stresses at the interface. It is convenient to express these equations in terms of the basal shear velocity u_*, defined by $\tau_{xz}(0) = u_*^2$. From the expression of the stress, one gets

$$u_* = \sqrt{gH \sin\theta}. \tag{1.11}$$

The stress field then reads:

$$p(z) = \frac{u_*^2}{\tan\theta}\left(1 - \frac{z}{H}\right), \tag{1.12}$$

$$\tau_{xz} = u_*^2\left(1 - \frac{z}{H}\right). \tag{1.13}$$

Integrating the shear stress with (1.7), one obtains the velocity field:

$$u(z) = \frac{u_*^2}{\nu}\left(z - \frac{z^2}{2H}\right). \tag{1.14}$$

It is interesting to derive the different dimensionless numbers for this Poiseuille-like flow, for which $\bar{u} = 8$ cm/s. The Reynolds number reads:

$$R = \frac{\bar{u}H}{\nu} = 220. \tag{1.15}$$

The Froude number is equal to:

$$\mathcal{F} = \frac{u_*^2 H}{3\nu\sqrt{gH}} = \frac{\sqrt{gH^3}\sin\theta}{3\nu}. \tag{1.16}$$

Finally, the Chézy number defined in (1.1) becomes:

$$C = \frac{3\nu}{\bar{u}H} = \left(\frac{3\nu}{u_* H}\right)^2. \tag{1.17}$$

1.5 Turbulent flow: Reynolds decomposition

Neither real nor laboratory-scale rivers present a laminar flow. It means that the velocity field presents fluctuations, although the driving is permanent and steady. The statistical description of turbulent fluctuations is a difficult, partly open, problem in itself. In the case of rivers, one can obtain a satisfactory description of the flow by a simple averaging over fluctuations. One can then ignore the modern aspects of turbulence (Ross *et al.* 2004, van Boxel *et al.* 1999) and start from the work performed by Reynolds and Prandtl before the second War. The main idea is, just like for the kinetic theory of gas, to split the velocity into two contributions: the mean velocity $U_i = \langle u_i(x,y,z,t)\rangle$ and the the random turbulent fluctuations u_i':

$$u_i(x,y,z,t) = U_i(x,y,z,t) + u_i'(x,y,z,t). \tag{1.18}$$

The exact meaning of the average operator can be safely ignored at this stage, provided that the fluctuation field has a zero average. It can represent an average over realizations of the same experiment or a low pass filtering in time of the velocity field. The same decomposition is also applied to the pressure field. Assuming that the Reynolds number is large, we first neglect the viscous stress. Taking the average of Navier-Stokes equations one obtains the Reynolds averaged equations (R.A.N.S) which is formally identical but written for mean velocities:

$$\partial_t U_i + U_j\partial_j U_i = g_i - \partial_i p + \partial_j \tau_{ij}, \tag{1.19}$$

$$\partial_i U_i = 0, \tag{1.20}$$

where p is now is averaged pressure field and τ_{ij} is the *Reynolds stress tensor* defined by

$$\tau_{ij} = -\left\langle u_i' u_j' \right\rangle. \tag{1.21}$$

It closely resembles the kinetic tensor that appears in the Virial relation, in the kinetic theory of gas. It reflects the transport of momentum by turbulent fluctuations.

If an upward velocity fluctuation is correlated with a rightward velocity fluctuation, then a vertical flux of horizontal momentum appears, on the average. From the point of view of the mean velocity field, turbulent fluctuations transport momentum in a way analogous to viscosity (itself related to the Brownian motion of particles).

In order to use the Reynolds averaged equations, the Reynolds stress tensor must be expressed as a functional of the average strain rate $\dot{\gamma}_{ij} = \partial_i U_j + \partial_j U_i$. This is known as the closure problem. Indeed, the equation governing the evolution of $\left\langle u_i' u_j' \right\rangle$ depends on the tensor $\left\langle u_i' u_j' u_k' \right\rangle$. The evolution equation for $\left\langle u_i' u_j' u_k' \right\rangle$ depends on $\left\langle u_i' u_j' u_k' u_l' \right\rangle$, and so on. The problem takes the form of an open hierarchy of equations. One therefore needs to introduce, at some order, a phenomenological condition that closes the problem. The simplest (first order) closure is to relate the Reynolds stress tensor to $\dot{\gamma}_{ij}$, in analogy with the rheology of Newtonian fluids:

$$\tau_{ij} = \nu_t \dot{\gamma}_{ij}. \tag{1.22}$$

ν_t is called the eddy viscosity. Note that one must in principle add the molecular viscosity ν to the turbulent one. ν_t must itself be expressed as a function of the characteristics of the flow.

1.6 Turbulent flow on an incline

Since the determination of the eddy viscosity plays a central role in the Reynolds averaged approach through the choice of the turbulent closure, we wish to perform a dimensional analysis of this quantity and understand its properties. We first consider the simplest case of a flow of infinite thickness over an inclined plane. ν_t has to depend on the properties of this flow and for this reason it must be written as a combination of characteristic quantities. Dimensionally it is equivalent to the product of a velocity by a length:

$$\nu_t = |u| \; L. \tag{1.23}$$

This combination is however useless since velocities are not galilean invariant and so should not be used to build an eddy viscosity. On the contrary, an invariant quantity is built from the derivative of the velocity $\partial_i u_j$, which, once rotations are removed, gives the strain rate $\dot{\gamma}_{ij} = \partial_i u_j + \partial_j u_i$. From the dimensional point of view we need to multiply the strain rate modulus by a squared length and we then can write:

$$\nu_t = L^2 \; |\dot{\gamma}| \,, \tag{1.24}$$

where $|\dot{\gamma}|^2 = \frac{1}{2}\dot{\gamma}_{ij}\dot{\gamma}_{ij}$ and L is called the Prandtl mixing length. Since the free surface is here located at infinity, the only relevant length we can adopt is the vertical distance to the bed: $L = \kappa\, z$ where the constant of proportionality $\kappa \simeq 0.4$ is the called the von Kármán constant. The eddy viscosity takes the form:

$$\nu_t = \kappa^2\, z^2\, |\dot{\gamma}|. \tag{1.25}$$

This closure associated to the Reynolds equations (1.19) and (1.20) gives us the steady and homogenous profile of the longitudinal velocity for a flow unconfined along the three directions:

$$u(z) = const_1 + \frac{u_*}{\kappa} \ln(z). \tag{1.26}$$

We immediately see that the value of the velocity at the bottom boundary $z = 0$ diverges. This non-physical problem can be overtaken by idealizing a sublayer of thickness z_0 where the fluid velocity vanishes, leading to:

$$u(z) = \frac{u_*}{\kappa} \ln(z/z_0). \tag{1.27}$$

z_0 is called the *hydrodynamic roughness*. Its physical origin can be of different sort, e.g. viscous effects, geometrical protrusions, sediment transport. The existence and the value of z_0 is the only thing that the turbulent flow above this surface layer needs to know. The flow is said to be hydrodynamically smooth when the roughness is controlled by the viscous length

$$z_0 \sim \nu/u_*. \tag{1.28}$$

For a granular bed, this implies $z_0 \gg d$ with d the grain size, and the thin layer just above the grains can be considered in laminar regime. On the other hand if the viscous length is on the same order or smaller than the geometrical lengths we can find at the bed surface (i.e. the grain size, transport layer thickness, bedforms etc), the flow is said to be hydrodynamically rough and z_0 will be controlled by these geometrical length scales. In our case the grains diameter d provides the relevant length scale with z_0 varying from a fraction of grain size to ten grains size, depending on whether there is transport or not.

In the case of a water flow of finite depth H, experimental data show that the logarithmic profile of the velocity does not hold only in proximity of the bed (as we would have $z \ll H$ and we could refer to the unbounded flow case), but all over the depth, including the region close to the free surface. This observation suggests that

for a turbulent, homogenous, steady, free surface flow, one can phenomenologically writes the velocity profile as

$$u(z) = \frac{u_*}{\kappa} \ln\left(1 + \frac{z}{z_0}\right). \tag{1.29}$$

The above expression for the velocity correctly verifies the vanishing condition at the bottom $u(0) = 0$. We write consistently the pressure and shear profiles

$$p(z) = \frac{u_*^2}{\tan\theta}\left(1 - \frac{z}{H}\right), \tag{1.30}$$

$$\tau_{xz} = -u_*^2\left(1 - \frac{z}{H}\right), \tag{1.31}$$

as imposed by stress balance, where the shear velocity u_* is still given by Eq. (1.11). Note that the sign convention for the shear stress between the turbulent and laminar descriptions are opposite. This is possible with the same expression for the turbulent viscosity as for the unbounded case, but with a modified expression for the mixing length:

$$L(z) = \kappa(z + z_0)\sqrt{1 - z/H}. \tag{1.32}$$

Far from the water surface ($z \ll H$), L scales as the distance the bed z, as for the unfounded case. For z close tot H, however, L is reduced, which can be interpreted as vortices limited by the presence of the water surface.
We can give now the final expression of the turbulent stress tensor τ_{ij} that we will frequently use later:

$$\tau_{ij} = \rho\kappa^2 L^2|\dot{\gamma}|\left(\frac{1}{3}\chi^2|\dot{\gamma}|\delta_{ij} - \dot{\gamma}_{ij}\right), \tag{1.33}$$

where χ is a phenomenological constant in the range 2.5 - 3.

Finally, for later use, we give below in the case of a free surface turbulent flow, the expressions of the dimensionless numbers mentioned above. First, the Reynolds number reads:

$$R = \frac{\bar{u}H}{\nu} = \frac{u_* H}{\kappa\nu}\left[\ln\left(1 + \frac{z_0}{H}\right) - 1\right]. \tag{1.34}$$

The Froude number is equal to:

$$\mathcal{F} = \frac{u_*}{\kappa\sqrt{gH}}\left[\ln\left(1 + \frac{z_0}{H}\right) - 1\right]. \tag{1.35}$$

Finally, the Chézy number defined in (1.1) becomes:

$$C = \left(\frac{u_*}{\bar{u}}\right)^2 = \frac{k^2}{\left[\ln\left(1 + \frac{z_0}{H}\right) - 1\right]^2}. \tag{1.36}$$

under the approximation of $z_0 \ll H$.

1.7 Depth averaged Saint Venant equations

The standard description of river flows used in Hydrology is the so-called depth-averaged Saint-Venant framework. In particular, it has been extensively used by Seminara and co-authors to investigate the meandering instability (Parker 1976, Zolezzi & Seminara 2001). On the other hand, such a model does not describe, by definition, the vertical structure of the flow. It therefore cannot contain the dynamical mechanism proposed by Einstein in 1926. It is important here to derive these equations, and discuss their limits. They will serve all along this manuscript as a reference to which our results will be compared.

Saint-Venant equation is a depth-averaged shallow water hydrodynamical equations derived from the laminar Navier-Stokes equations. The approximation of shallow water means that the longitudinal and the transversal dimensions of the river geometry are much larger than the vertical one. Consequently on can assume:

$$\lambda \gg H \tag{1.37}$$
$$W \gg H. \tag{1.38}$$

where $\lambda = 2\pi/k$ is the typical wavelength of the meandering oscillation of the river, W and H are the river width and depth respectively. These conditions are equivalent to:

$$kH \ll 1 \tag{1.39}$$
$$\beta \equiv W/H \gg 1. \tag{1.40}$$

We will now derive the depth averaged Saint-Venant equations, emphasizing the fact that it is an uncontrolled approximation of the three-dimensional equations. We will perform the derivation from two different perspectives. Let us first consider the limit of small Reynolds numbers. Then, inertial terms can be neglected so that the momentum equation reduces to:

$$g_i - \partial_i p + \nu \partial_{jj} u_i = 0. \tag{1.41}$$

Using now the fact that the vertical dimension is much smaller than the two others, the diffusion of momentum mostly takes place along this direction:

$$\partial_{zz} u_i \gg \partial_{xx} u_i. \tag{1.42}$$

One then deduces that the pressure field is hydrostatic along the direction z:

$$g \cos\theta - \partial_z p = 0, \tag{1.43}$$

and that the equation governing the velocity in the x and y directions reads:

$$g_i - \partial_i p + \nu \partial_{zz} u_i = 0. \tag{1.44}$$

These equations can be integrated and predict a semi-parabolic velocity profile similar to that obtained in the homogeneous case. This asymptotic regime constitutes the so-called lubrication approximation. It is a rigorous and controlled derivation in the limit $kH \ll 1$, $\beta \gg 1$ and $Re \ll 1$. The extension of this equation to inertial laminar flows constitutes an uncontrolled further step. The idea is to consider that the velocity profile is still semi-parabolic in that case and to plug it as a test function in the Navier-Stokes equations. The integration over the flow depth then serves to project the equation on this test function. As the vertical structure of the flow is lost, even in the shallow water regime, the approximation is not rigorous but may reflect the physics correctly.

Saint-Venant equations can be derived from the macroscopic conservation equations of the mass and for momentum. We note $Z(x, y, t)$ the bed form elevation and $h(x, y, t)$ the water surface. In the laminar case, the stress gradient writes

$$\partial_j \tau_{ij} = -3\nu \frac{u_i}{h^2}, \tag{1.45}$$

and the pressure is

$$p(x, y, t) = g\left[Z(x, y, t) + h(x, y, t)\right]. \tag{1.46}$$

From (1.8), we can then write the St-Venant laminar moment equation for a flow over a bed of profile as:

$$\partial_t u_i + u_j \partial_j u_i \;=\; -g\,\partial_i\left(Z + h\right) - 3\nu \frac{u_i}{h^2}. \tag{1.47}$$

and the continuity equation (1.6) reads

$$\partial_j (h u_j) = 0. \tag{1.48}$$

In the case of a turbulent flow, we have instead

$$\partial_j \tau_{ij} = -C \frac{|\mathbf{u}| u_i}{h}, \tag{1.49}$$

where C is the Chézy number, and the depth-averaged RANS equations give

$$\partial_t u_i + u_j \partial_j u_i \;=\; -g\,\partial_i\left(Z + h\right) - C \frac{|\mathbf{u}| u_i}{h}, \tag{1.50}$$

$$\partial_j (h u_j) \;=\; 0. \tag{1.51}$$

Chapter 2

Flow in a channel

In the previous chapter we have introduced the first brick to study the meandering instability: the hydrodynamics on an infinite inclined plane in the case of a free surface flow. The phenomenological description we used involves a Prandtl-like closure of the stress tensor, which depends on a mixing length L function of z and on the water depth H. In order to discuss the robustness of hydrodynamical descriptions, we also derived two sets of equations that are commonly used in studies on rivers: respectively the turbulent and laminar formulations of the depth-averaged Saint-Venant equations.

The next step, which we address in this chapter, is to account for a confined system along the transversal direction, i.e. provide a coherent description of banks which takes into account their effects on the flow. This will serve to define a base state of the river geometry on which we will perform a linear stability analysis.

2.1 Bank description

A transversally confined system, like meandering rivers, introduce a new dimension, the channel width W, and consequently a new dimensionless parameter: the aspect ratio β, defined as:

$$\beta = \frac{W}{H} \,. \tag{2.1}$$

It is not simple to determine with precision the aspect ratio of rivers because the transversal profile is irregular. We show in figure 9.13 such a profile that we have measured in the Leyre river, for which $\beta \simeq 20$ ($\beta \simeq 4$ at food plate).

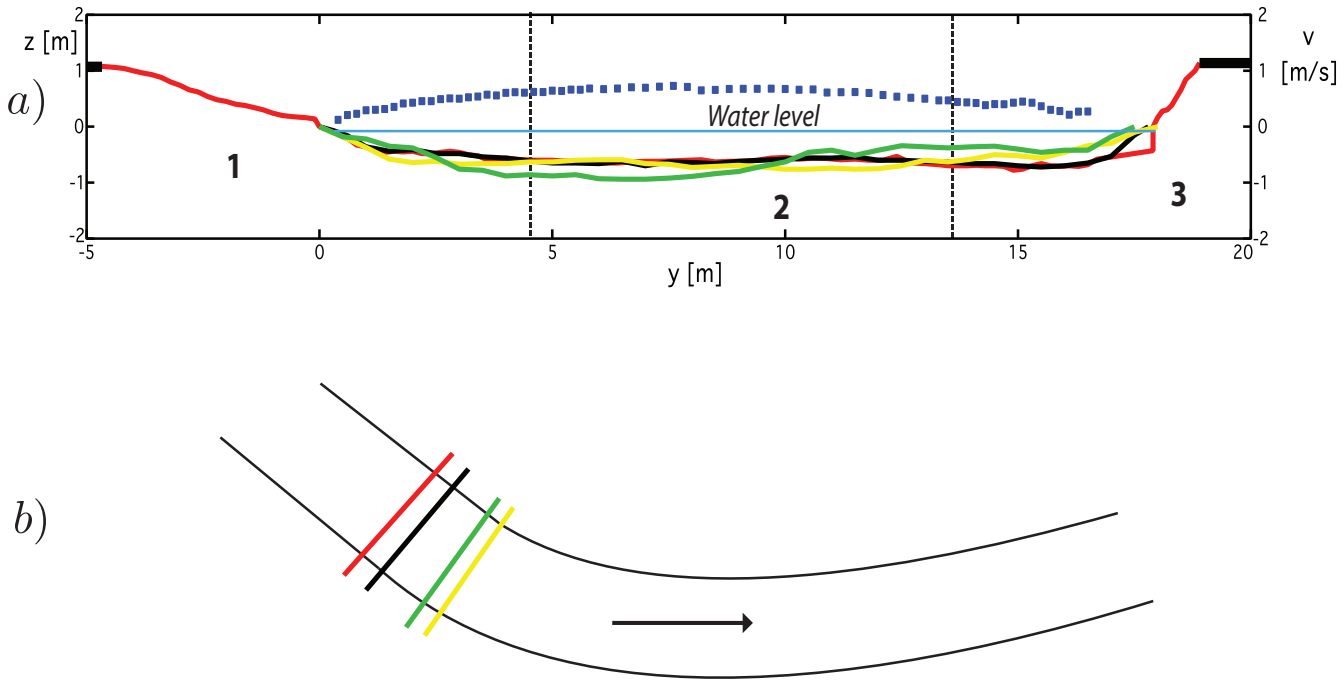


Figure 2.1: a) Different transverse profiles of the river Leyre (44° 30′ N, 0° 49′ W) in which we can identify three different regions: the middle of the river and the boundary layers close to the banks. b) Schematic top view of the place where the profiles were measured.

One can virtually split the river profile into three zones: two regions close to the banks (regions **1** and **3**) where the bed is inclined down to the third zone, in the middle of the river (region **2**), in which the profile of the bed is mainly horizontal. This decomposition is better defined for large aspect ratios, but less obvious in small scale rivers ($\beta \simeq 1$), as the middle flat part can be no longer present.

The typical size of the regions close to the banks scale with the water depth H. Because transversal and vertical velocity variations are of the same order, these regions have an influence on the velocity in a layer of width $W_b \sim H$. In the central zone, of size $\sim W$, the approximation of an unbounded flow (previous chapter) is well verified. For asymptotically large aspect ratios, the banks can then be idealized as boundary conditions for the channel, and to which the velocity of the flow must be parallel. In the next section, we will use this limit to defined the geometry of the base state for our linear stability analysis, and we will not describe the bank layer itself, inside which the velocity decreases to zero.

2.2 Geometry of the base state and mode decomposition

As mentioned at the beginning of this chapter, we need a base state configuration over which we can perform a linear stability analysis of the meandering instability. The base state, describing the reference steady and homogeneous flow, will be expressed having in mind rivers of large aspect ratio. We consider a channel composed of a flat bed and of two vertical walls that follow longitudinally the flow direction. A scheme of this geometry is provided by Fig. 2.2 – a. Let us call $Y^{L/R}$ respectively the right and the left banks with respect the direction of the river flow. We set the axes origin at the bed surface and in the middle of the channel. The longitudinal x-axis is oriented along the flow direction, the vertical one z is oriented from the bed toward the free surface of the river and the transversal direction y is pointing to the left bank. The banks are located at:

$$Y^{L/R} = \pm y_0 \,, \tag{2.2}$$

where $y_0 = W/2$. The river bed $Z(x, y)$ is flat and depends on the channel slope θ exclusively (see Fig. 1.2):

$$Z(x, y) = Z_0(x) = -x \, \tan\theta \,. \tag{2.3}$$

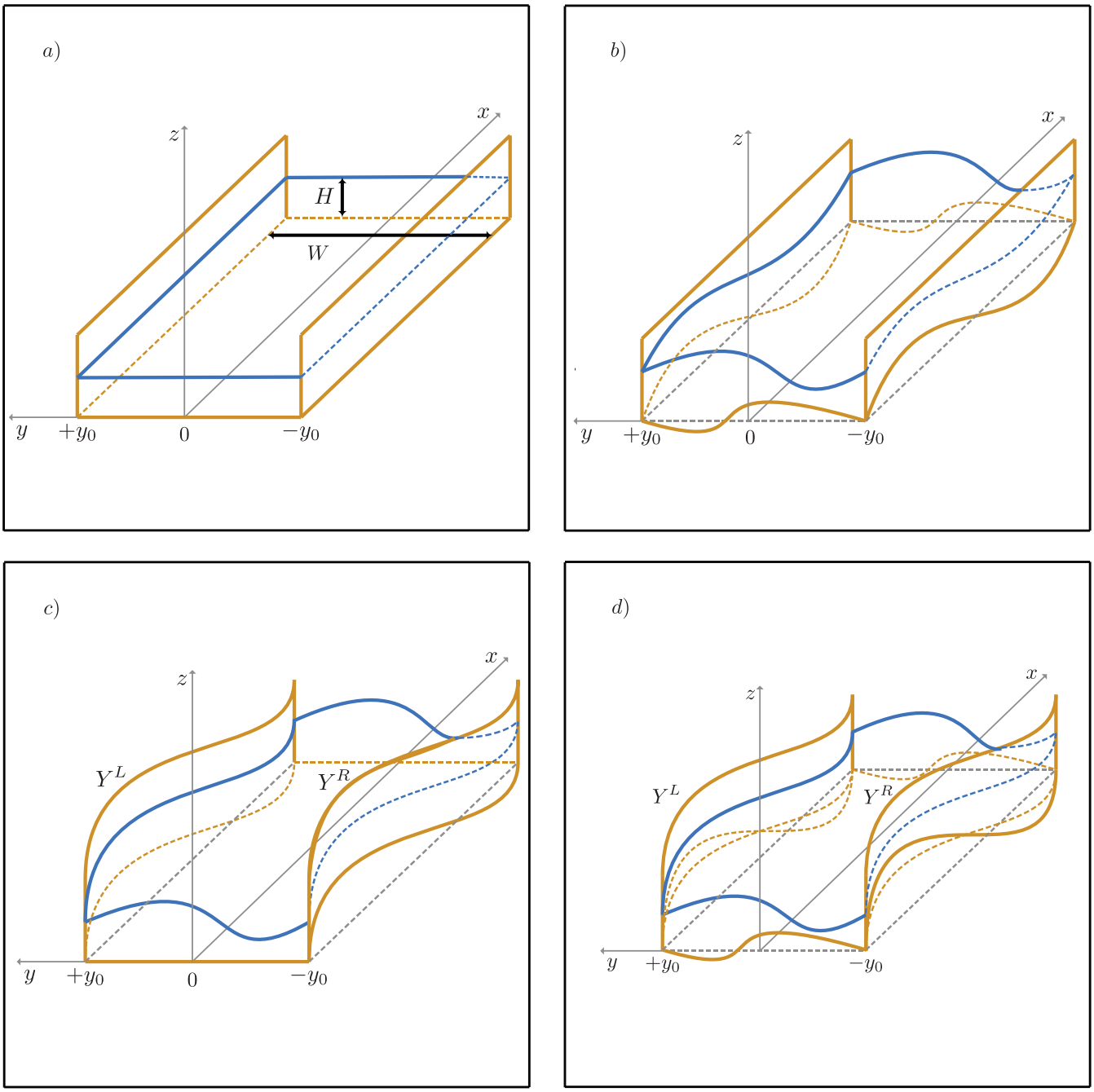


Figure 2.2: Schematics of a river channel with (a) straight banks and a flat bed, (b) straight banks and an undulated bed, (c) meandering banks and a flat bed, (d) meandering banks and an undulated bed.

2.2.1 Analogy with wave guides

For this configuration hydrodynamics is described by the general equations detailed in chapter 1, with the additional requirement of slip a condition for the flow at the banks, which is equivalent to say that the y-component of the velocity vanishes at the banks:

$$v(\pm y_0) = 0\,. \tag{2.4}$$

The flow is invariant along x and obeys to symmetry relations in the transverse direction y. The problem is analogous to wave guides in electromagnetism, for which in the unbounded case the modes are on the form of plane waves $e^{ikx+iry}$, where k and r are the longitudinal and transversal wavenumbers. In the presence of transversally bounded scenario, the eigenmodes of the system are imposed by symmetry and correspond to the superposition of two plane waves $e^{\pm iry}$. A generic field ψ can then be expressed as:

$$\psi = \left[\psi^+\left(e^{iry}+e^{-iry}\right)+\psi^-\left(e^{iry}-e^{-iry}\right)\right]\,e^{ikx}\,, \tag{2.5}$$

decomposed on even and odd waves, respectively represented by the first and the second term of the function ψ. Taking the transverse velocity $\psi = v$, we see that the boundary conditions at the banks (2.4) impose $v^+ = 0$, i.e. a discretization of the transverse wave number

$$r_n = n\frac{\pi}{W}\,, \tag{2.6}$$

where n is an integer.

2.2.2 $\langle$Bra$|$ket$\rangle$ formalism

From this analogy, we see that a convenient way to describe hydrodynamics in a rectangular section is to decompose all field on the Fourier eigenmodes of the system. We introduce for the next sections the functions:

$$|c_n\rangle = \cos\left[n\pi\left(\frac{y}{2y_0}+\frac{1}{2}\right)\right], \tag{2.7}$$

$$|s_n\rangle = \sin\left[n\pi\left(\frac{y}{2y_0}+\frac{1}{2}\right)\right], \tag{2.8}$$

where $n \geq 1$ is an integer. We will also need the vector $|1\rangle = |c_0\rangle$ to complete the basis of sines. All these functions verify the two derivative laws

$$\partial_y|c_n\rangle = -r_n|s_n\rangle, \tag{2.9}$$

$$\partial_y|s_n\rangle = r_n|c_n\rangle, \tag{2.10}$$

where

$$r_n = \frac{n\pi}{2y_0}\,. \tag{2.11}$$

We define the projection operator as:

$$\langle \phi | \psi \rangle = \int_{-y_0}^{y_0} \phi(y)\psi(y)dy. \tag{2.12}$$

For the base vectors $n, m \geq 1$ we get:

$$\langle c_n | c_m \rangle = y_0 \delta_{nm}, \tag{2.13}$$

and

$$\langle s_n | s_m \rangle = y_0 \delta_{nm}, \tag{2.14}$$

where δ_{nm} is the Kronecker symbol. However, notice that

$$\langle s_n | 1 \rangle = \frac{2y_0}{n\pi}\,[1-(-1)^n] = \frac{4y_0}{n\pi}\,\theta_n = \frac{2}{r_n}\,\theta_n, \tag{2.15}$$

where θ_n is null for even n and equal to 1 for odd n.

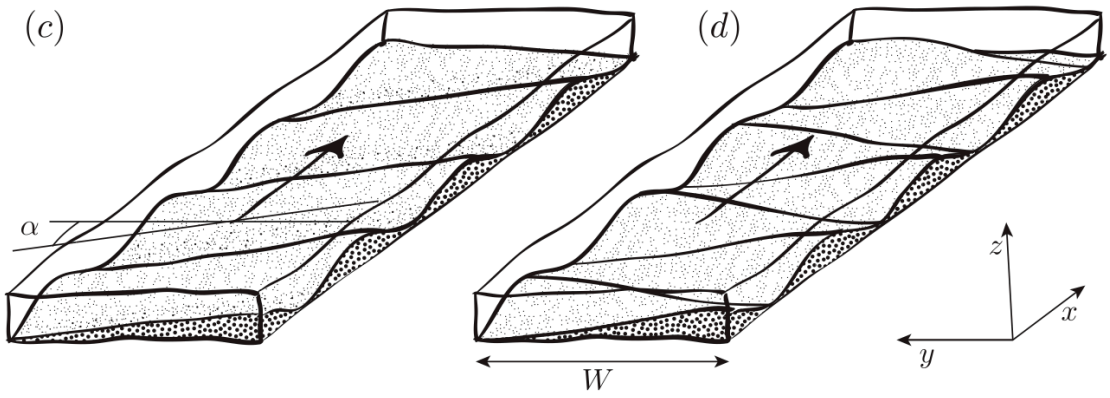


Figure 2.3: (a) Schematic showing a plane wave mode inclined at an angle α with respect to the flow direction. (b) Schematic showing alternate bars in a channel of width W. They correspond to guided modes obtained by superimposing two plane waves propagating with opposite angles.

2.3 Bed and banks modulations

In order to be able to perform the linear stability analysis of a rectangular channel, we need to describe the hydrodynamical response of disturbances of the base state. These perturbations can be divided into two independent problems: the flow in a channel with straight banks and an undulated bottom, and the flow in a meandering channel which presents a flat bed. At linear order, the general case can simply be thought of as the superposition of these two situations. Before proceeding to the rather technical aspects of the derivation of these hydrodynamic calculations (next two chapters), we show here in a simple way how we write the problem. We also anticipate the physical discussion of the main output of these calculations, namely the basal shear stress. As a matter of fact, this is the relevant quantity that controls sediment transport.

2.3.1 Undulated bed

We consider a perturbation to the flat bed, with a topography given by:

$$Z(x,y) = Z_0(x) + Z_1(x,y)\,. \tag{2.16}$$

The perturbation Z_1 can be decomposed on the eigenvalues of the system as described in the previous section and reads, using the bracket formalism:

$$k|Z_1\rangle = e^{ikx} \sum_{n=1}^{\infty} kZ_n\,|c_n\rangle\,, \tag{2.17}$$

where k is the wavenumber of the disturbance. All dimensionless amplitudes kZ_n are assumed to be small in front of 1. In Fig. 2.3b, we schematically show the mode $n = 1$, for which the angle α of the undulations with respect to the flow direction verifies $\tan\alpha = r_1/k$.

The linear response of all hydrodynamical quantities with respect to the bed perturbation (2.17) can be similarly expanded as sums over the Fourier modes. For example for the water depth we will have:

$$k|h_1\rangle = e^{ikx} \sum_{n=1}^{\infty} kZ_n\,H_n\,|c_n\rangle, \tag{2.18}$$

where H_n is a dimensionless coefficient, which must be computed from the hydrodynamic equations chosen to describe the flow – e.g. Navier-Stokes, RANS or Saint-

Venant equations. We can do the same for the velocities:

$$|u_1\rangle = u_* e^{ikx} \sum_{n=1}^{\infty} kZ_n U_n |c_n\rangle \tag{2.19}$$

$$|v_1\rangle = u_* e^{ikx} \sum_{n=1}^{\infty} kZ_n V_n |s_n\rangle \tag{2.20}$$

where U_n and V_n are similarly dimensionless functions of kz. Note that we have defined these coefficients taking the shear velocity u_* as the dimension quantity. Note also that, the velocity perturbation v_1 must be decomposed over the $|s_n\rangle$ in order to respect its symmetry properties along the y-axis.

2.3.2 Meandering banks

We now consider a flow in a meandering channel, as seen in Fig. 2.2 – c. The left (L) and right (R) banks of the channel are now slightly disturbed from the straight configuration of the base state while the bed is here considered plate: $Z(x, y) = Z_0(x)$. Without loss of generality, we can consider banks described by:

$$Y^{L,R} = \pm y_0 + \Upsilon e^{ikx}, \tag{2.21}$$

where Υ and k are respectively the amplitude and the wavenumber of the modulation. The dimensionless parameter $k\Upsilon$ is assumed to be small in front of 1. For this meandering configuration, the condition that the flow velocity must be parallel to the bank is now written as:

$$v(Y^L) = v(Y^L)\,\partial_x Y^L\,, \tag{2.22}$$

$$v(Y^R) = v(Y^R)\,\partial_x Y^R\,. \tag{2.23}$$

Similarly to the previous paragraph, we can write all hydrodynamical quantities in response to this bank perturbation as expansions on the Fourier modes. The water depth, for instance, reads

$$k|h_1\rangle = k\Upsilon\, e^{ikx} \sum_{n=1}^{\infty} H_n |c_n\rangle, \tag{2.24}$$

where H_n is still (another) dimensionless coefficient to be computed. The transversal

and longitudinal components of the fluid velocity are written as:

$$|u_1\rangle = u_* \, k\Upsilon \, e^{ikx} \sum_{n=1}^{\infty} U_n \, |c_n\rangle \tag{2.25}$$

$$|v_1\rangle = u_* \, k\Upsilon \, e^{ikx} \left\{ i|1\rangle + \sum_{n=1}^{\infty} V_n \, |s_n\rangle \right\} \tag{2.26}$$

Note importantly that the transversal velocity perturbation $|v_1\rangle$ has a term along the vector $|1\rangle$. This additional term to the sum over the $|s_n\rangle$ physically comes from the fact that the boundary contidions (2.22) and (2.23) must be verified:

$$v_1(\pm y_0) = iku_0 \, e^{ikx} \, . \tag{2.27}$$

Mathematically, the set of $|s_n\rangle$ is an incomplete basis for the description of the problem and become complete by adding the unity vector $|1\rangle$.

2.4 The basal shear stress

As already mentioned, the flow establishes in response to the bed and the bank profiles, but also generates bed/bank erosion or deposition through sediment transport. The main relevant quantity is the basal shear stress, i.e. the shear stress that the flow exerts on the bed of the channel. Its two x and y components τ_b^{xz} and τ_b^{yz} are amongst the hydrodynamical fields that we will compute for given bed or bank perturbations. We wish to express them within the same framework, i.e. as expansions over the Fourier modes. Taking u_*^2 as the dimension factor (recall that the fluid density is omitted), the basal shear stress in response to the bed perturbation can be generically written, at first order in kZ_n, as

$$|\tau_{1,b}^{xz}\rangle = u_*^2 \, e^{ikx} \sum_{n=1}^{\infty} kZ_n(A_x^n + iB_x^n) \, |c_n\rangle \tag{2.28}$$

$$|\tau_{1,b}^{yz}\rangle = u_*^2 \, e^{ikx} \sum_{n=1}^{\infty} kZ_n(iA_y^n - B_y^n) \, |s_n\rangle. \tag{2.29}$$

Similarly, in response to the bank perturbation, we write

$$|\tau_{1,b}^{xz}\rangle = u_*^2 k\Upsilon \, e^{ikx} \sum_{n=1}^{\infty} (C_x^n + iD_x^n) \, |c_n\rangle \tag{2.30}$$

$$|\tau_{1,b}^{yz}\rangle = u_*^2 k\Upsilon \, e^{ikx} \left\{ i\sqrt{C}|1\rangle + \sum_{n=1}^{\infty} (iC_y^n - D_y^n) \, |s_n\rangle \right\} . \tag{2.31}$$

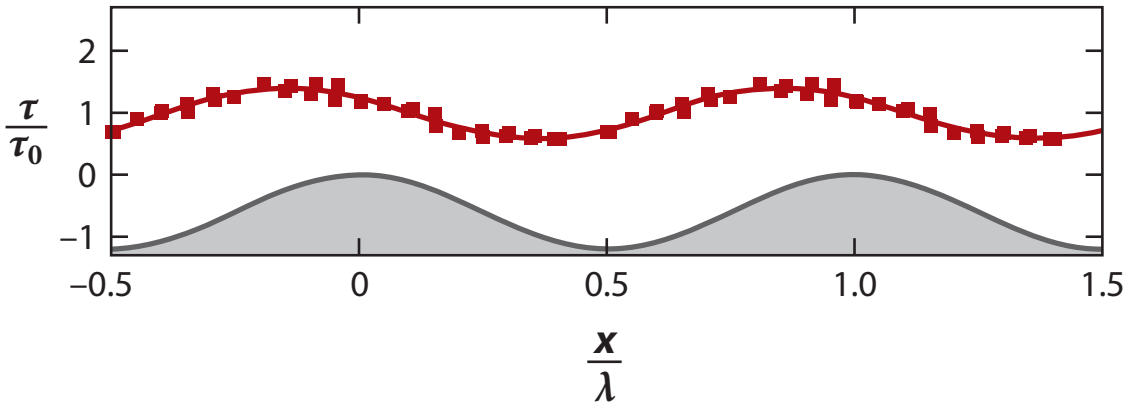


Figure 2.4: Red squares: measurements by Zilker et al. (1977) of the basal stress over a transverse sinusoidal bottom (schematics in grey). Red solid line: sinusoidal fit, at the bottom wavelength.

We call the $A^n_{x,y}$, $B^n_{x,y}$, $C^n_{x,y}$, $D^n_{x,y}$ the basal shear stress coefficients, defined here as dimensionless *real numbers*. Note that the τ_b^{xz} component is expressed on the $|c_n\rangle$ basis, whereas τ_b^{yz} is on the $|s_n\rangle$ basis, as to respect their symmetry along the y-axis. Note also that, as for v_1 in the previous section, the stress τ_b^{yz} in response to meandering banks has a component on the vector $|1\rangle$.

We can give an intuitive picture of these coefficients as follows. Consider, for the sake of simplicity, a purely transverse sinusoidal bottom $Z_1 = \zeta e^{ikx}$, i.e. infinite and homogeneous along the y axis (no banks). Then, there is one single component for the basal shear stress, τ_b^{xz}, which, similarly to Eq. (3.67), simply writes $\tau_b^{xz} = u_*^2\, e^{ikx} k\zeta(A_x + iB_x)$. This means that the shear stress over such a bed is also sinusoidal, but not necessarily in phase with the bottom (see Fig. 2.4). In fact, A_x quantifies the component *in phase* with the bottom, while B_x does that *in quadrature*. The physical origin of the coefficient A_x is the pinching of the streams lines on humps (Bernouilli effect): since the shear stress is proportional to the velocity gradient, it must be larger on bed maxima and smaller on bed minima. There is however a phase shift φ between the basal shear stress and the topography, given by $\tan\varphi = B_x/A_x$. When B_x is positive, the shear stress is *in advance* with respect to the topography, as for the data of Fig. 2.4, which is the generic case when $kH \gg 1$ (a large water depth with respect to the wavelength of the perturbation). This shift originates from the combined effects of fluid inertia and dissipation (Fourrière et al. 2010, Charru et al. 2013). A_x and B_x are functions of k and other quantities

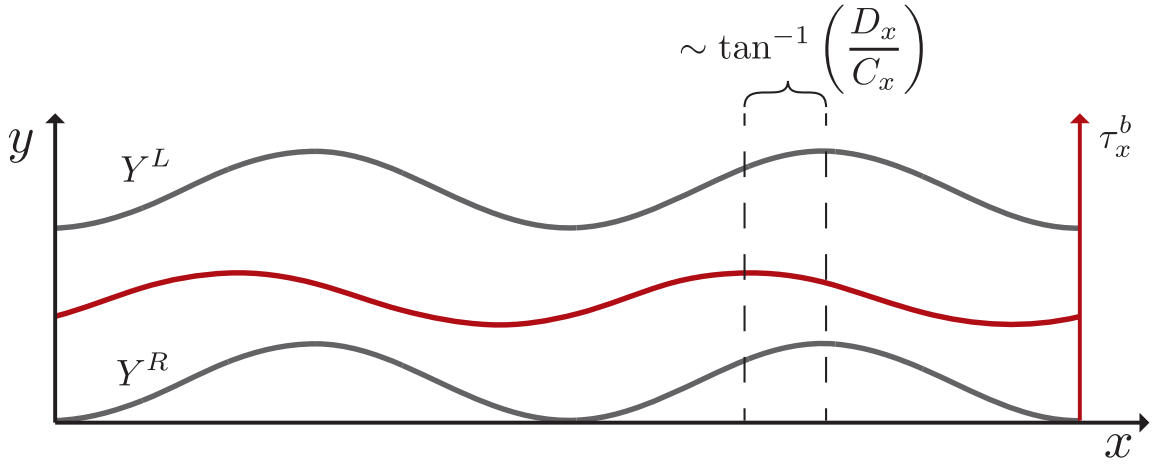


Figure 2.5: Schematic representation of basal stress τ_{yz}^b in response to meandering banks.

(water depth, Froude number). Their expressions in the limit very small kz_0 can be deduced from the asymptotic calculations of Jackson and Hunt (1975) and then improved by Sykes (1980), see also Belcher & Hunt (1998). In the transitional regime ($10^{-5} < kz_0 < 10^{-3}$) measurements have been performed by Zilker *et al.* (1977) and Frederick & Hanratty (1988) while models have been provided by Buckles *et al.* (1984), Cherukat *et al.* (1998), de Angelis *et al.* (1997), Henn & Sykes (1999), Zilker & Hanratty (1979). The quantitative description of flow separation for a sinusoidal bottom has been completely described by Lagree (2003). Furthermore, in the context of sub-aqueous ripples and dune formation, they have been computed by Fourrière et al. (2010).

In the more general case of a channelized flow, this analysis applies for each transversal mode labelled by the integer n. The coefficients A_y and B_y similarly quantifies the in-phase and in-quadrature parts of the y-component of the basal shear τ_b^{yz}. As for the flow in response to bank perturbations, the coefficients $C_{x,y}^n$ (resp. $D_{x,y}^n$) are the equivalent to $A_{x,y}^n$ (resp. $B_{x,y}^n$). In particular, the tangent of the phase shift between the shear τ_b^{xz} and the topography is given by the ratio D_x^n/C_x^n, for the mode labelled n.

2.5 Conclusion

In this chapter we have discussed the first ingredients necessary to perform a linear stability analysis of the meandering instability. We have identified two kinds of perturbations to the base rectangle-shaped channel: (i) straight banks and an undulated bottom, (ii) meandering banks and a flat bed. We have posed the framework inside which we will compute the hydrodynamical fields in response to these perturbations, and defined in particular the basal shear stress coefficients. The goal of the next two chapters is to compute these fields in the cases (i) and (ii) respectively.

Once this is done, we will be able to combine the bed and bank perturbations to solve the whole meander problem where both are coupled. All the fields will be written, at the linear order, as the superposition of the two contributions. For example for the longitudinal and transversal velocities perturbations we will have:

$$|u_1\rangle = u_* e^{ikx} \sum_{n=1}^{\infty} \left(U_n^Z \, kZ_n + U_n^B \, k\Upsilon \right) |c_n\rangle , \tag{2.32}$$

$$|v_1\rangle = u_* e^{ikx} \left\{ ik\Upsilon |1\rangle + \sum_{n=1}^{\infty} \left(V_n^Z \, kZ_n + V_n^B \, k\Upsilon \right) |s_n\rangle \right\} , \tag{2.33}$$

where U_n^Z, V_n^Z and U_n^B, V_n^B are respectively the bed and banks contributions. Similarly, we can write the longitudinal and traversal basal stress perturbations as:

$$|\tau_{1,b}^{xz}\rangle = {u_*}^2 e^{ikx} \sum_{n=1}^{\infty} \left[(A_x^n + iB_x^n) \, kZ_n + (C_x^n + iD_x^n) \, k\Upsilon \right] |c_n\rangle , \tag{2.34}$$

$$|\tau_{1,b}^{yz}\rangle = {u_*}^2 e^{ikx} \left\{ i\sqrt{C} k\Upsilon |1\rangle + \sum_{n=1}^{\infty} \left[\left(iA_y^n - B_y^n \right) kZ_n + \left(iC_y^n - D_y^n \right) k\Upsilon \right] |s_n\rangle \right\} \tag{2.35}$$

These stresses will be controlling the sediment transport disturbance, and thus the bed evolution.

Chapter 3

Hydrodynamics in a channel with straight banks and an undulated bottom

We now enter into the details of the linear response of hydrodynamics to an undulated bed in a straight channel. All physical quantities will be forced by the disturbed bottom

$$k|Z\rangle = e^{ikx} \sum_{n=1}^{\infty} kZ_n \, |c_n\rangle \,, \tag{3.1}$$

and they will be similarly written as first order expansion with respect to the small dimensionless parameters kZ_n. One of the most important quantities we are interested in is the basal stress τ^b, and more precisely the coefficients A_x^n, B_x^n, A_y^n, and B_y^n introduced in the previous chapter. The aim of this chapter is to compute these coefficients for different hydrodynamical models, both in the laminar and turbulent regimes.

3.1 Laminar regime

In this section, we consider the water flow in the laminar regime.

3.1.1 Base flow

Using the water depth H, the longitudinal bed wavenumber k and the viscous length ν/u_*, we introduce the following dimensionless quantities:

$$\eta = kz, \tag{3.2}$$
$$\eta_0 = k\nu/u_*, \tag{3.3}$$
$$\eta_H = kH, \tag{3.4}$$

We then define the dimensionless base velocity profile $\mathcal{U}$ as

$$\mathcal{U}(\eta) = \frac{\eta}{\eta_0}\left(1 - \frac{\eta}{2\eta_H}\right). \tag{3.5}$$

Using these notations, the expressions of the base state derived in paragraph (1.4) can be rewritten as

$$u = u_* \mathcal{U}(\eta), \tag{3.6}$$
$$v = 0, \tag{3.7}$$
$$w = 0, \tag{3.8}$$
$$p = u_*^2 \frac{1}{\tan\theta}\left(1 - \frac{\eta}{\eta_H}\right), \tag{3.9}$$
$$\tau_{xz} = u_*^2 \left(1 - \frac{\eta}{\eta_H}\right), \tag{3.10}$$

and the Froude number as

$$\mathcal{F} = \frac{\eta_H}{2\eta_0}\sqrt{\sin\theta}\,. \tag{3.11}$$

3.1.2 First order equations

In response to the disturbance induced by the bed, the free surface is also modulated: $H + h_1(x, y, t)$. The first order perturbation of the water depth (2.18) reads:

$$k|h_1\rangle = e^{ikx} \sum_{n=1}^{\infty} kZ_n H_n \,|c_n\rangle \tag{3.12}$$

Similarly, we write first order disturbances for the velocity and stress components as

$$
\begin{aligned}
|u_1\rangle &= u_* \, e^{ikx} \sum_{n=1}^{\infty} kZ_n U_n(\eta) \, |c_n\rangle \\
|v_1\rangle &= u_* e^{ikx} \sum_{n=1}^{\infty} kZ_n V_n(\eta) \, |s_n\rangle \\
|w_1\rangle &= u_* e^{ikx} \sum_{n=1}^{\infty} kZ_n W_n(\eta) \, |c_n\rangle \\
|\tau_1^{xz}\rangle &= u_*^2 \, e^{ikx} \sum_{n=1}^{\infty} kZ_n S_n^{xz}(\eta) \, |c_n\rangle \\
|\tau_1^{xy}\rangle &= u_*^2 \, e^{ikx} \sum_{n=1}^{\infty} kZ_n S_n^{xy}(\eta) \, |s_n\rangle \\
|\tau_1^{yz}\rangle &= u_*^2 \, e^{ikx} \sum_{n=1}^{\infty} kZ_n S_n^{yz}(\eta) \, |s_n\rangle \\
|p_1 - \tau_1^{zz}\rangle &= u_*^2 \, e^{ikx} \sum_{n=1}^{\infty} kZ_n S_n^{p}(\eta) \, |c_n\rangle \\
|\tau_1^{xx}\rangle &= u_*^2 \, e^{ikx} \sum_{n=1}^{\infty} kZ_n S_n^{xx}(\eta) \, |c_n\rangle \\
|\tau_1^{yy}\rangle &= u_*^2 \, e^{ikx} \sum_{n=1}^{\infty} kZ_n S_n^{yy}(\eta) \, |c_n\rangle \\
|\tau_1^{zz}\rangle &= u_*^2 \, e^{ikx} \sum_{n=1}^{\infty} kZ_n S_n^{zz}(\eta) \, |c_n\rangle
\end{aligned}
\tag{3.13}
$$

The quantities U_n, V_n, ..., S_n^{zz} are functions of the dimensionless elevation η, which we want to determine from the Navier-Stokes equations. Note that v_1 vanishes at the banks as it should. At the linear order, the stress equations (1.7) can be simplified

into

$$
\begin{aligned}
S_n^{xz} &= \eta_0 \left(U_n' + iW_n\right), && (3.14)\\
S_n^{xy} &= \eta_0 \left(-\frac{r_n}{k} U_n + iV_n\right), && (3.15)\\
S_n^{yz} &= \eta_0 \left(V_n' - \frac{r_n}{k} W_n\right), && (3.16)\\
S_n^{xx} &= 2\eta_0 \, iU_n, && (3.17)\\
S_n^{yy} &= 2\eta_0 \frac{r_n}{k} V_n, && (3.18)\\
S_n^{zz} &= 2\eta_0 \, W_n'. && (3.19)
\end{aligned}
$$

They give the following two differential equations:

$$
\begin{aligned}
U_n' &= -iW_n + \frac{1}{\eta_0} S_n^{xz}, && (3.20)\\
V_n' &= \frac{r_n}{k} W_n + \frac{1}{\eta_0} S_n^{yz}. && (3.21)
\end{aligned}
$$

The Navier-Stokes equations (1.8,1.6) lead to

$$
\begin{aligned}
W_n' &= -iU_n - \frac{r_n}{k} V_n, && (3.22)\\
S_n^{xz\prime} &= i\mathcal{U} U_n + \mathcal{U}' W_n + i\left(S_n^p + S_n^{zz} - S_n^{xx}\right) - \frac{r_n}{k} S_n^{xy}, && (3.23)\\
S_n^{yz\prime} &= i\mathcal{U} V - \frac{r_n}{k}\left(S_n^p + S_n^{zz} - S_n^{yy}\right) - iS_n^{xy} && (3.24)\\
S_n^{p\prime} &= -i\mathcal{U} W_n + iS_n^{xz} + \frac{r_n}{k} S_n^{yz}. && (3.25)
\end{aligned}
$$

Note that the stress tensor is traceless: $S_{kk} = 0$. Eliminating S_{xx}, S_{yy} and S_{xy}, we eventually get the four following differential equations:

$$
\begin{aligned}
{W_n}' &= -iU_n - \frac{r_n}{k} V_n, && (3.26)\\
S_n^{xz\prime} &= \left(i\mathcal{U} + \eta_0 \left[4 + \left(\frac{r_n}{k}\right)^2\right]\right) U_n - 3i\eta_0 \frac{r_n}{k} V_n + \mathcal{U}' W_n + iS_n^p, && (3.27)\\
S_n^{yz\prime} &= 3i\eta_0 \frac{r_n}{k} U_n + \left(i\mathcal{U} + \eta_0 \left[1 + 4\left(\frac{r_n}{k}\right)^2\right]\right) V_n - \frac{r_n}{k} S_n^p, && (3.28)\\
S_n^{p\prime} &= -i\mathcal{U} W_n + iS_n^{xz} + \frac{r_n}{k} S_n^{yz}. && (3.29)
\end{aligned}
$$

Equations (3.20,3.21) and (3.26-3.29), which form a closed differential system, can be integrated with the following boundary conditions:

(i) The velocity vanishes on the bed

$$U_n(0) = -\mathcal{U}'(0) = -\frac{1}{\eta_0}, \quad V_n(0) = 0 \quad \text{and} \quad W_n(0) = 0; \tag{3.30}$$

(ii) The normal velocity vanishes at the free surface

$$W_n(\eta_H) = i\mathcal{U}(\eta_H)\, H_n; \tag{3.31}$$

(iii) The shear and normal stesses vanish at the free surface

$$S_n^{xz}(\eta_H) = \frac{H_n}{\eta_H}, \quad S_n^{yz}(\eta_H) = 0 \quad \text{and} \quad S_n^{p}(\eta_H) = \frac{H_n}{\eta_H \tan\theta}. \tag{3.32}$$

These conditions select the values of H_n, $S_n^{xz}(0)$, $S_n^{yz}(0)$, $S_n^{p}(0)$ that are related to the basal coefficients A_x^n, B_x^n, A_y^n and B_y^n by the following definitions:

$$A_x^n + iB_x^n \equiv -\frac{1}{\eta_H} + S_n^{xz}(0)\,, \tag{3.33}$$

$$iA_y^n - B_y^n \equiv S_n^{yz}(0)\,.. \tag{3.34}$$

3.1.3 Average velocity

For later use, we also introduce the average velocity coefficients $\bar{U}_n$ defined such that

$$\bar{u} = \frac{1}{H + h_1 - Z}\int_Z^{H+h_1} u(z)dz = u_* \left\{ \bar{\mathcal{U}} + e^{ikx} \sum_{n=1}^{\infty} kZ_n \bar{U}_n^Z \, |c_n\rangle \right\}, \tag{3.35}$$

where $\bar{\mathcal{U}} = \frac{1}{\eta_H}\int_0^{\eta_H}\mathcal{U}(\eta)d\eta$. From this definition and those of $|u_1\rangle$ and $|h_1\rangle$, we get:

$$\bar{U}_n^Z = \frac{1}{\eta_H}\left(\bar{\mathcal{U}} + H_n\left[\mathcal{U}(\eta_H) - \bar{\mathcal{U}}\right] + \int_0^{\eta_H} U_n(\eta)d\eta\right). \tag{3.36}$$

As $\mathcal{U}(\eta_H) = \eta_H/(2\eta_0)$ and $\bar{\mathcal{U}} = \eta_H/(3\eta_0)$, one finally obtains:

$$\bar{U}_n^Z = \frac{1}{3\eta_0} + \frac{H_n}{6\eta_0} + \frac{1}{\eta_H}\int_0^{\eta_H} U_n(\eta)d\eta. \tag{3.37}$$

3.1.4 Numerical integration

We write the differential equations for the disturbance induced by the undulated bed under the form:

$$\frac{d}{d\eta}\vec{X}_n = \mathcal{P}_n \vec{X}_n, \tag{3.38}$$

with $\vec{X}_n = (U_n, V_n, W_n, S_n^{xz}, S_n^{yz}, S_n^p)$ and

$$\mathcal{P}_n = \begin{pmatrix} 0 & 0 & -i & \frac{1}{\eta_0} & 0 & 0 \\ 0 & 0 & \frac{r_n}{k} & 0 & \frac{1}{\eta_0} & 0 \\ -i & -\frac{r_n}{k} & 0 & 0 & 0 & 0 \\ i\mathcal{U} + \eta_0\left[4 + \left(\frac{r_n}{k}\right)^2\right] & -3i\eta_0\frac{r_n}{k} & \mathcal{U}' & 0 & 0 & i \\ 3i\eta_0\frac{r_n}{k} & i\mathcal{U} + \eta_0\left[1 + 4\left(\frac{r_n}{k}\right)^2\right] & 0 & 0 & 0 & -\frac{r_n}{k} \\ 0 & 0 & -i\mathcal{U} & i & \frac{r_n}{k} & 0 \end{pmatrix}. \tag{3.39}$$

Making use of the linearity of the equations, we seek for a solution under the form $\vec{X}_n = \vec{X}_n^Z + a_n^{xz}\vec{X}_n^{xz} + a_n^{yz}\vec{X}_n^{yz} + a_n^p\vec{X}_n^p$, where the vectors $\vec{X}_n^Z$, $\vec{X}_n^{xz}$, $\vec{X}_n^{yz}$ and $\vec{X}_n^p$ are solutions of the following equations:

$$\frac{d}{d\eta}\vec{X}_n^Z = \mathcal{P}_n\vec{X}_n^Z \quad \text{with} \quad \vec{X}_n^Z(0) = \left(-\frac{1}{\eta_0}, 0, 0, 0, 0, 0\right), \tag{3.40}$$

$$\frac{d}{d\eta}\vec{X}_n^{xz} = \mathcal{P}_n\vec{X}_n^{xz} \quad \text{with} \quad \vec{X}_n^{xz}(0) = (0, 0, 0, 1, 0, 0), \tag{3.41}$$

$$\frac{d}{d\eta}\vec{X}_n^{yz} = \mathcal{P}_n\vec{X}_n^{yz} \quad \text{with} \quad \vec{X}_n^{yz}(0) = (0, 0, 0, 0, 1, 0), \tag{3.42}$$

$$\frac{d}{d\eta}\vec{X}_n^p = \mathcal{P}_n\vec{X}_n^p \quad \text{with} \quad \vec{X}_n^p(0) = (0, 0, 0, 0, 0, 1). \tag{3.43}$$

Then the boundary conditions on the bed (3.30) are automatically satisfied. The values of the three coeffcients a_n^{xz}, a_n^{yz} and a_n^p, as well as the value of H_n, are determined by those at the free surface (3.31,3.32).

3.1.5 Saint-Venant calculation

We call u_0 the depth averaged base flow velocity. By definition of the Chézy number, the ratio of the mean velocity to the basal shear velocity reads:

$$\frac{u_0}{u_*} = \frac{1}{\sqrt{C}} = \frac{\eta_H}{3\eta_0}.$$

At the linear order, the continuity equation (1.48) can be simplified into

$$H\partial_x|u_1\rangle + u_0\partial_x|h_1\rangle + H\partial_y|v_1\rangle = 0\,, \tag{3.44}$$

and, similarly, the two momentum equations (1.47) give

$$u_0\partial_x|u_1\rangle = -g\partial_x\left(|Z\rangle + |h_1\rangle\right) - C\frac{u_0}{H}|u_1\rangle + 2C\frac{u_0^2}{H^2}|h_1\rangle\,, \tag{3.45}$$

$$u_0\partial_x|v_1\rangle = -g\partial_y\left(|Z\rangle + |h_1\rangle\right) - C\frac{u_0}{H}|v_1\rangle\,. \tag{3.46}$$

The above equations, once projected on the $(|c_n\rangle,\, |s_n\rangle)$ base, give

$$iU_n + \frac{i}{\eta_H\sqrt{C}}H_n + \frac{r_n}{k}V_n = 0\,, \tag{3.47}$$

$$i\eta_H U_n + i\,\frac{1}{\mathcal{F}^2\sqrt{C}}(1+H_n) + CU_n - \frac{2\sqrt{C}}{\eta_H}H_n = 0\,, \tag{3.48}$$

$$i\eta_H V_n - \frac{r_n}{k}\,\frac{1}{\mathcal{F}^2\sqrt{C}}(1+H_n) + CV_n = 0\,, \tag{3.49}$$

that can finally solved into:

$$U_n = \frac{1}{\sqrt{C}}\,\frac{\eta_H - iC\left[1 - 2\left(\frac{r_n}{k}\right)^2\right]}{(\eta_H - iC)\left\{\eta_H\left[1 - \mathcal{F}^2 + \left(\frac{r_n}{k}\right)^2\right] + 3iC\mathcal{F}^2\right\}}\,, \tag{3.50}$$

$$V_n = \frac{1}{\sqrt{C}}\,\frac{(3C + i\eta_H)\frac{r_n}{k}}{(\eta_H - iC)\left\{\eta_H\left[1 - \mathcal{F}^2 + \left(\frac{r_n}{k}\right)^2\right] + 3iC\mathcal{F}^2\right\}}\,, \tag{3.51}$$

$$H_n = -\frac{\eta_H\left[1 + \left(\frac{r_n}{k}\right)^2\right]}{\eta_H\left[1 - \mathcal{F}^2 + \left(\frac{r_n}{k}\right)^2\right] + 3iC\mathcal{F}^2}\,. \tag{3.52}$$

These equations can be simplified with the following transformation:

$$\tilde{k} = \frac{\eta_H}{C}\,, \tag{3.53}$$

$$\tilde{r}_n = \frac{H}{C}\,r_n\,, \tag{3.54}$$

$$\tilde{U}_n = \eta_H\sqrt{C}\,U_n\,, \tag{3.55}$$

$$\tilde{V}_n = \eta_H\sqrt{C}\,V_n\,, \tag{3.56}$$

$$\tilde{H}_n = H_n\,. \tag{3.57}$$

The system of Eqs. (3.47-3.49) then leads to

$$i\tilde{k}(\tilde{U}_n + \tilde{H}_n) + \tilde{r}_n \tilde{V}_n = 0\,, \tag{3.58}$$

$$i\tilde{k}\tilde{U}_n + i\,\frac{\tilde{k}}{\mathcal{F}^2}(1+\tilde{H}_n) + \tilde{U}_n - 2\tilde{H}_n = 0\,, \tag{3.59}$$

$$i\tilde{k}\tilde{V}_n - \frac{\tilde{r}_n}{\mathcal{F}^2}(1+\tilde{H}_n) + \tilde{V}_n = 0\,, \tag{3.60}$$

whose solution is:

$$\tilde{U}_n = \frac{\tilde{k}^2\,(\tilde{k}-i) + 2i\,\tilde{r}_n^2}{(\tilde{k}-i)\,[\tilde{k}^2 - \mathcal{F}^2\tilde{k}(\tilde{k}-3i) + \tilde{r}_n^2]}\,, \tag{3.61}$$

$$\tilde{V}_n = \frac{(3+i\tilde{k})\tilde{k}\tilde{r}_n}{(\tilde{k}-i)\,[\tilde{k}^2 - \mathcal{F}^2\tilde{k}(\tilde{k}-3i) + \tilde{r}_n^2]}\,, \tag{3.62}$$

$$\tilde{H}_n = -\frac{\tilde{k}^2 + \tilde{r}_n^2}{\tilde{k}^2 - \mathcal{F}^2\tilde{k}(\tilde{k}-3i) + \tilde{r}_n^2}\,. \tag{3.63}$$

The basal stress is not part of the Saint-Venant equation variables. We define it from Eq. (1.45) as

$$\vec{\tau}_b = C\frac{H}{h}\,u_0\vec{u}. \tag{3.64}$$

In this way, the last term of the momentum equation $-CHu_0\frac{\vec{u}}{h^2}$ can be identified as the depth-averaged stress gradient $\frac{1}{h}\int \partial_z\vec{\tau}\,dz = -\frac{1}{h}\vec{\tau}_b$. The x and y components of the basal stress are then, at the first order

$$|\tau_1^{xz}\rangle = Cu_0|u_1\rangle - C\frac{u_0^2}{H}|h_1\rangle, \tag{3.65}$$

$$|\tau_1^{yz}\rangle = Cu_0|v_1\rangle. \tag{3.66}$$

Introducing the stress coefficients $A^n_{x,y}$ and $B^n_{x,y}$ as

$$|\tau_1^{xz}\rangle = u_*^2\,e^{ikx+\sigma t}\sum_{n=1}^{\infty} kZ_n(A_x^n + iB_x^n)\,|c_n\rangle \tag{3.67}$$

$$|\tau_1^{yz}\rangle = u_*^2\,e^{ikx+\sigma t}\sum_{n=1}^{\infty} kZ_n(iA_y^n - B_y^n)\,|s_n\rangle, \tag{3.68}$$

and comparing them to the equations (3.65) and (3.66) we get then the following relations between the *basal coefficients* and the dimensionless coefficients U_n, V_n and

H_n:

$$A_x^n + iB_x^n = \sqrt{C}\, U_n - \frac{1}{\eta_H} H_n, \tag{3.69}$$

$$iA_y^n - B_y^n = \sqrt{C}\, V_n. \tag{3.70}$$

With the rescaled variables, these coefficients can be expressed as

$$A_x^n + iB_x^n = \frac{1}{\eta_H}\left(\tilde{U}_n - \tilde{H}_n\right) = \frac{1}{C\tilde{k}}\left(\tilde{U}_n - \tilde{H}_n\right), \tag{3.71}$$

$$iA_y^n - B_y^n = \frac{1}{\eta_H}\tilde{V}_n = \frac{1}{C\tilde{k}}\tilde{V}_n. \tag{3.72}$$

3.1.6 Basal shear stress coefficients

In figures 3.1 and 3.2, we display the basal shear stress coefficients A_x, B_x, A_y and B_y as functions of the rescaled wave number kH, for two values of the transverse mode ($n = 1$ and $n = 3$ respectively) and a rather large channel aspect ratio ($\beta = 200$). We can compare on these graphs the results of the full three-dimensional Navier-Stokes description (orange lines) and the depth averaged Saint Venant model (blue lines). We see that the agreement between the two description is qualitatively very good for A_x and A_y, with a quantitative difference when kH becomes typically larger than 10^{-2}. In particular, in the large wavelength limit ($kH \ll 1$), A_x is negative and, as can be deduced from Eqs. 3.71 and 3.61 - 3.63, it goes like

$$A_x^n \sim -1/k\,. \tag{3.73}$$

Similarly, A_y is positive and constant at the value

$$A_y^n \sim 3/r_n\,, \tag{3.74}$$

where we remind that $r_n = 2y_0/n\pi$. Regarding the coefficients B_x and B_y, the agreement is also quantitatively good in the limit $kH \to 0$ with

$$B_x^n \sim 2 + 3\mathcal{F}^2/r_n^2, \tag{3.75}$$

$$B_y^n \sim \left(-9\mathcal{F}^2/r_n^3 - 2/r_n\right)k\,, \tag{3.76}$$

but there is a qualitative difference between the two descriptions for the larger values of kH's the Saint-Venant model predicts a change of sign for B_x when Navier-Stokes equations do not, and vice-versa for B_y. This means that the predictions of NS and

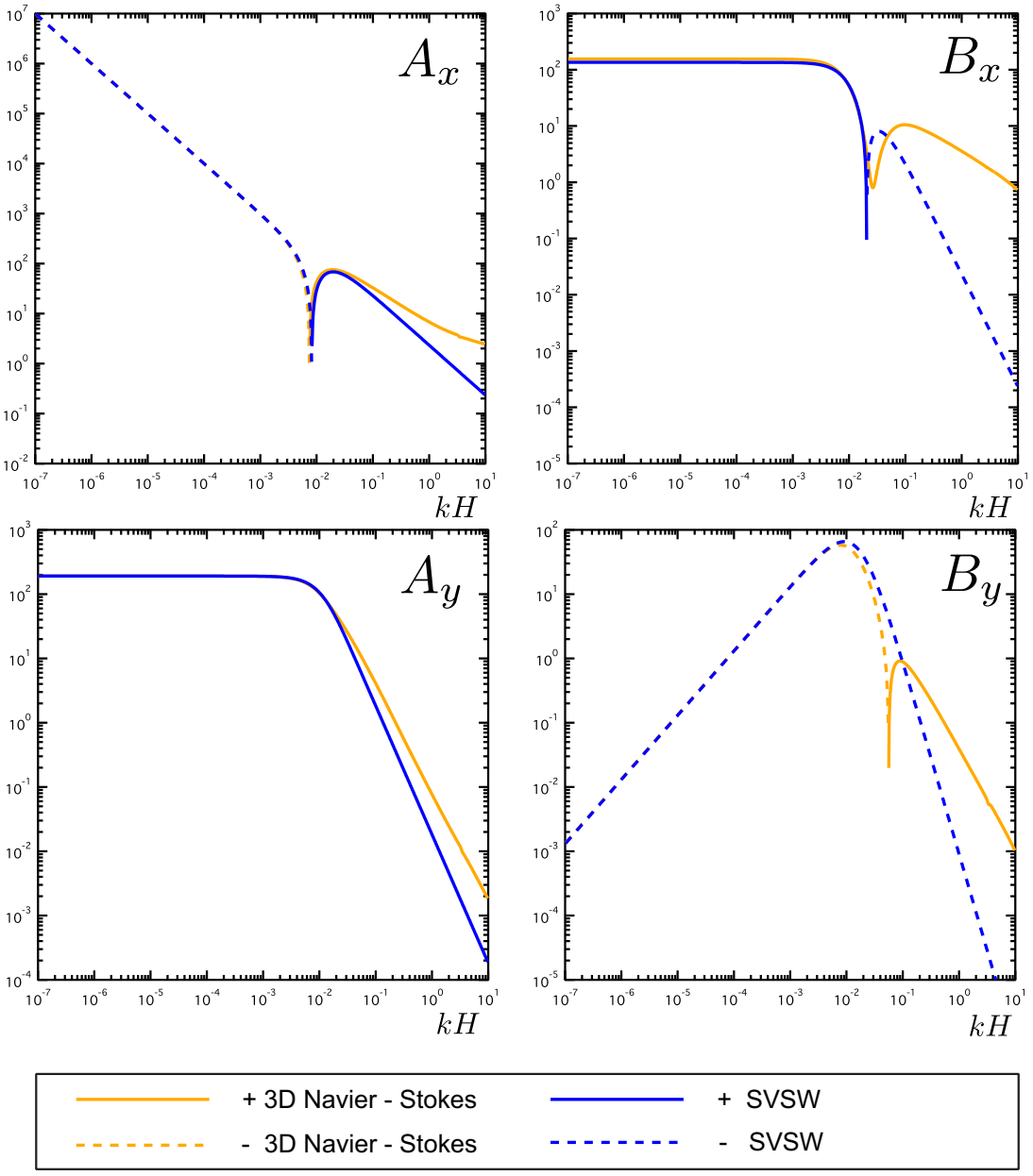


Figure 3.1: Basal shear stress coefficients A_x, B_x, A_y and B_y from Navier-Stokes (orange lines) and St-Venant (blue lines) equations for laminar flows as functions of the rescaled wave number kH. These curves have been computed for the transverse mode $n = 1$ (i.e. a transverse wavenumber $r_1 = \pi/(2y_0)$), and with $\beta = 200$, $Re \simeq 15$ ($C \simeq 0.2$) and $\mathcal{F} \simeq 0.6$. Graphical convention for log-log plots: negative values are plotted in absolute value, but are displayed with a type of line different from positive ones (see legend)

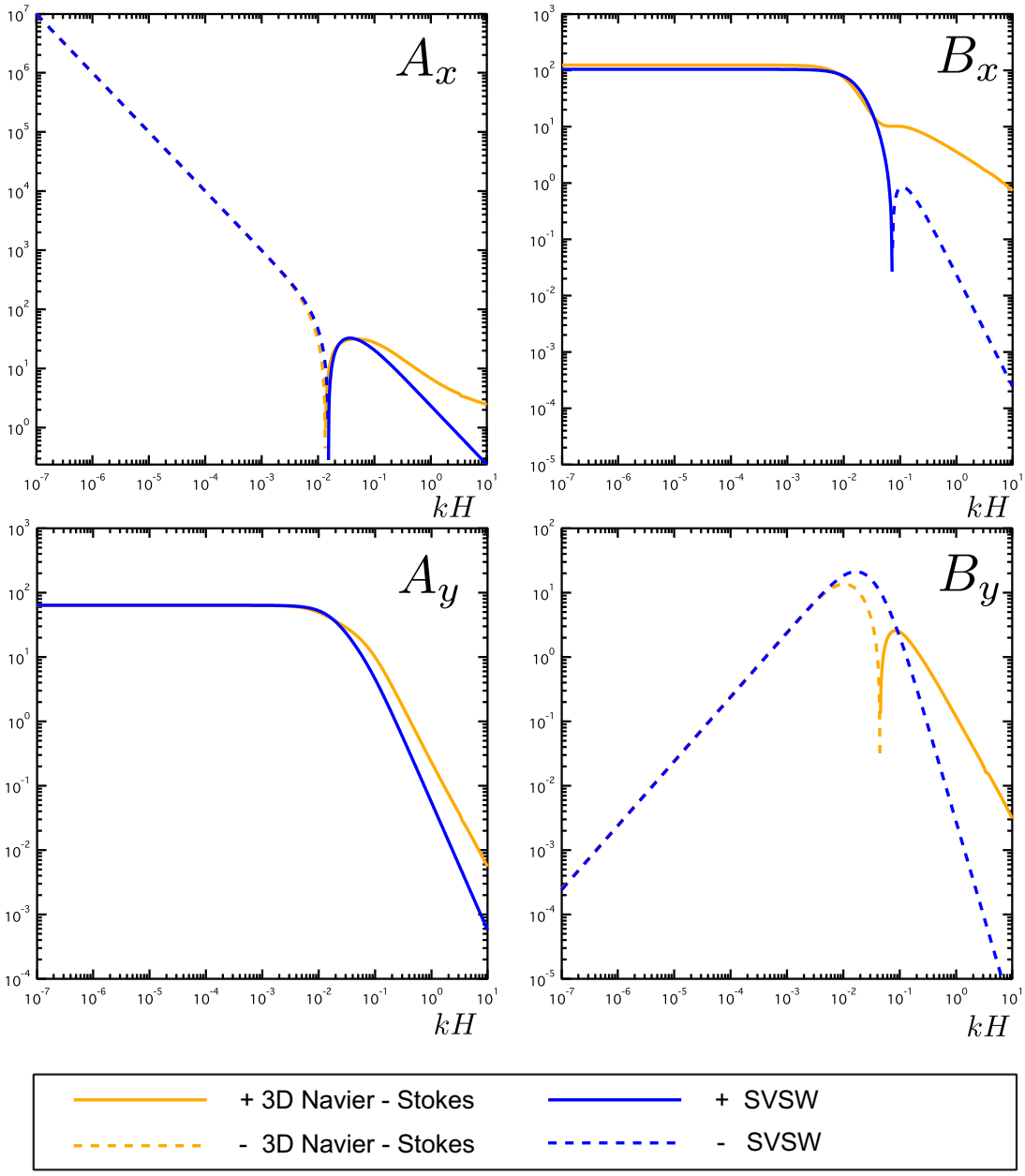


Figure 3.2: Same as Fig. 3.1, but for the transverse mode $n = 3$ (i.e. a transverse wavenumber $r_3 = 3\pi/(2y_0)$).

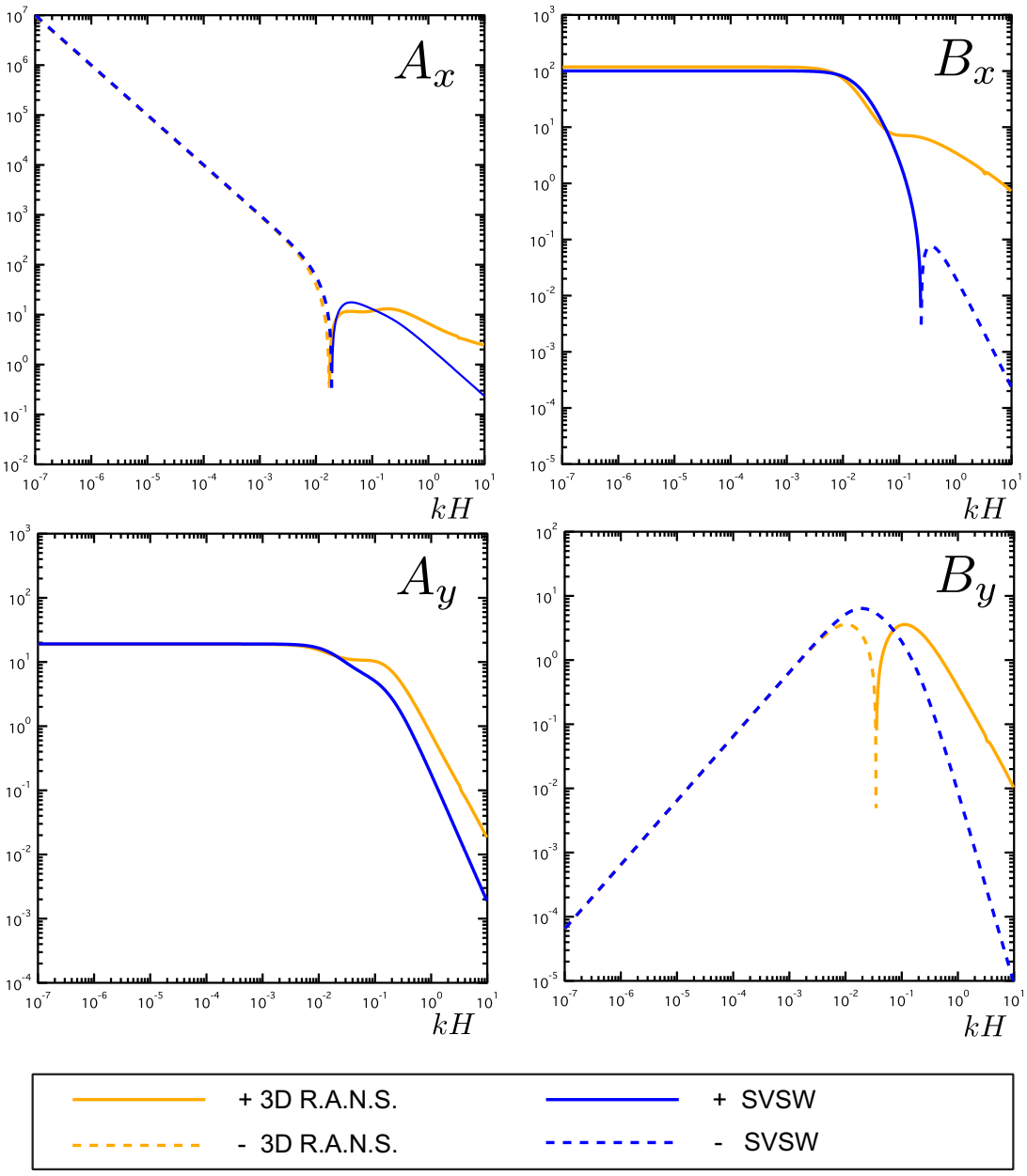


Figure 3.3: Same as Fig. 3.1, but for smaller aspect ratio $\beta = 20$.

SVSW for the phase shift between basal shear stress and topography are opposite in this limit of small wavelengths. This discrepancy between the hydrodynamical descriptions is not very surprising as we cannot expect the shallow water equations to be valid when the wavelength of the perturbation becomes on the order of the water depth. However, it is important to keep in mind that such a qualitative difference (a sign difference) for the coefficients B is a major consequence on the prediction of bedform growth. In figure 3.3 we show also the hydrodynamical response to a perturbed bed in a channel with an aspect ratio $\beta = 20$, close to the channel's aspect ratio that we will get in our experiments: in this case the basal coefficients slightly change but without big differences with respect the case at larger aspect ratio. We have also investigated the dependency of the basal coefficients on the Froude number: we have observed in our simulation that keeping this number below 1 (at which one switches from the fluvial to the torrential regime, see Fourrier *et al.* 200), the hydrodynamical response of a perturbed bed is not affected by modification of the Froude number itself.

3.2 Turbulent flow

In this section, we similarly proceed in the turbulent case, i.e. with RANS equations.

3.2.1 Base flow

We introduce as before the following notations:

$$\eta = kz, \tag{3.77}$$
$$\eta_0 = kz_0, \tag{3.78}$$
$$\eta_H = kH. \tag{3.79}$$

Note that the surface layer is described here in term of the geometrical roughness z_0 instead of the viscous length u_*/ν, an explanation is provided in section 1.6. The dimensionless longitudinal base velocity profile $\mathcal{U}$ is now defined by:

$$\mathcal{U}(\eta) = \frac{1}{\kappa} \ln\left(1 + \frac{\eta}{\eta_0}\right). \tag{3.80}$$

Using these notations, the base state reads

$$
\begin{aligned}
u &= u_* \mathcal{U}(\eta), && (3.81)\\
v &= 0, && (3.82)\\
w &= 0, && (3.83)\\
p &= u_*^2 \frac{1}{\tan\theta}\left(1-\frac{\eta}{\eta_H}\right), && (3.84)\\
\tau_{xz} &= -u_*^2\left(1-\frac{\eta}{\eta_H}\right), && (3.85)\\
& && (3.86)
\end{aligned}
$$

and the Froude number is related to the slope by:

$$\sin\theta = \left(\frac{\mathcal{F}}{\mathcal{U}(\eta_H)}\right)^2. \tag{3.87}$$

3.2.2 First order equations

Because of the free surface modulation $H + h_1(x, y, t)$, the expression for the mixing length (1.32) is modified and reads now:

$$L = (z_0 + z - Z)\sqrt{\frac{H + h_1 - z}{H + h_1 - Z}}. \tag{3.88}$$

We assume all kZ_n to be small, so that, at the linear order, we can write (3.12):

$$k|h_1\rangle = e^{ikx} \sum_{n=1}^{\infty} kZ_n H_n \, |c_n\rangle. \tag{3.89}$$

Similarly to the laminar case, we write the first order disturbances of the velocity and stress components as

$$
\begin{aligned}
|u_1\rangle &= u_* e^{ikx} \sum_{n=1}^{\infty} kZ_n U_n(\eta)\,|c_n\rangle \\
|v_1\rangle &= u_* e^{ikx} \sum_{n=1}^{\infty} kZ_n V_n(\eta)\,|s_n\rangle \\
|w_1\rangle &= u_* e^{ikx} \sum_{n=1}^{\infty} kZ_n W_n(\eta)\,|c_n\rangle \\
|\tau_1^{xz}\rangle &= -u_*^2 e^{ikx} \sum_{n=1}^{\infty} kZ_n S_n^{xz}(\eta)\,|c_n\rangle \\
|\tau_1^{xy}\rangle &= -u_*^2 e^{ikx} \sum_{n=1}^{\infty} kZ_n S_n^{xy}(\eta)\,|s_n\rangle \\
|\tau_1^{yz}\rangle &= -u_*^2 e^{ikx} \sum_{n=1}^{\infty} kZ_n S_n^{yz}(\eta)\,|s_n\rangle \\
|p_1 + \tau_1^{zz}\rangle &= u_*^2 e^{ikx} \sum_{n=1}^{\infty} kZ_n S_n^{p}(\eta)\,|c_n\rangle \\
|\tau_1^{xx}\rangle &= u_*^2 e^{ikx} \sum_{n=1}^{\infty} kZ_n S_n^{xx}(\eta)\,|c_n\rangle \\
|\tau_1^{yy}\rangle &= u_*^2 e^{ikx} \sum_{n=1}^{\infty} kZ_n S_n^{yy}(\eta)\,|c_n\rangle \\
|\tau_1^{zz}\rangle &= u_*^2 e^{ikx} \sum_{n=1}^{\infty} kZ_n S_n^{zz}(\eta)\,|c_n\rangle
\end{aligned}
\tag{3.90}
$$

The quantities U_n, V_n, ..., S^{zz} are functions of η. At the linear order, the stress equations 1.33 can be simplified into

$$S_n^{xz} = \frac{2}{\mathcal{U}'}\left(1-\frac{\eta}{\eta_H}\right)\left(U_n' + iW_n - \kappa\mathcal{U}'^2 + \frac{\mathcal{U}'}{2\eta_H} + \frac{\eta\mathcal{U}'H_n}{2\eta_H^2\left(1-\frac{\eta}{\eta_H}\right)}\right), \tag{3.91}$$

$$S_n^{xy} = \frac{1}{\mathcal{U}'}\left(1-\frac{\eta}{\eta_H}\right)\left(-\frac{r_n}{k}U_n + iV_n\right), \tag{3.92}$$

$$S_n^{yz} = \frac{1}{\mathcal{U}'}\left(1-\frac{\eta}{\eta_H}\right)\left(V_n' - \frac{r_n}{k}W_n\right), \tag{3.93}$$

$$S_n^{xx} - S_n^{zz} = \frac{2}{\mathcal{U}'}\left(1-\frac{\eta}{\eta_H}\right)\left(-iU_n + W_n'\right), \tag{3.94}$$

$$S_n^{yy} - S_n^{zz} = \frac{2}{\mathcal{U}'}\left(1-\frac{\eta}{\eta_H}\right)\left(-\frac{r_n}{k}V_n + W_n'\right), \tag{3.95}$$

They give the following two differential equations:

$$U_n' = -iW_n + \frac{1}{2}\frac{\mathcal{U}'}{1-\frac{\eta}{\eta_H}}S_n^{xz} + \kappa\mathcal{U}'^2 - \frac{\mathcal{U}'}{2\eta_H} - \frac{\eta\mathcal{U}'H_n}{2\eta_H^2\left(1-\frac{\eta}{\eta_H}\right)}, \tag{3.96}$$

$$V_n' = \frac{r_n}{k}W_n + \frac{\mathcal{U}'}{1-\frac{\eta}{\eta_H}}S_n^{yz}. \tag{3.97}$$

The Reynolds averaged Navier-Stokes equations (1.19,1.20) lead to

$$W_n' = -iU_n - \frac{r_n}{k}V_n, \tag{3.98}$$

$$S_n^{xz\prime} = i\mathcal{U}U_n + \mathcal{U}'W_n + i\left(S_n^p + S_n^{xx} - S_n^{zz}\right) - \frac{r_n}{k}S_n^{xy}, \tag{3.99}$$

$$S_n^{yz\prime} = i\mathcal{U}V - \frac{r_n}{k}\left(S_n^p + S_n^{yy} - S_n^{zz}\right) - iS_n^{xy} \tag{3.100}$$

$$S_n^{p\prime} = -i\mathcal{U}W_n + iS_n^{xz} + \frac{r_n}{k}S_n^{yz}. \tag{3.101}$$

Note that the stress tensor is traceless: $S_{kk} = 0$. Eliminating S_{xx}, S_{yy} and S_{xy}, we eventually get the four following differential equations:

$$W_n{}' = -iU_n - \frac{r_n}{k} V_n, \tag{3.102}$$

$$S_n^{xz\prime} = \left\{ i\mathcal{U} + \frac{1}{\mathcal{U}'}\left(1 - \frac{\eta}{\eta_H}\right)\left[4 + \left(\frac{r_n}{k}\right)^2\right]\right\} U_n - 3i\frac{1}{\mathcal{U}'}\left(1 - \frac{\eta}{\eta_H}\right)\frac{r_n}{k} V_n + \mathcal{U}' W_n + iS_n^p, \tag{3.103}$$

$$S_n^{yz\prime} = 3i\frac{1}{\mathcal{U}'}\left(1 - \frac{\eta}{\eta_H}\right)\frac{r_n}{k} U_n + \left\{ i\mathcal{U} + \frac{1}{\mathcal{U}'}\left(1 - \frac{\eta}{\eta_H}\right)\left[1 + 4\left(\frac{r_n}{k}\right)^2\right]\right\} V_n - \frac{r_n}{k} S_n^p, \tag{3.104}$$

$$S_n^{p\prime} = -i\mathcal{U} W_n + iS_n^{xz} + \frac{r_n}{k} S_n^{yz}. \tag{3.105}$$

Equations (3.96,3.97) and (3.102-3.105), which form a closed differential system, can be integrated with the following boundary conditions:

(i) The velocity vanishes on the bed

$$U_n(0) = -\mathcal{U}'(0) = -\frac{1}{\kappa\eta_0}, \quad V_n(0) = 0 \quad \text{and} \quad W_n(0) = 0; \tag{3.106}$$

(ii) The normal velocity vanishes at the free surface

$$W_n(\eta_H) = i\mathcal{U}(\eta_H)\, H_n; \tag{3.107}$$

(iii) The shear and normal stesses vanish at the free surface

$$S_n^{xz}(\eta_H) = \frac{H_n}{\eta_H}, \quad S_n^{yz}(\eta_H) = 0 \quad \text{and} \quad S_n^{p}(\eta_H) = \frac{H_n}{\eta_H \tan\theta}. \tag{3.108}$$

These conditions select the values of $S_n^{xz}(0)$, $S_n^{yz}(0)$, $S_n^{p}(0)$ and H_n. Recall that the basal coefficients are related to these functions (see Eqs. 3.33, 3.34).

3.2.3 Average velocity

For later use, we also introduce the average velocity coefficients $\bar{U}_n$ defined such that

$$\bar{u} = \frac{1}{H + h_1 - Z}\int_Z^{H+h_1} u(z)dz = u_* \left\{ \bar{\mathcal{U}} + e^{ikx+\sigma t} \sum_{n=1}^{\infty} kZ_n \bar{U}_n^Z \, |c_n\rangle \right\}, \tag{3.109}$$

where $\bar{\mathcal{U}} = \frac{1}{\eta_H}\int_0^{\eta_H}\mathcal{U}(\eta)d\eta$. From this definition and those of $|u_1\rangle$ and $|h_1\rangle$, we get:

$$\bar{U}_n^Z = \frac{1}{\eta_H}\left(\bar{\mathcal{U}} + H_n\left[\mathcal{U}(\eta_H) - \bar{\mathcal{U}}\right] + \int_0^{\eta_H} U_n(\eta)d\eta\right). \tag{3.110}$$

As $\mathcal{U}(\eta_H) = \frac{1}{\kappa}\ln\left(1+\frac{\eta_H}{\eta_0}\right)$ and $\bar{\mathcal{U}} = \frac{1}{\kappa}\left[\ln\left(1+\frac{\eta_H}{\eta_0}\right) - 1\right]$, one finally obtains:

$$\bar{U}_n^Z = \frac{1}{\kappa\eta_H}\left[\ln\left(1+\frac{\eta_H}{\eta_0}\right) - 1\right] + \frac{H_n}{\kappa\eta_H} + \frac{1}{\eta_H}\int_0^{\eta_H} U_n(\eta)d\eta. \tag{3.111}$$

3.2.4 Numerical integration

We write the differential equations for the disturbance induced by the undulated bed under the form:

$$\frac{d}{d\eta}\vec{X}_n = \mathcal{P}_n\vec{X}_n + \vec{S}_n^Z + H_n\vec{S}_n^H, \tag{3.112}$$

with the vector $\vec{X}_n = (U_n, V_n, W_n, S_n^{xz}, S_n^{yz}, S_n^p)$, the matrix

$$\mathcal{P}_n = \begin{pmatrix} 0 & 0 & -i & \frac{1}{2}\frac{\mathcal{U}'}{1-\frac{\eta}{\eta_H}} & 0 & 0 \\ 0 & 0 & \frac{r_n}{k} & 0 & \frac{\mathcal{U}'}{1-\frac{\eta}{\eta_H}} & 0 \\ -i & -\frac{r_n}{k} & 0 & 0 & 0 & 0 \\ i\mathcal{U} + \frac{1}{\mathcal{U}'}\left(1-\frac{\eta}{\eta_H}\right)\left[4+\left(\frac{r_n}{k}\right)^2\right] & -3i\frac{1}{\mathcal{U}'}\left(1-\frac{\eta}{\eta_H}\right)\frac{r_n}{k} & \mathcal{U}' & 0 & 0 & i \\ 3i\frac{1}{\mathcal{U}'}\left(1-\frac{\eta}{\eta_H}\right)\frac{r_n}{k} & i\mathcal{U} + \frac{1}{\mathcal{U}'}\left(1-\frac{\eta}{\eta_H}\right)\left[1+4\left(\frac{r_n}{k}\right)^2\right] & 0 & 0 & 0 & -\frac{r_n}{k} \\ 0 & 0 & -i\mathcal{U} & i & \frac{r_n}{k} & 0 \end{pmatrix}, \tag{3.113}$$

and the two vectors

$$\vec{S}_n^Z = \left(\kappa\mathcal{U}'^2 - \frac{\mathcal{U}'}{2\eta_H}, 0, 0, 0, 0, 0\right), \tag{3.114}$$

$$\vec{S}_n^H = \left(-\frac{\eta\,\mathcal{U}'}{2\eta_H^2\left(1-\frac{\eta}{\eta_H}\right)}, 0, 0, 0, 0, 0\right). \tag{3.115}$$

Making use of the linearity of the equations, we seek for a solution under the form $\vec{X}_n = \vec{X}_n^Z + a_n^{xz}\vec{X}_n^{xz} + a_n^{yz}\vec{X}_n^{yz} + a_n^p\vec{X}_n^p + H_n\vec{X}_n^H$, where the vectors $\vec{X}_n^Z$, $\vec{X}_n^{xz}$, $\vec{X}_n^{yz}$, $\vec{X}_n^p$

and $\vec{X}_n^H$ are solutions of the following equations:

$$\frac{d}{d\eta}\vec{X}_n^Z = \mathcal{P}_n\vec{X}_n^Z + \vec{S}_n^Z \quad \text{with} \quad \vec{X}_n^Z(0) = \left(-\frac{1}{\kappa\eta_0}, 0, 0, 0, 0, 0\right), \tag{3.116}$$

$$\frac{d}{d\eta}\vec{X}_n^{xz} = \mathcal{P}_n\vec{X}_n^{xz} \quad \text{with} \quad \vec{X}_n^{xz}(0) = (0, 0, 0, 1, 0, 0), \tag{3.117}$$

$$\frac{d}{d\eta}\vec{X}_n^{yz} = \mathcal{P}_n\vec{X}_n^{yz} \quad \text{with} \quad \vec{X}_n^{yz}(0) = (0, 0, 0, 0, 1, 0), \tag{3.118}$$

$$\frac{d}{d\eta}\vec{X}_n^{p} = \mathcal{P}_n\vec{X}_n^{p} \quad \text{with} \quad \vec{X}_n^{p}(0) = (0, 0, 0, 0, 0, 1). \tag{3.119}$$

$$\frac{d}{d\eta}\vec{X}_n^{H} = \mathcal{P}_n\vec{X}_n^{H} + \vec{S}_n^H \quad \text{with} \quad \vec{X}_n^{H}(0) = (0, 0, 0, 0, 0, 0). \tag{3.120}$$

Then, the boundary conditions on the bed (3.106) are automatically satisfied. The values of the three coeffcients a_n^{xz}, a_n^{yz} and a_n^p, as well as the value of H_n, are determined by those at the free surface (3.107,3.108).

3.2.5 St-Venant

Following the laminar case and taking similar notations, the linear order of the continuity equation (1.51) simply writes

$$H\partial_x|u_1\rangle + u_0\partial_x|h_1\rangle + H\partial_y|v_1\rangle = 0, \tag{3.121}$$

and, similarly, the two momentum equations (1.50) give

$$u_0\partial_x|u_1\rangle = -g\partial_x\left(|Z\rangle + |h_1\rangle\right) - 2C\frac{u_0}{H}|u_1\rangle + C\frac{u_0^2}{H^2}|h_1\rangle, \tag{3.122}$$

$$u_0\partial_x|v_1\rangle = -g\partial_y\left(|Z\rangle + |h_1\rangle\right) - C\frac{u_0}{H}|v_1\rangle. \tag{3.123}$$

These equations, once projected on the $(|c_n\rangle, |s_n\rangle)$ base, give

$$iU_n + \frac{i}{\eta_H\sqrt{C}}H_n + \frac{r_n}{k}V_n = 0, \tag{3.124}$$

$$i\eta_H U_n + i\frac{1}{\mathcal{F}^2\sqrt{C}}(1 + H_n) + 2CU_n - \frac{\sqrt{C}}{\eta_H}H_n = 0, \tag{3.125}$$

$$i\eta_H V_n - \frac{r_n}{k}\frac{1}{\mathcal{F}^2\sqrt{C}}(1 + H_n) + CV_n = 0. \tag{3.126}$$

These equations solve into:

$$U_n = \frac{1}{\sqrt{C}} \frac{\eta_H - iC\left[1-\left(\frac{r_n}{k}\right)^2\right]}{(\eta_H - iC)\left\{\eta_H\left[1-\mathcal{F}^2+\left(\frac{r_n}{k}\right)^2\right]+3iC\mathcal{F}^2\right\} - iC\eta_H\left(\frac{r_n}{k}\right)^2}, \quad (3.127)$$

$$V_n = \frac{1}{\sqrt{C}} \frac{(3C+i\eta_H)\frac{r_n}{k}}{(\eta_H - iC)\left\{\eta_H\left[1-\mathcal{F}^2+\left(\frac{r_n}{k}\right)^2\right]+3iC\mathcal{F}^2\right\} - iC\eta_H\left(\frac{r_n}{k}\right)^2}, \quad (3.128)$$

$$H_n = -\frac{(\eta_H - iC)\eta_H\left[1+\left(\frac{r_n}{k}\right)^2\right] - iC\eta_H\left(\frac{r_n}{k}\right)^2}{(\eta_H - iC)\left\{\eta_H\left[1-\mathcal{F}^2+\left(\frac{r_n}{k}\right)^2\right]+3iC\mathcal{F}^2\right\} - iC\eta_H\left(\frac{r_n}{k}\right)^2}. \quad (3.129)$$

We can make these equations simpler with the following transformation:

$$\tilde{k} = \frac{\eta_H}{C}, \quad (3.130)$$

$$\tilde{r}_n = \frac{H}{C} r_n, \quad (3.131)$$

$$\tilde{U}_n = \eta_H \sqrt{C}\, U_n, \quad (3.132)$$

$$\tilde{V}_n = \eta_H \sqrt{C}\, V_n, \quad (3.133)$$

$$\tilde{H}_n = H_n. \quad (3.134)$$

The system of Eqs. (3.124-3.126) is then changed into

$$i\tilde{k}(\tilde{U}_n + \tilde{H}_n) + \tilde{r}_n \tilde{V}_n = 0, \quad (3.135)$$

$$i\tilde{k}\tilde{U}_n + i\,\frac{\tilde{k}}{\mathcal{F}^2}(1+\tilde{H}_n) + 2\tilde{U}_n - \tilde{H}_n = 0, \quad (3.136)$$

$$i\tilde{k}\tilde{V}_n - \frac{\tilde{r}_n}{\mathcal{F}^2}(1+\tilde{H}_n) + \tilde{V}_n = 0, \quad (3.137)$$

whose solution is

$$\tilde{U}_n = \frac{\tilde{k}^2(\tilde{k}-i) + i\,\tilde{r}_n^2}{(\tilde{k}-i)\left[\tilde{k}^2 - \mathcal{F}^2\tilde{k}(\tilde{k}-3i) + \tilde{r}_n^2\right] - i\tilde{r}_n^2}, \quad (3.138)$$

$$\tilde{V}_n = \frac{(3+i\tilde{k})\tilde{k}\tilde{r}_n}{(\tilde{k}-i)\left[\tilde{k}^2 - \mathcal{F}^2\tilde{k}(\tilde{k}-3i) + \tilde{r}_n^2\right] - i\tilde{r}_n^2}, \quad (3.139)$$

$$\tilde{H}_n = -\frac{(\tilde{k}-i)(\tilde{k}^2+\tilde{r}_n^2) - i\tilde{r}_n^2}{\tilde{k}^2 - \mathcal{F}^2\tilde{k}(\tilde{k}-3i) + \tilde{r}_n^2 - i\tilde{r}_n^2}. \quad (3.140)$$

Again, the basal stress is not part of the SVSW equation variables. We defined it in (1.49) as

$$\vec{\tau}_b = C|\vec{u}|\vec{u}. \tag{3.141}$$

In this way, the last term of the momentum equation $-C\frac{|\vec{u}|\vec{u}}{h}$ can be identified as the depth-averaged stress gradient $\frac{1}{h}\int \partial_z \vec{\tau}\, dz = -\frac{1}{h}\vec{\tau}_b$. The x and y components of the basal stress are then, at the first order

$$|\tau_1^{xz}\rangle = 2Cu_0|u_1\rangle, \tag{3.142}$$
$$|\tau_1^{yz}\rangle = Cu_0|v_1\rangle. \tag{3.143}$$

Comparing these two expressions with equations (3.67) and (3.68), we then get the stress coefficients $A^n_{x,y}$ and $B^n_{x,y}$ as:

$$A^n_x + iB^n_x = 2\sqrt{C}\, U_n, \tag{3.144}$$
$$iA^n_y - B^n_y = \sqrt{C}\, V_n. \tag{3.145}$$

With the rescaled variables, these coefficients can be expressed as

$$A^n_x + iB^n_x = \frac{2}{\eta_H}\tilde{U}_n = \frac{2}{C\tilde{k}}\tilde{U}_n, \tag{3.146}$$
$$iA^n_y - B^n_y = \frac{1}{\eta_H}\tilde{V}_n = \frac{1}{C\tilde{k}}\tilde{V}_n. \tag{3.147}$$

3.2.6 Basal shear stress coefficients

The behaviour of the basal shear stress coefficients in this turbulent case is displayed in figures 3.4 and 3.5 for the transverse modes $n = 1$ and $n = 3$ respectively. The curves are similar to those in the laminar case. The comparison of the two hydrodynamical descriptions (3D RANS and shallow water Saint-Venant equations) is also similar. For A_x and A_y, we get a quantitative match between the two in the region $kH \lesssim 10^{-2}$, and a qualitative agreement only at larger wavenumbers. In this limit we have from Eqs. (3.146) and (3.138) – (3.140):

$$A^n_x \sim -1/k\,. \tag{3.148}$$

Similarly, A_y is positive and constant at the value

$$A^n_y \sim \frac{3}{2r_n}\,, \tag{3.149}$$

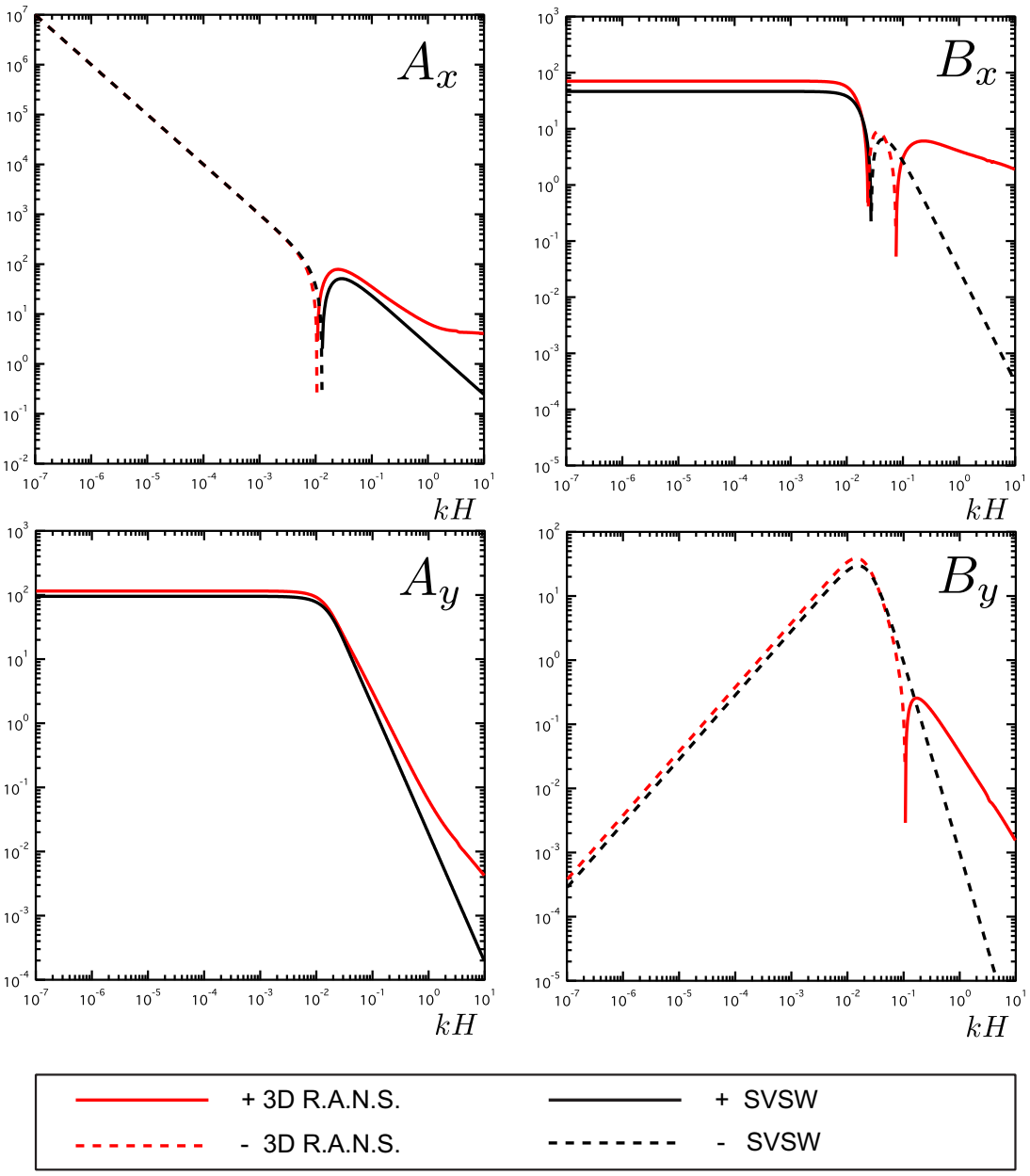


Figure 3.4: Same figure as Fig. 3.1 (first transverse mode $n = 1$, $\beta = 200$ and $\mathcal{F} \simeq 0.6$), but in the turbulent case.

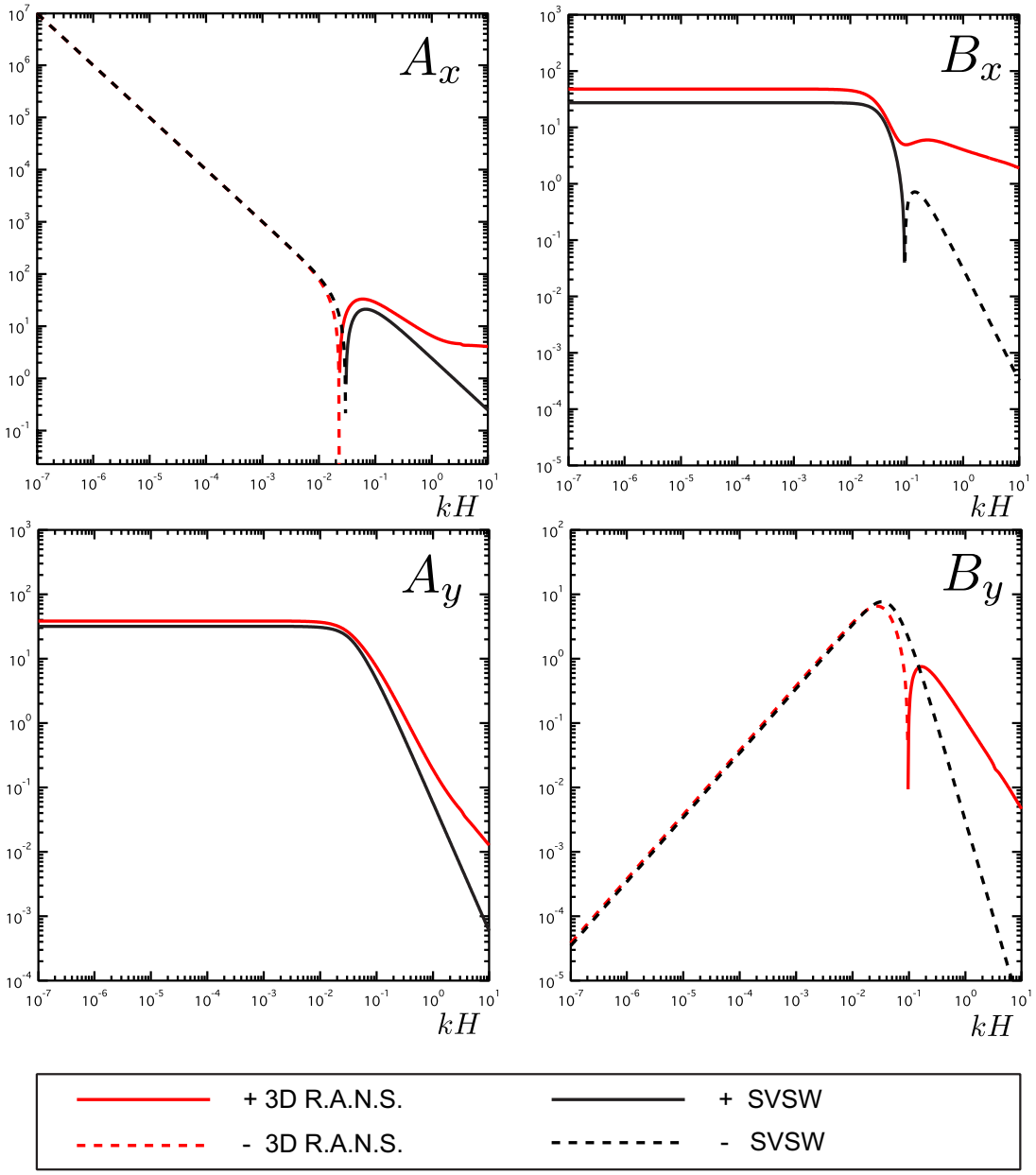


Figure 3.5: Same as Fig. 3.4, but for the transverse mode $n = 3$ (i.e. a transverse wavenumber $r_3 = 3\pi/(2y_0)$).

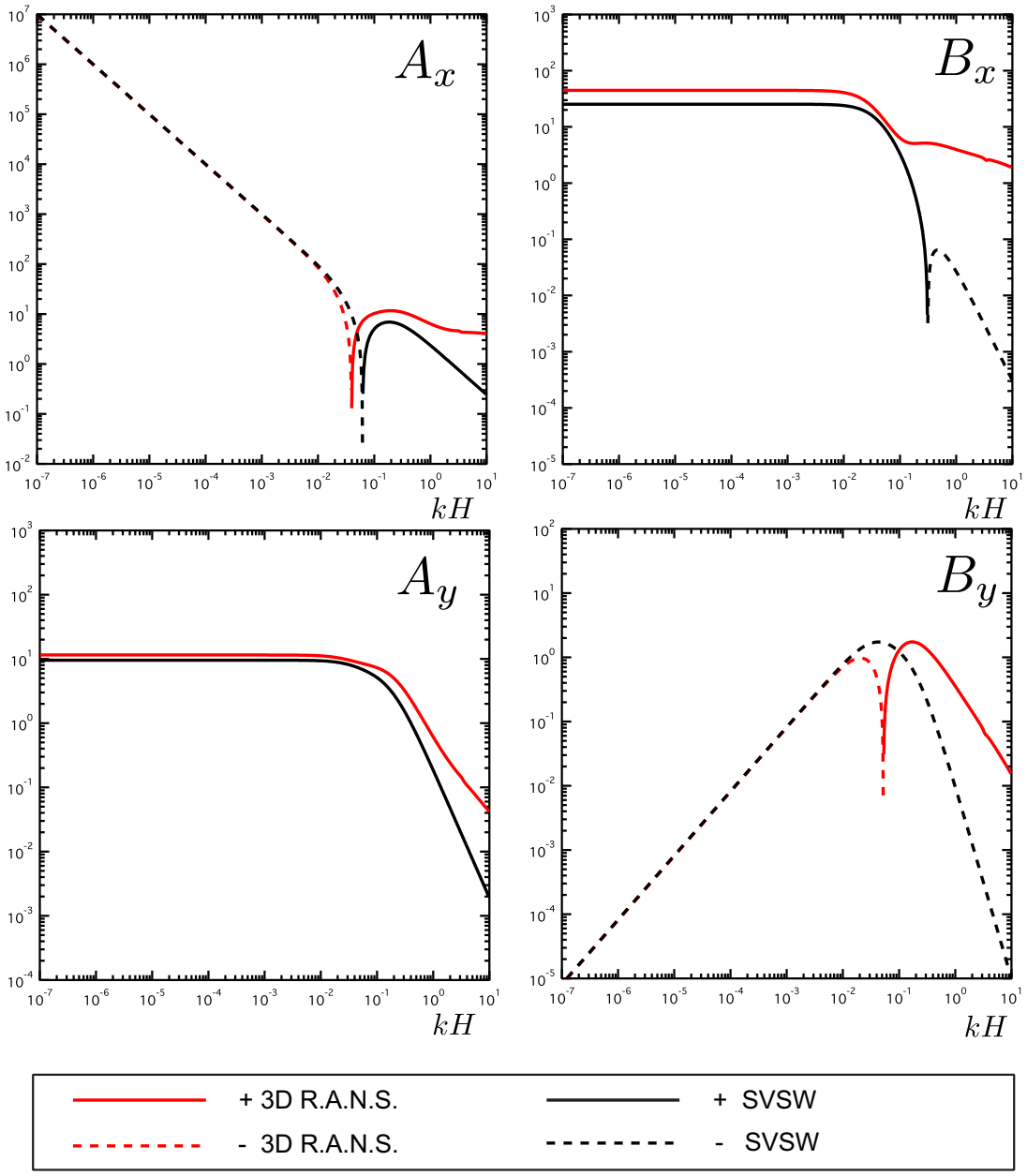


Figure 3.6: Same as Fig. 3.4, but for a smaller aspect ratio $\beta = 20$.

where $r_n = 2y_0/n\pi$. For B_x and B_y, the two models show a significant (sign) difference at large $kH \gtrsim 0.1$, and a fair agreement at small wavenumbers, though less good than in the laminar case, in which we have for $kH \to 0$:

$$B_x^n \sim \frac{1}{2} + \frac{3\mathcal{F}^2}{2r_n^2}, \tag{3.150}$$

$$B_y^n \sim -\left(\frac{9\mathcal{F}^2}{4r_n^3} + \frac{1}{4r_n}\right) k\,, \tag{3.151}$$

Figure 3.6 shows the hydrodynamical response of a perturbed bed in a channel of aspect ratio $\beta = 20$: a discrepancy with the basal coefficients at larger β is observed, in particular the B_x of the three dimensional model does not change sign over the range contrarily to the case $\beta = 200$.

Chapter 4

Hydrodynamics in a channel with meandering banks and a flat bottom

In a strict parallel manner to the previous chapter, we investigate here the details of the linear response of hydrodynamics to a flat bed in a meandering channel. All physical quantities will be forced by the undulated banks described by:

$$Y^{L,R} = \pm y_0 + \Upsilon e^{ikx}, \tag{4.1}$$

and they will be similarly written as first order expansions with respect to the small dimensionless parameters $k\Upsilon$. Again, we are interested in the basal stress τ^b, and technically to the basal stress coefficients C_x^n, D_x^n, $C_y^n$and D_y^n previously introduced, which we will compute for different hydrodynamical models and both in laminar and turbulent regimes.

4.1 Laminar flow

In this section, we consider the water flow in the laminar regime. The base flow is obviously the same as before.

4.1.1 First order equations

Similarly to the previous section, we use the representation:

$$
\begin{aligned}
k|h_1\rangle &= k\Upsilon\, e^{ikx} \sum_{n=1}^{\infty} H_n\,|c_n\rangle \\
|u_1\rangle &= u_* k\Upsilon\, e^{ikx} \sum_{n=1}^{\infty} U_n(\eta)\,|c_n\rangle \\
|v_1\rangle &= u_* k\Upsilon e^{ikx}\left\{ i\,\mathcal{U}(\eta)|1\rangle + \sum_{n=1}^{\infty} V_n(\eta)\,|s_n\rangle \right\} \\
|w_1\rangle &= u_* k\Upsilon e^{ikx} \sum_{n=1}^{\infty} W_n(\eta)\,|c_n\rangle \\
|\tau_1^{xz}\rangle &= u_*^2 k\Upsilon\, e^{ikx} \sum_{n=1}^{\infty} S_n^{xz}(\eta)\,|c_n\rangle \\
|\tau_1^{xy}\rangle &= u_*^2 k\Upsilon\, e^{ikx}\left\{ -\eta_0\,\mathcal{U}|1\rangle + \sum_{n=1}^{\infty} S_n^{xy}(\eta)\,|s_n\rangle \right\} \\
|\tau_1^{yz}\rangle &= u_*^2 k\Upsilon\, e^{ikx}\left\{ i\eta_0\,\mathcal{U}'(\eta)|1\rangle + \sum_{n=1}^{\infty} S_n^{yz}(\eta)\,|s_n\rangle \right\} \\
|p_1 - \tau_1^{zz}\rangle &= u_*^2 k\Upsilon\, e^{ikx} \sum_{n=1}^{\infty} S_n^{p}(\eta)\,|c_n\rangle \\
|\tau_1^{xx}\rangle &= u_*^2 k\Upsilon\, e^{ikx} \sum_{n=1}^{\infty} S_n^{xx}(\eta)\,|c_n\rangle \\
|\tau_1^{yy}\rangle &= u_*^2 k\Upsilon\, e^{ikx} \sum_{n=1}^{\infty} S_n^{yy}(\eta)\,|c_n\rangle \\
|\tau_1^{zz}\rangle &= u_*^2 k\Upsilon\, e^{ikx} \sum_{n=1}^{\infty} S_n^{zz}(\eta)\,|c_n\rangle
\end{aligned}
\tag{4.2}
$$

Note that the slip boundary conditions at the banks (2.22 and 2.23) have been used, and are responsible for the term in $|1\rangle$ in the expression of v_1. This additional term in v_1 also generates terms in $|1\rangle$ for τ_1^{xy} and τ_1^{yz}. The stress equations remain the same as before. However, due to the terms $\langle s_n|1\rangle/\langle s_n|s_n\rangle$, the Navier-Stokes equation projected along the y-axis is modified and now leads to:

$$
\begin{aligned}
S_n^{yz\prime} &= 3i\eta_0 \frac{r_n}{k}\,U_n + \left(i\mathcal{U} + \eta_0\left[1 + 4\left(\frac{r_n}{k}\right)^2\right]\right) V_n - \frac{r_n}{k}\,S_n^p \\
&+ \frac{4}{n\pi}\left[i\eta_0(\mathcal{U} - \mathcal{U}'') - \mathcal{U}^2\right]\theta_n,
\end{aligned}
\tag{4.3}
$$

The boundary conditions needed to integrate the equations are now the following:

(i) The velocity vanishes on the bed

$$U_n(0) = 0, \quad V_n(0) = 0 \quad \text{and} \quad W_n(0) = 0; \tag{4.4}$$

(ii) The normal velocity vanishes at the free surface

$$W_n(\eta_H) = i\mathcal{U}(\eta_H)\, H_n; \tag{4.5}$$

(iii) The shear and normal stesses vanish at the free surface

$$S_n^{xz}(\eta_H) = \frac{H_n}{\eta_H}, \quad S_n^{yz}(\eta_H) = 0 \quad \text{and} \quad S_n^{p}(\eta_H) = \frac{H_n}{\eta_H \tan\theta}. \tag{4.6}$$

These conditions select the values of $S_n^{xz}(0)$, $S_n^{yz}(0)$, $S_n^{p}(0)$ and H_n that are related to the basal coefficients A_x^n, B_x^n, A_y^n and B_y^n by the following definitions:

$$C_x^n + iD_x^n \equiv S_n^{xz}(0), \tag{4.7}$$

$$iC_y^n - D_y^n \equiv S_n^{yz}(0). \tag{4.8}$$

4.1.2 Average velocity

As before, we introduce the average velocity coefficients $\bar{U}_n$ defined by

$$\bar{u} = u_* \left\{ \bar{\mathcal{U}} + k\Upsilon e^{ikx} \sum_{n=1}^{\infty} \bar{U}_n^{\Upsilon} \, |c_n\rangle \right\}, \tag{4.9}$$

and obtain:

$$\begin{aligned} \bar{U}_n^{\Upsilon} &= \frac{1}{\eta_H} \left(H_n \left[\mathcal{U}(\eta_H) - \bar{\mathcal{U}} \right] + \int_0^{\eta_H} U_n(\eta) d\eta \right) \\ &= \frac{H_n}{6\eta_0} + \frac{1}{\eta_H} \int_0^{\eta_H} U_n(\eta) d\eta. \end{aligned} \tag{4.10}$$

4.1.3 Numerical integration

We write the differential equations for the disturbance induced by the undulated banks under the form:

$$\frac{d}{d\eta}\vec{X}_n = \mathcal{P}_n \vec{X}_n + \vec{S}_n^{\Upsilon}, \tag{4.11}$$

with $\vec{X}_n = (U_n, V_n, W_n, S_n^{xz}, S_n^{yz}, S_n^p)$ and

$$\mathcal{P}_n = \begin{pmatrix} 0 & 0 & -i & \frac{1}{\eta_0} & 0 & 0 \\ 0 & 0 & \frac{r_n}{k} & 0 & \frac{1}{\eta_0} & 0 \\ -i & -\frac{r_n}{k} & 0 & 0 & 0 & 0 \\ i\mathcal{U} + \eta_0 \left[4 + \left(\frac{r_n}{k}\right)^2\right] & -3i\eta_0 \frac{r_n}{k} & \mathcal{U}' & 0 & 0 & i \\ 3i\eta_0 \frac{r_n}{k} & i\mathcal{U} + \eta_0 \left[1 + 4\left(\frac{r_n}{k}\right)^2\right] & 0 & 0 & 0 & -\frac{r_n}{k} \\ 0 & 0 & -i\mathcal{U} & i & \frac{r_n}{k} & 0 \end{pmatrix}, \tag{4.12}$$

and

$$\vec{S}_n^{\Upsilon} = \begin{pmatrix} 0 \\ 0 \\ 0 \\ 0 \\ \frac{4}{n\pi}\left[i\eta_0(\mathcal{U} - \mathcal{U}'') - \mathcal{U}^2\right]\theta_n \\ 0 \end{pmatrix}. \tag{4.13}$$

We then write $\vec{X}_n = \vec{X}_n^{\Upsilon} + b_n^{xz}\vec{X}_n^{xz} + b_n^{yz}\vec{X}_n^{yz} + b_n^p \vec{X}_n^p$, where the vectors $\vec{X}_n^{\Upsilon}$, $\vec{X}_n^{xz}$, $\vec{X}_n^{yz}$ and $\vec{X}_n^p$ are respectively solutions of the following equations:

$$\frac{d}{d\eta}\vec{X}_n^{\Upsilon} = \mathcal{P}_n \vec{X}_n^{\Upsilon} + \vec{S}_n^{\Upsilon} \quad \text{with} \quad \vec{X}_n^{\Upsilon}(0) = (0,0,0,0,0,0) \tag{4.14}$$

$$\frac{d}{d\eta}\vec{X}_n^{xz} = \mathcal{P}_n \vec{X}_n^{xz} \quad \text{with} \quad \vec{X}_n^{xz}(0) = (0,0,0,1,0,0)\,, \tag{4.15}$$

$$\frac{d}{d\eta}\vec{X}_n^{yz} = \mathcal{P}_n \vec{X}_n^{yz} \quad \text{with} \quad \vec{X}_n^{yz}(0) = (0,0,0,0,1,0)\,, \tag{4.16}$$

$$\frac{d}{d\eta}\vec{X}_n^{p} = \mathcal{P}_n \vec{X}_n^{p} \quad \text{with} \quad \vec{X}_n^{p}(0) = (0,0,0,0,0,1)\,. \tag{4.17}$$

The values of H_n, b_n^{xz}, b_n^{yz} and b_n^p are determined by (4.50,4.51).

4.1.4 Saint-Venant calculation

The linearized equations (1.47) to solve are

$$H\partial_x|u_1\rangle + u_0\partial_x|h_1\rangle + H\partial_y|v_1\rangle = 0, \tag{4.18}$$

$$u_0\partial_x|u_1\rangle = -g\partial_x|h_1\rangle - C\frac{u_0}{H}|u_1\rangle + 2C\frac{u_0^2}{H^2}|h_1\rangle, \tag{4.19}$$

$$u_0\partial_x|v_1\rangle = -g\partial_y|h_1\rangle - C\frac{u_0}{H}|v_1\rangle. \tag{4.20}$$

Due to the terms $\langle s_n|1\rangle/\langle s_n|s_n\rangle$ now present due to the expansion of $|v_1\rangle$, the momentum equation projected along the y-axis is modified in comparison to the calculation in the previous chapter, and the above equations, once projected, now lead to:

$$iU_n + \frac{i}{\eta_H\sqrt{C}}H_n + \frac{r_n}{k}V_n = 0, \tag{4.21}$$

$$i\eta_H U_n + i\frac{1}{\mathcal{F}^2\sqrt{C}}H_n + CU_n - \frac{2\sqrt{C}}{\eta_H}H_n = 0, \tag{4.22}$$

$$i\eta_H V_n - \frac{r_n}{k}\frac{1}{\mathcal{F}^2\sqrt{C}}H_n + CV_n = \frac{4}{n\pi}\frac{1}{\sqrt{C}}(\eta_H - iC)\theta_n, \tag{4.23}$$

whose solution is

$$U_n = \frac{4\theta_n}{n\pi}\frac{1}{\sqrt{C}}\frac{(\eta_H + 2iC\mathcal{F}^2)\frac{r_n}{k}}{\eta_H\left[1-\mathcal{F}^2+\left(\frac{r_n}{k}\right)^2\right]+3iC\mathcal{F}^2}, \tag{4.24}$$

$$V_n = \frac{4\theta_n}{n\pi}\frac{1}{\sqrt{C}}\frac{-i\eta_H + \mathcal{F}^2(3C+i\eta_H)}{\eta_H\left[1-\mathcal{F}^2+\left(\frac{r_n}{k}\right)^2\right]+3iC\mathcal{F}^2}, \tag{4.25}$$

$$H_n = -\frac{4\theta_n}{n\pi}\frac{1}{\sqrt{C}}\frac{(\eta_H - iC)\mathcal{F}^2\frac{r_n}{k}3\eta_0}{\eta_H\left[1-\mathcal{F}^2+\left(\frac{r_n}{k}\right)^2\right]+3iC\mathcal{F}^2}. \tag{4.26}$$

With the rescaling (3.53-3.57), the above equations (4.21-4.23) read:

$$i\tilde{k}(\tilde{U}_n + \tilde{H}_n) + \tilde{r}_n\tilde{V}_n = 0, \tag{4.27}$$

$$i\tilde{k}\tilde{U}_n + i\frac{\tilde{k}}{\mathcal{F}^2}\tilde{H}_n + \tilde{U}_n - 2\tilde{H}_n = 0, \tag{4.28}$$

$$i\tilde{k}\tilde{V}_n - \frac{\tilde{r}_n}{\mathcal{F}^2}\tilde{H}_n + \tilde{V}_n = \frac{4}{n\pi}\eta_H(\tilde{k}-i)\theta_n, \tag{4.29}$$

whose solution is

$$\tilde{U}_n = \eta_H\frac{4\theta_n}{n\pi}\frac{(\tilde{k}+2i\mathcal{F}^2)\tilde{r}_n}{\tilde{k}^2 - \mathcal{F}^2\tilde{k}(\tilde{k}-3i)+\tilde{r}_n^2}, \tag{4.30}$$

$$\tilde{V}_n = \eta_H\frac{4\theta_n}{n\pi}\frac{\tilde{k}[\mathcal{F}^2(3+ik)-ik]}{\tilde{k}^2 - \mathcal{F}^2\tilde{k}(\tilde{k}-3i)+\tilde{r}_n^2}, \tag{4.31}$$

$$\tilde{H}_n = -\eta_H\frac{4\theta_n}{n\pi}\frac{(\tilde{k}-i)\mathcal{F}^2\tilde{r}_n}{\tilde{k}^2 - \mathcal{F}^2\tilde{k}(\tilde{k}-3i)+\tilde{r}_n^2}. \tag{4.32}$$

We now wish to express the basal stress. Equation (3.64) relating $\vec{\tau}_b$ to $\vec{u}$ is still valid. Because $|v_1\rangle$ has a contribution along the vector $|1\rangle$, we must write the first order components of $\vec{\tau}_b$ under the following form:

$$|\tau_1^{xz}\rangle = u_*^2 k\Upsilon\, e^{ikx} \sum_{n=1}^{\infty} (C_x^n + iD_x^n)\,|c_n\rangle \tag{4.33}$$

$$|\tau_1^{yz}\rangle = u_*^2 k\Upsilon\, e^{ikx} \left\{ i\sqrt{C}\,|1\rangle + \sum_{n=1}^{\infty} (iC_y^n - D_y^n)\,|s_n\rangle \right\}. \tag{4.34}$$

From equations (3.65) and (3.66), we get the stress coefficients $C_{x,y}^n$ and $D_{x,y}^n$:

$$C_x^n + iD_x^n = \sqrt{C}\left(U_n - \frac{1}{3\eta_0} H_n\right), \tag{4.35}$$

$$iC_y^n - D_y^n = \sqrt{C}\, V_n, \tag{4.36}$$

i.e., once C has been replaced by its expression:

$$C_x^n + iD_x^n = \sqrt{C}\, U_n - \frac{1}{\eta_H} H_n, \tag{4.37}$$

$$iC_y^n - D_y^n = \sqrt{C}\, V_n, \tag{4.38}$$

With the rescaled variables, these coefficients can be expressed as

$$C_x^n + iD_x^n = \frac{1}{\eta_H}\left(\tilde{U}_n - \tilde{H}_n\right) = \frac{1}{C\tilde{k}}\left(\tilde{U}_n - \tilde{H}_n\right), \tag{4.39}$$

$$iC_y^n - D_y^n = \frac{1}{\eta_H}\tilde{V}_n = \frac{1}{C\tilde{k}}\tilde{V}_n. \tag{4.40}$$

4.1.5 Basal coefficients

The influence of the modulated banks on the basal shear stress is shown through the coefficients C and D in figures 4.1 and 4.2. These coefficients have simple behaviours at small wave numbers (typically $kH \lesssim 10^{-2}$), for which both Navier-Stokes and shallow water Saint-Venant descriptions quantitatively agree with each other. Similarly to the case of a perturbed bed in a straight channel, the agreement between the two descriptions is still qualitatively correct for the coefficients C_x and C_y at larger kH. Asymptotic expressions derived from (4.39, 4.40) and (4.30 - 4.32) give:

$$C_x^n \sim \frac{4\theta_n}{n\pi}\left(\frac{4\mathcal{F}^4}{r_n^3} + \frac{1}{r_n}\right) k\,. \tag{4.41}$$

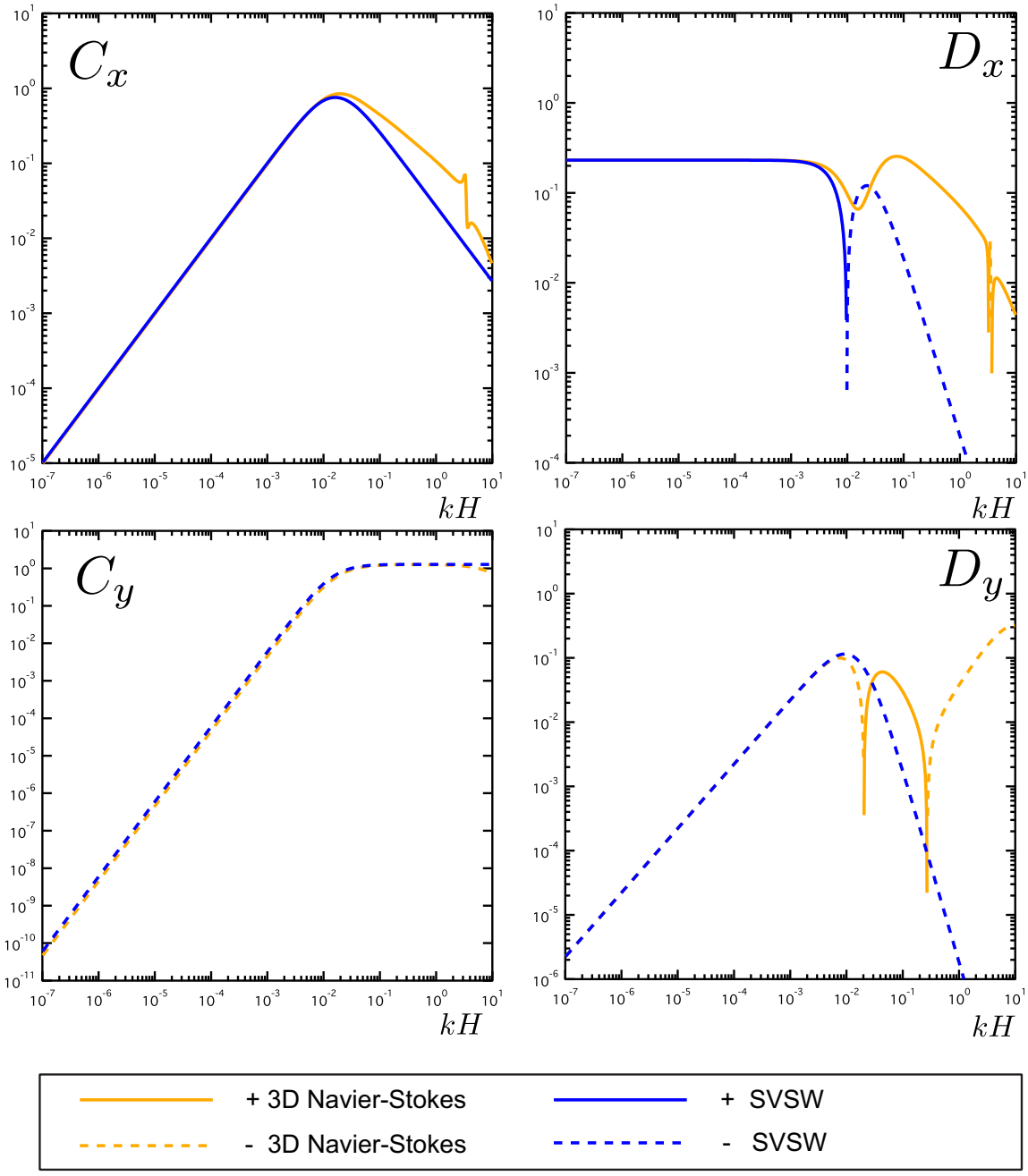


Figure 4.1: Basal shear stress coefficients C_x, D_x, C_y, D_y from Navier-Stokes (blue) and St-Venant (orange) equations for laminar flows. These curves have been computed for the transverse mode $n = 1$ (i.e. a transverse wavenumber $r_1 = \pi/(2y_0)$), and with $\beta = 200$, $Re \simeq 15$ ($C \simeq 0.2$) and $\mathcal{F} \simeq 0.6$. The graphical convention is the same as in Fig. 3.1.

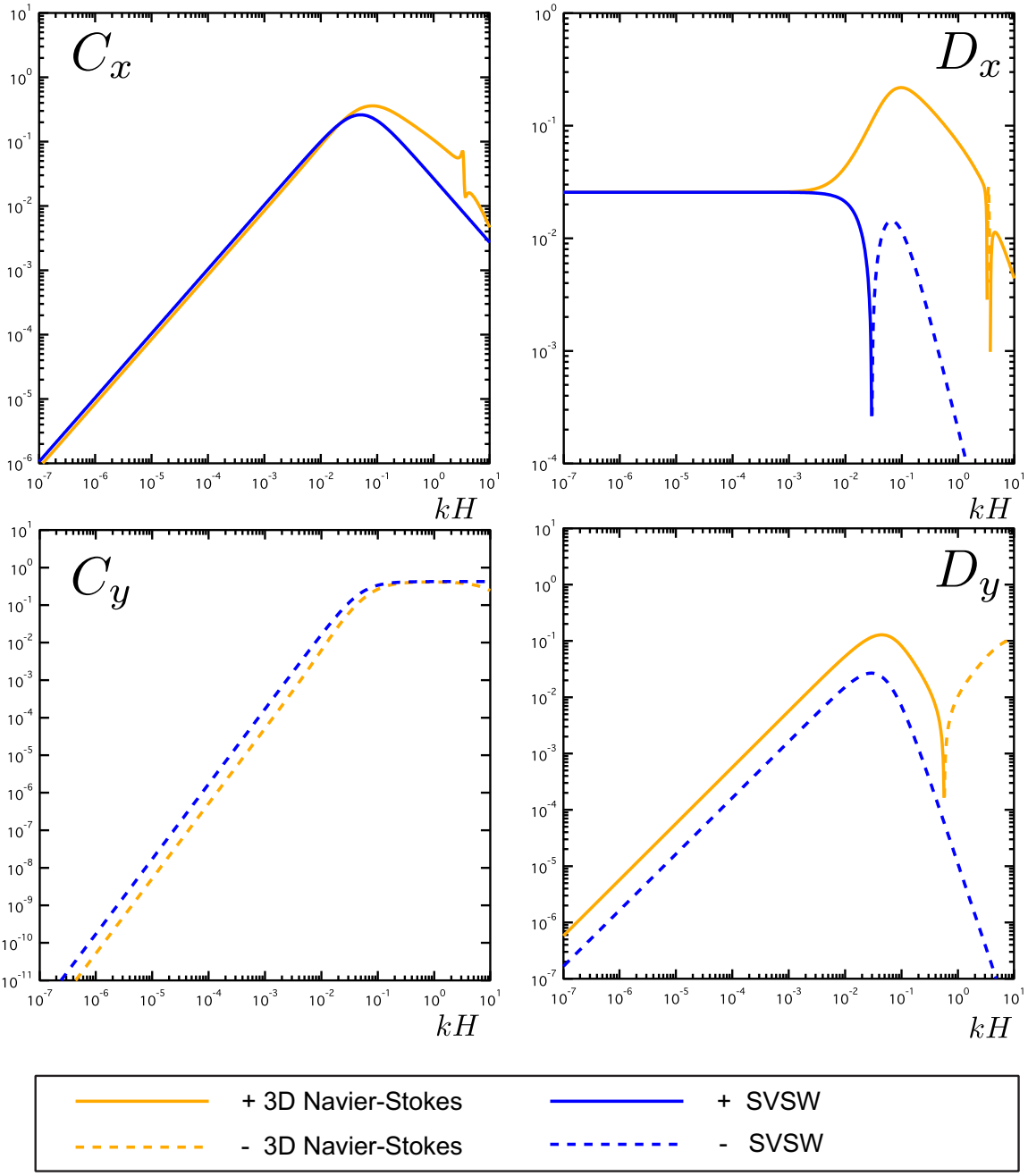


Figure 4.2: Same as Fig. 4.1, but for the transverse mode $n = 3$ (i.e. a transverse wavenumber $r_3 = 3\pi/(2y_0)$).

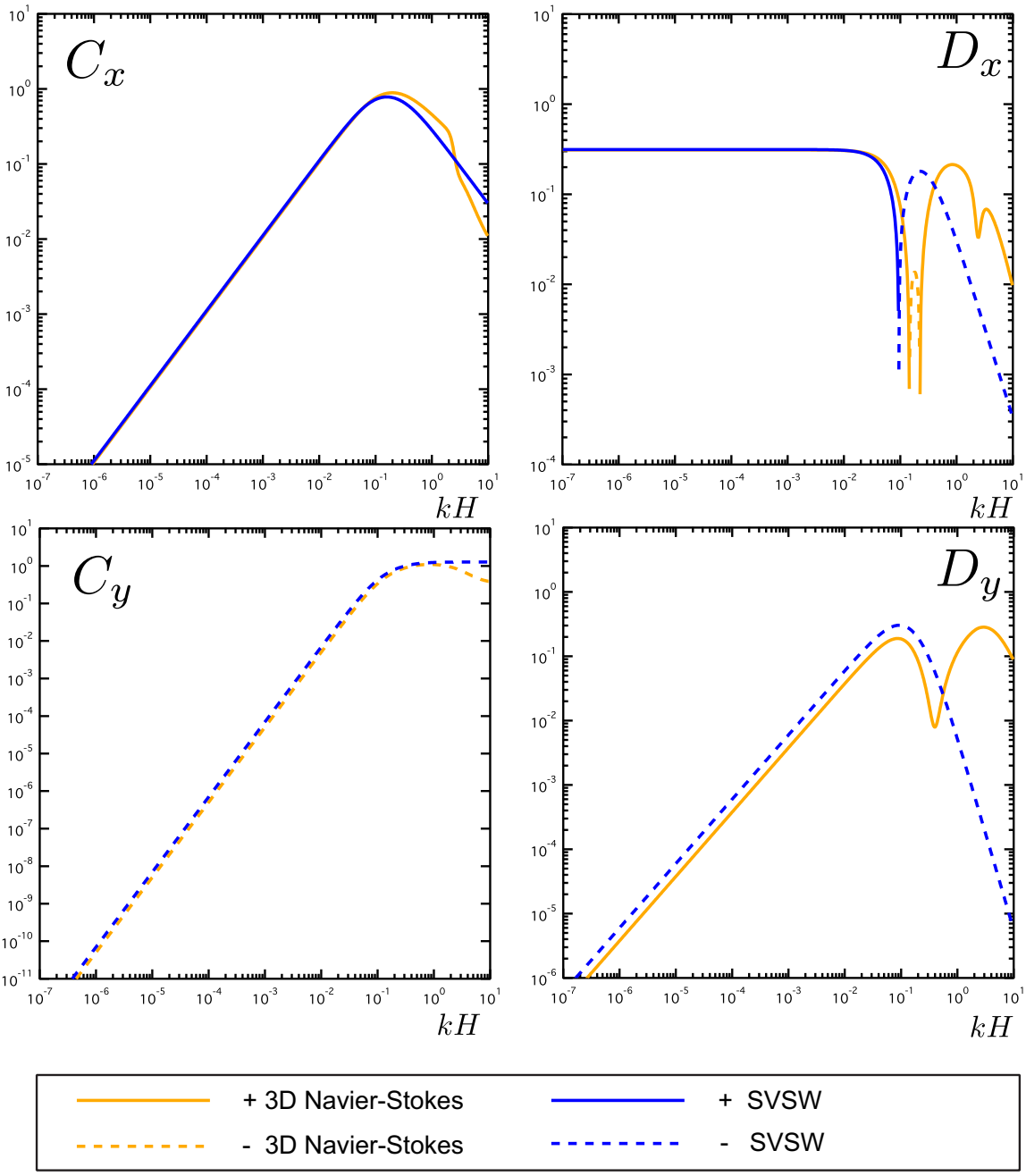


Figure 4.3: Same as Fig. 4.1, but for a smaller aspect ratio $\beta = 20$.

Similarly, C_y is negative over all the range and its asymptotic behavior is:

$$C_y^n \sim -\frac{4\theta_n}{n\pi}\left(\frac{6\mathcal{F}^4}{r_n^4}+\frac{1-\mathcal{F}^2}{r_n^2}\right)k^2\,, \tag{4.42}$$

where $r_n = 2y_0/n\pi$. By contrast, sign differences are observed for D_x and D_y for $kH \gtrsim 10^{-2}$, the asymptotic behaviors for $kH \to 0$ are:

$$D_x^n \sim \frac{4\theta_n}{n\pi}\frac{\mathcal{F}^2}{r_n}, \tag{4.43}$$

$$D_y^n \sim -\frac{4\theta_n}{n\pi}\frac{3\mathcal{F}^2}{2r_n^2}k\,, \tag{4.44}$$

As in the precedent chapter, the basal coefficients show a very slight dependence on the Froude number. The anomalous peak, or sign switch, around $kH \sim 4$ is caused by a resonance induced by the water depth of thickness H.

4.2 Turbulent flow

In this section, we similarly proceed as in the turbulent case, i.e. with RANS equations. The base flow has the same logarithmic form (3.81) as in the turbulent paragraph of the previous chapter.

4.2.1 First order equations

Similarly to the previous section, we use the representation:

$$
\begin{aligned}
k|h_1\rangle &= k\Upsilon\, e^{ikx} \sum_{n=1}^{\infty} H_n\,|c_n\rangle \\
|u_1\rangle &= u_* k\Upsilon\, e^{ikx} \sum_{n=1}^{\infty} U_n(\eta)\,|c_n\rangle \\
|v_1\rangle &= u_* k\Upsilon e^{ikx} \left\{ i\,\mathcal{U}(\eta)|1\rangle + \sum_{n=1}^{\infty} V_n(\eta)\,|s_n\rangle \right\} \\
|w_1\rangle &= u_* k\Upsilon e^{ikx} \sum_{n=1}^{\infty} W_n(\eta)\,|c_n\rangle \\
|\tau_1^{xz}\rangle &= -u_*^2 k\Upsilon\, e^{ikx} \sum_{n=1}^{\infty} S_n^{xz}(\eta)\,|c_n\rangle \\
|\tau_1^{xy}\rangle &= -u_*^2 k\Upsilon\, e^{ikx} \left\{ -\frac{\mathcal{U}}{\mathcal{U}'}\left(1-\frac{\eta}{\eta_H}\right)|1\rangle + \sum_{n=1}^{\infty} S_n^{xy}(\eta)\,|s_n\rangle \right\} \\
|\tau_1^{yz}\rangle &= -u_*^2 k\Upsilon\, e^{ikx} \left\{ i\left(1-\frac{\eta}{\eta_H}\right)|1\rangle + \sum_{n=1}^{\infty} S_n^{yz}(\eta)\,|s_n\rangle \right\} \\
|p_1+\tau_1^{zz}\rangle &= u_*^2 k\Upsilon\, e^{ikx} \sum_{n=1}^{\infty} S_n^{p}(\eta)\,|c_n\rangle \\
|\tau_1^{xx}\rangle &= u_*^2 k\Upsilon\, e^{ikx} \sum_{n=1}^{\infty} S_n^{xx}(\eta)\,|c_n\rangle \\
|\tau_1^{yy}\rangle &= u_*^2 k\Upsilon\, e^{ikx} \sum_{n=1}^{\infty} S_n^{yy}(\eta)\,|c_n\rangle \\
|\tau_1^{zz}\rangle &= u_*^2 k\Upsilon\, e^{ikx} \sum_{n=1}^{\infty} S_n^{zz}(\eta)\,|c_n\rangle
\end{aligned}
\tag{4.45}
$$

Note that the slip boundary conditions have been used, and are responsible for the term in $|1\rangle$ in the expression for v_1. This additional term in v_1 also generates terms

in $|1\rangle$ for τ_1^{xy} and τ_1^{yz}. The stress equations remain the same as before, except for τ_1^{xz}, which is simpler because the mixing length is simpler

$$L = (z_0 + z)\sqrt{\frac{H + h_1 - z}{H + h_1}} \tag{4.46}$$

due to the flat bed configuration ($Z = 0$) considered in this case. This modifies the equation on U_n' as follows:

$$U_n' = -iW_n + \frac{1}{2}\frac{\mathcal{U}'}{1 - \frac{\eta}{\eta_H}} S_n^{xz} - \frac{\eta \mathcal{U}' H_n}{2\eta_H^2\left(1 - \frac{\eta}{\eta_H}\right)}\,. \tag{4.47}$$

Moreover, due to the terms $\langle s_n|1\rangle/\langle s_n|s_n\rangle$, the Navier-Stokes equation projected along the y-axis is modified and now leads to:

$$\begin{aligned} S_n^{yz\prime} &= 3i\frac{1}{\mathcal{U}'}\left(1 - \frac{\eta}{\eta_H}\right)\frac{r_n}{k}U_n + \left\{i\mathcal{U} + \frac{1}{\mathcal{U}'}\left(1 - \frac{\eta}{\eta_H}\right)\left[1 + 4\left(\frac{r_n}{k}\right)^2\right]\right\}V_n \\ &- \frac{r_n}{k}S_n^p + \frac{4}{n\pi}\left[i\frac{\mathcal{U}}{\mathcal{U}'}\left(1 - \frac{\eta}{\eta_H}\right) + \frac{i}{\eta_H} - \mathcal{U}^2\right]\theta_n, \end{aligned} \tag{4.48}$$

The boundary conditions needed to integrate the equations are now the following.

(i) The velocity vanishes on the bed

$$U_n(0) = 0, \quad V_n(0) = 0 \quad \text{and} \quad W_n(0) = 0; \tag{4.49}$$

(ii) The normal velocity vanishes at the free surface

$$W_n(\eta_H) = i\mathcal{U}(\eta_H)\, H_n; \tag{4.50}$$

(iii) the shear and normal stesses vanish at the free surface

$$S_n^{xz}(\eta_H) = \frac{H_n}{\eta_H}, \quad S_n^{yz}(\eta_H) = 0 \quad \text{and} \quad S_n^p(\eta_H) = \frac{H_n}{\eta_H \tan\theta}. \tag{4.51}$$

These conditions select the values of $S_n^{xz}(0)$, $S_n^{yz}(0)$, $S_n^p(0)$ and H_n. Recall that the basal coefficients are related to these functions (see Eqs. 4.7, 4.8).

4.2.2 Average velocity

As before, we compute the average velocity coefficients $\bar{U}_n$ defined such that

$$\bar{u} = u_* \left\{ \bar{\mathcal{U}} + k\Upsilon e^{ikx} \sum_{n=1}^{\infty} \bar{U}_n^{\Upsilon} |c_n\rangle \right\}, \tag{4.52}$$

and obtain:

$$\begin{aligned} \bar{U}_n^{\Upsilon} &= \frac{1}{\eta_H} \left(H_n \left[\mathcal{U}(\eta_H) - \bar{\mathcal{U}} \right] + \int_0^{\eta_H} U_n(\eta) d\eta \right) \\ &= \frac{H_n}{\kappa \eta_H} + \frac{1}{\eta_H} \int_0^{\eta_H} U_n(\eta) d\eta. \end{aligned} \tag{4.53}$$

4.2.3 Numerical integration

We write the differential equations for the disturbance induced by the oscillating banks under the form:

$$\frac{d}{d\eta} \vec{X}_n = \mathcal{P}_n \vec{X}_n + \vec{S}_n^{\Upsilon} + H_n \vec{S}_n^H, \tag{4.54}$$

with the vector $\vec{X}_n = (U_n, V_n, W_n, S_n^{xz}, S_n^{yz}, S_n^p)$, the matrix

$$\mathcal{P}_n = \begin{pmatrix} 0 & 0 & -i & \frac{1}{2}\frac{\mathcal{U}'}{1-\frac{\eta}{\eta_H}} & 0 & 0 \\ 0 & 0 & \frac{r_n}{k} & 0 & \frac{\mathcal{U}'}{1-\frac{\eta}{\eta_H}} & 0 \\ -i & -\frac{r_n}{k} & 0 & 0 & 0 & 0 \\ i\mathcal{U} + \frac{1}{\mathcal{U}'}\left(1-\frac{\eta}{\eta_H}\right)\left[4+\left(\frac{r_n}{k}\right)^2\right] & -3i\frac{1}{\mathcal{U}'}\left(1-\frac{\eta}{\eta_H}\right)\frac{r_n}{k} & \mathcal{U}' & 0 & 0 & i \\ 3i\frac{1}{\mathcal{U}'}\left(1-\frac{\eta}{\eta_H}\right)\frac{r_n}{k} & i\mathcal{U} + \frac{1}{\mathcal{U}'}\left(1-\frac{\eta}{\eta_H}\right)\left[1+4\left(\frac{r_n}{k}\right)^2\right] & 0 & 0 & 0 & -\frac{r_n}{k} \\ 0 & 0 & -i\mathcal{U} & i & \frac{r_n}{k} & 0 \end{pmatrix}, \tag{4.55}$$

and the two vectors

$$\vec{S}_n^Z = \left(0, 0, 0, 0, \frac{4}{n\pi}\left[i\frac{\mathcal{U}}{\mathcal{U}'}\left(1-\frac{\eta}{\eta_H}\right) + \frac{i}{\eta_H} - \mathcal{U}^2\right]\theta_n, 0\right), \tag{4.56}$$

$$\vec{S}_n^H = \left(-\frac{\eta\,\mathcal{U}'}{2\eta_H^2\left(1-\frac{\eta}{\eta_H}\right)}, 0, 0, 0, 0, 0\right). \tag{4.57}$$

We then proceed similarly and write $\vec{X}_n = \vec{X}_n^{\Upsilon} + b_n^{xz}\vec{X}_n^{xz} + b_n^{yz}\vec{X}_n^{yz} + b_n^p\vec{X}_n^p + H_n\vec{X}_n^H$, where the vectors $\vec{X}_n^{\Upsilon}$, $\vec{X}_n^{xz}$, $\vec{X}_n^{yz}$, $\vec{X}_n^p$ and $\vec{X}_n^H$ are respectively solutions of the fol-

lowing equations:

$$\frac{d}{d\eta}\vec{X}_n^{\Upsilon} = \mathcal{P}_n\vec{X}_n^{\Upsilon} + \vec{S}_n^{\Upsilon} \quad \text{with} \quad \vec{X}_n^{\Upsilon}(0) = (0,0,0,0,0,0) \tag{4.58}$$

$$\frac{d}{d\eta}\vec{X}_n^{xz} = \mathcal{P}_n\vec{X}_n^{xz} \quad \text{with} \quad \vec{X}_n^{xz}(0) = (0,0,0,1,0,0)\,, \tag{4.59}$$

$$\frac{d}{d\eta}\vec{X}_n^{yz} = \mathcal{P}_n\vec{X}_n^{yz} \quad \text{with} \quad \vec{X}_n^{yz}(0) = (0,0,0,0,1,0)\,, \tag{4.60}$$

$$\frac{d}{d\eta}\vec{X}_n^{p} = \mathcal{P}_n\vec{X}_n^{p} \quad \text{with} \quad \vec{X}_n^{p}(0) = (0,0,0,0,0,1)\,. \tag{4.61}$$

$$\frac{d}{d\eta}\vec{X}_n^{H} = \mathcal{P}_n\vec{X}_n^{H} + \vec{S}_n^{H} \quad \text{with} \quad \vec{X}_n^{H}(0) = (0,0,0,0,0,0)\,, \tag{4.62}$$

Now, the values of H_n, b_n^{xz}, b_n^{yz} and b_n^{p} are determined by (4.50,4.51).

4.2.4 St-Venant

The linearised equations (1.50 and 1.51) to solve are

$$H\partial_x|u_1\rangle + u_0\partial_x|h_1\rangle + H\partial_y|v_1\rangle = 0, \tag{4.63}$$

$$u_0\partial_x|u_1\rangle = -g\partial_x|h_1\rangle - 2C\frac{u_0}{H}|u_1\rangle + C\frac{u_0^2}{H^2}|h_1\rangle, \tag{4.64}$$

$$u_0\partial_x|v_1\rangle = -g\partial_y|h_1\rangle - C\frac{u_0}{H}|v_1\rangle. \tag{4.65}$$

Taking not account the terms $\langle s_n|1\rangle/\langle s_n|s_n\rangle$, the above equations, once projected on the $(|c_n\rangle,\, |s_n\rangle)$ base, lead to:

$$iU_n + \frac{i}{\eta_H\sqrt{C}}H_n + \frac{r_n}{k}\,V_n = 0, \tag{4.66}$$

$$i\eta_H U_n + i\,\frac{1}{\mathcal{F}^2\sqrt{C}}\,H_n + 2CU_n - \frac{\sqrt{C}}{\eta_H}H_n = 0, \tag{4.67}$$

$$i\eta_H V_n - \frac{r_n}{k}\,\frac{1}{\mathcal{F}^2\sqrt{C}}\,H_n + CV_n = \frac{4}{n\pi}\,\frac{1}{\sqrt{C}}\,(\eta_H - iC)\theta_n, \tag{4.68}$$

whose solution is

$$U_n = \frac{4\theta_n}{n\pi}\frac{1}{\sqrt{C}}\frac{(\eta_H - iC)(\eta_H + iC\mathcal{F}^2)\frac{r_n}{k}}{(\eta_H - iC)\left\{\eta_H\left[1-\mathcal{F}^2+\left(\frac{r_n}{k}\right)^2\right]+3iC\mathcal{F}^2\right\} - iC\eta_H\left(\frac{r_n}{k}\right)^2}, \quad (4.69)$$

$$V_n = \frac{4\theta_n}{n\pi}\frac{1}{\sqrt{C}}\frac{(\eta_H - iC)\left[-i\eta_H + \mathcal{F}^2(3C + i\eta_H)\right]}{(\eta_H - iC)\left\{\eta_H\left[1-\mathcal{F}^2+\left(\frac{r_n}{k}\right)^2\right]+3iC\mathcal{F}^2\right\} - iC\eta_H\left(\frac{r_n}{k}\right)^2}, \quad (4.70)$$

$$H_n = -\frac{4\theta_n}{n\pi}\frac{1}{\sqrt{C}}\frac{(\eta_H - iC)(\eta_H - 2iC)\mathcal{F}^2\frac{r_n}{k}\sqrt{C}\eta_H}{(\eta_H - iC)\left\{\eta_H\left[1-\mathcal{F}^2+\left(\frac{r_n}{k}\right)^2\right]+3iC\mathcal{F}^2\right\} - iC\eta_H\left(\frac{r_n}{k}\right)^2}. \quad (4.71)$$

With the rescaling (3.130-3.134), the above equations (4.66-4.68) write:

$$i\tilde{k}(\tilde{U}_n + \tilde{H}_n) + \tilde{r}_n\tilde{V}_n = 0, \quad (4.72)$$

$$i\tilde{k}\tilde{U}_n + i\frac{\tilde{k}}{\mathcal{F}^2}\tilde{H}_n + 2\tilde{U}_n - \tilde{H}_n = 0, \quad (4.73)$$

$$i\tilde{k}\tilde{V}_n - \frac{\tilde{r}_n}{\mathcal{F}^2}\tilde{H}_n + \tilde{V}_n = \frac{4}{n\pi}\eta_H(\tilde{k} - i)\theta_n, \quad (4.74)$$

whose solution is

$$\tilde{U}_n = \eta_H\frac{4\theta_n}{n\pi}\frac{(\tilde{k}-i)(\tilde{k}+i\mathcal{F}^2)\tilde{r}_n}{(\tilde{k}-i)\left[\tilde{k}^2 - \mathcal{F}^2\tilde{k}(\tilde{k}-3i) + \tilde{r}_n^2\right] - i\tilde{r}_n^2}, \quad (4.75)$$

$$\tilde{V}_n = \eta_H\frac{4\theta_n}{n\pi}\frac{\tilde{k}(\tilde{k}-i)[\mathcal{F}^2(3+ik) - ik]}{(\tilde{k}-i)\left[\tilde{k}^2 - \mathcal{F}^2\tilde{k}(\tilde{k}-3i) + \tilde{r}_n^2\right] - i\tilde{r}_n^2}, \quad (4.76)$$

$$\tilde{H}_n = -\eta_H\frac{4\theta_n}{n\pi}\frac{(\tilde{k}-i)(\tilde{k}-2i)\mathcal{F}^2\tilde{r}_n}{(\tilde{k}-i)\left[\tilde{k}^2 - \mathcal{F}^2\tilde{k}(\tilde{k}-3i) + \tilde{r}_n^2\right] - i\tilde{r}_n^2}. \quad (4.77)$$

We now wish to express the basal stress. Equation (3.141) relating $\vec{\tau}_b$ to $\vec{u}$ is still valid. Because $|v_1\rangle$ has a contribution along the vector $|1\rangle$, we write the first order components of $\vec{\tau}_b$ under the following form:

$$|\tau_1^{xz}\rangle = u_*^2 k\Upsilon\, e^{ikx}\sum_{n=1}^{\infty}(C_x^n + iD_x^n)\,|c_n\rangle \quad (4.78)$$

$$|\tau_1^{yz}\rangle = u_*^2 k\Upsilon\, e^{ikx}\left\{i\sqrt{C}|1\rangle + \sum_{n=1}^{\infty}(iC_y^n - D_y^n)\,|s_n\rangle\right\}. \quad (4.79)$$

From equations (3.142) and (3.143), we get the stress coefficients $C^n_{x,y}$ and $D^n_{x,y}$:

$$C^n_x + iD^n_x = 2\sqrt{C}\,U_n, \tag{4.80}$$
$$iC^n_y - D^n_y = \sqrt{C}\,V_n. \tag{4.81}$$

With the rescaled variables, these coefficients can be expressed as

$$C^n_x + iD^n_x = \frac{2}{\eta_H}\tilde{U}_n = \frac{2}{C\tilde{k}}\tilde{U}_n, \tag{4.82}$$
$$iC^n_y - D^n_y = \frac{1}{\eta_H}\tilde{V}_n = \frac{1}{C\tilde{k}}\tilde{V}_n. \tag{4.83}$$

4.2.5 Basal Coefficients

The behavior of the basal shear stress coefficients in this turbulent case is displayed in figures 4.4 and 4.5 for the transverse modes $n = 1$ and $n = 3$ respectively. The curves are similar to those in the laminar case. The comparison of the two hydrodynamical descriptions (3D RANS and shallow water Saint-Venant equations) is also similar. Through the definitions (4.82 - 4.83) and (4.75 - 4.77) we derive the asymptotic behaviors, at kH small, for the C^n_x and C^n_y coefficients:

$$C^n_x \sim \frac{4\theta_n}{n\pi}\left(\frac{3\mathcal{F}^4}{2r_n^3} + \frac{1}{2}\frac{2-\mathcal{F}^2}{r_n}\right)k\,. \tag{4.84}$$

Similarly, C_y is negative over all the range and its asymptotic behavior is:

$$C^n_y \sim -\frac{4\theta_n}{n\pi}\,\frac{9\mathcal{F}^4 + 2r_n^2 - 5\mathcal{F}^2 r_n^2}{4r_n^4}\,k^2\,, \tag{4.85}$$

where $r_n = 2y_0/n\pi$. By contrast, sign differences are observed for D_x and D_y for $kH \gtrsim 10^{-2}$, the asymptotic behaviors for $kH \to 0$ are:

$$D^n_x \sim \frac{4\theta_n}{n\pi}\frac{\mathcal{F}^2}{r_n}, \tag{4.86}$$
$$D^n_y \sim -\frac{4\theta_n}{n\pi}\frac{3\mathcal{F}^2}{2r_n^2}k\,, \tag{4.87}$$

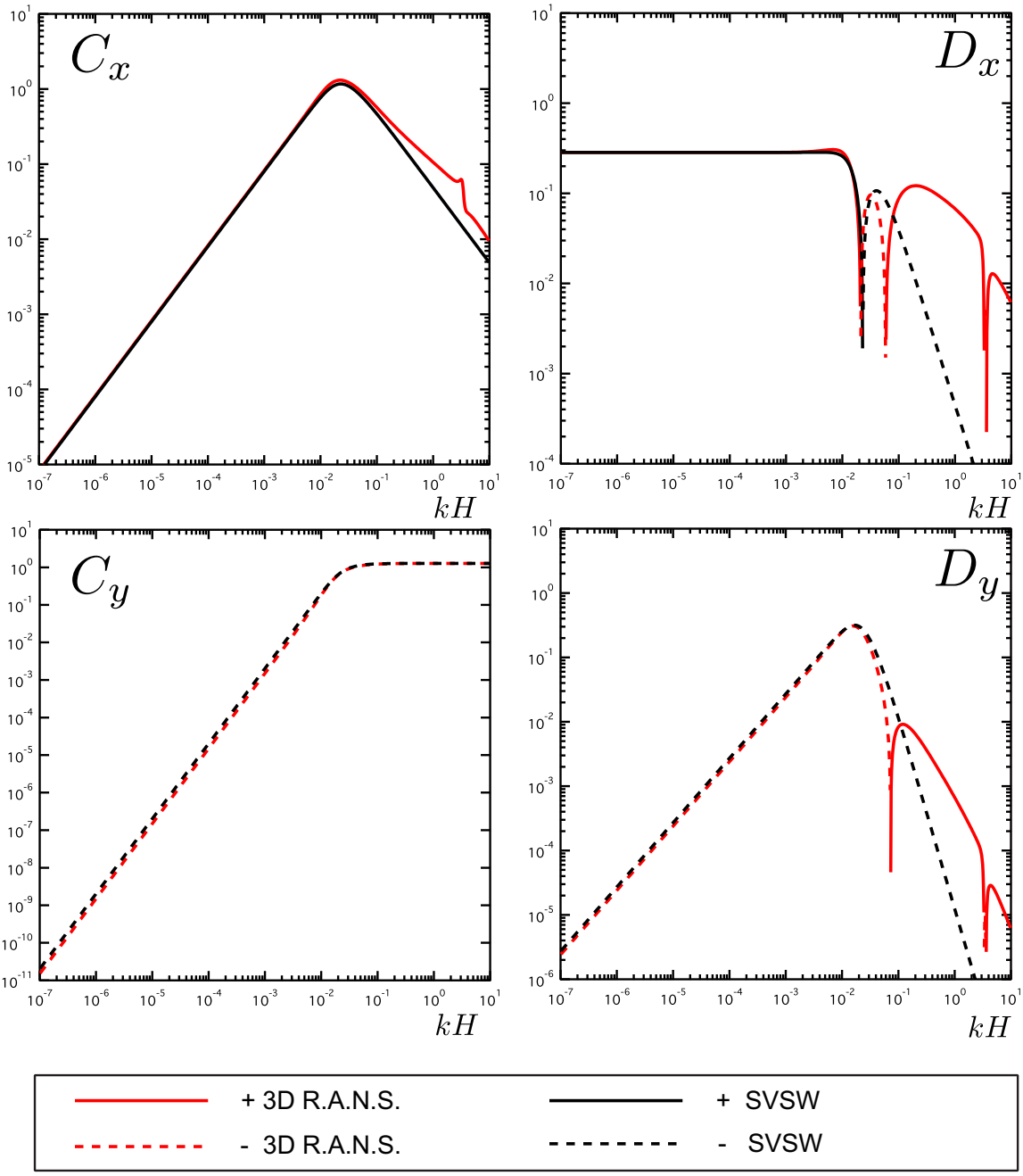


Figure 4.4: Basal shear stress coefficients C_x, D_x, C_y, D_y from RANS (black) and Saint-Venant (red) equations for turbulent flows. These curves have been computed for the transverse mode $n = 1$ (i.e. a transverse wavenumber $r_1 = \pi/(2y_0)$), and with $\beta = 200$, $H/z_0 \simeq 1.9$ ($C \simeq 0.2$) and $\mathcal{F} \simeq 0.6$. The graphical convention is the same as in Fig. 3.1.

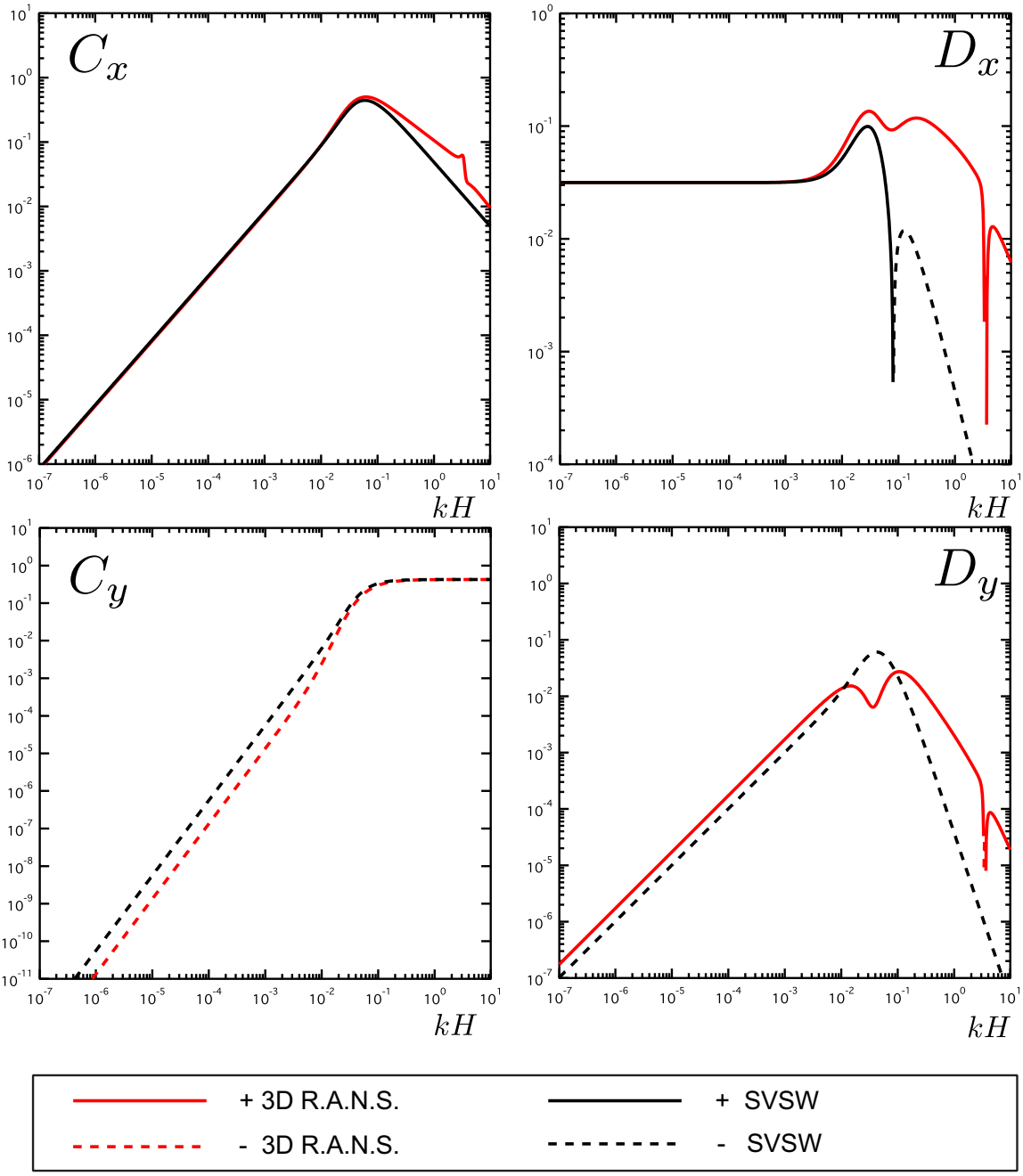


Figure 4.5: Same as Fig. 4.4, but for the transverse mode $n = 3$ (i.e. a transverse wavenumber $r_3 = 3\pi/(2y_0)$).

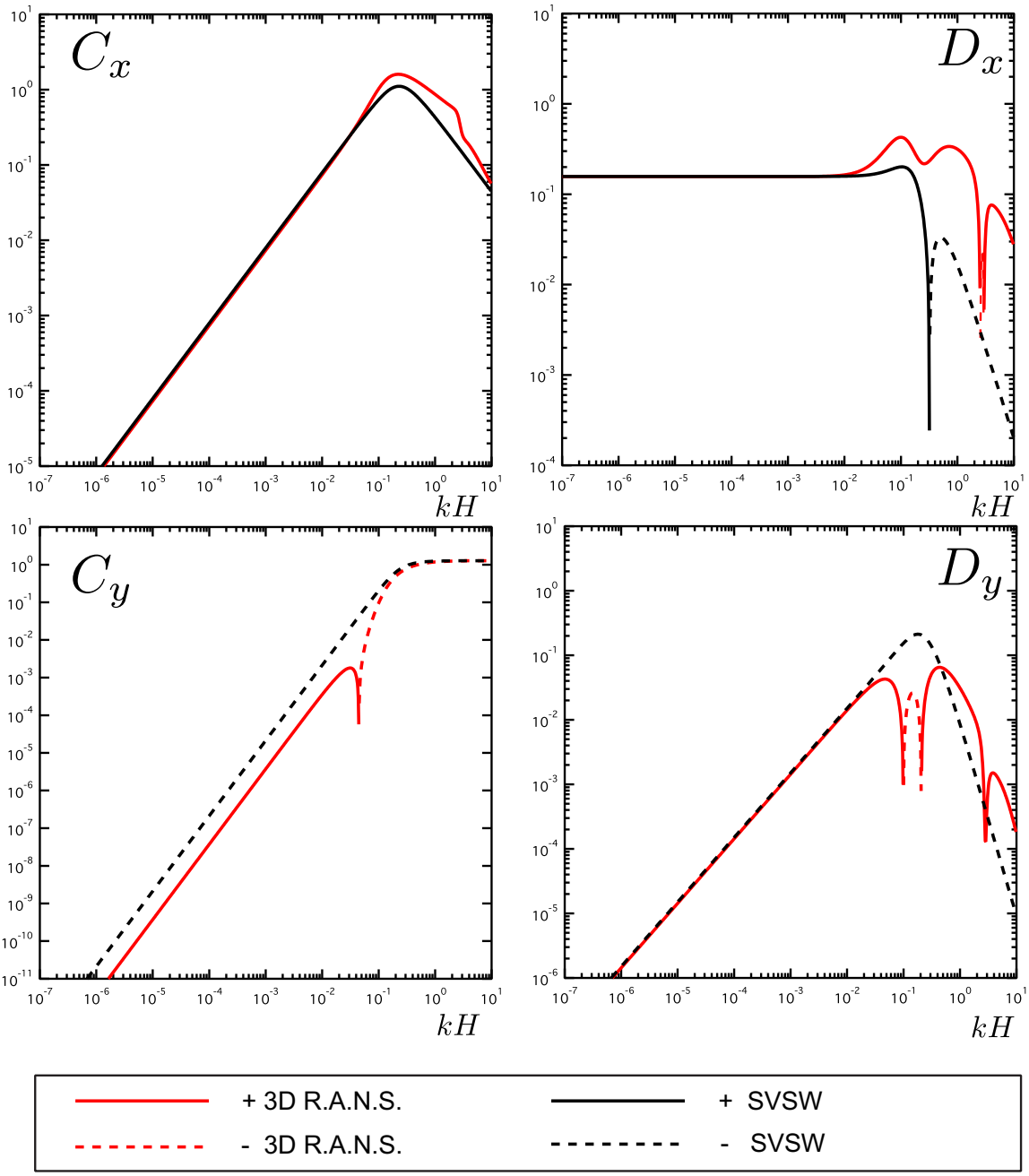


Figure 4.6: Same as Fig. 4.4, but for a smaller aspect ratio $\beta = 20$.

Part II

Transport

Chapter 5

Sediment transport

In this chapter we discuss how the description of sediment transport can be abstracted into a few key quantities, namely the Shields number, the saturated flux and the saturation length. This discussion is essentially a short review of the literature on the subject based on chapters of Andreotti & Claudin (2012) and Andreotti *et al.* (2013), as we need all these concepts for our main goal – the bar and meander instabilities. The following chapter will detail our contribution to the problem, based on a two-phase flow model.

5.1 Bed load and suspension

One usually distinguish different modes of sediment transport depending on the nature of the forces dominating the particle dynamics (Fig. 5.1). When hydrodynamic forces are much larger than contact forces, whatever the hydrodynamic regime (viscous, inertial but laminar or turbulent), sediment transport is said to be in suspension. This is typically the case for the transport of fine particles (silt, clay). When the effect of gravity is large enough to confine transport to a thin layer at the surface of the bed the transport mode is called bed load. Bed load is the preferred mode of transport of sand, gravels, pebbles and boulders in rivers. It is responsible for the formation of subaqueous ripples and dunes. The grains transported in bedload are entrained by the flow and, because they remain permanently in contact with the bed, are submitted to a friction exerted by the bed. In the next chapter, we will see how to describe the transition between these two modes of transport.

To understand the emergence and the evolution of the bars and meanders, it is necessary to develop an adequate formalism to relate the sediment flux to the fluid flow for these different modes of transport. This raises the question of the

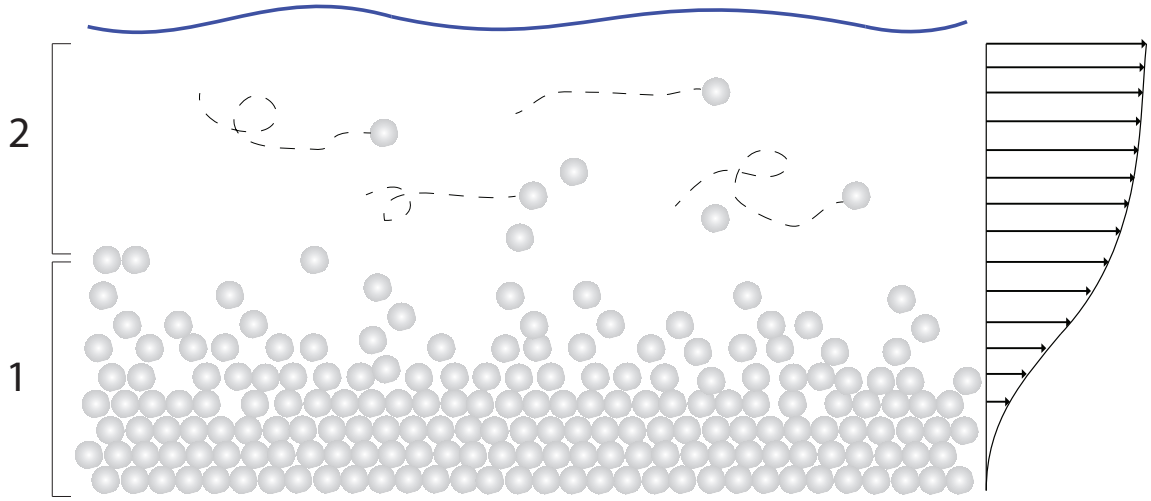


Figure 5.1: Schematic diagram showing the different modes of transport. Region 1: bed load. Region 2: suspension.

transport threshold, the question of the amount of material that a steady flow is able to transport (saturated flux) and the problems of transients, when the topography or the flow present spatial and temporal variations. To tackle these issues, we need to establish a connection between processes at the scale of the grain and the resulting mass transfers at the scale of the topography.

5.2 Shields number and transport threshold

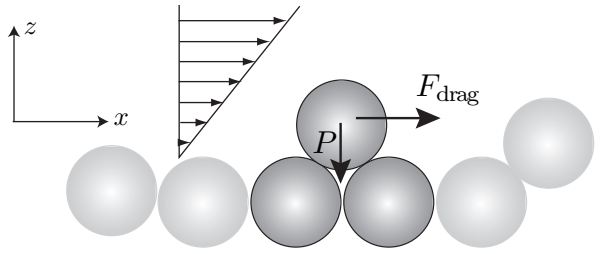


Figure 5.2: Origin of the sediment transport threshold at the scale of the grain.

5.2.1 Dimensional Analysis

Consider a spherical particle trapped between two of its (fixed) neighbours and submitted on its upper side to a fluid flow (Fig. 5.2). Assuming that the grains interact by friction only, the grain loses equilibrium when the driving force F_{drag} is equal to the weight of the grain reduced by the buoyancy $P \sim \pi/6\ (\rho_p - \rho_f) g d^3$, and multiplied by the effective friction coefficient μ. One obtains a quantitative criterion for the entrainment based on the ratio $F_{\text{drag}}/(\rho_p - \rho_f) g d^3$.

In order to obtain a criterion on the flow, we need to relate this force applied to the particle to the parameters controlling hydrodynamics. Dimensionally, the hydrodynamic force exerted by the fluid on a flat surface of the size of a grain is proportional to $\tau^f d^2$, where τ^f is the shear stress at the interface between grains and fluid. We therefore deduce that the transport threshold is controlled by a dimensionless number, called the Shields number, defined by:

$$\Theta = \frac{\tau^f}{(\rho_p - \rho_f) g d}. \tag{5.1}$$

Another important number is the dimensionless grains size d/d_ν. d_ν is a characteristic length, called the viscous diameter, which gives us informations about the influence of viscous effects at the level of grain size. It is the grain size for which viscous effects and gravity are of the same magnitude:

$$d_\nu = \left(\frac{\rho_p}{\rho_f} - 1 \right)^{-1/3} \nu^{2/3}\, g^{-1/3}, \tag{5.2}$$

In the experiments (described in chapter 9) we have used grains of diameter around $140\,\mu m$ for a viscous diameter of $220\,\mu m$. This gives a ratio $d/d_\nu = 0.64$.

This analysis at the grain scale suggests that the motion threshold is controlled by a threshold Shields number, $\Theta_{\text{th}} \propto \mu$, independent of the size of the grain, its density and the nature of the surrounding fluid. Figure 5.3 shows threshold Shields number measured in liquids of different viscosities ν and for natural sand of different sizes in laminar and turbulent regimes. One observes that the critical Shields number is nearly constant at large grain diameter but grows systematically as d decreases. This dependence suggests that the relationship between the drag force F_{drag} and the basal shear stress τ^f is more subtle than first appeared.

We can write this driving force in the form $\frac{\pi}{8} d^2 C_d \rho_f U^2$, where the phenomenological drag coefficient is written as $C_d = [C_\infty^{1/2} + s\mathcal{R}_d^{-1/2}]^2$, and where $\mathcal{R}_d = Ud/\nu$ is the Reynolds number based on the size of the grain. For natural sand, these constants apply $C_\infty \simeq 1$ and $s \simeq 5$ (Ferguson *et al.* 2004). The difficulty is to correctly

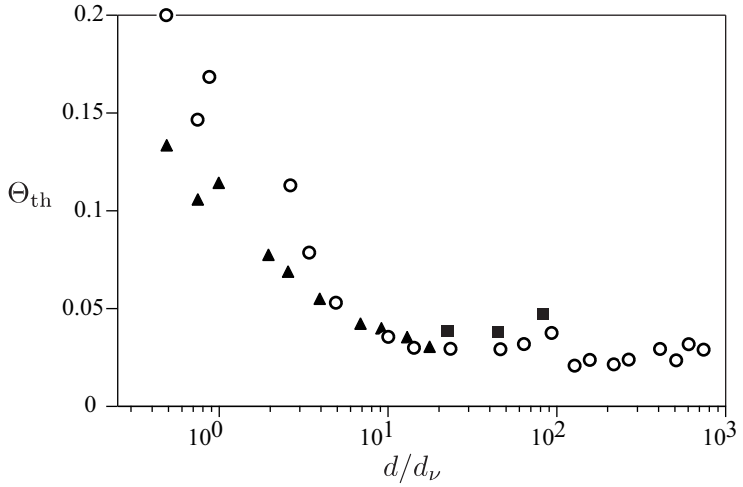


Figure 5.3: Shields number $\Theta_{\rm th}$ above which a flow can entrain natural sand grains of size d into motion. The grain size is made dimensionless using the viscous diameter d_ν. The symbols correspond to measurements carried out by (Fernandez Luque *et al.* 1976) (■) and those collected by (Yalin *et al.* 1979) in water (○) and in more viscous liquids (▲).

calculate the velocity of the fluid at the level of the grain U (for example at altitude $z = d/2$) to connect it to shear τ. This can be done by decomposing the shear into a viscous term and a contribution of the turbulent Reynold stress. Within purely viscous and turbulent limits, one obtains the following thresholds, respectively:

$$\Theta_{\rm th} = \frac{8\mu}{3s^2}, \tag{5.3}$$

$$\Theta_{\rm th} = \frac{4\mu\kappa^2}{3C_\infty \ln^2[1 + d/(2z_0)]}\,. \tag{5.4}$$

In the second term, $\kappa = 0.4$ is the von Kármán constant and z_0 the hydrodynamic roughness. This model efficiently replicates the experimental measurements obtained under water (figure 5.4 – **a**) in the literature.

Finally, the threshold is increased if a supplementary cohesion force exists between grains (Claudin *et al.* 2006). This is the case for our experiments, and we expect a threshold Shields number inthe range 0.2–0.25.

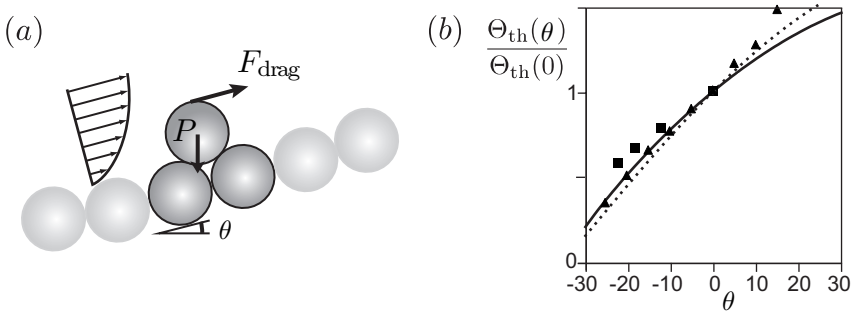


Figure 5.4: (a) Diagram showing the dependence of the threshold Shields number Θ_{th} with the tilt angle θ of the sand bed. (b) The black symbols correspond to measurements performed in water by Fernandez Luque & van Beek (1976) (■) and Dey (2003) (▲) for natural sand grains. The solid line shows the model prediction for natural sand grains, with $\mu = 0.7$. The dashed curve shows the approximation $\cos\theta + \sin\theta/\mu$.

5.2.2 The influence of longitudinal slope

Let us consider the case of a sandy bed inclined at an angle θ along to the flow direction (Fig. 5.4 – **a**). If the slope is positive, the flow velocity must be stronger to drive the grains. If the slope is negative, the threshold is lower (Fernandez Luque *et al.* 1976, Inversen *et al.* 1994, Rasmussen *et al.* 1996). By re-writing the force balance on a grain, we obtain a modified tangential force $F_{\text{drag}} - P\sin\theta$ and a normal force in $P\cos\theta$. Consequently, the threshold is reached when $F_{\text{drag}} - P\sin\theta = \mu P\cos\theta$. This results in the following equation:

$$\Theta_{\text{th}}(\theta) = \Theta_{\text{th}}(0)\left(\cos\theta + \frac{\sin\theta}{\mu}\right). \tag{5.5}$$

This law has been observed experimentally, but with an effective friction coefficient slightly higher than the avalanche slope (Fig. 5.4 – **b**). The effect is therefore slightly weaker than expected.

The influence of a transverse slope on the threshold has a quadratic effect only, and it will be neglected. However, below, there can be detected a mass transfer along the direction perpendicular to the flow. For bedforms transverse to the flow such as ripples or dunes, only the threshold correction is important, but for rivers or bars, which present transverse slopes, a correction in the direction of the sediment flux will be involved.

5.3 Interface and fluxes

The concepts of erosion and sediment transport implies the existence of an interface between two phases: a bed composed of grains and a flowing fluid. In this section, we will see how it is possible to define such an interface and we will introduce the sediment fluxes that describe the exchange through the interface and along it.

5.3.1 Interface between sediment bed and fluid

To define the interface between the sediment bed and the fluid, two approaches are possible. The first is to define the interface ξ_s between static and mobile grains (Fig. 5.5*a*). As a first approximation, we can consider that the fluid velocity vanishes at ξ_s. This interface can be defined either from dynamic fields (partition of stresses into grain-borne stress and fluid-borne stress) or kinematic (interface between static and moving grains). A second definition, less immediate, but useful to express the mass conservation equation, is to define a fictitious interface ξ which corresponds to the position that the sediment bed would have if all the moving grains were deposited at the bottom (Fig. 5.5*b*). For a description by a continuous concentration field ϕ, the effective position of the interface reads:

$$\xi = \int_{-\infty}^{\infty} \frac{\phi}{\phi_c} \, \mathrm{d}z, \tag{5.6}$$

where ϕ_c is the bed volume fraction. In the case of a thick granular flow entrained by a fluid, ξ_s is the position of the interface between the static and the rolling phases, and ξ the interface between the rolling and the fluid phases.

In most interesting situations, the difference between the two interfaces ξ_s and ξ is small. Thereafter, when not otherwise specified, it will be assumed that the two interfaces defined in Figure 5.5 coincide and we will named it Z.

5.3.2 Flux and mass conservation

To describe sediment transport quantitatively, one usually introduces two types of integrated fluxes that must be clearly distinguished. The first, denoted by q^m, measures the mass transport. It is by definition the mass crossing per unit time a surface of unit width transverse to the direction of transport, and which extends vertically from the ground to infinity (Fig. 5.6 – **a**). We also define a volumic flux which is the equivalent in volume, at the bed volume fraction, of the transported masses:

$$\mathbf{q} = \frac{\mathbf{q}^m}{\rho_p \phi_c}. \tag{5.7}$$

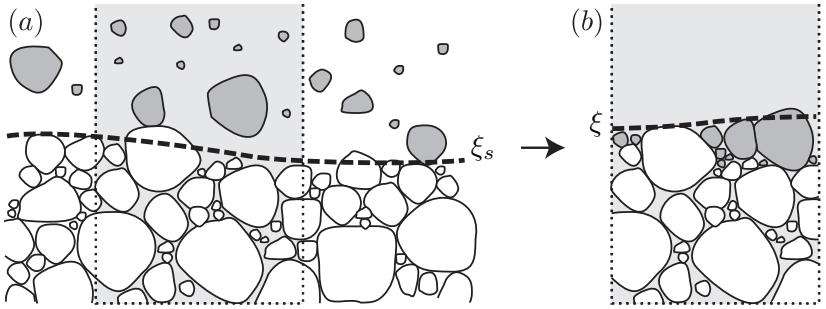


Figure 5.5: (a) Schematic defining the interface ξ_s between the static bed and a phase composed by fluid and mobile grains. (b) By depositing virtually the transported grains on the surface, one builds an effective granular bed of homogeneous volume fraction, which allows one to define the interface position ξ.

In the case of a description by a continuous concentration field ϕ and a velocity field $\mathbf{u}^p$, the mass and volumic fluxes read:

$$\mathbf{q} = \int_{-\infty}^{\infty} \frac{\phi}{\phi_c} \mathbf{u}^p \, \mathrm{d}z. \tag{5.8}$$

The flux q is a volume per unit width and per unit time. It is therefore homogeneous to a diffusion coefficient (L^2T^{-1}). Using the effective position Z of the sand bed, the mass conservation equation, which is known in geomorphology as Exner's equation, reads:

$$\frac{\partial Z}{\partial t} = -\vec{\nabla} \cdot \mathbf{q}. \tag{5.9}$$

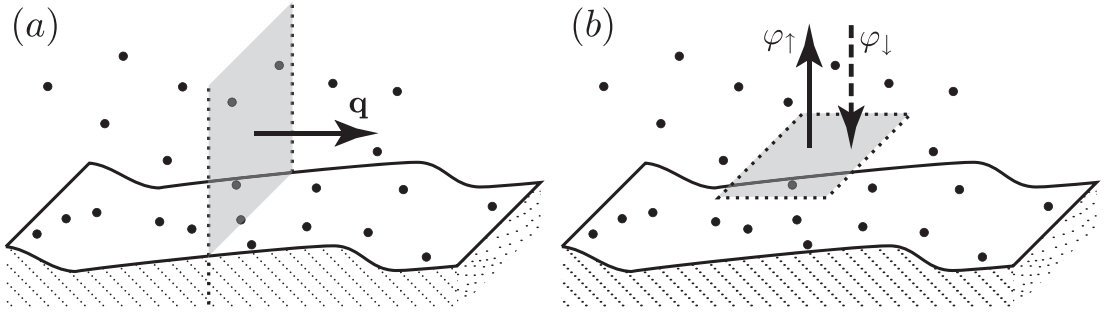


Figure 5.6: Schematics defining (a) the horizontal flux $\mathbf{q}$ and (b) the upward $\varphi_\uparrow$ and downward $\varphi_\downarrow$ fluxes.

One also defines the upward $\varphi^m_\uparrow(z)$ and downward $\varphi^m_\downarrow(z)$ fluxes as the masses crossing per unit time a unit horizontal area at altitude z, respectively from bottom to top and from top to bottom (Fig. 5.6 – **b**). In the case of a continuous description, one can express the mass conservation across this control interface. One uses in that case the mass per unit area located below the altitude z:

$$\frac{\partial}{\partial t}\int_{-\infty}^{z} \rho_p \phi \, \mathrm{d}z = \varphi^m_\downarrow(z) - \varphi^m_\uparrow(z) = -\rho_p \phi \, \mathbf{u^p} \cdot \mathbf{e_z} \; . \tag{5.10}$$

We can apply these definitions to the interface $z = Z$ between the static bed and the phase composed of fluid and mobile grains. $\varphi^m_\uparrow$ becomes the mass eroded per unit area and per unit time and is called the mass erosion rate. The mass deposition rate $\varphi^m_\downarrow$ is on the opposite the deposited mass per unit area and per unit time. As before, we prefer to use volume fluxes, homogeneous to velocities (LT^{-1}):

$$\varphi_\downarrow = \frac{\varphi^m_\downarrow}{\rho_p \phi_c} \quad \text{and} \quad \varphi_\uparrow = \frac{\varphi^m_\uparrow}{\rho_p \phi_c}. \tag{5.11}$$

The balance between erosion and deposition, which governs the evolution of the bed, then reads:

$$\frac{\partial Z}{\partial t} = \varphi_\downarrow - \varphi_\uparrow. \tag{5.12}$$

One should note that the difference $\varphi_\downarrow - \varphi_\uparrow$ between the deposition rate and the erosion rate is simply the velocity of the sand surface. It can be simply measured by using a dipstick buried in the granular bed. The bed surface velocity is not material because, by definition, the velocity of the grains at the surface of the static bed is null.

5.4 Saturated flux

Let us now consider the simplest case of an infinite flat sediment bed submitted to a steady flow. After a transient time, an equilibrium between flow and particle transport is reached, which is characterised by a flux $q = q_{\text{sat}}$ called the saturated flux. As this flux is spatially homogeneous, there is no erosion nor deposition of particles. One can equivalently state that there are as many particles deposited as particles eroded from the bed, the erosion and deposition fluxes balance each other: $\varphi = \varphi_\downarrow = \varphi_\uparrow$.

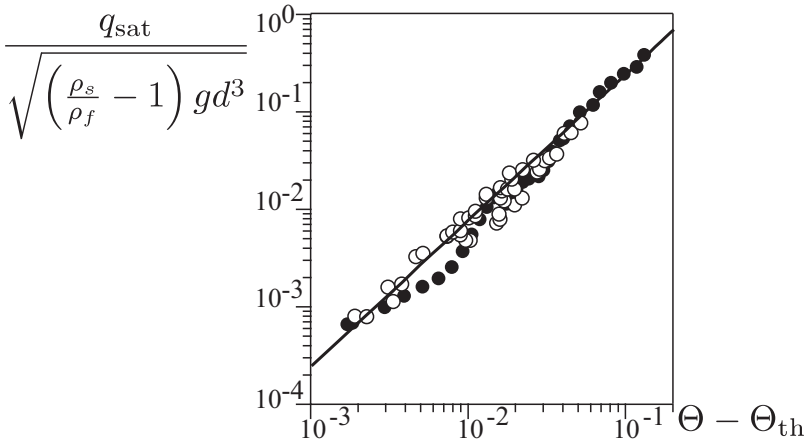


Figure 5.7: Measurements of the saturated flux in the case of bed load transport under water. (○) Luque & van Beek (1976), (●) data collected by Julien (1998). Solid line: $q_{\rm sat} \propto (\Theta - \Theta_{\rm th})^{3/2}$.

5.4.1 Transport law

The stronger the flow, the more it can carry grains at equilibrium: the saturated flux is therefore an increasing function of the shear velocity u_* which vanishes below the threshold shear velocity. The understanding and the calibration of the relationship between saturated flux $q_{\rm sat}$ and velocity u_* – the transport law – is essential to understand and predict sediment morphodynamics.

For the bed load the behaviour of the saturated flux is shown in figure 5.7: the data are traditionally fitted by an empirical formula due to Meyer-Peter & Müller (1948):

$$q_{\rm sat} \propto \sqrt{\frac{\rho_p - \rho_f}{\rho_p} g d^3}\, (\Theta - \Theta_{\rm th})^{3/2} \ . \tag{5.13}$$

Such a scaling law can be understood from Bagnold's original ideas (Bagnold 1956). The saturated flux can then be decomposed as the product of the number n of transported grains per unit area by the mean grain horizontal velocity $\bar{u}^p$: $q_{\rm sat} = \pi d^3/(6\phi_c) n \bar{u}^p$. The total shear stress $\rho_f u_*^2$ can be decomposed as the sun of the fluid-borne shear stress τ^f and the grain-borne shear stress τ^p. Now τ^p is proportional to the moving grain density n and to the drag force f_d acting on a grain moving at the average velocity $\bar{u}^p$ due to a flow at the velocity u. If the grains are in a steady motion, the drag force f_d balances a resistive force due granular friction, collisions with the bed, etc. These different dissipative mechanisms can be modeled as an

overall effective friction force characterized by a friction coefficient. Assuming that the transported grains do not disturb the flow, the flow velocity around grains u must be proportional to the shear velocity, so that $\bar{u}^p$ scales linearly with u_* (or $\sqrt{\Theta}$). Furthermore, saturation is reached when the fluid-borne shear stress equals the transport threshold at the surface of the static bed. As consequence, the number of transported particles per unit area is proportional to the excess shear stress, or $\Theta - \Theta_{\rm th}$. Taking the product of n and $\bar{u}^p$, we effectively get a transport law of the form of Eq. 5.13.

Now considering suspensions, for which the setting velocity $V_{\rm fall}$ is smaller than the shear velocity, the basal concentration and thus the overall transport are governed by the rate of entrainment $\varphi_\uparrow$ of grains from the static sand bed (or 'pick-up function'). As this entrainment results from the hydrodynamical drag on the grains, $\varphi_\uparrow$ is controlled by the basal shear stress. Empirical measurements show that $\varphi_\uparrow$ is a growing function of u_* above a threshold $u_{\rm th} \propto V_{\rm fall}$ (van Rijn, 1984a), typically proportional to $(u_*^2 - u_{\rm th}^2)$ (Partheniades, 1965), see Fig. 5.7b. In the saturated regime, the concentration ϕ is almost homogeneous and controlled by the mass conservation across the interface between static and mobile grains, leading to $\phi \simeq \varphi_\uparrow / V_{\rm fall}$. The saturated flux $q_{\rm sat} \propto \phi u_* H$, where H is the water depth, thus scales as

$$q_{\rm sat} \propto \Theta^{3/2} \tag{5.14}$$

far from the threshold, which is the regime in which suspended load takes place.

5.4.2 Generic description of the sediment flux

In the following chapters dealing with the bar and meander instabilities, we use the generic following phenomenological form for the saturated flux:

$$\vec{q}_{\rm sat} = \Omega \, (\tau_b - \tau_{\rm th})^\gamma \, \vec{t}, \tag{5.15}$$

where Ω is a dimensionfull constant of proportionality, $\tau_{\rm th}$ is the stress threshold, and γ is an empirical exponent (typically $\gamma \simeq 3/2$, as discussed in the previous subsection). The saturated flux is a vector with a component along the longitudinal direction x and another along the transverse direction y, just like the the basal shear stress: $\vec{\tau}_b = (\tau_b^{xz}, \tau_b^{yz})$. For the base state (a flow along the x direction over a plane of infinite x and y dimensions), $\tau_b = u_*^2$, $\vec{t} = \vec{e}_x$ and the reference threshold is $\tau_{\rm th} = \tau_{\rm th}^0 \equiv (u_{\rm th}^0)^2$.

As discussed above, the longitudinal slope of the bed $\partial_x Z$ modifies the threshold. At the first order we have

$$\tau_{\rm th} = \tau_{\rm th}^0 \left(1 + \frac{1}{\mu} \partial_x Z \right), \tag{5.16}$$

where μ is the effective friction coefficient. The transverse slope $\partial_y Z$ comes into the expression of the unit vector $\vec{t}$, which, at the first order, writes

$$\vec{t} = \vec{e}_{\parallel} - \frac{u_{\rm th}^0}{u_*} \frac{\partial_y Z}{\mu} \vec{e}_{\perp}, \tag{5.17}$$

where $\vec{e}_{\parallel} = \vec{\tau}_b/\tau_b$ is the unit vector in the direction of the basal shear and $\vec{e}_{\perp} = (-\tau_b^{yz}, \tau_b^{xz})/\tau_b$ is its orthogonal counterpart. Combining these above expressions, the first order contributions to the saturation flux can be computed and read:

$$q_{\rm sat,1}^x = Q \left[\frac{\tau_1^{xz}}{u_*^2} - \frac{1}{\mu} \left(\frac{u_{\rm th}^0}{u_*} \right)^2 \partial_x Z \right], \tag{5.18}$$

$$q_{\rm sat,1}^y = \frac{Q}{\gamma} \left[1 - \left(\frac{u_{\rm th}^0}{u_*} \right)^2 \right] \left[\frac{\tau_1^{yz}}{u_*^2} - \frac{1}{\mu} \frac{u_{\rm th}^0}{u_*} \partial_y Z \right], \tag{5.19}$$

where we have defined the reference flux $Q = \gamma \Omega \left[u_*^2 - (u_{\rm th}^0)^2 \right]^{\gamma - 1} u_*^2$, and where the subscript b for 'basal' has been dropped to simplify notations.

5.5 Saturation length

Let us now consider a situation in which the flow or the relief are not homogeneous anymore but vary in space or in time. The process of saturation of the transport described above does not occur instantly: the grain flux q readjusts to reach its saturated flux $q_{\rm sat}$ controlled by the local value of the basal shear stress, but with a delay in time and space (Bagnold, 1941; Sauermann *et al.*, 2001; Andreotti et al., 2002, 2004; Valance & Langlois, 2005; Charru, 2006; Andreotti et al. 2010; Devauchelle *et al.* 2010 b; Charru et al. 2013). By linearising the problem around the saturated state, we can account for these delays by a simple first order relaxation equation:

$$T_{\rm sat} \frac{\partial \mathbf{q}}{\partial t} + L_{\rm sat} \left(\mathbf{t} \cdot \vec{\nabla} \right) \mathbf{q} = \mathbf{q}_{\rm sat} - \mathbf{q}, \tag{5.20}$$

where $T_{\rm sat}$ is the saturation time and $L_{\rm sat}$ is the saturation length of the flux.

To measure these two characteristics, we must consider separately two extreme situations. We first consider the case of a homogeneous sand bed submitted to a homogeneous flow but whose velocity is suddenly increased. The flux is then spatially uniform but relaxes exponentially in time to the new saturated flux with a relaxation time $T_{\rm sat}$. The saturation time $T_{\rm sat}$ is generally short in front of the time-scale over which the relief evolves and can in general be neglected. As a consequence,

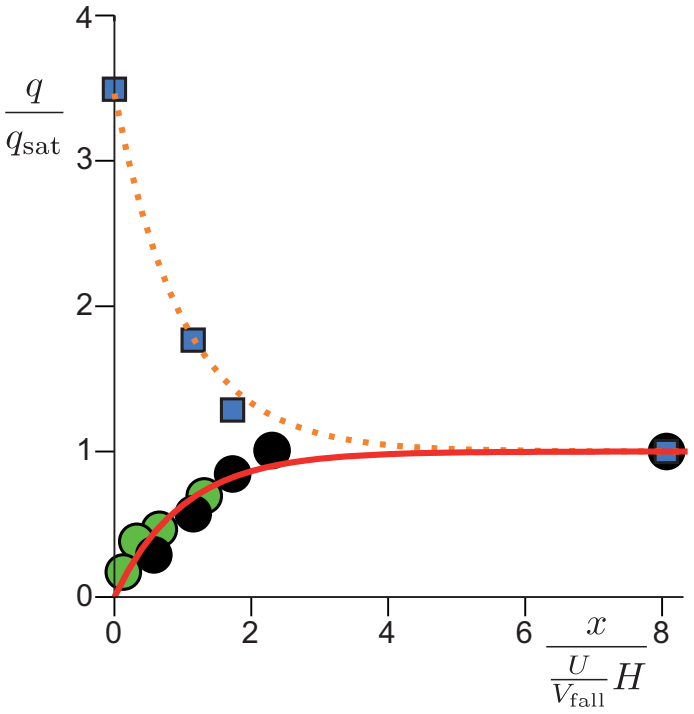


Figure 5.8: Erosion and deposition experiments performed by Van Rijn, Ashida and Okabe – from Charru et al., 2013.

both hydrodynamics and transport can be considered as steady. The second basic configuration is to consider a homogeneous flow on a sand bed, which extends only in the half space $x > 0$. Upstream of this bed ($x < 0$), we consider that the ground cannot be eroded and has the same hydrodynamic roughness as sand. The flux q at the upwind boundary ($x = 0$) of the sand bed is zero; it grows and then relaxes exponentially towards the saturated flux q_{sat}, with a relaxation length L_{sat}.

The presented formalism can account for the fact that neither the flux q nor the erosion rate are functions of the shear stress τ^f. Indeed, when the flux is locally larger than the saturated flux, it decreases over space so that grains are deposited (see Fig. 5.8). If the flux is locally smaller than the saturated flux, it grows over space, causing erosion of the sand bed. The saturation equation therefore reflects the possibility of erosion or deposition even for very large values of the flow velocity. We will now discuss, for each mode of transport, the nature of the dynamical mechanisms responsible for the saturation of transport and the related scaling laws for L_{sat}.

Saturation length for turbulent suspension

As discussed by Claudin et al. (2011), the flux saturation of suspended transport is related to the mixing of the particles at a scale of the finite thickness H of the flow. The saturation time is found to scale with the deposition sedimentation of a grain over the height H:

$$T_{\rm sat} \propto \frac{H}{V_{\rm fall}}. \tag{5.21}$$

The saturation length corresponds to the length traveled during the time $T_{\rm sat}$:

$$L_{\rm sat} \propto \frac{u_* H}{V_{\rm fall}}. \tag{5.22}$$

This last scaling is well verified by experiments (see Fig. 5.8). Interestingly, the saturation length for suspended transport is proportional to the water depth. Moreover, the velocity ratio $u_*/V_{\rm fall}$ can be as large, so that one expects $L_{\rm sat}$ in the range 10–100H. As shown by Andreotti et al. (2012), such a large value of the saturation number $L_{\rm sat}/H$ favours the emergence of inclined bedforms with respect to transverse ones.

Saturation length for bed load

The saturation length has never been directly measured in the case of bed load. As a matter of fact, indirect estimates from ripples wavelengths give very small values scaling with the grain diameter, typically 10–20d (Fourrière et al., 2010). A possibility is to have a scaling similar to what has been obtained in the aeolian case, for which the saturation length is proportional to the drag length: $L_{\rm sat} \propto \rho_p/\rho_f\, d$ (Andreotti *et al.* 2010, Duran *et al.* 2011). This would mean that the grain inertia is responsible for the relaxation towards saturation. Another possibility is that a similar deposition process as in the suspension case occurs, but at the scale of the transport layer, i.e. commensurate with the grain size: $L_{\rm sat} \propto u_*/V_{\rm fall}\, d$ (Charru & Hinch, 2006). The answer to this open problem probably depends on the grain Reynolds number, and requires careful experiments, or numerical simulations in the continuation of those of Durán et al. (2012) performed for a steady and homogenous situation.

Chapter 6

A two phase flow model of sediment transport: transition from bed-load to suspended-load

6.1 Introduction

When a sedimentary bed is sheared by a water flow of sufficient strength, the particles are entrained into motion. In a homogeneous and steady situation, the fluid flow can be characterised by a unique quantity: the shear velocity u_*. The flux of sediments transported by the flow is an increasing function of u_*, for which numerous transport laws have been proposed, both for turbulent flows (Meyer-Peter & Müller, 1948; Einstein, 1950; Bagnold, 1956; Yalin, 1963; van Rijn, 1984; Ribberink, 1998; Camemen & Larson, 2005; Wong & Parker, 2006; Lajeunesse et al., 2010) and laminar flows (Charru & Mouilleron-Arnould, 2002; Cheng, 2004; Charru et al. 2004, Charru & Hinch 2006). Despite a wide literature, some fundamental aspects of sediment transport are still partly understood. For instance, the dynamical mechanisms limiting transport, in particular the role of the bed disorder (Charru, 2006) and turbulent fluctuations (Marchioli et al., 2006; Le Louvetel-Poilly et al., 2009), remain a matter of discussion. Also, derivations of transport laws have a strong empirical or semi-empirical basis, thus lacking more physics-related inputs. Here we investigate the properties of sediment transport using a two-phase continuum description. In particular, we examine the transition from bed-load to suspension when the shear velocity is increased.

A classical reference work for two-phase continuum models describing particle-laden flows, is the formulation of Anderson & Jackson (1967), later revisited by

Jackson (1997). With this type of description, Ouriemi et al. (2009) and Aussillous et al. (2013) have addressed the case of bed-load transport in laminar sheared flows. Similarly, Revil-Baudard & Chauchat (2012) have modeled granular sheet flows in the turbulent regime. In their description, these authors decompose the domain into two layers. An upper 'fluid layer' where only the fluid phase momentum equation is solved, and a lower 'sediment bed layer' where they apply a two-phase description. Inspired from these works, we propose in this paper a general model which is able to describe sediment transport both in the laminar viscous regime and in the turbulent regime, and which does not require to split the domain into several layers.

A lot of emphasis has been put in the literature on the process of averaging the equations of motion and defining stresses (Jackson 2000). However, an important issue beyond the averaging problem is how to close the equations consistently with observations. Here, the closure for the fluid phase is described by a Reynolds dependent mixing length that has been recently proposed in direct numerical simulations of sediment transport (Durán et al., 2012). In the same spirit as the three above cited works, the granular phase is described by a constitutive relation based on recent developments made in dense suspension and granular flows (GDR MIDI, 2004; Cassar et al., 2005; Jop et al., 2006; Forterre & Pouliquen, 2008; Boyer et al., 2011; Andreotti et al. 2012; Trulsson et al. 2012; Lerner et al. 2012). Our model then takes into account both fluid and particle velocity fluctuations.

The paper is constructed as follows. In section 2, we describe our two-phase model, putting emphasis on the novelties we propose with respect to the previous works, namely the introduction of a Reynolds stress and particle diffusion induced both by turbulent fluctuations and by the motion of the particles themselves. The section 3 is devoted to the study of homogeneous and steady transport, simplifying the equations under the assumption of a quasi-parallel flow. The results of the model integration are presented in section 4. We discuss the evolution of the velocity, stress and concentration profiles when the shear velocity is increased, as well as the transport law. We end the paper with a summary and draw a few perspectives.

6.2 Two-phase model

6.2.1 Continuity equation

We define the particle volume fraction ϕ so that $1-\phi$ is the fraction of space occupied by the fluid. We respectively denote u_i^p and u_i^f, the particle and fluid Eulerian velocities. We assume incompressibility for both granular and fluid phases: the densities ρ_p et ρ_f are considered as constant. Furthermore, we assume that correlated

fluctuations of velocity and volume fraction lead to an effective diffusion of particles of coefficient D. The continuity equation then reads:

$$\frac{\partial \phi}{\partial t} + \frac{\partial u_i^p \phi}{\partial x_i} = \frac{\partial}{\partial x_i}\left(D \frac{\partial \phi}{\partial x_i}\right) , \tag{6.1}$$

$$\frac{\partial (1-\phi)}{\partial t} + \frac{\partial u_i^f (1-\phi)}{\partial x_i} = -\frac{\partial}{\partial x_i}\left(D \frac{\partial \phi}{\partial x_i}\right) , \tag{6.2}$$

where the right hand term is a particle flux resulting from Reynolds averaging and equal to the mean product of velocity and volume fraction fluctuations. We will propose later on a closure for the diffusion coefficient D. As from now, it is important to underline that two types of velocity fluctuations will be taken into account: (i) those induced by the shearing of the grains, which are associated to the large non-affine displacements of particles in the dense limit and (ii) those induced by turbulent velocity fluctuations. The introduction of this term corrects a major flaw of previously proposed two-phase models. Whenever particle-borne stresses tend to create a migration of particles, diffusion counteracts and tends to homogenize ϕ. The formulation chosen assumes that the ensemble composed by the particles and the fluid is globally incompressible and does not diffuse: adding (6.1) and (6.2), one simply gets a relation between Euler velocities for the two phases:

$$\frac{\partial [u_i^p \phi + u_i^f (1-\phi)]}{\partial x_i} = 0 \tag{6.3}$$

6.2.2 Equations of motion

The equations of motion are simply written as two Eulerian equations expressing the conservation of momentum for each phase

$$\rho_p \phi \left(\frac{\partial u_i^p}{\partial t} + u_j^p \frac{\partial u_i^p}{\partial x_j}\right) = \rho_p \phi g_i + \frac{\partial \sigma_{ij}^p}{\partial x_j} + f_i , \tag{6.4}$$

$$\rho_f (1-\phi) \left(\frac{\partial u_i^f}{\partial t} + u_j^f \frac{\partial u_i^f}{\partial x_j}\right) = \rho_f (1-\phi) g_i + \frac{\partial \sigma_{ij}^f}{\partial x_j} - f_i . \tag{6.5}$$

The force density f_i couples the two equations and represents the average resultant force exerted by the fluid on the particles. g_i is the gravity acceleration. σ_{ij}^p and σ_{ij}^f are respectively the stresses exerted on the particles and on the fluid. The stresses are additive: the total stress exerted on the effective medium (grains and fluid) is given by $\sigma_{ij}^p + \sigma_{ij}^f$ and f_i becomes an internal force for this system.

6.2.3 Force exerted by one phase on the other

The standard hypothesis, introduced by Jackson (2000), is to split the force density $\mathbf{f}$ exerted by the liquid on the solid into a component due to the Archimedes effect – the resultant force exerted on the contour of the solid, replacing the later by liquid – and a drag force due to the relative velocity of the two phases. We write this force under the form

$$f_i = \phi \frac{\partial \sigma_{ij}^f}{\partial x_j} + \frac{3}{4}\phi C_d(\mathcal{R})\rho_f \frac{|\mathbf{u}^r|\ u_i^r}{d}\ , \tag{6.6}$$

where $\mathbf{u}^r = \mathbf{u}^f - \mathbf{u}^p$ is the relative velocity and d is the grain size. The drag coefficient C_d is a function of the grain based Reynolds number $\mathcal{R}$ defined by

$$\mathcal{R} = \frac{|\mathbf{u}^r|\ d}{\nu} \tag{6.7}$$

using the fluid kinematic viscosity ν. We write the drag coefficient under the convenient phenomenological form

$$C_d = \left(C_\infty^{1/2} + s\mathcal{R}^{-1/2}\right)^2 \tag{6.8}$$

to capture the transition from viscous to inertial drag (Ferguson & Church, 2004). Both C_∞ and s *a priori* depend on ϕ. However, for the sake of simplicity, we will neglect this dependence and consider that s is on the order of $\simeq \sqrt{24} \simeq 5$, as in the dilute limit. Similarly, we will take a constant asymptotic drag coefficient C_∞ equal to 1.

After inserting the expression of f_i, the equations of motion modify into :

$$\begin{aligned}
\rho_p\phi\left(\frac{\partial u_i^p}{\partial t} + u_j^p\frac{\partial u_i^p}{\partial x_j}\right) &= \rho_p\phi g_i + \frac{\partial \sigma_{ij}^p}{\partial x_j} + \phi\frac{\partial \sigma_{ij}^f}{\partial x_j} + \frac{3}{4}\phi\, C_d(\mathcal{R})\rho_f\frac{|\mathbf{u}^r|\ u_i^r}{d}, \\
\rho_f(1-\phi)\left(\frac{\partial u_i^f}{\partial t} + u_j^f\frac{\partial u_i^f}{\partial x_j}\right) &= \rho_f(1-\phi)g_i + (1-\phi)\frac{\partial \sigma_{ij}^f}{\partial x_j} - \frac{3}{4}\phi\, C_d(\mathcal{R})\rho_f\frac{|\mathbf{u}^r|\ u_i^r}{d}.
\end{aligned} \tag{6.9}$$

6.2.4 Fluid constitutive relation

In order to close the equations, one needs to express the stress tensors. For the fluid, we choose a local isotropic constitutive relation which allows us to recover the well-known regimes:

$$\sigma_{ij}^f = -P^f\delta_{ij} + \eta_{\text{eff}}\ \dot{\gamma}_{\text{ij}}^f, \quad \text{with} \quad \dot{\gamma}_{\text{ij}}^f = \frac{\partial u_i^f}{\partial x_j} + \frac{\partial u_j^f}{\partial x_i} \tag{6.10}$$

The effective viscosity η_{eff} takes into account both the molecular viscosity and the mixing of momentum induced by turbulent fluctuations. The Reynolds stress is modeled using a Prandtl mixing length closure, which works fine for turbulent shear flows:

$$\eta_{\text{eff}} = \rho_f \left(\nu + \ell^2 |\dot{\gamma}^f|\right) \tag{6.11}$$

where ℓ is the mixing length and $|\dot{\gamma}^f|$ the typical mixing rate. For the sake of simplicity, we neglect the influence of particles on the fluid effective rheology. This equation can be easily generalized to include a multiplicative factor $(1 + 5\phi/2)$ in front of the viscosity ν. The Einstein viscosity is then recovered in the limit of dilute suspensions. Even close to the jamming transition, the effective fluid viscosity remains finite; the presence of particles only adds new solid boundary conditions and therefore reduces the fraction of volume where shear is possible. The dominant effect actually results from particle interactions, as discussed below. We have checked that the Einstein correction can be safely ignored for the description of sediment transport.

In the fully developed turbulent regime, far from the sand bed, the mixing length ℓ is proportional to the distance z to the bed. Conversely, in the viscous regime, below some Reynolds number R_t, there is no velocity fluctuation so that ℓ must vanish. A common phenomenological approach (van Driest's model for instance, see van Driest (1956) or Pope (2000)) is to express the turbulent mixing length as a function of the Reynolds number and z. However, this imposes to define an interphase between the static and mobile zones, below which ℓ must vanish. To avoid the need of such a somewhat arbitrary definition, we propose instead a differential equation

$$\frac{d\ell}{dz} = \kappa \left[1 - \exp\left(-\sqrt{\frac{\ell u^f}{R_t \nu}}\right)\right] \tag{6.12}$$

where $\kappa \simeq 0.4$ is the von Kármán constant and the dimensionless parameter $R_t \simeq 7$ is determined to recover the experimental 'law of the wall'. The ratio $u^f \ell/\nu$ is the local Reynolds number based on the mixing length. Note that a function other than the exponential can in principle be used, provided it has the same behavior in 0 and $-\infty$, although the present choice provides a quantitative agreement with standard data (Durán et al., 2012). This formulation allows us to define ℓ both inside and above the static granular bed.

6.2.5 Granular constitutive relation

For the granular phase, we first decompose the stress tensor into pressure P^p and deviatoric stress $\tilde{\sigma}^{\mathbf{p}}$:

$$\sigma_{ij}^p = -P^p \, \delta_{ij} \; + \tilde{\sigma}_{ij}^p \tag{6.13}$$

As introduced by Ouriemi et al. (2009), we write the constitutive relation as a simple friction law:

$$P^p = \frac{|\tilde{\sigma}^{\mathbf{p}}|}{\mu(\phi)} \tag{6.14}$$

The equality becomes an inequality i.e. a Coulomb failure criterion for a static bed, for which $|\dot{\gamma}^p| = 0$. The friction coefficient μ decreases with the volume fraction ϕ. Here we use a linear expansion around jamming ($\phi = \phi_c$):

$$\mu(\phi) \simeq \mu_c + \mu_c' \, (\phi_c - \phi) \, , \tag{6.15}$$

with $\mu_c = 0.5$ and $\mu_c' = 0.1$

Following recent experimental and numerical results, the granular viscosity is written as:

$$\tilde{\sigma}_{ij}^p = \psi(\phi) \; \left(\rho_f \nu + \alpha \rho_p d^2 |\dot{\gamma}^p| \right) \dot{\gamma}_{\mathrm{ij}}^p, \quad \text{with} \quad \dot{\gamma}_{\mathrm{ij}}^p = \frac{\partial u_i^p}{\partial x_j} + \frac{\partial u_j^p}{\partial x_i} \tag{6.16}$$

where $\psi(\phi)$ diverges at the critical volume fraction ϕ_c like

$$\psi(\phi) = \upsilon \frac{\phi^2}{(\phi_c - \phi)^2}, \tag{6.17}$$

where υ is a numerical constant. The experimental values are approximately $\phi_c = 0.615$ and $\upsilon = 2.1$ (Ovarlez et al., 2006; Bonnoit et al., 2010). Note however that the results presented here have been computed for $\phi_c = 0.64$ and $\upsilon = 1$.

Close to jamming, mechanical properties of dense suspensions are related to the contact network geometry (Wyart et al. 2005; van Hecke, 2010; Lerner et al., 2012) and not to long range hydrodynamic interactions as in the dilute limit. The statistical properties of grain trajectories and in particular their cooperative non-affine motions are mostly controlled by the volume fraction ϕ, whatever the nature of the dissipative mechanisms (Andreotti et al., 2012). To move by a distance as the crow flies equal to its diameter d, a grain makes a random-like motion whose average length diverges as $\sim d(\phi_c - \phi)^{-1}$, leading to a stress tensor diverging as $\psi(\phi) \sim (\phi_c - \phi)^{-2}$ (Boyer et al., 2011; Andreotti et al., 2012; Trulsson et al., 2012; Lerner et al., 2012). Numerical simulations have furthermore suggested that the function $\mu(\phi)$ does not depend on

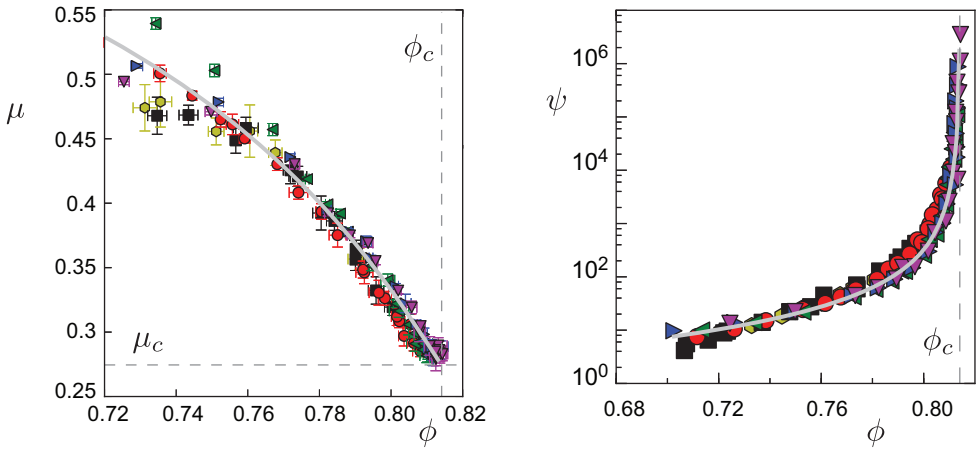


Figure 6.1: Calibration of the functions $\mu(\phi)$ and $\psi(\phi)$ in a 2D numerical simulation taking into account viscous drag, inertia, contact force, solid friction and lubrication forces (Trulsson et al., 2012). The different colors correspond to different values of the Stokes number $\rho_p d^2|\dot{\gamma}^p|/\rho_f \nu$, which characterizes the relative amplitude of the two terms in Eq. 6.16.

the microscopic interparticle friction coefficient nor on the flow regime (overdamped or inertial), see Fig. 6.1. However, the critical volume fraction ϕ_c does depend on this microscopic interparticle friction coefficient. This constitutes the most important consequence of having lubricated quasi-contacts rather than true frictional ones.

Here again, we argue for the simplicity of the asymptotic expression of $\psi(\phi)$ to use it, even in the dilute limit. The model could be easily generalized to a more complex choice for $\psi(\phi)$. We have checked that the results presented here do not depend much on such refinements.

6.2.6 Diffusion

Beside convective transport associated with the mean flow, velocity fluctuations lead to a mixing of particles and tend to homogenize the volume fraction ϕ. We model these effects by two diffusive terms. The first is associated to turbulent fluctuations. Turbulent diffusivity is usually found to scale on the turbulent viscosity and is thus proportional to $\ell^2|\dot{\gamma}^f|$. The second source of diffusion is the non-affine motion of particles in the dense regime. The particle induced diffusivity therefore scales as

$d^2|\dot{\gamma}^p|\psi(\phi)$. Adding the two contributions, the diffusion coefficient reads

$$D = \frac{\ell^2|\dot{\gamma}^f|}{\mathrm{Sc}} + \frac{d^2|\dot{\gamma}^p|\psi(\phi)}{S_\phi} \tag{6.18}$$

The constant Sc is called the turbulent Schmidt number and lies in the range 0.5–1 (Coleman 1970; Celik & Rodi 1988; Nielsen 1992). We have introduced here a second phenomenological constant S_ϕ, that we take equal to 1.

6.3 Homogeneous steady transport

6.3.1 Dimensional analysis

We now apply the two phase flow model to the description of sediment transport. In this article, we will limit ourselves to the analysis of saturated transport over a flat bed, for which both phases are in a steady homogenous state. In the following, we will keep the equations dimensional. It is still interesting to perform the dimensional analysis of the problem. We will consider that the characteristic length is set by the grain diameter d, that the characteristic density is given by ρ_f, and that $(\rho_p - \rho_f)gd$ provides the characteristic stress. Besides the constant of the model, there are two control parameters and therefore two dimensionless numbers. The first, called the Shields number, is the rescaled shear stress:

$$\Theta = \frac{\rho_f u_*^2}{(\rho_p - \rho_f)gd}\,. \tag{6.19}$$

It compares the fluid-borne shear stress to the buoyancy-free gravity. The second parameter is based on the kinematic viscosity ν of the fluid. Combining this viscosity with gravity, one builds the viscous diameter:

$$d_\nu = \left(\frac{\rho_p}{\rho_f} - 1\right)^{-1/3} \nu^{2/3}\, g^{-1/3}, \tag{6.20}$$

which corresponds to the grain size for which inertial, gravity and viscous effects are of the same order of magnitude. The dimensionless number is then the ratio d/d_ν. Equivalently, the Galileo number is defined as $(d/d_\nu)^3$; the Reynolds number in Stokes sedimentation is $\frac{1}{18}(d/d_\nu)^3$. Other dimensionless numbers, like the particle Reynolds number in the flow are obtained by combining the Shields number Θ and the dimensionless diameter d/d_ν.

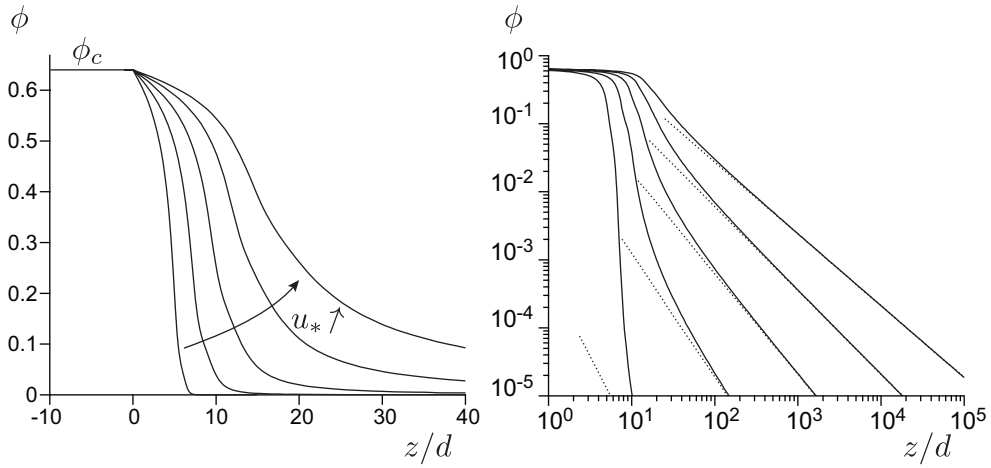


Figure 6.2: Vertical profiles $\phi(z)$ of the volume fraction in lin-lin (left) and log-log (right) representation, for five values of the shear velocity: $u_*/\sqrt{\left(\frac{\rho_p}{\rho_f}-1\right)gd} = 0.3, 0.4, 0.5, 0.6, 0.7$. The dotted line correspond to the power-law obtained in the dilute asymptotic limit (Eq. 6.39).

6.3.2 Quasi-parallel flow assumption

We consider a flat sand bed homogeneous along the x axis. The continuity equation then reads:

$$\phi u_z^p = (\phi - 1) u_z^f = D \frac{d\phi}{dz} \,. \tag{6.21}$$

It expresses the balance between the convective flux associated with the downward particle motion and the turbulent diffusive flux. As they are related by the continuity equation, the vertical velocities can be expressed as functions of their relative velocity u_z^r: $u_z^f = \phi u_z^r$ and $u_z^p = (\phi - 1) u_z^r$. We consider the asymptotic limit where horizontal velocities are much larger than vertical ones.

Making use of the homogeneity along x, the vertical equations of motion simplify into

$$\begin{aligned} \rho_p \phi u_z^p \frac{du_z^p}{dz} &= -(\rho_p - \rho_f)\phi g + \frac{d\sigma_{zz}^p}{dz} + \phi \frac{d\sigma_{zz}^f}{dz} + \frac{3}{4}\phi\, C_d(\mathcal{R}) \rho_f \frac{|\mathbf{u}^r|\; u_z^r}{d}, \\ \rho_f (1-\phi) u_z^f \frac{du_z^f}{dz} &= (1-\phi)\frac{d\sigma_{zz}^f}{dz} - \frac{3}{4}\phi\, C_d(\mathcal{R}) \rho_f \frac{|\mathbf{u}^r|\; u_z^r}{d}. \end{aligned} \tag{6.22}$$

One can eliminate the fluid normal stress σ_{zz}^f between these two equations and, under

the quasi-parallel flow assumption, neglect the LHS inertial terms, leading to:

$$\frac{d\sigma^p_{zz}}{dz} = (\rho_p - \rho_f)g\phi - \frac{3\phi C_d(\mathcal{R})}{4(1-\phi)}\,\rho_f \frac{|\mathbf{u}^r|\; u^r_z}{d} \tag{6.23}$$

In the dense regime, this equation reduces to the hydrostatic equation. In the dilute regime, the particle normal stress vanishes and the vertical velocity tends to the settling velocity (see Eq. 6.37 below).

The horizontal equations of motion read:

$$\begin{aligned} \rho_p \phi u^p_z \frac{du^p_x}{dz} &= \frac{d\sigma^p_{xz}}{dz} + \phi\frac{d\sigma^f_{xz}}{dz} + \frac{3}{4}\phi C_d(\mathcal{R})\rho_f \frac{|\mathbf{u}^r|\; u^r_x}{d}, \\ \rho_f(1-\phi) u^f_z \frac{du^f_x}{dz} &= (1-\phi)\frac{d\sigma^f_{xz}}{dz} - \frac{3}{4}\phi C_d(\mathcal{R})\rho_f \frac{|\mathbf{u}^r|\; u^r_x}{d}. \end{aligned} \tag{6.24}$$

Under the quasi parallel flow assumption, LHS inertial terms can be again neglected and these equations lead to:

$$\frac{d\sigma^f_{xz}}{dz} = -\frac{d\sigma^p_{xz}}{dz} = \frac{3\phi}{4(1-\phi)} C_d(\mathcal{R})\rho_f \frac{|\mathbf{u}^r|\; u^r_x}{d}. \tag{6.25}$$

Due to an overall conservation of the momentum flux, the total stress $\sigma^p_{xz} + \sigma^f_{xz}$ is a constant, noted τ. It can be identified to the fluid shear stress far from the bed, where the particle borne shear stress vanishes. We also introduce the shear velocity u_*, related to the total stress by:

$$\tau \equiv \rho_f u_*^2 = \sigma^p_{xz} + \sigma^f_{xz} \tag{6.26}$$

Under the quasi-parallel flow assumption, the strain rate modulus is simply the shear rate:

$$|\dot\gamma^f| = \dot\gamma^f_{\rm xz} = \frac{du^f_x}{dz} \quad \text{and} \quad |\dot\gamma^p| = \dot\gamma^p_{\rm xz} = \frac{du^p_x}{dz}\,. \tag{6.27}$$

The fluid and particle constitutive relation then simply write

$$\sigma^f_{xz} = \rho_f \left(\nu + \ell^2 \left|\frac{du^f_x}{dz}\right|\right) \frac{du^f_x}{dz} \tag{6.28}$$

$$\sigma^p_{xz} = \psi(\phi) \left(\rho_f \nu + \alpha \rho_p d^2 \left|\frac{du^p_x}{dz}\right|\right) \frac{du^p_x}{dz} \tag{6.29}$$

which must be complemented, when the granular phase is unjammed, by the frictional relation $|\sigma^p_{xz}| = \mu(\phi)\sigma^p_{zz}$. Combining the vertical and horizontal equations of motion,

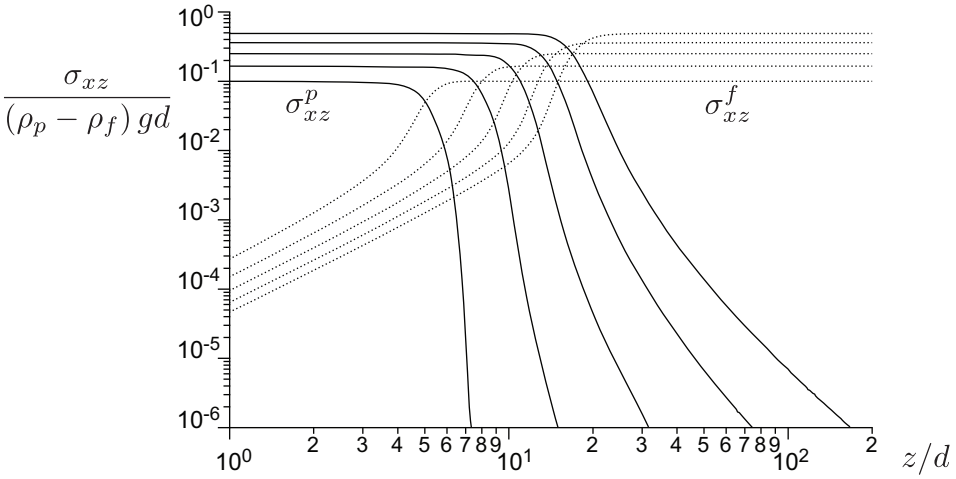


Figure 6.3: Vertical profiles of the particle-borne shear stress σ^p_{xz} (solid lines) and of the fluid-borne shear stress σ^f_{xz} (dotted lines) for the same shear velocity values as in Figure 6.2. The sum of σ^p_{xz} and σ^f_{xz} is constant, equal to $\rho_f u_*^2$. Note the evolution of the altitude at which $\sigma^f_{xz} = \sigma^p_{xz}$ when u_* is varied.

one gets an equation relating the derivative of the volume fraction to the vertical velocity:

$$-(\rho_p - \rho_f)g + \frac{3\, C_d(\mathcal{R})}{4(1-\phi)}\, \rho_f \frac{|\mathbf{u}^r|}{d} \left(\frac{u^r_x}{\mu(\phi)} + u^r_z \right) + \frac{\mu'(\phi)\sigma^p_{xz}}{\phi\mu(\phi)^2}\, \frac{d\phi}{dz} = 0. \tag{6.30}$$

Combining it with Eq. (6.21), which involves the same quantities, one can deduce u^r_z and $d\phi/dz$

6.3.3 Static bed

We define $z = 0$ as the position at which the Coulomb criterion is reached, so that, for $z < 0$, the bed is strictly static i.e. the grain velocity is exactly null ($u^p_x = 0$ and $u^p_z = 0$). Right at $z = 0$, the volume fraction reaches the critical volume fraction ϕ_c. Assuming that there is no hysteresis of friction, we get for $z < 0$:

$$\phi = \phi_c \quad \text{and} \quad P^p = P_0 - (\rho_p - \rho_f)\phi_c g z. \tag{6.31}$$

The equations describing the fluid in the bed then simplify into:

$$\frac{d\sigma^f_{xz}}{dz} = \frac{3\phi_c}{4(1-\phi_c)}\, C_d(\mathcal{R})\rho_f \frac{\left|u^f_x\right| u^f_x}{d}\,, \tag{6.32}$$

$$\sigma^f_{xz} = \rho_f \left(\nu + \ell^2 \left|\frac{du^f_x}{dz}\right|\right) \frac{du^f_x}{dz}. \tag{6.33}$$

Deep inside the static bed, the fluid velocity u^f tends to 0, and one gets the asymptotic solution in the limit $z \to -\infty$:

$$u^f_x \approx U\, \exp(z/\zeta) \quad \text{with} \quad \zeta = \sqrt{\frac{4(1-\phi_c)}{3\phi_c}}\, \frac{d}{s}\,. \tag{6.34}$$

The flow velocity thus decays over a distance which is a fraction of the grain diameter. U is a shooting parameter that is determined by the matching with the velocity far above the bed. In the same limit, the mixing length equation can be approximated by:

$$\frac{d\sqrt{\ell}}{dz} \approx \frac{\kappa}{2}\sqrt{\frac{u^f}{R_t\nu}} \approx \frac{\kappa}{2}\sqrt{\frac{U}{R_t\nu}}\, \exp\left(\frac{z}{2\zeta}\right) \tag{6.35}$$

As ℓ must vanish when $z \to -\infty$, we get the asymptotic expression:

$$\ell \approx \frac{\kappa^2\zeta^2 U}{R_t\nu}\, \exp\left(\frac{z}{\zeta}\right) \approx \frac{\kappa^2\zeta^2}{R_t\nu}\, u^f_x \tag{6.36}$$

6.3.4 Dilute zone

When z tends to $+\infty$, the volume fraction ϕ, the horizontal component of the relative velocity u^r_x and the grain-borne shear stress σ^p_{xz} all tend to zero. As a consequence, the vertical velocity $u^r_z = -u^p_z = V_{\text{fall}}$ is the settling velocity defined by:

$$\frac{3}{4}\, C_d(\mathcal{R})\, \rho_f \frac{V^2_{\text{fall}}}{d} = (\rho_p - \rho_f)g \tag{6.37}$$

The vertical fluid velocity vanishes like $u^f_z = \phi u^r_z$. The mixing length tends to $\ell = \kappa(z + z_0)$, where z_0, called the hydrodynamic roughness, is a result of the integration. The horizontal velocities tend to:

$$u^f_x \simeq u^p_x \sim \frac{u_*}{\kappa} \ln(1 + z/z_0) \tag{6.38}$$

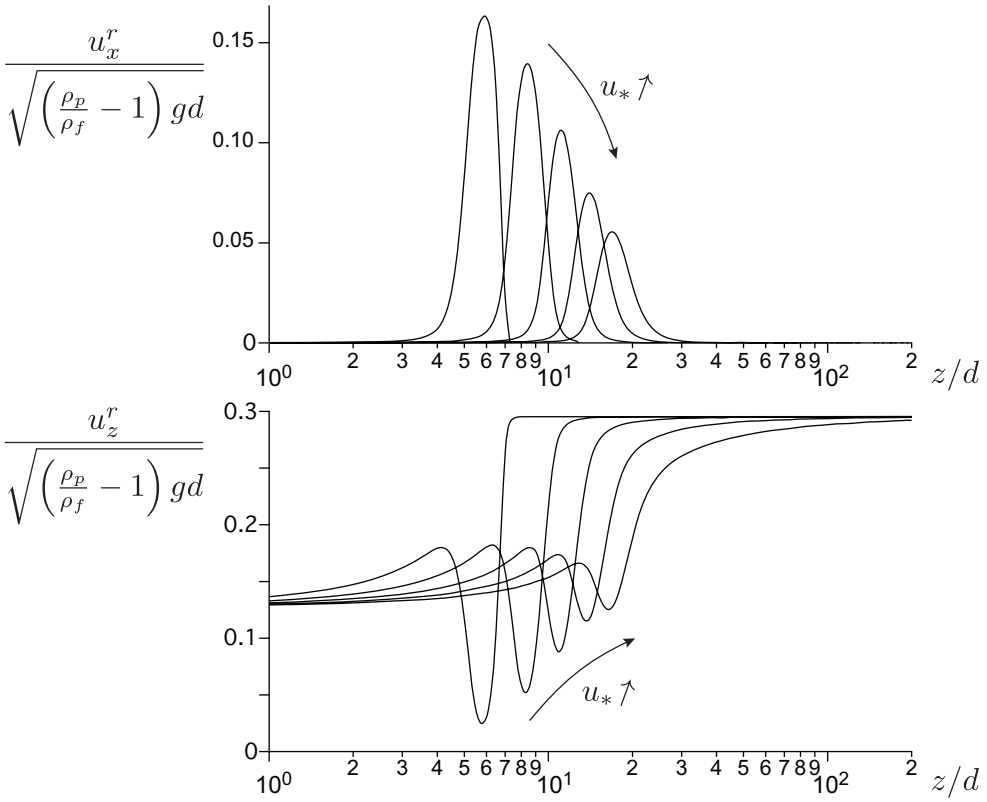


Figure 6.4: Vertical profiles of the two components of the velocity difference between the two phases. Top: horizontal component u_x^r. Bottom: vertical component u_z^r. The different lines correspond to the same shear velocity values as in Figure 6.2.

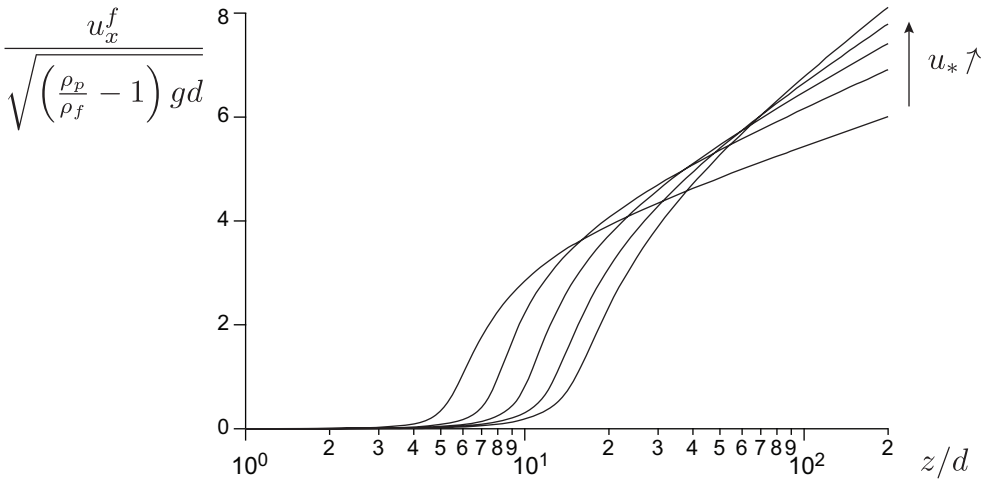


Figure 6.5: Vertical profiles of the horizontal fluid velocity u_x^f, for the same shear velocities as in Figure 6.2.

Using the asymptotic expression of the diffusivity $D \sim \kappa u_*(z+z_0)/\mathrm{Sc}$ and the velocity $u_z^r \sim V_{\mathrm{fall}}$, the continuity equation integrates into:

$$\phi \sim \frac{\phi_0}{(1+z/z_0)^\beta} \quad \text{with} \quad \beta = \frac{\mathrm{Sc}\, V_{\mathrm{fall}}}{\kappa\, u_*}, \tag{6.39}$$

The shooting parameter ϕ_0 is selected by the asymptotic expressions derived inside the static bed. β is known as the Rouse number.

6.4 Results

The equations governing the evolution of u_x^f, σ_{xz}^f, ℓ, u_x^p and ϕ can been integrated numerically, using a shooting method to satisfy the asymptotic expansions on both sides of the integration domain. We detail and comment in this section the results obtained for a rescaled viscosity $\nu/\sqrt{\left(\frac{\rho_p}{\rho_f}-1\right)gd^3} = 10^{-1}$, or $d/d_\nu \simeq 4.64$. For quartz grains in water, this value corresponds to a mean diameter of $d \simeq 180\mu$m. For the shear velocities we have considered (see caption of Fig. 6.2), the viscous length ν/u_* is a fraction of the grain diameter: in the range 0.14–0.33d. As shown below, this is small in comparison to size of the transport layer (typically 5–20d), so that the curves we present here correspond to transport in the turbulent regime.

Varying systematically the shear velocity or, equivalently, the Shields number, we find that the asymptotic conditions on both sides cannot be matched (i.e. there is no

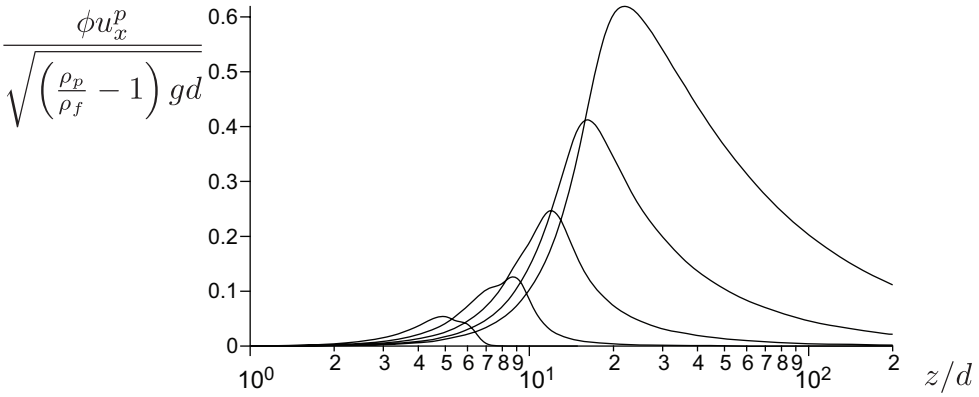


Figure 6.6: Vertical profiles of the flux density ϕu_x^p, for the same shear velocities as in Figure 6.2.

solution) below a threshold value $u_{\rm th} \simeq 0.2\sqrt{\left(\frac{\rho_p}{\rho_f}-1\right)gd}$. Experimentally, a similar dimensionless threshold velocity is found, though slightly larger, equal to 0.26 (see Andreotti et al. 2013 and references therein).

Figure 6.2 shows the volume fraction vertical profiles $\phi(z)$ in log-log and lin-lin scales. Close to the static sand bed, grains are transported in a rather dense layer whose thickness increases with u_*. This corresponds to a form of bed load were several granular layers are entrained (sheet flow). Far from the static bed, the volume fraction decreases as a power law of height, as expected (Eq. 6.39).

Figure 6.3 shows the vertical profile of the grain-borne and the particle-borne shear stresses for five values of u_*. The sum of σ_{xz}^p and σ_{xz}^f is constant, equal to $\rho_f u_*^2$. Far above the static bed the whole shear stress is carried by the fluid. Furthermore, close to the static bed, it is carried by the grains and transmitted through contact forces. The transfer of momentum flux from the fluid to the particles occurs at the top of the bed load layer. One observes in Figure 6.4a) a peak in the profile of the horizontal velocity difference u_x^r, whose position increases with u_*. This relative velocity between the two phases is associated with a horizontal drag force: the momentum flux serves to balance friction and entrain the particles from the bed into motion. Figure 6.4b) shows the vertical velocity profile. As expected, it tends to the settling velocity $V_{\rm fall}$ above the bed load layer. Inside the bed-load layer, one observes that u_z^r is still large, which means that there is a balance between pressure-induced migration and shear-induced diffusion.

The fluid velocity profile $u_x^f(z)$ (see Figure 6.5) is, as expected, logarithmic far above the static bed, but is strongly reduced in the dense transport layer: when

particles are accelerated by the flow, the flow, in turn, is decelerated. This negative feedback mechanism takes place over a thicker and thicker region, as u_* increases, which coincides with the transport layer.

The average sediment transport at the altitude z is characterized by the product of the volume fraction ϕ by the particle velocity u_x^p. More precisely, $\rho_p \phi u_x^p$ is the density of mass flux; $\phi u_x^p/\phi_c$ is the density of volume flux. Figure 6.6 shows that ϕu_x^p presents a peak at the top of the bed load layer, followed by a tail associated with the dilute turbulent suspension. The total sediment flux is obtained by integration over the vertical direction:

$$q = \int_0^\infty \phi \, u_x^p \, dz \tag{6.40}$$

By definition it quantifies the volume of grain crossing a unit length transverse to the flow per unit time. The mass flux is $\rho_p q$ and the volumetric flux at the bed volume fraction is q/ϕ_c.

Figure 6.7a) shows the dependence of the sediment flux q on the Shields number Θ. It vanishes below the threshold Shields number $\Theta_{\rm th}$ and beyond, it increases with Θ. It diverges at the Shields number Θ_m for which the Rouse number β reaches 1. In real conditions, the total sediment flux does not diverge at Θ_m because it is limited by the finite flow thickness. We have kept here an unbounded flow in order to highlight the transition to a turbulent suspension.

Integrating the asymptotic expressions obtained far from the sediment bed, we can deduce the contribution of turbulent suspension to the sediment flux:

$$q_{\rm sus} = \frac{\phi_0 u_*}{\kappa} \int_0^\infty (1 + z/z_0)^{-\beta} \ln(1 + z/z_0) \, dz = \frac{\phi_0 u_* z_0}{\kappa (1-\beta)^2} \tag{6.41}$$

One observes in Figure 6.7a) that the suspended load (dashed line) indeed becomes dominant around the inflection point of the curve $q(\Theta)$. In order to determine precisely the contribution $q_{\rm bl}$ of bed-load to the total flux, we have integrated the equations in the limit of infinite turbulent Schmidt number Sc, i.e. without any diffusion of particles resulting from turbulent fluctuations. We have checked that $q_{\rm bl} + q_{\rm sus}$ accurately gives q. The bed load contribution is dominant at low shear velocity. It is extremely well fitted by a Meyer Peter-Muller-like relation:

$$q_{\rm bl} \propto (\Theta - \Theta_{\rm th})^{3/2} \tag{6.42}$$

For the parameters chosen in this paper, the best fit gives a threshold shear velocity $u_{\rm th} \simeq 0.19 \sqrt{\left(\frac{\rho_p}{\rho_f} - 1\right) gd}$ and equivalently a threshold Shields number $\Theta_{\rm th} \simeq 0.37$.

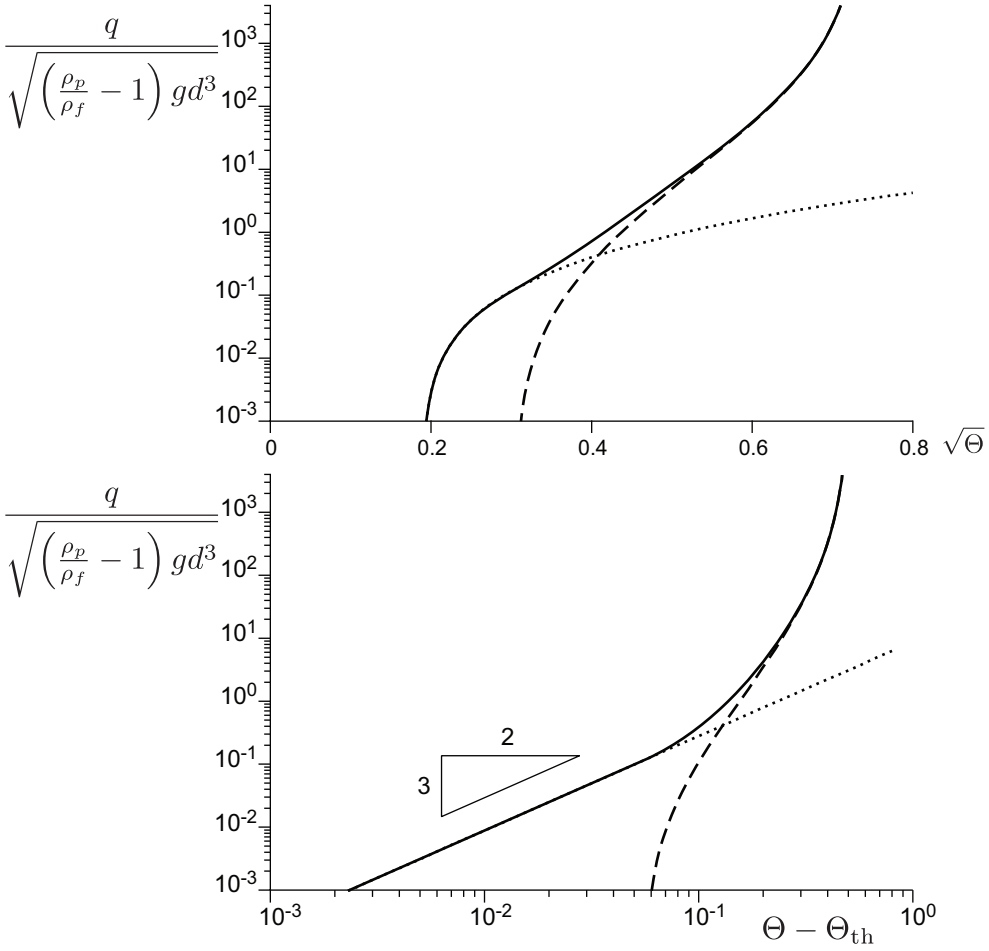


Figure 6.7: Dependence of the sediment flux q on the Shields number Θ. (a) q as a function of the rescaled shear velocity $\sqrt{\Theta}$. (b) q as a function of $\Theta - \Theta_{\mathrm{th}}$. Solid line: total flux. Dashed line: contribution of the suspended load, determined from the asymptotic expansions obtained in the dilute limit (Eq. 6.41). Dotted line: contribution of bed load, determined from calculations performed in the limit $Sc \to \infty$. The bed load flux q follows the Meyer Peter-Muller scaling in $(\Theta - \Theta_{\mathrm{th}})^{3/2}$.

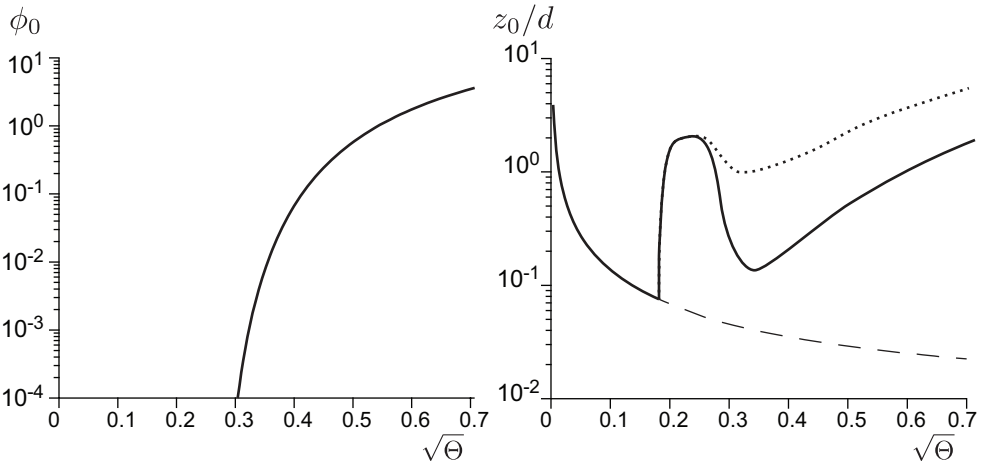


Figure 6.8: (a) Dependence of the apparent basal volume fraction ϕ_0 on the Shields number Θ. Starting from the expansion of Eq. (6.39) in the region of suspension, ϕ_0 appears as an extrapolated value of the volume fraction at the bed. From the point of view of the turbulent suspension, $V_{\rm fall}\,\phi_0$ is the effective erosion rate. (b) Dependence of the hydrodynamic roughness on Θ, with (solid line) and without transport (dashed line). Dotted line: roughness obtained with pure bed load, in the limit $Sc \to \infty$.

Amongst the novel aspects of our approach, we are able to predict the effective erosion rate seen by the turbulent suspension or, more precisely, the rate at which the bed load particles are injected in this suspension. Figure 6.8a) shows the parameters extracted from the asymptotic expansions in the upper zone. The apparent basal volume fraction ϕ_0 is defined from Eq. (6.39). It increases rapidly and saturates to a value of order 1 at the suspension threshold. Figure 6.8b) shows the hydrodynamic roughness. In the absence of transport, z_0 decreases as ν/u_*. At the transport threshold, it suddenly increases by one order of magnitude before dropping again when suspension becomes dominant. As this quantity can be accessed experimentally at a distance from the bed, it could be used to show the existence of a negative feedback of sediment transport on the flow, in the turbulent regime.

6.5 Concluding remarks

The two-phase flow model derived here is an extension of models previously proposed to describe dense viscous flows and turbulent suspensions. We have added two novelties with respect to these works: the description of dense flows at large Stokes

numbers and the diffusion of particles induced by non-affine motion. This last effect turns out to be extremely important, as it counteracts particle migration. Although qualitatively discussed in the literature (Fall et al., 2010), this effect had never been modeled so far. Future work will have to calibrate this diffusive term (the factor S_ϕ), and to test it against experimental results obtained using heterogeneous shear flows (Bonnoit et al., 2010).

From the point of view of sediment transport, the two-phase flow model derived here is able to describe all regimes: viscous and turbulent, bed-load and suspension. Regarding bed-load, we have relaxed one hypothesis used in previous models: the volume fraction is not assumed to be homogeneous, equal to ϕ_c, in the bed-load layer. On the opposite, we predict that the sediment transport layer is rather dilute, with a volume fraction profile continuously decreasing to 0 away from the static bed. At large shear velocity, when the sediment transport mostly takes place in suspension, our model is able to predict the erosion/deposition rate into the bulk from the equations of mechanics, by matching to the bed load zone. One does not have to introduce a phenomenological erosion rate, balanced by sedimentation, as in previous models of turbulent suspension. Future work will have to test and calibrate this erosion/deposition model, which sensitively depends on the particle shear induced diffusion.

With this two-phase description, we recover the scaling law proposed phenomenologically by Meyer Peter-Muller for bed-load transport. However, one expects the model to become inaccurate close to the transport threshold, were the sparse mobile grains hardly constitute an eulerian phase. The analysis of forces and torques on a single grain (Andreotti et al. 2013) seem to provide a better understanding of the transport threshold than the continuum modeling, where the grain size appears indirectly in the decay of the flow velocity inside the static bed. If a fine tuning of parameters could improve the agreement of the model with observations in this range of velocities, it may well be that the dynamics is actually dominated by fluctuations (of the bed surface structure in particular), and could therefore not be described in a mean field manner.

On the opposite, we expect the two-phase approach to provide an accurate description of the transition from bed load to suspension. It can therefore be directly applied to different problems of river morphodynamics like the formation of ripples, alternate bars and meanders by linear instability (for reviews, see Charru et al (2013) and Andreotti & Claudin (2013), as well as references therein). Beside the expression of the saturated flux, function of the shear velocity, morphodynamical models must incorporate two important dynamical mechanisms: the dependence of sediment transport on the bed slope and the relaxation of the sediment flux towards satura-

tion. We expect such a two-phase modeling to provide some clues to resolve ongoing controversies on the emergence of bed forms.

Part III

Bars and Meanders

Chapter 7

The bar instability revisited

Bars are large scale river bedforms whose wavelength is comparable to channel width and whose height is comparable to flow depth. Due to these two large length-scales, bars interact with structures and navigation, and have a profound impact on several aspects of river engineering like river control (channel shift) and hazard prevention (bank failures).

Since the seminal work of Kennedy (1963), there is a wide agreement that bedforms – both free bars and sand ripples – develop by linear instability of an erodible bed subject to a turbulent flow: infinitesimal perturbations of the bed (and therefore of the flow) are selectively amplified at certain wavelengths in the course of their downstream migration. By contrast with sand ripples, which are transverse to the flow, bars develop from a three-dimensional instability of the sediment bed in which the most unstable modes are inclined with respect to the flow (Chang & Simons, 1970; Chang et al., 1971; Schumm & Khan, 1972; Ikeda, 1983; Fujita & Muramoto, 1985; Lisle et al., 1991, 1997; Lanzoni, 2000a, 2000b; Devauchelle et al., 2010a, 2010b; Andreotti et al., 2012). Like optical or acoustical wave-guides do, the channel selects a discrete number of guided unstable modes labelled by the number n of rows of bar perturbations ($n = 1$ corresponds to alternate bars), see chapter 3. The transverse wave-number is therefore directly selected by the channel width (Parker, 1976). Several increasingly refined linear stability analysis have been published in the literature (Callander, 1969; Engelund & Skovgaard, 1973; Parker, 1976; Fredsøe 1978; Colombini et al., 1987; García & Niño, 1993). These theories predict the dispersion relation – both the growth rate $\sigma(k)$ and the propagation velocity $c(k)$ of perturbations of longitudinal wavenumber k – within the linear regime, the marginal stability conditions in the space of flow and sediment parameters and the wavenumber $k_{\max}$ selected by the instability mechanism, i.e. those corresponding

to the maximum growth rate. The parameter controlling the instability is the width to depth ratio $\beta = W/H$ characterising the cross section of the channel.

One of the most important property of the linear instability is the existence of a particular value of β for which the migration speed of the marginally stable mode vanishes (Blondeaux & Seminara, 1985). This so-called 'resonant' condition is the key ingredient of the 'bend theory' of meandering, which assumes a weak coupling between bars and banks. River meanders are assumed to excite the bar instability without affecting the shape of the modes nor the dispersion relation; then, the coupling is optimal when non-growing free bars do not propagate with respect to the banks.

Recent reviews have claimed that the topic can be considered as fairly settled (Tubino et al., 1999; Seminara, 2010). Most theories for bars in rivers are based on depth-averaged Saint-Venant shallow water (SVSW) equations (an exception in the list cited above is the work of Engelund & Skovgaard (1973)), which assume that the length-scale over which the flow varies is much smaller than the flow thickness H, and have been used when bed-load is the main mode of sediment transport. In contrast, suspension is expected to be dominant for the formation of tidal bars, and 3D Reynolds averaged Navier Stokes (RANS) equations have been used to describe the water flow, coupled to an advection-diffusion equation for the sediment (Seminara & Tubino 2001, Solari *et al.* 2002,). In this chapter, our primary goal is to investigate the robustness of the results previously obtained, when the hydrodynamical disturbances are computed with Reynolds averaged Navier Stokes equations, which describe the vertical structure of the flow.

Moreover, most of the previous papers do not explicitly take into account the fact that sediment transport adapts to a variation of the flow strength with a spatial lag. This sediment transport saturation transient, characterised by the so-called saturation length L_{sat}, plays a dominant role in the linear instability of subaqueous sand ripples and aeolian dunes, as it controls the emergent wavelength from a flat bed (Andreotti et al., 2002; Lagrée, 2003; Elbelrhiti et al., 2005; Valance, 2005; Valance & Langlois, 2005; Claudin & Andreotti, 2006; Charru, 2006; Narteau et al., 2009; Fourrière et al., 2010; Durán et al., 2011; Charru et al., 2013). The saturation length allows one to build a new dimensionless number L_{sat}/H, the saturation number , which compares the stabilising effect of the sediment transport relaxation transient to that of the free surface (Andreotti et al., 2012). Our second aim is to look at the influence of this dimensionless parameter on the bar instability.

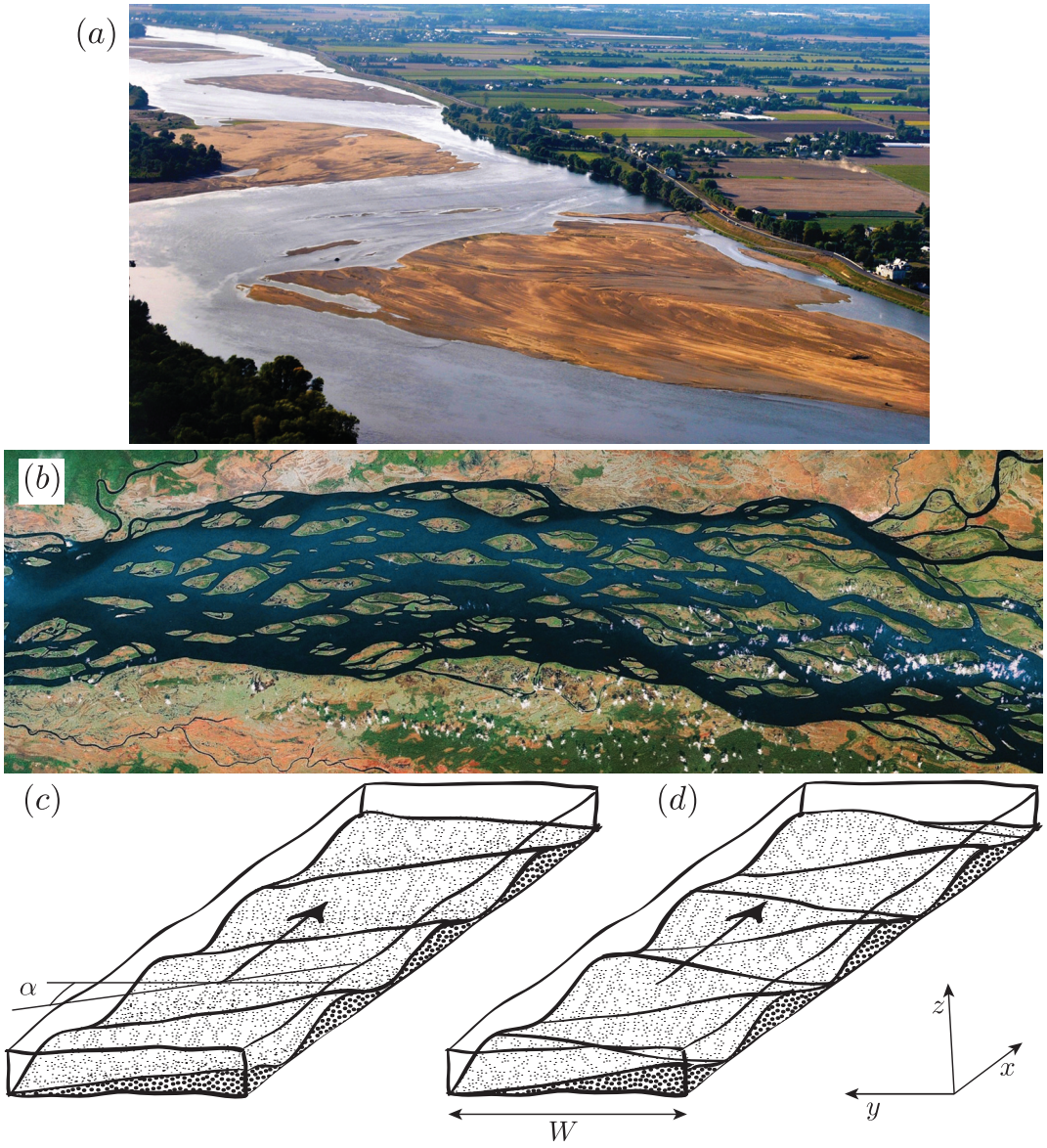


Figure 7.1: (a) Free alternate bars in the Loire river, close to St-Mathurin-sur-Loire (France; 47° 24' 50" N, 0° 19' 04" W). Photo credit: S. Rodrigues, université François Rabelais of Tours. These bars, of wavelength $\lambda \simeq 2000$ m, mostly evolve during annual floods, characterised by a typical flow depth $H \simeq 4$ m. Sediment transport then mostly takes place in suspension, with a saturation length $L_{\rm sat}$ around 160 m. The saturation number $L_{\rm sat}/H$ is therefore around 40. As the river width W is around 480 m, the aspect ratio $\beta = W/H$ is around 120. (b) Multiple bars in the Congo river, with a similar mean wavelength around $\lambda \simeq 2000$ m. The relevant flow depth H is uneasy to define but is smaller than 10 m. As the river width W is around 9000 m, the typical aspect ratio $\beta = W/H$ lies in the range $1000 - 2000$. (c) Schematic showing a plane wave mode inclined by an angle α with respect to the flow direction. (d) Schematic showing free alternate bars in a channel of width W. They correspond to guided modes obtained by superimposing two plane waves propagating with opposite angles. See chapter 3.

7.1 Linear stability analysis

We consider a turbulent flow in a straight channel, as described in the section 2 of chapter 4. Following the notations introduced in chapter 3, the perturbation to the flat bed is written as

$$k|Z\rangle = e^{ikx+\sigma t} \sum_{n=1}^{\infty} kZ_n \, |c_n\rangle, \tag{7.1}$$

where k is the longitudinal wave-number of these disturbances, and σ their growth rate. We call α the angle made by a plane wave with respect to the flow direction. For a given mode n, we have $\tan\alpha = r_n/k$. Hydrodynamics over such an undulated bottom for both RANS and shallow water equations have been described and discussed in chapter 3.

The bed evolution is governed by the conservation of sediment mass:

$$\partial_t Z + \vec{\nabla} \cdot \vec{q} = 0. \tag{7.2}$$

The sediment flux $\vec{q}$ relaxes towards its saturated value $\vec{q}_{\rm sat}$ over a typical distance $L_{\rm sat}$. Following chapter 5, we describe this process by the following first order relaxation equation:

$$L_{\rm sat} \left(\vec{t} \cdot \vec{\nabla}\right) \vec{q} = \vec{q}_{\rm sat} - \vec{q} \tag{7.3}$$

Since the base flux is homogeneous in x and y, the operator $\vec{t} \cdot \vec{\nabla}$ must be taken at the zeroth order, and thus reduces to ∂_x. Consequently, we have:

$$\vec{q}_1 = \frac{1}{1 + ikL_{\rm sat}} \, \vec{q}_{{\rm sat},1}. \tag{7.4}$$

At first order in kZ_n, the saturated flux corrections read

$$|q^x_{{\rm sat},1}\rangle = Q \, e^{ikx+\sigma t} \sum_{n=1}^{\infty} kZ_n \left[A^n_x + iB^n_x - \frac{i}{\mu} \left(\frac{u^0_{\rm th}}{u_*} \right)^2 \right] |c_n\rangle, \tag{7.5}$$

$$|q^y_{{\rm sat},1}\rangle = \frac{Q}{\gamma} \left[1 - \left(\frac{u^0_{\rm th}}{u_*} \right)^2 \right] e^{ikx+\sigma t} \sum_{n=1}^{\infty} kZ_n \left[\left(iA^n_y - B^n_y \right) + \frac{1}{\mu} \frac{r_n}{k} \frac{u^0_{\rm th}}{u_*} \right] |s_n\rangle, \tag{7.6}$$

where we have defined the reference flux $Q = \gamma\Omega \left[u_*^2 - (u^0_{\rm th})^2\right]^{\gamma-1} u_*^2$, which involves the avalanche slope μ, the shear velocity threshold $u_{\rm th}$ and the exponent γ of the transport law, see chapter 5 on the description of sediment transport over a flat bed. Finally, $A^n_{x,y}$ and $B^n_{x,y}$ are the basal stress coefficients, which are functions of k, have been studied in chapter 3.

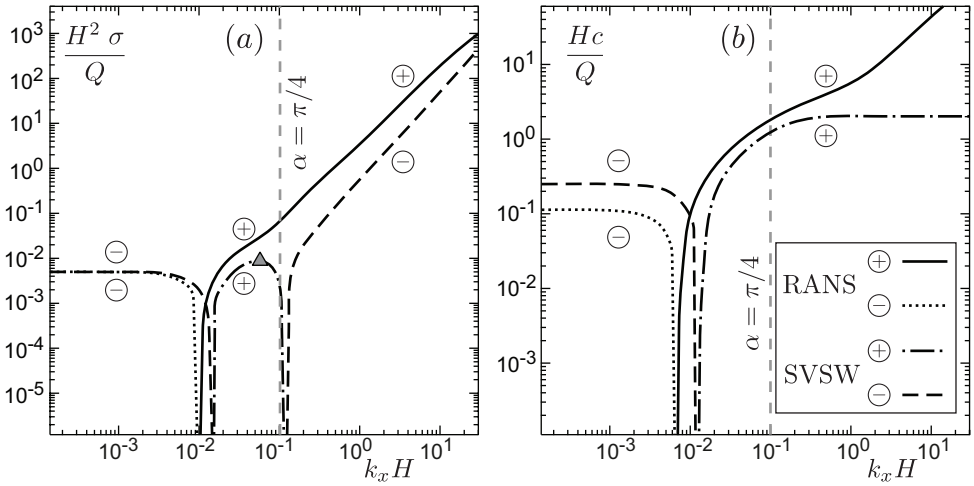


Figure 7.2: Rescaled growth rate σ and phase velocity c of inclined modes $n > 0$ as functions of kH, computed with either RANS or Saint-Venant stress coefficients. Sediment transport is assumed to be locally saturated. These curves correspond to the limit $L_{\rm sat} = 0$. These plots have been obtained for $\beta/n = 31.4$ (i.e. for $r_n H = 0.1$), $u_*/u^0_{\rm th} = 2$, $\mathcal{F} = 0.1$ and $H/z_0 = 10^2$. The triangle indicates the location of the maximum growth rate on the Saint-Venant curve. The absence of such a maximum on the RANS curve shows that it is an artefact of SVSW approximation. The graphical convention is the same as in Fig. 3.1 (see legend).

Computing the actual flux with (7.4), the continuity equation (7.2) gives, once projected on $\langle c_n|$, the dispersion relation of the nth bed mode:

$$\sigma = -\frac{ik^2 Q}{1+ikL_{\rm sat}} \times \left\{ A^n_x + iB^n_x - \frac{i}{\mu}\left(\frac{u^0_{\rm th}}{u_*}\right)^2 + \frac{1}{\gamma}\frac{r_n}{k}\left[1-\left(\frac{u^0_{\rm th}}{u_*}\right)^2\right]\left[A^n_y + iB^n_y - \frac{i}{\mu}\frac{u^0_{\rm th}}{u_*}\frac{r_n}{k}\right]\right\}. \qquad (7.7)$$

7.2 Dispersion relations

7.2.1 Assuming a locally saturated sediment transport

We first assume, as usually done in former articles on the formation of bars, that sediment transport is in local equilibrium with the flow, i.e. $\vec{q} = \vec{q}_{\rm sat}$ evaluated with

the local basal shear stress. We will see that this strong hypothesis must be relaxed and that it is necessary to take the relaxation of transport towards saturation into account.

The growth rate σ and the phase velocity c are plotted in Fig. 7.2 as functions of kH, for a given set of parameters. One observes that the differences between hydrodynamical predictions obtained with SVSW and RANS have qualitative consequences on the instability. A first difference affects the growth rate curves: while SVSW description shows an unstable region ($\sigma > 0$) with a most unstable mode corresponding to an intermediate wavenumber $k_{\max}H \simeq 0.05$ (triangle in Fig. 7.2), the RANS hydrodynamical calculation does not present any maximum growth rate for kH of order one or smaller. This discrepancy results from the fact that Saint-Venant equations predict the wrong sign for B_x for this range of kH, i.e. a phase delay of the basal shear stress with respect to topography instead of a phase advance. Large wavenumbers thus appear to be artificially stabilised. Consequently, the selection of a maximum growth wavenumber determined using Saint-Venant equations should be taken as an artefact. This strong conclusion holds for all realistic values of β, $u_*/u_{\rm th}^0$, $\mathcal{F}$ and H/z_0. Although less crucial, the velocity curves also qualitatively differ in the large wavenumber limit, with asymptotic constant (SVSW) or growing (RANS) values of c.

The conclusion is twofold. First, the linear stability analysis previously proposed in the literature to explain the formation of bars suffer from the flaws of Saint-Venant shallow water, the observed maximum growth rate being an artefact. Second, with a more reliable hydrodynamical model, the growth rate does not present any maximum in the range of wavenumbers where bars are expected. We will now show that refining the sediment transport model by taking into account flux saturation transients allows the model to predict the formation of bars. We will see that SVSW and RANS based approaches can be partly reconciled when the so-called saturation length is introduced in the description.

7.2.2 Introducing the saturation length

The description of the saturation transient brings a new dimensionless number in the problem, that we propose to call the saturation number, defined as the ratio $L_{\rm sat}/H$ between the saturation length and the flow depth (Andreotti et al., 2012). The saturation number is larger than 1 for suspended load (Claudin et al. 2011): it is typically on the order of 10^1 or 10^2 during flooding events. It can also be larger than 1 in braided gravel streams where the particles can have a size comparable to

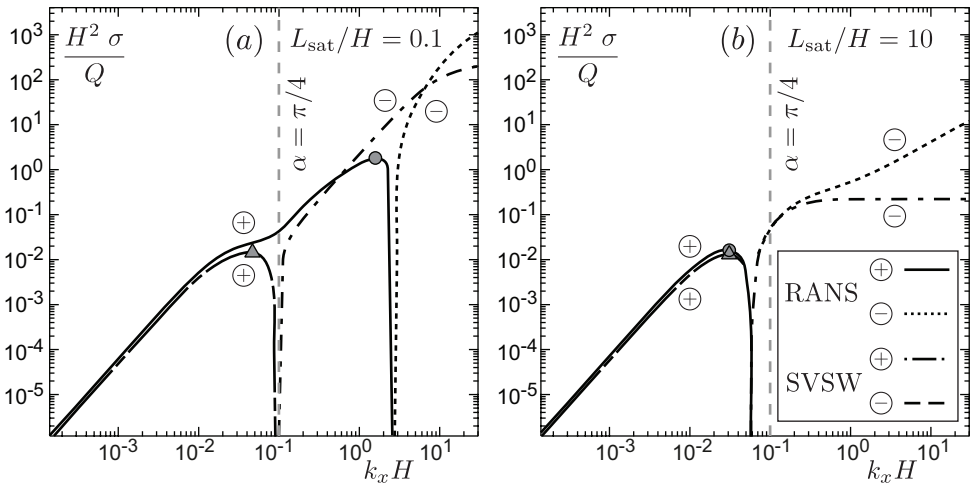


Figure 7.3: Comparison of the dispersion relation of inclined modes $n > 0$ at small and large saturation parameter L_{sat}/H. Growth rate as a function of $k_x H$ for (a) $L_{sat}/H = 0.1$ and (b) $L_{sat}/H = 10$. The other parameters are $\beta/n = 31.4$ (i.e. for $r_n H = 0.1$), $u_*/u_{\rm th}^0 = 1$, $\mathcal{F} = 0.1$ and $H/z_0 = 10^2$. The triangle (resp. circle) indicates the location of the maximum growth rate on the Saint-Venant (resp. RANS) curve. The most unstable modes only coincide at large L_{sat}/H. At small L_{sat}/H, the maximum growth rate on the SVSW curve is due to a spurious description of hydrodynamics at large wavenumber. The graphical convention is the same as in Fig. 3.1 (see legend).

the flow thickness.

The new factor $(1 + ik_x L_{\rm sat})^{-1}$ in Eq. 7.7 shows that the transport saturation transient has a stabilising effect on wavelengths comparable or smaller than $L_{\rm sat}$. The dispersion relation is plotted in Fig. 7.3 for two values of $L_{\rm sat}/H$. On all curves, the growth rate σ is now negative at large wavenumber and presents a maximum controlled by $L_{\rm sat}$. Comparing SVSW and RANS based approaches, the most unstable mode is located at different values of $k_x H$ for small $L_{\rm sat}/H$, but coincides at large $L_{\rm sat}/H$. When the saturation length is large enough, the transport saturation transient stabilises all wavenumbers, for which Saint-Venant equations are not reliable. The two predictions then coincide in the whole range of unstable wavenumbers.

To conclude this paragraph, we now consider the mode $n = 0$, which corresponds to bedforms transverse to the flow. Fig. 7.4 compares the dispersion relation obtained for SVSW and RANS hydrodynamical models, for a small but finite value of $L_{\rm sat}/H$. As already noted by different authors, the Saint-Venant completely misses the in-

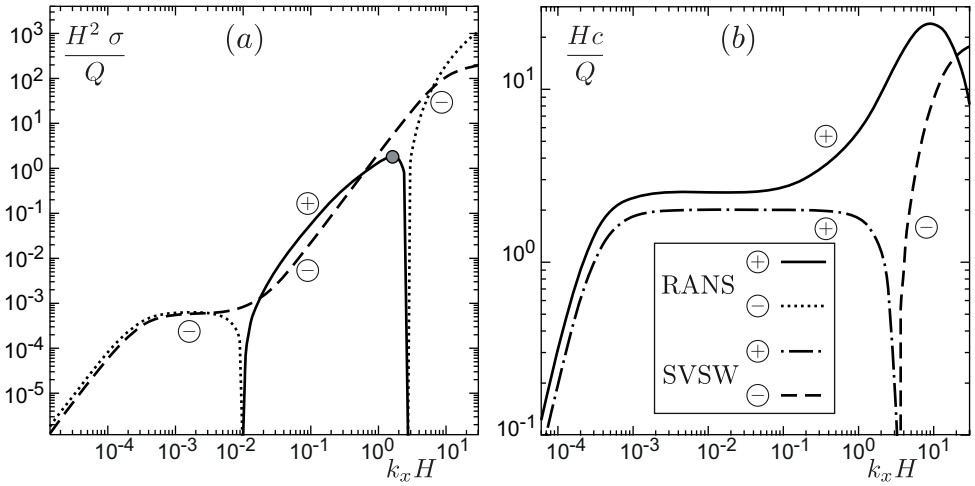


Figure 7.4: Consequences of the hydrodynamical model on the dispersion relation of transverse modes $n = 0$. Rescaled growth rate σ and phase velocity c as functions of kH, computed with either RANS or Saint-Venant stress coefficients. These plots have been obtained for $L_{sat}/H = 0.1$, $u_*/u^0_{\rm th} = 1$, $\mathcal{F} = 0.1$ and $H/z_0 = 10^2$. The circle indicates the location of the maximum growth rate on the RANS curve. In Saint-Venant approximation the instability of transverse modes is missed ($\sigma < 0$). The graphical convention is the same as in Fig. 3.1 (see legend).

stability of these modes, and therefore the emergence of ripples. By contrast, using a more reliable hydrodynamical calculation, one observes that transverse bedforms are unstable in a range wave-numbers going from a lower cut-off scaling on $1/H$ to an upper cut-off scaling on $1/L_{\rm sat}$. We therefore reach a new important conclusion regarding the instability of a flat sediment bed: ripples ($n = 0$) and bars ($n > 0$) form by the very same instability, but possibly in different regimes. In order to find the most unstable mode, one must compare all the modes, including $n = 0$. Due to the artefacts of Saint-Venant approach at large kH, this mode has been ignored so far in the discussion of the bar instability.

7.3 Revisiting the bar instability

In the first part of the chapter, we have shown that the maximum growth rate deduced from Saint-Venant equations, when the transport saturation transient is ignored, is a pure arte-fact. We have then shown that the introduction of the saturation length is necessary to address the bar instability, once hydrodynamics is properly

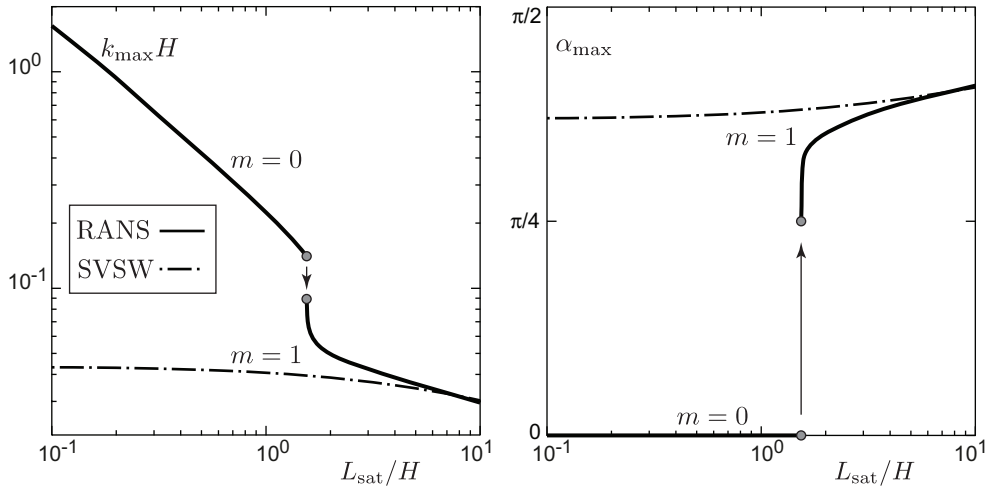


Figure 7.5: Transition from transverse ($n = 0$) to inclined ($n = 1$) bedforms controlled by the saturation number $L_{\rm sat}/H$. Longitudinal wavenumber $k_{\max}$ (a) and angle $\alpha_{\max}$ (b) of the most unstable mode as a function of $L_{\rm sat}/H$. The other parameters are $\beta = 31.4$ (i.e. $r_1 H = 0.1$), $u_*/u_{\rm th}^0 = 1$, $\mathcal{F} = 0.1$ and $H/z_0 = 10^2$. At the transition point (circles), the maximum growth rates of modes $n = 0$ and $n = 1$ are equal.

described. We will now focus on the RANS based approach to revisit the basic properties of the instability, and produce stability and bedform-phase diagrams. When necessary, we will still show the differences with the SVSW based approach.

7.3.1 Influence of the saturation parameter $L_{\rm sat}/H$

In order to study in more details the influence of the value of $L_{\rm sat}/H$ on the maximum growth rate, we have systematically varied this ratio between the two values used in Fig. 7.3. We display in Fig. 7.5 the longitudinal wavenumber $k_{\max}$ and the wave angle $\alpha_{\max}$ of the most unstable mode. One observes that the saturation parameter $L_{\rm sat}/H$ triggers a sharp transition from transverse ($n = 0$) to inclined bedforms ($\alpha_{\max}$ switches from 0 to $\simeq 3\pi/8$). At the transition, located at $L_{\rm sat}/H \simeq 1.6$ for the parameters chosen to compute Fig. 7.5, the wavenumber $k_{\max}$ drops by half a decade. Below the transition, one observes in Fig. 7.5 – **a** that $k_{\max}H$ decreases as the inverse of the saturation parameter. Therefore, the wavelength of the transverse patterns ($\alpha_{\max} = 0$) is proportional to $L_{\rm sat}$, which corresponds to sand ripples. Beyond the transition, the selected mode corresponds to alternate bars ($\alpha_{\max} > 0$). The most

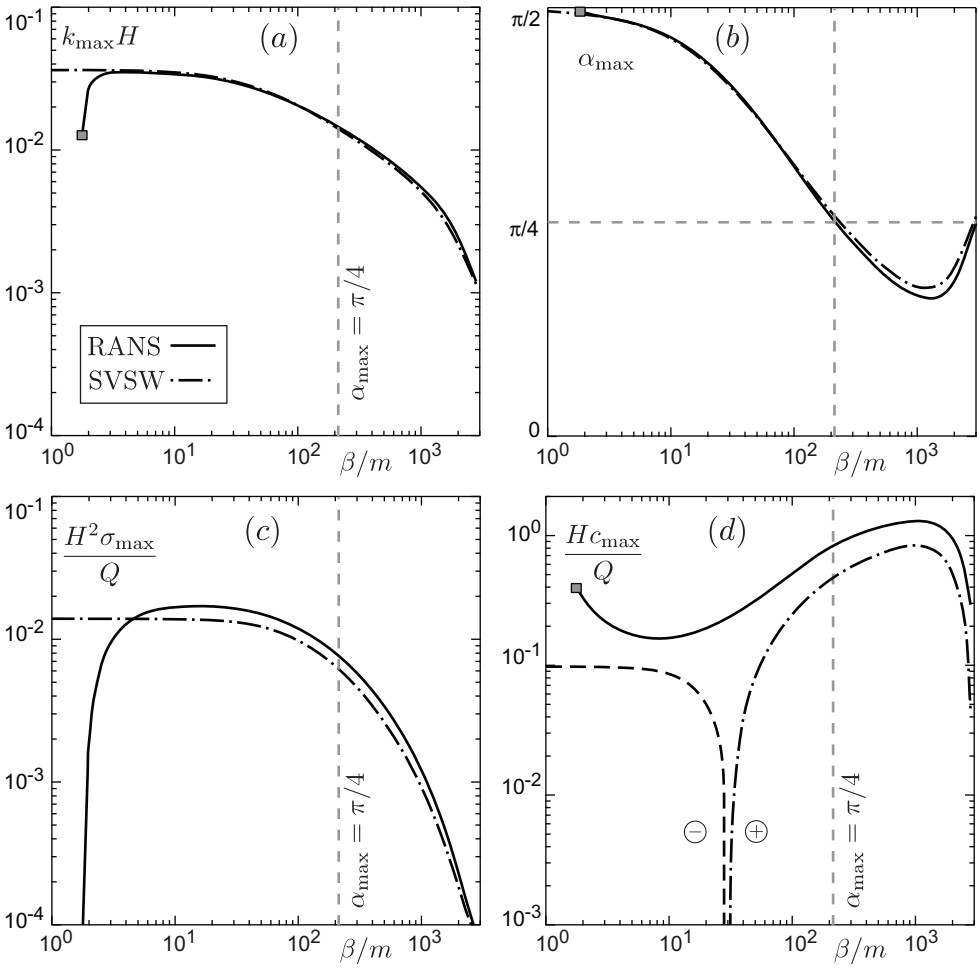


Figure 7.6: Rescaled horizontal wavenumber (a), wave angle (b), growth rate (c) and phase velocity (d), all computed for the most unstable mode, as functions of the channel aspect ratio divided by the mode number. These curves have been computed for $u_*/u_{\rm th}^0 = 1$. The other parameters are $L_{\rm sat}/H = 10$, $\mathcal{F} = 0.1$ and $H/z_0 = 10^2$. The graphical convention is the same as in Fig. 3.1 (see legend).

amplified wavenumber presents a much weaker dependance on L_{sat}. The wavelength approximately scales as $H^{2/3}L_{\text{sat}}^{1/3}/C$. Importantly, the SVSW approach completely misses this transition from transverse to inclined bedforms.

7.3.2 Influence of the ratio u_*/u_{th}^0

In this subsection we study the influence of the ratio u_*/u_{th}^0 on the dispersion relation (7.7). We focus on the large saturation number regime, for which bars ($n > 0$) are more unstable than ripples ($n = 0$). This ratio enters the problem when the influence of the longitudinal and transverse slopes on the shear threshold is taken into account. In Figs. 7.6-7.8, we plot the longitudinal wavenumber $k_{\max}$, the wave angle $\alpha_{\max}$, the growth rate $\sigma_{\max}$ and the phase velocity $c_{\max}$ of the most unstable mode as functions of the channel aspect ratio β, for three different values of u_*/u_{th}^0. The saturation length is fixed at the value $L_{\text{sat}}/H = 10$, for which we have seen above that Saint-Venant and RANS based predictions are comparable.

Close to the transport threshold, for $u_*/u_{\text{th}}^0 \to 1$, there is no influence of the transverse sediment transport. There is a stabilising effect of the longitudinal slope which vanishes as α tends to $\pi/2$. In the other limit, when $u_*/u_{\text{th}}^0 \to \infty$, the transverse sediment transport becomes important, but the slope effect disappears. In the intermediate range of shear velocities, both transverse sediment transport and slope effects are present. In particular, the transverse slope effect has a stabilising effect when α tends to $\pi/2$. Looking only at the results based on the RANS approach, the general shape of the curves is very similar. For a given mode $n > 0$, the bar instability presents a threshold controlled by β/n. In both limits of shear velocities close to the transport threshold and far from it, this instability threshold is mostly due to a decrease of the stress component B_x at large $r_n H$ (we recall that B_x controls the destabilising effect). In the intermediate range of shear velocities, the transverse slope effect adds a further stabilising effect which leads to an increased value of the threshold aspect ratio, β_c. Above this threshold, one can distinguish three zones of β/n. At small β/n, the wavelength is controlled by H/C, the angle is close to $\pi/2$, and the propagation speed increases with β. In the intermediate range of β/n, the angle decreases with β; the wavelength roughly scales as $\sqrt{HW/C}$, and the propagation speed still increases with β. Finally, at high β/n, the growth rate drops. For a given β, modes of higher n are therefore more amplified.

Comparing the results obtained with SVSW equations to those obtained with RANS approach, one observes a global agreement in the trends. However, for

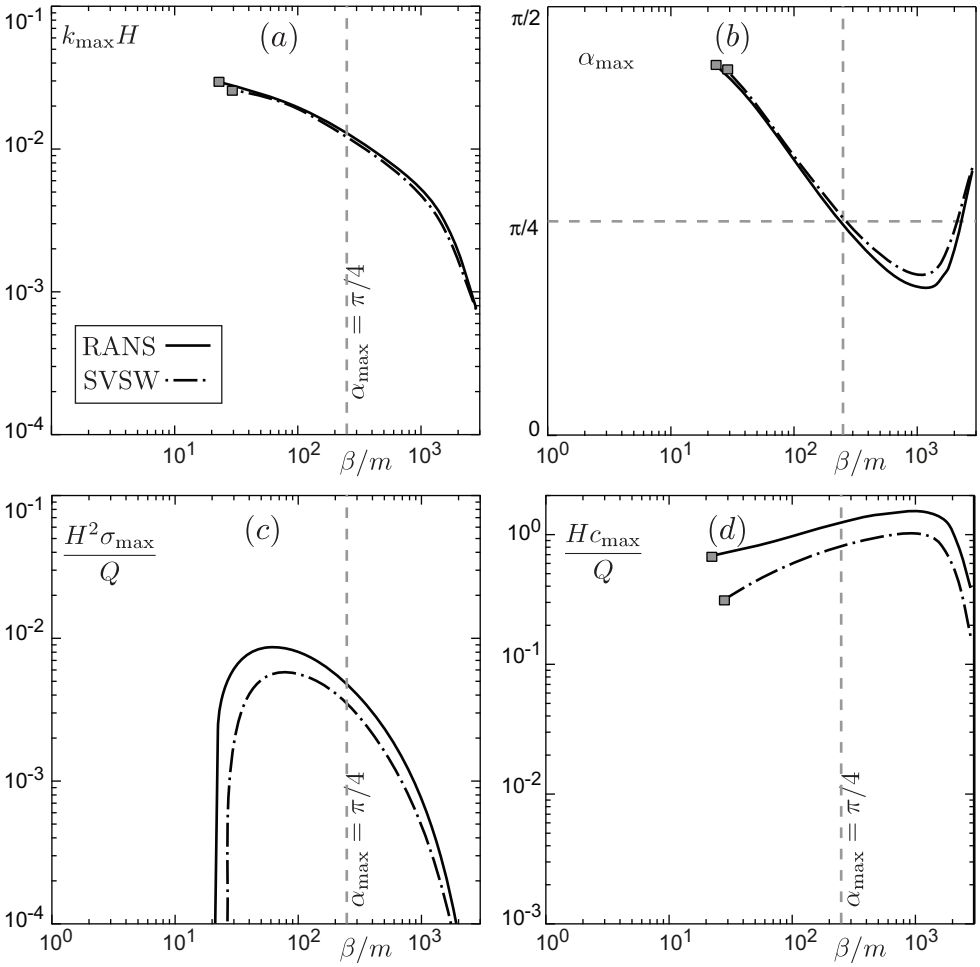


Figure 7.7: Same as Fig. 7.6, but for $u_*/u_{\rm th}^0 = 2$.

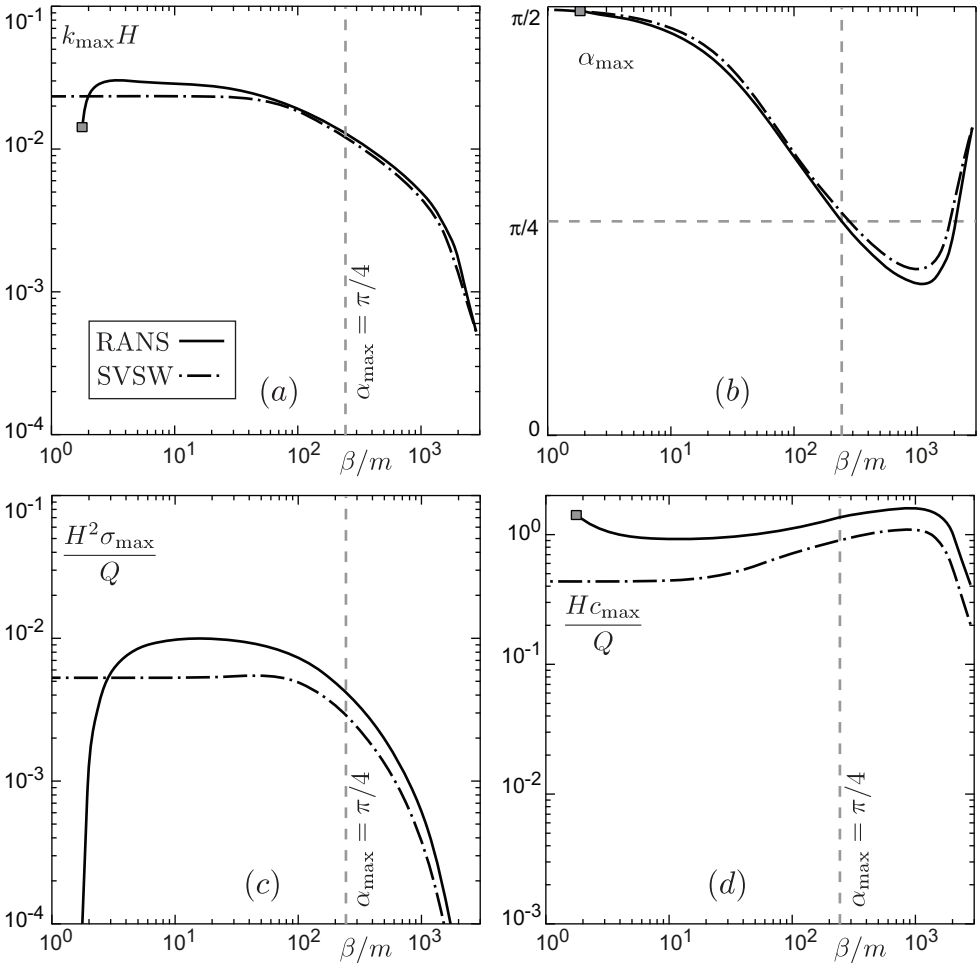


Figure 7.8: Same as Fig. 7.6, but for $u_*/u_{\rm th}^0 \to \infty$.

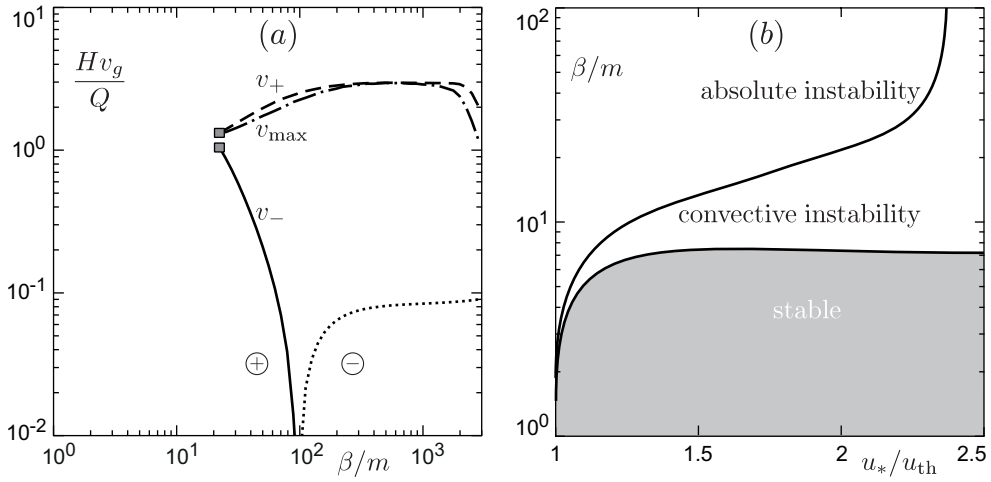


Figure 7.9: (a) Group velocity v_g as a function of β/n. The three curves correspond to three particular points of the dispersion relation $\sigma(kH)$: the most unstable mode (dotted dashed line), and the two marginal modes at high (dashed line) and low (solid and dotted lines) wavenumbers. The latter changes sign, and we use a graphical convention similar to that described in Fig. 3.1, with a concomitant change of line symbol. These curves have been computed with $u_*/u_{\rm th}^0 = 2$. (b) Stability diagram in the plane $(\beta/n, u_*/u_{\rm th}^0)$. The line separating convective from absolute instabilities corresponds to vanishing group velocity. For both panels, the other parameters are $L_{\rm sat}/H = 10$, $\mathcal{F} = 0.1$ and $H/z_0 = 10^2$.

$u_*/u_{\rm th}^0 \to 1$ and $u_*/u_{\rm th}^0 \to \infty$, Saint-Venant equations miss the instability threshold at small β, i.e. when $k_n H/C$ is too large to get correct hydrodynamical results. Furthermore, these equations predict a change of sign of the propagation speed $c_{\max}$, close to the transport threshold, which is due to a wrong sign of A_x at large transverse wavenumbers (see chapter 4). Interestingly, the results obtained with both models are very close to each other in the intermediate range of shear velocities, thanks to the stabilising transverse slope effects: as the threshold β_c is higher, Saint-Venant equations are correct in the whole range of unstable modes.

7.3.3 From alternate to multiple bars

We have seen that the presence of the banks selects a discrete though infinite set of modes (chapter 3). More precisely, the boundary conditions lead to a selection of the transverse wavenumber: $r_n H = n\pi/\beta$. Consider an initial sediment bed randomly disturbed, say, by a white noise. Then all modes, characterised by the pair (k,n)

have statistically the same mean squared amplitude. The mode that emerges is the most unstable one, i.e. that with the maximum growth rate σ with respect to k *and* n. By contrast, in the previous paragraphs, we have analysed the properties of the maximum growth rate at a given transverse number n. The phase diagram of Fig. 7.10 presents the value of n selected as a function of $L_{\rm sat}/H$ and β, keeping $u_*/u_{\rm th} = 2$ fixed.

The diagram first shows that the saturation number $L_{\rm sat}/H$ controls the transition from transverse patterns (ripples) to bars. The second dominant feature of the diagram is the existence of an instability threshold. At low $L_{\rm sat}/H$, the dimensionless parameter controlling this threshold is the ratio $W/L_{\rm sat}$. At large $L_{\rm sat}/H$, the saturation length becomes a subdominant parameter and the bedform pattern becomes controlled by the channel aspect ratio β. At small β, a flat sand bed is stable. In an intermediate range of β, alternate bars ($n = 1$) are the most unstable modes. Finally, increasing the aspect ratio β, multiple bars form with an increasing value of n. This last regime could explain the formation and the dynamics of bars in braided rivers (Fig. 7.1 – **b**).

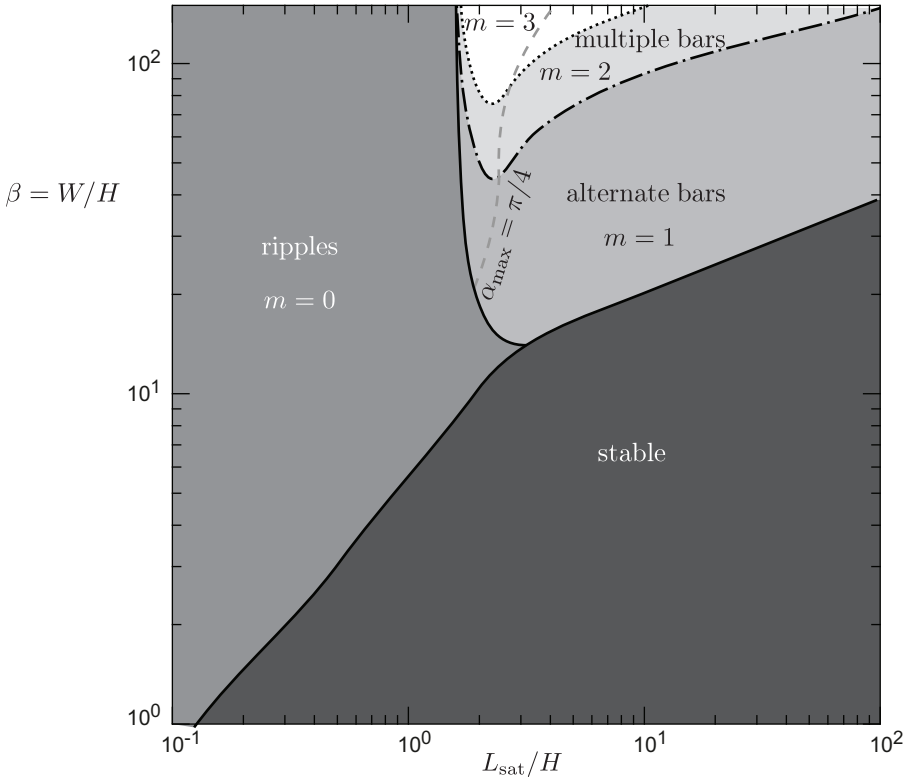


Figure 7.10: Diagram showing the different bedform regions in the plane (β,$L_{\rm sat}/H$). In the bottom-right dark-grey region, the bed is stable. In the left middle-grey region, ripples ($n = 0$) are the most unstable bedforms. In the remaining up-right part of the plane, higher modes ($n > 0$) are dominant: the dashed-dotted line separates alternate bars ($n = 1$) from double bars ($n = 2$). The dotted lines shows the transition to $n = 3$. The dashed line ($\alpha_{\rm max} = \pi/4$) separates rather transverse to more elongated bars. These curves have been computed with $u_*/u^0_{\rm th} = 2$, $\mathcal{F} = 0.1$ and $H/z_0 = 10^2$.

Chapter 8

The meander instability

After having revisited the bar instability in the previous chapter, we wish now to address the meanders instability. This necessitates to account for the evolution of the banks, in addition to that of the bed as previously discussed for the bars. We will perform in this chapter a linear stability analysis, using turbulent RANS equations for hydrodynamics. However, as in the previous chapter, some of the results will also be derived with SVSW depth-integrated equations. We will systematically vary the parameters of the model – namely the Froude number $\mathcal{F}$, Chézy number C, the channel aspect ratio β, the bed friction coefficient μ and the velocity ratio $u_*/u_{\rm th}$ – and discuss their influence on the most unstable mode. A comparison of the model with some experimental data is provided in the next chapter.

8.1 Adding bed and banks contributions

The forcing of hydrodynamics and sediment transport now comes from two independent contributions. As for the case of bars, one is that of the bed Z, which is represented as before on the basis $|c_n\rangle$:

$$k|Z\rangle = e^{ikx+\sigma t} \sum_{n=1}^{\infty} kZ_n \, |c_n\rangle \, . \tag{8.1}$$

Similarly, following the formalism developed in chapter 2, the left and right banks of the meandering channel are respectively written as:

$$Y^L = \Upsilon \, e^{ikx+\sigma t} + y_0 \, , \tag{8.2}$$

$$Y^R = \Upsilon \, e^{ikx+\sigma t} - y_0 \, . \tag{8.3}$$

Both kZ_n and $k\Upsilon$ are assumed to be small, and at the linear order, bed and banks contributions can simply be added (see discussion in chapter 2), as detailed below. The real part of σ is the growth rate of the meandering channel (note that, as for the bars, we will keep calling it σ) and its imaginary part ω is related to the migration velocity of the meander ($c = \omega/k$)

8.1.1 Hydrodynamics

As for the hydrodynamical response to both bed and banks perturbations, we are mostly interested in the longitudinal and transverse components of the velocity and the of basal shear stress. Following Eqs. 2.32, 2.33, 2.34 and 2.35, we write their time evolution as:

$$|u_1\rangle = u_* \, e^{ikx+\sigma t} \sum_{n=1}^{\infty} \left(U_n^Z \, kZ_n + U_n^B \, k\Upsilon \right) |c_n\rangle \, , \tag{8.4}$$

$$|v_1\rangle = u_* \, e^{ikx+\sigma t} \left\{ ik\Upsilon |1\rangle + \sum_{n=1}^{\infty} \left(V_n^Z \, kZ_n + V_n^B \, k\Upsilon \right) |s_n\rangle \right\} , \tag{8.5}$$

and

$$|\tau_{1,b}^{xz}\rangle = {u_*}^2 \, e^{ikx+\sigma t} \sum_{n=1}^{\infty} \left[(A_x^n + iB_x^n) \, kZ_n + (C_x^n + iD_x^n) \, k\Upsilon \right] |c_n\rangle \, , \tag{8.6}$$

$$|\tau_{1,b}^{yz}\rangle = {u_*}^2 \, e^{ikx+\sigma t} \left\{ i\sqrt{C} k\Upsilon |1\rangle + \sum_{n=1}^{\infty} \left[\left(iA_y^n - B_y^n \right) \, kZ_n + \left(iC_y^n - D_y^n \right) \, k\Upsilon \right] |s_n\rangle \right\} . \tag{8.7}$$

We recall that the dimensionless velocity and stress coefficients $U_n^{Z,B}$, $V_n^{Z,B}$, $A_{x,y}^n$, ... $D_{x,y}^n$ have been computed in chapters 3 and 4, both for RANS and SVSW equations, and are now used 'as they are' without further adjustment.

8.1.2 Sediment transport

Similarly for the flux of sediment, using the generic description discussed in chapter 5 (Eqs. 5.15-5.19), we have for the two components of the first order saturated flux:

$$|q^x_{1,\mathrm{sat}}\rangle = Q\, e^{ikx+\sigma t} \sum_{n=1}^{\infty} \left\{ kZ_n \left[A^n_x + iB^n_x - i\,\frac{1}{\mu}\left(\frac{u^0_{\mathrm{th}}}{u_*}\right)^2 \right] + k\Upsilon\left(C^n_x + iD^n_x\right) \right\} |c_n\rangle\,, \tag{8.8}$$

$$|q^y_{1,\mathrm{sat}}\rangle = \frac{Q}{\gamma}\left[1-\left(\frac{u^0_{\mathrm{th}}}{u_*}\right)^2\right] e^{ikx+\sigma t} \left\{ i|1\rangle + \sum_{n=1}^{\infty} \left[kZ_n \left(iA^n_y - B^n_y + \frac{1}{\mu}\,\frac{r_n}{k}\,\frac{u^0_{\mathrm{th}}}{u_*} \right) + k\Upsilon\left(iC^n_y - D^n_y\right) \right] \right\} |s_n\rangle\,. \tag{8.9}$$

We assume that the timescale of flux relaxation T_{sat} is much smaller than the timescale of meanders evolution. We also hypothesize that the spatial relaxation of the flux occurs along the sediment transport direction $\vec{t}$ following the first order relaxation equation (5.20). Since the base flux is homogeneous in x and y, the operator $\vec{t}\cdot\vec{\nabla}$ must be taken at the zeroth order, and thus reduces to ∂_x. Consequently, the flux perturbation $\vec{q}_1$ is simply related to that of the saturated flux $\vec{q}_{1,\mathrm{sat}}$ as:

$$|q^x_1\rangle = \frac{1}{1+ikL_{\mathrm{sat}}}\,|q^x_{1,\mathrm{sat}}\rangle\,, \tag{8.10}$$

$$|q^y_1\rangle = \frac{1}{1+ikL_{\mathrm{sat}}}\,|q^y_{1,\mathrm{sat}}\rangle\,. \tag{8.11}$$

8.2 Derivation of the dispersion relation

Describing the time evolution of the bed and the banks, we can now compute the dispersion relation which gives σ for a given wavenumber k.

8.2.1 Bed evolution

The evolution of the bed form is controlled by the mass conservation equation (5.9):

$$\partial_t Z + \vec{\nabla}\cdot\vec{q} = 0\,. \tag{8.12}$$

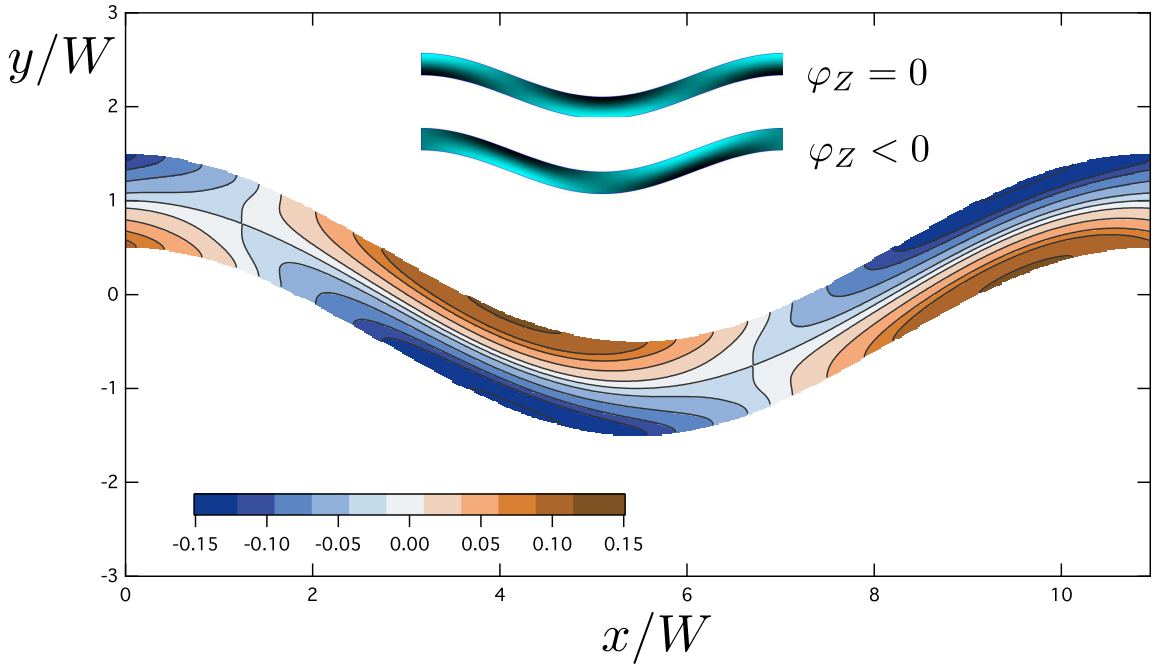


Figure 8.1: Bed elevation predicted by Eq. 8.13, for the wavenumber $kW = 0.57$. The flow is from right to left. Here we display the summed contribution of the first three odd modes: $Z/\Upsilon = |Z_1|e^{ik_{\max}x+\varphi_1^Z}|c_1\rangle + |Z_3|e^{ik_{\max}x+\varphi_3^Z}|c_3\rangle + |Z_5|e^{ik_{\max}x+\varphi_5^Z}|c_5\rangle$. Positive (elevated) regions are displayed in brown. Negative (low) regions are displayed in blue. The channel aspect ration has been set to $\beta = 4$. Inset: schematics showing the sign convention for the phase φ^Z.

Under the assumption that the time scale over which the bed evolves is much shorter than that of the banks, we can, for the study of the meandering instability, neglect $\partial_t Z$, leading to $\vec{\nabla} \cdot \vec{q} = 0$. This means that the bed is considered 'in equilibrium' with respect to the bank profile, and implies that the bed coefficients, noted Z_n^{eq}, are

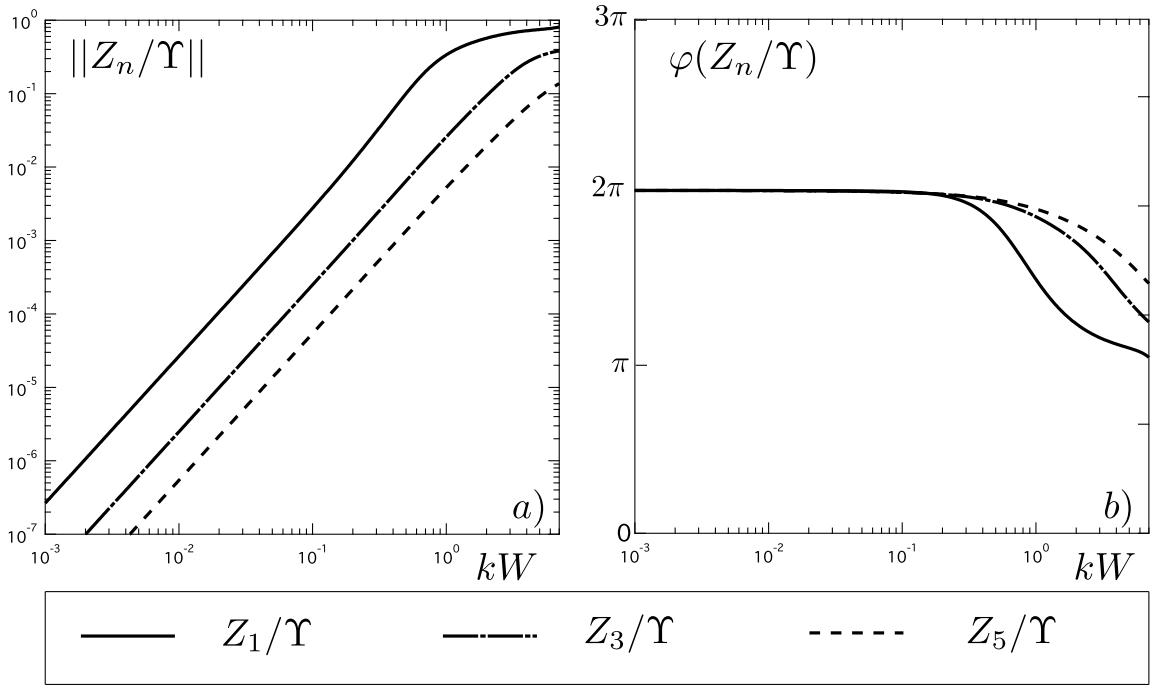


Figure 8.2: Modulus (a) and phase (b) of the ratio $Z_n^{\rm eq}/\Upsilon$ between the amplitude of the mode n of the bed perturbation and that of the bank modulation, as a function of kW, for $n = 1$, 3 and 5 (see legend). These curves have been computed with $C = 0.1$, $\beta = 4$, $\mathcal{F} = 0.77$, $\mu = 0.45$ and $u_*/u_{\rm th} = 1.6$.

related to the bank modulation Υ by the analytical expression:

$$\begin{aligned}\frac{Z_n^{\rm eq}}{\Upsilon} &= -\frac{1}{\left[-\left(B_x^n+\mathcal{K}_nB_y^n\right)+\mathcal{J}_n\right]^2+\left[A_x^n+\mathcal{K}_nA_y^n\right]^2} \\ &\times \Big\{\left[B_x^n+\mathcal{K}_nB_y^n-\mathcal{J}_n\right]\left[D_x^n+\mathcal{K}_nD_y^n\right]+\left[A_x^n+\mathcal{K}_nA_y^n\right]\left[C_x^n+\mathcal{K}_nC_y^n\right] \\ &\quad +i\left[-\left(B_x^n+\mathcal{K}_nB_y^n\right)+\mathcal{J}_n\right]\left[C_x^n+\mathcal{K}_nC_y^n\right] \\ &\quad +i\left[A_x^n+\mathcal{K}_nA_y^n\right]\left[D_x^n+\mathcal{K}_nD_y^n\right]\Big\},\end{aligned} \tag{8.13}$$

where we have defined

$$\mathcal{K}_n = \frac{1}{\gamma}\left[1-\left(\frac{u^0_{\rm th}}{u_*}\right)^2\right]\frac{r_n}{k}\,, \tag{8.14}$$

$$\mathcal{J}_n = \frac{1}{\mu}\left(\frac{u^0_{\rm th}}{u_*}\right)^2 + \frac{1}{\mu}\,\frac{u^0_{\rm th}}{u_*}\,\frac{1}{\gamma}\left[1-\left(\frac{u^0_{\rm th}}{u_*}\right)^2\right]\left(\frac{r_n}{k}\right)^2\,. \tag{8.15}$$

Note that the relation (8.13) is independent of the saturation length $L_{\rm sat}$. We can also see that the transversal slope contained into the term $\mathcal{J}_n$ mostly affects the $B^n_{x,y}$ coefficients, and is in factor of the $D^n_{x,y}$'s.

In figure 8.1, we display a contour plot representing the bed elevation predicted by Eq. 8.13, for the wavenumber $kW = 0.57$, corresponding to the most unstable wavenumber $k_{\rm max}W$ in the experiment, see next chapter. We clearly see the alternation of low and high regions ('pools' and 'beaches'), phased with respect to the bank modulation, which are typical of a meandering channel: beaches occur in the inside of the channel bent, slightly downstream of it.

In figure 8.2 we display the modulus and the phase of the ratio $Z_n{\rm eq}/\Upsilon$ for the first three modes as a function of kW. As discussed in the next chapter, the value of the ratio Z_1/Υ is about 0.1–0.2 for $kW = 0.5$–1, in agreement with the experimental data around the maximum of instability. Higher modes, Z_n/Υ for $n \geq 3$, have much smaller moduli than the first one, as Fig. 8.2 – **a** shows. For example, if we set to 100% the $\sum_{n=1}^{5} Z_n/\Upsilon$, the respective contributions (at $kW = 0.57$) are distributed as:

Modes	Intensity (%)
Z_1/Υ	93%
Z_3/Υ	6%
Z_5/Υ	1%

From Eq. 8.13, we can also deduce the phase φ_Z of the bed modes with respect to the bank modulation. For the first three odd modes we have negative phases (we display $2\pi - \varphi_Z$ as a function of kW in figure 8.2 – **b**. Evaluating the phase at $kW = 0.57$, we have:

Modes	value (rad)
φ^Z_1	-0.65
φ^Z_3	-0.22
φ^Z_5	-0.18

8.2.2 Bank evolution

In contrast to the case of the bed, there is no rigourous and well established equation for the time evolution of the banks. For the sake of simplicity and in order to ease interpretation, we take the following relationship (Odgaard 1987, Pizzuto & Meckelnburg 1989):

$$\partial_t Y^{L,R} = \pm\mathcal{E}\left[\bar{u}(\pm y_0) - u_* \bar{\mathcal{U}}\right] . \tag{8.16}$$

It phenomenologically links the erosion/deposition processes at the banks to the depth-averaged excess velocity of the flow at the boundaries. $\mathcal{E}$ represents the erosion (dimensionless) coefficient of the banks and it could be measured experimentally.

We have tried more sophisticated laws, which involve more phenomenological parameters. For example, the above equation 8.16 does not allow for a phase difference between the flow and the bank evolution. However, as far as the dispersion relation is concerned, we did not find substantial differences that would convince us to dismiss this simple choice as a first reasonable step.

The expression of $\bar{u}$ can be now replaced by the superposition of relations (3.109) and (4.52). Using also $Z_n = Z_n^{\mathrm{eq}}$, we can write:

$$\bar{u} = u_* \left\{ \bar{\mathcal{U}} + k\Upsilon e^{ikx+\sigma t} \sum_{n=1}^{\infty} \left(\bar{U}_n^{\Upsilon} + \frac{Z_n^{\mathrm{eq}}}{\Upsilon} \bar{U}_n^{Z} \right) |c_n\rangle \right\} . \tag{8.17}$$

Recall that $|c_n\rangle = \cos\left[n\pi(y/2y_0 + 1/2)\right]$, we have $|c_n\rangle(+y_0) = (-1)^n$ and $|c_n\rangle(-y_0) = 1$ for odd n, and $|c_n\rangle(\pm y_0) = 0$ for even n. The expression (8.16) then gives the dispersion relation of the river banks:

$$\sigma = -\mathcal{E} u_* k \sum_{n=1}^{\infty} \left[\bar{U}_n^{\Upsilon} + \frac{Z_n^{\mathrm{eq}}}{\Upsilon} \bar{U}_n^{Z} \right] . \tag{8.18}$$

Note again that only odd modes contribute to this sum.

8.2.3 Coupling the bed and the banks

One can relax the assumption that the evolution time scale of the bed is much smaller than that of the banks. In that case, we cannot forget the term $\partial_t Z$ in equation 8.12,

which once projected on the basis $\langle c_n|$, give:

$$\sigma Z_n + \frac{iQk^2}{1+ikL_{\rm sat}}\left\{\left[A_x^n + iB_x^n - \frac{i}{\mu}\left(\frac{u_{\rm th}^0}{u_*}\right)^2\right] Z_n + \left(C_x^n + iD_x^n\right)\Upsilon \quad + \right.$$
$$\left.\frac{1}{\gamma}\frac{r_n}{k}\left[1-\left(\frac{u_{\rm th}^0}{u_*}\right)^2\right]\left[\left(A_y^n + iB_y^n - \frac{i}{\mu}\frac{r_n}{k}\frac{u_{\rm th}^0}{u_*}\right) Z_n + \left(C_y^n + iD_y^n\right)\Upsilon\right]\right\} \quad = \quad 0. \tag{8.19}$$

Note that, as it should, this expression gives the dispersion relation for the bars when one sets $\Upsilon = 0$ (see Eq. 7.7 in chapter 7). Keeping equation 8.16 for the evolution of the banks, one gets:

$$\sigma\,\Upsilon + \mathcal{E}u_* k \sum_{n=1}^{\infty}\left[\bar{U}_n^{\Upsilon}\Upsilon + \bar{U}_n^{Z} Z_n\right] = 0 \tag{8.20}$$

If we truncate the sum in the above equation, keeping only the modes $n = 1$, $n = 3$, ..., $n = 2p+1$, then equations 8.19 and 8.20 form a homogeneous linear system of size $p+2$ where the unknowns are the $p+1$ coefficients Z_n and Υ. The dispersion relation is then computed under the condition that the determinant of the corresponding $(p+2)\times(p+2)$ matrix must vanish. For $n = 1$ (or $p = 0$), the determinant gives a quadratic polynomial in σ, so that this computation is analytically tractable to the end. Again, although this time, $L_{\rm sat}$ does not factorize out, the growth rate of the meanders is not substantially different from that computed in the simple case.

8.3 Properties of the dispersion relation

In this section, we study the properties of the relation (8.18).

8.3.1 Growth rate and angular velocity

In Figure 8.3 - **a**, we show the rescaled growth rate $\sigma H/\mathcal{E}u_*$ as a function of the dimensionless wavenumber kW for the first four odd modes ($n = 1$, $n = 3$, $n = 5$ and $n = 7$), and adding them up. As we can see, the dominating mode is the first one $n = 1$, while the contribution of the three others is much smaller. This suggests that the sum (8.18) can be reasonably truncated. In parallel, the figure 8.3 - **b** shows $\sigma(k)$ for different channel aspect ratios β. We observe that the unstable region ($\sigma > 0$), and consequently the most unstable mode, move towards smaller wavenumbers for

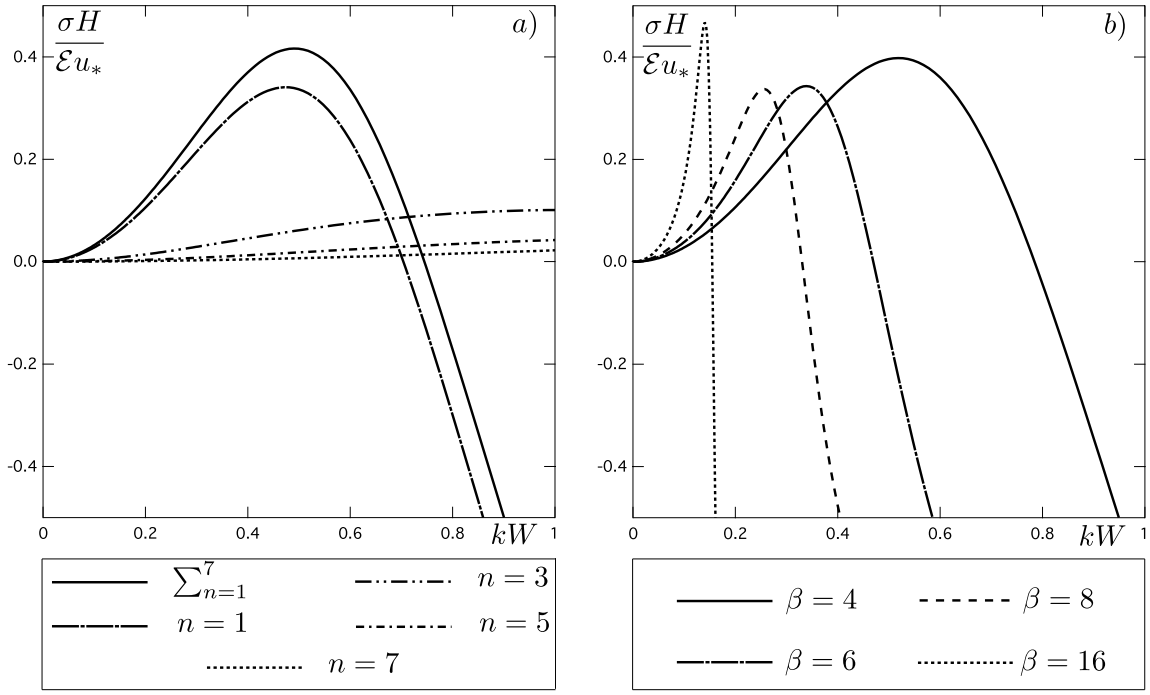


Figure 8.3: Growth rate as a function of the wavenumber (a) for the three first odd modes, as well as their sum, and (b) for different values of the aspect ratio. Panel (a): $\beta = 4$. Panel (b): σ summed over the first four odd modes. The other parameters are $\mathcal{F} = 0.77$, $C = 0.1$, $\mu = 0.45$ and $u_*/u_{\rm th} = 1.6$.

larger β. This is in agreement with meanders in real rivers (see below).

Similarly, we display in figure 8.4 - **a** the angular velocity ω defined as the imaginary part of the complex growth rate. We see that the main contribution also comes from first mode. As already mentioned the angular velocity is related to the propagation velocity c of the meanders as $c = \omega/k$. Meanders migrating downstream present a positive angular frequency $\omega > 0$, whereas those migrating upstream have a negative angular frequency $\omega < 0$. We see in figure 8.4 - **b** that for all the value of the aspect ratio β, the curves have a positive sign in the range $0 \leq kW \leq 1$. This means that in such cases the meanders migrate downstream.

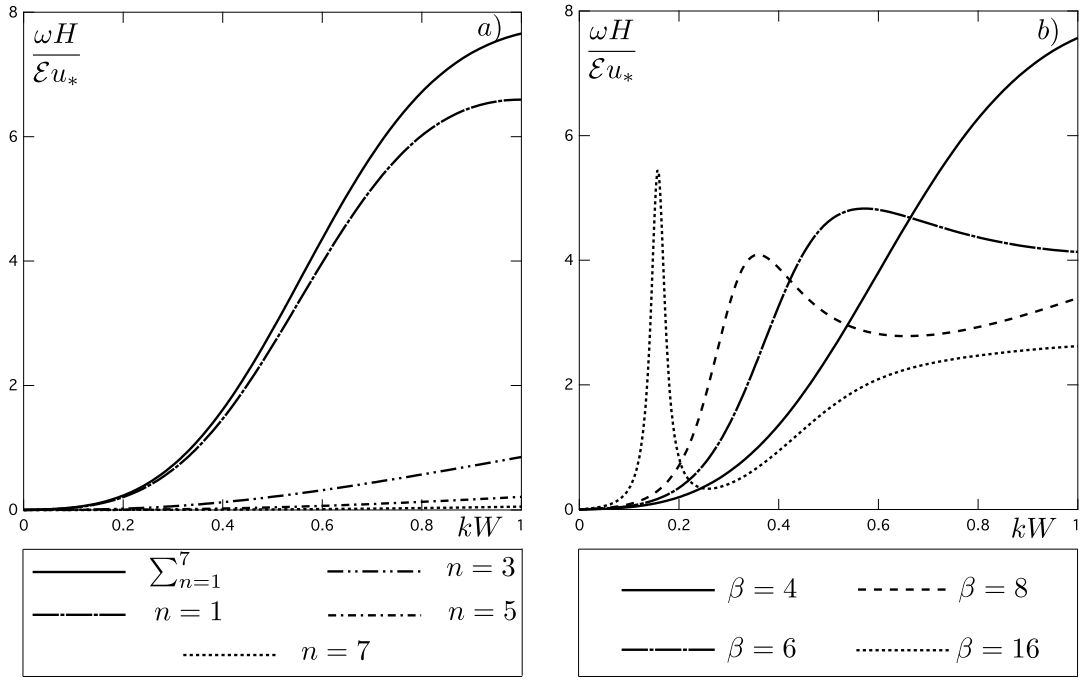


Figure 8.4: Angular velocity ω as a function of the wavenumber (a) for the four first odd modes, as well as their sum, and (b) for different values of the aspect ratio. Panel (a): $\beta = 4$. Panel (b): ω summed over the first four odd modes. The other parameters are $\mathcal{F} = 0.77$, $C = 0.1$, $\mu = 0.45$ and $u_*/u_{\rm th} = 1.6$.

8.3.2 Influence of the parameters on the most unstable mode

Now we focus on the dependence of the most unstable mode on the different parameters of the model.

Channel aspect ratio β

We display in figure 8.5 the dependence of the wavenumber $k_{\max}W$ corresponding to the most unstable mode (the maximum growth rate) on the channel aspect ratio. We first see that there is a critical value β_c below which the instability does not exist. This value is larger for larger Chézy number. With the values of the other parameters chosen here, we typically have $\beta_c \simeq 0.5$. Above this critical value, $k_{\max}W$ sharply decreases, and then its variations are weak when β is changed by two orders of magnitude. An approximatively constant value of kW, or a wavelength $\lambda \propto W$ is precisely an empirical scaling law observed for natural meanders, as reported in

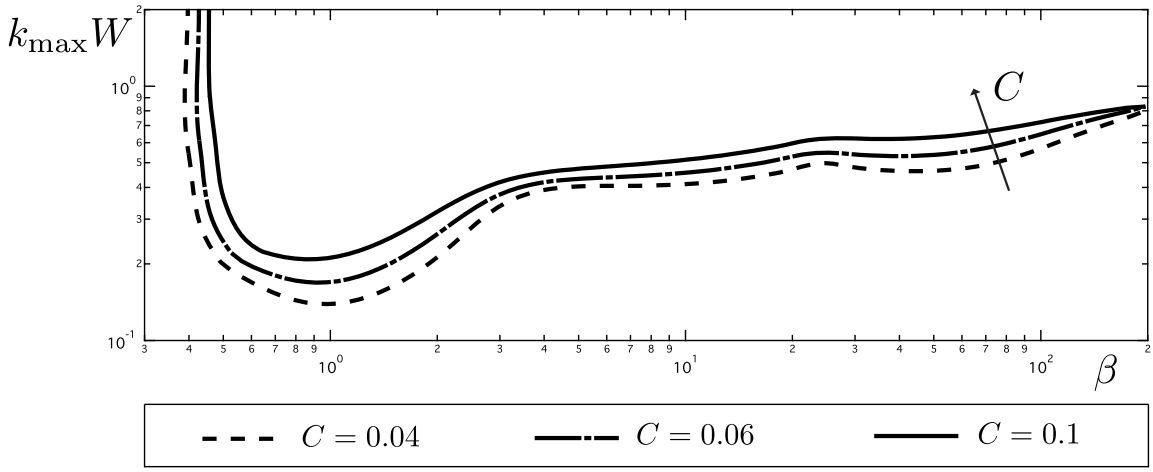


Figure 8.5: Wavenumber of the most unstable mode $k_{\max}W$ as a function of the aspect ratio β for different values of the Chézy number (see legend). The other parameters are $\mathcal{F} = 0.77$, $\mu = 0.45$ and $u_*/u_{\text{th}} = 1.6$.

figure 8.6 with a rather large and diverse data set.

Similarly, we show the behavior of the angular velocity ω with β in figure 8.7 - **b**. More precisely, we have computed both the angular velocity ω its counterpart $\omega_g \equiv k\, d\omega/dk$ based on the group velocity. For completeness, in figure 8.7 - **a** we also display the migration velocity c and the group velocity of the meanders. A first observation is that both these velocities change their sign from positive to negative values at the same value β_r, here on the order of 25. In between β_c and β_r, ω and ω_g stay approximatively constant.

The divergence at β_r can be associated to the *resonance* predicted by Blondeaux & Seminara (1985). This phenomenon can clearly be seen in figure 8.8, where the dispersion relation is plotted for that value of the aspect ratio: one can see a divergence of the growth rate at some value of kW. An infinite growth rate breaks the hypothesis that the evolution of the banks is much faster than that of the bed, and such a divergence is effectively regularized when the coupling between the bed and the banks is taken into account (paragraph 8.2.3). Importantly, although our model is able to reproduce this effect, we will show below that the mechanism responsible for the emergence of meanders is not related to this resonance for moderate β.

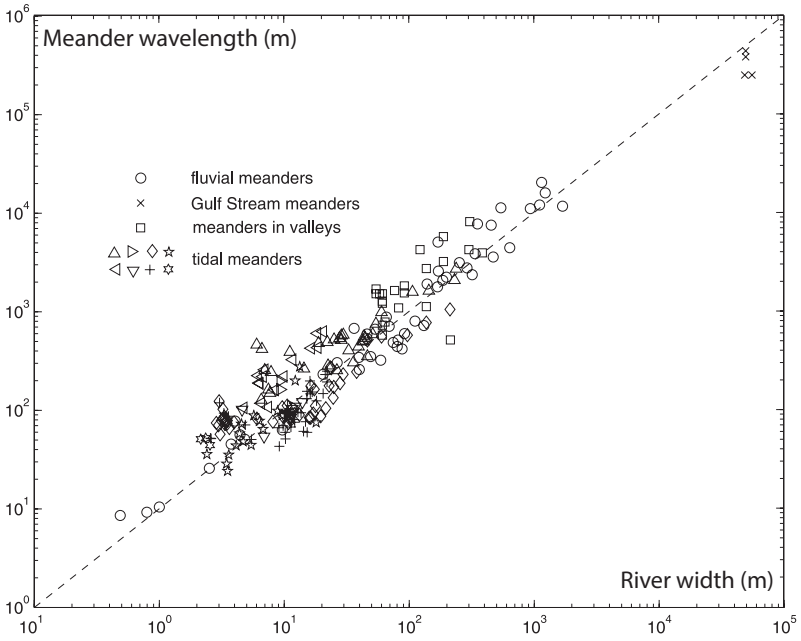


Figure 8.6: Wavelength of natural meanders as a function of river width for different kind of rivers. Data collected by Marani et al. (2002). Dashed line: slope at $\lambda/W = 10$ that correspond to $kW \simeq 0.63$. All the data fall in the range $0.12 < kW < 3$ approximately.

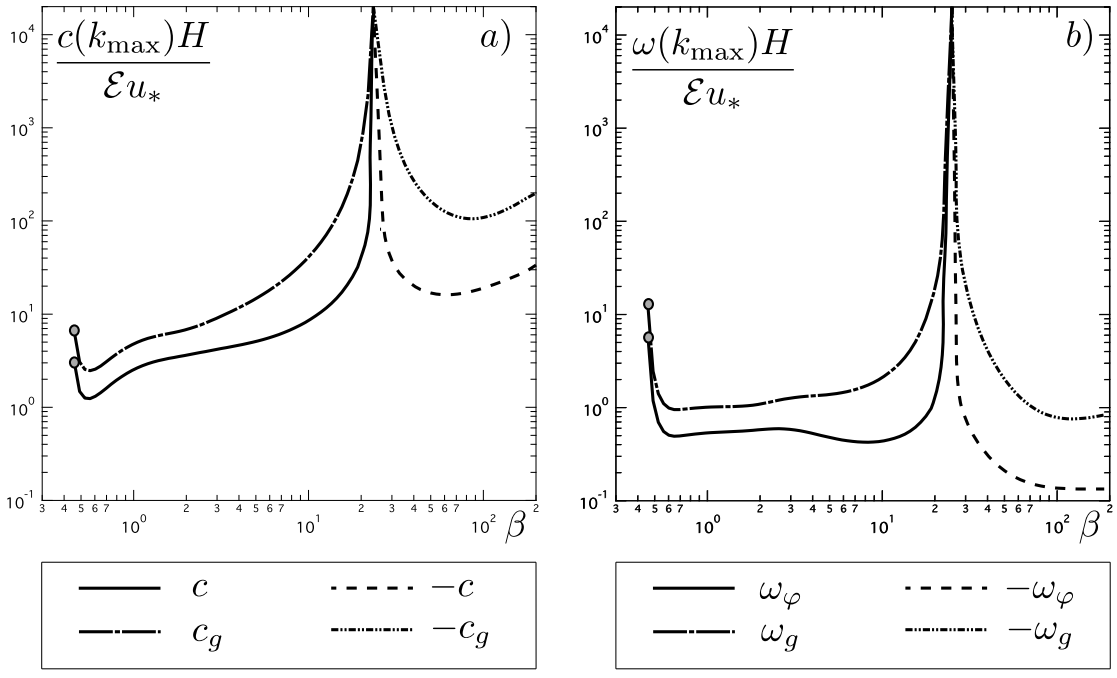


Figure 8.7: (a) Phase and group velocities determined at the wavenumber corresponding to the maximum of the instability. (b) Phase and group angular velocities corresponding to the most unstable mode as function of the channel aspect ratio. The other parameters are $\mathcal{F} = 0.77$, $C = 0.1$, $\mu = 0.45$ and $u_*/u_{\rm th} = 1.6$. Graphical convention: see legend.

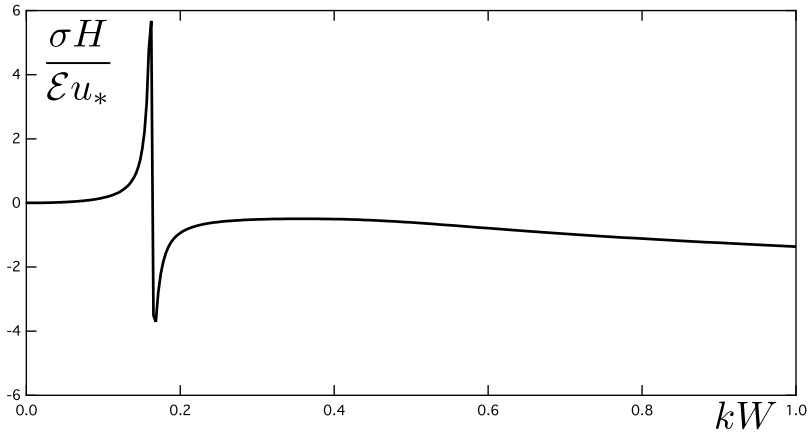


Figure 8.8: Dispersion relation for: $\beta = 16$, $C = 0.1$, $\mu = 0.45$ and $u_*/u_{\text{th}} = 1.42$.

Chézy number C

The influence of the Chézy number C on the most unstable mode is summarized in figure 8.9 – **a**. Consistently with the curves displayed in figure 8.5, we see only weak variations of $k_{\max}W$, with the exception of the curve at lowest aspect ratio for very small values of C. As detailed in the next chapter, relevant values of C in our experiments are in the range 0.03–0.15. As for natural rivers, a typical value of the Chézy number is $C \simeq 0.04$.

Froude number $\mathcal{F}$

The role of the Froude number is shown in figure 8.9 – **b**. We see that the value of $k_{\max}W$ is almost insensitive to $\mathcal{F}$ in the relevant range 0–1 (fluvial regime).

Velocity ratio u_*/u_{th}

The last parameter to study is the ratio of the shear velocity on the threshold velocity. The most unstable wavenumber is rather sensitive to this ratio, especially just above the threshold of sediment transport (Figure 8.10 – **a**). Two interesting limit are represented by $u_*/u_{\text{th}}^0 \to \infty$ and $u_*/u_{\text{th}}^0 \to 1$: in the first case we are in pure suspended load, the term u_{th}^0/u_* goes to zero together with the coefficient $\mathcal{J}_n$, the consequence is a stable dispersion relation. In the second case we are at the threshold, the coefficients $\mathcal{K}_n$ vanish and we have no longer transversal effects on sediment transport: the result is again a stable dispersion relation.

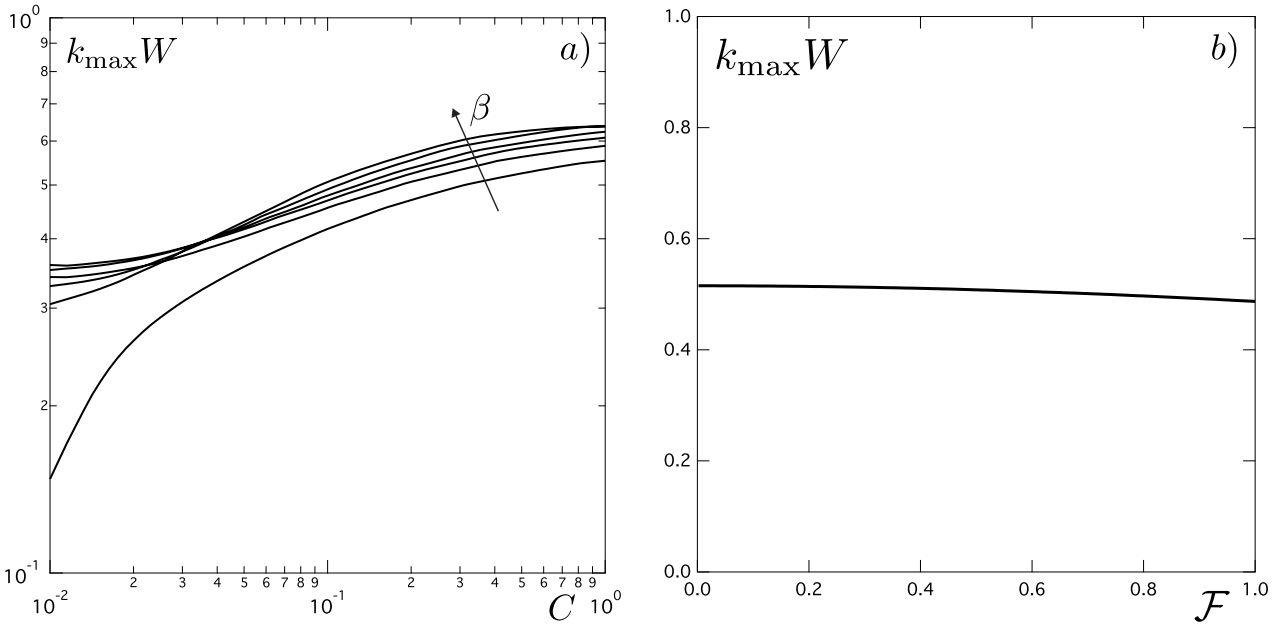


Figure 8.9: (a) Rescaled wavenumber of the most unstable mode $k_{\max}W$ as a function of the Chézy number C, for different values of β. From bottom to top, the curves have been respectively computed for $\beta = 3, 4, 5, 6, 8$ and 10. The other parameters are $u_*/u_{\rm th} = 1.6$ and $\mu = 0.45$. (b) $k_{\max}W$ vs the Froude number $\mathcal{F}$.

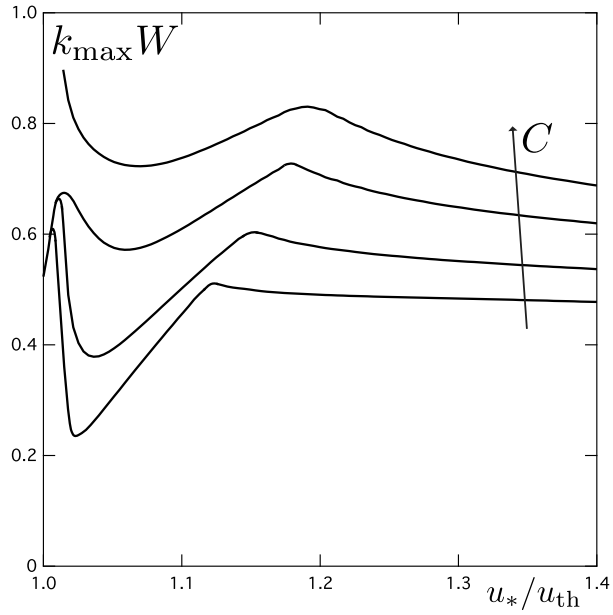


Figure 8.10: $k_{\max}W$ versus $u_*/u_{\rm th}$ for different values of Chézy number: from the bottom we have $C = 0.04$, $C = 0.06$, $C = 0.1$ and $C = 0.4$ for $\beta = 4$ and $\mu = 0.45$.

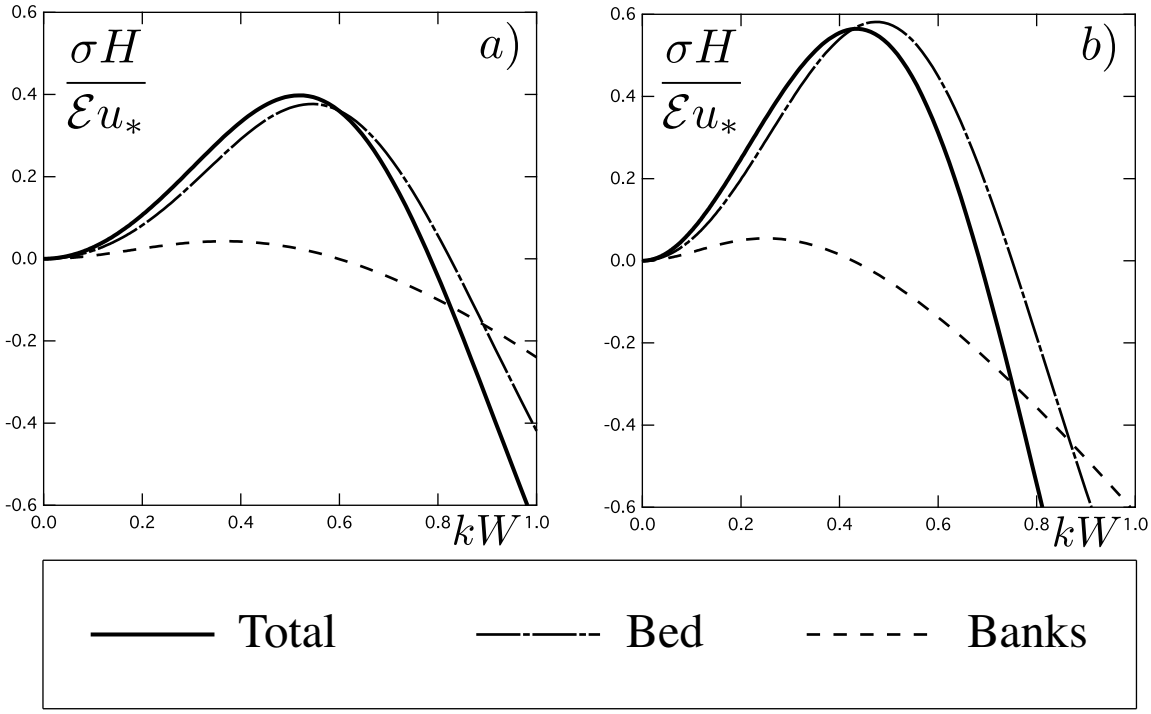


Figure 8.11: 'Bank' and 'bed' contributions to the dispersion relation. (a) Growth rate computed for the parameters corresponding to the laboratory experiments ($\mathcal{F} = 0.77$, $\beta = 4$, $C = 0.1$, $u_*/u_{\text{th}} = 1.6$ and $\mu = 0.45$). (b) Same for the parameters corresponding to the Leyre river ($\mathcal{F} = 0.29$, $\beta = 4$, $C = 0.04$, $u_*/u_{\text{th}} = 2$ and $\mu = 0.5$). σ has been computed as the sum over the first three odd modes. Graphical convention: see legend.

8.4 Instability mechanism

We now discuss the instability mechanisms responsible for the emergence of meanders.

8.4.1 Bed and banks contributions

We can first study in more details the dispersion relation (8.18) by computing separately the contributions of each term to the instability. The expression giving σ can basically be splitted into two terms: the first one results from the direct influence of the banks on hydrodynamics through the averaged velocity $\bar{U}_\Upsilon$. We consequently

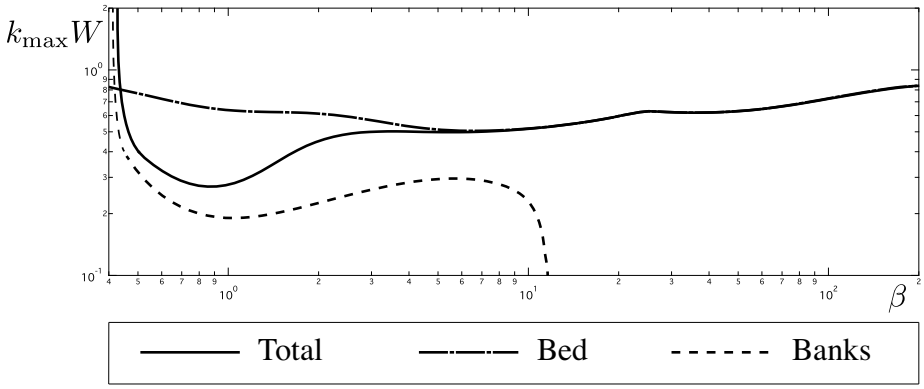


Figure 8.12: Most unstable mode of the two contributions versus the aspect ratio β for $\mathcal{F} = 0.77$, $\beta = 4$, $C = 0.1$, $u_*/u_{\text{th}} = 1.6$ and $\mu = 0.45$ (i.e. the experimental configuration). σ has been computed as the sum over the first three odd modes. Graphical convention: see legend.

define the 'bank' contribution as:

$$\sigma_{\text{banks}} = -\mathcal{E} u_* k \sum_{n=1}^{\infty} \bar{U}_{\Upsilon} \,. \tag{8.21}$$

The other one is related to the averaged velocity of the perturbed bed $\bar{U}_Z$, mixed with the bed shape Z^{eq}/Υ. We similarly define the 'bed' contribution as:

$$\sigma_{\text{bed}} = -\mathcal{E} u_* k \sum_{n=1}^{\infty} \frac{Z_n^{\text{eq}}}{\Upsilon} \bar{U}_n^Z \,. \tag{8.22}$$

Importantly, because of the bed shape factor Z_n^{eq}/Υ, the above expression is also an indirect contribution of the bank through their influence of the bed.

Figure 8.11 compares the importance of these two contributions for parameters corresponding to the laboratory experiments and to the Leyre river (see next chapter). It is clear that, in the range for which an instability is observed (positive σ) the dominant contribution comes from σ_{bed}, which controls the most unstable mode. By observing figure 8.12 we notice that the contribution σ_{banks} presents a maximum at the same wavenumber as σ for small aspect ratio ($\beta < 0.6$). An intermediate zone ($0.6 < \beta < 3$) in which the two contributions are both important and together determine the $k_{\max}W$ of instability. Finally for larger β the bed contribution is dominant and we have the same $k_{\max}W$ for the the maximum of σ_{bed} and σ: furthermore, the

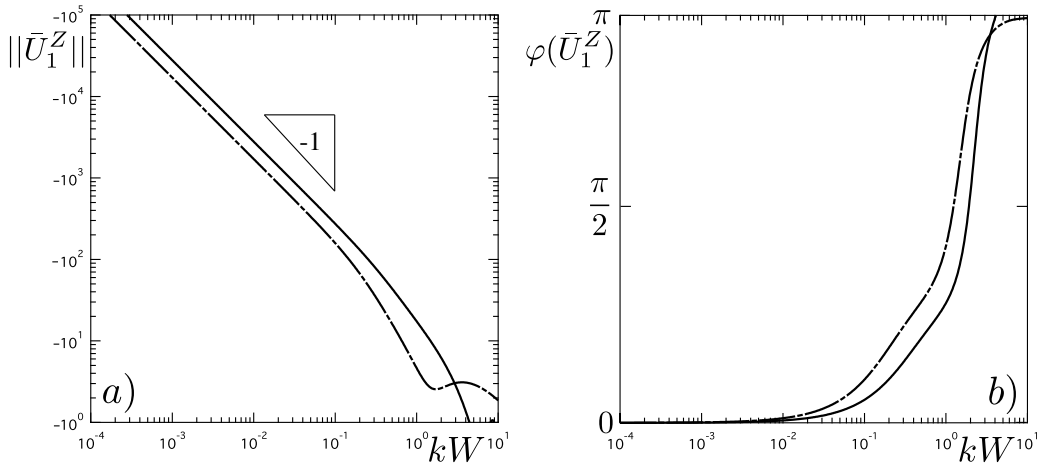


Figure 8.13: Average velocity induced by the bed as a function of kW, plotted for parameters corresponding to the laboratory experiments ($\mathcal{F} = 0.77$, $\beta = 4$, $C = 0.1$) in solid line and to the Leyre river ($\mathcal{F} = 0.29$, $\beta = 4$, $C = 0.04$) in dashed line. These data have been computed for the first mode. (a) Moduli and (b) Phases.

bank contribution can be negative at the maximum growth rate for aspect ratios of $\beta \gtrsim 12$.

8.4.2 Analysis of the bed contribution

We now provide more details on the properties of the bed contribution (Eq. 8.22). One of the factors is the averaged velocity $\bar{U}_n^Z$ induced by the bed perturbation. We display the modulus and the phase of this quantity taken at $n = 1$ in figure 8.13. We can see that, in the relevant range $0 \leq kW \leq 1$, $\bar{U}_1^Z$ scales like the inverse of the wavenumber: $\bar{U}_1^Z \sim -1/k$. This behaviour comes from the fact that $\bar{U}_n^Z$ is dominated by the third integral term in Eq. (3.111). This integral is in practice independent of its upper bound η_H (which can be sent to infinity), because in the outer layer the velocity correction decreases exponentially, as for a perfect fluid. This scaling law can be also deduced from the idea that the expression for the averaged velocity in the base state $\bar{u}^2 = gH \sin\theta/C$ (Eq. 1.1) is also valid for the perturbed flow of depth $H - Z$. Then, the first order correction to the base averaged velocity is $-u_* \frac{1}{2\sqrt{C}} \frac{Z}{H}$, leading, in the $|c_n\rangle$ representation, to the coefficients

$$\bar{U}_n^Z = -\frac{1}{2\eta_H \sqrt{C}} \tag{8.23}$$

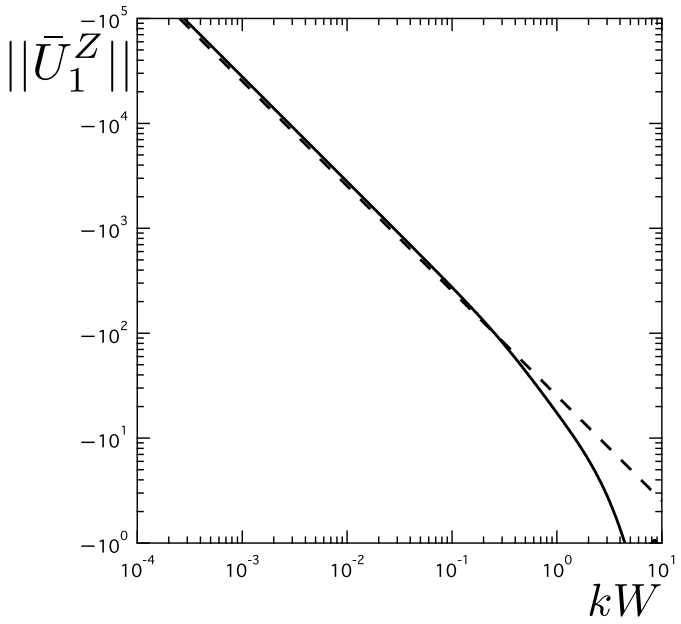


Figure 8.14: RANS (solid) and analytical (dashed) velocities associated with a bed perturbation ($\mathcal{F} = 0.77$, $\beta = 4$, $C = 0.1$).

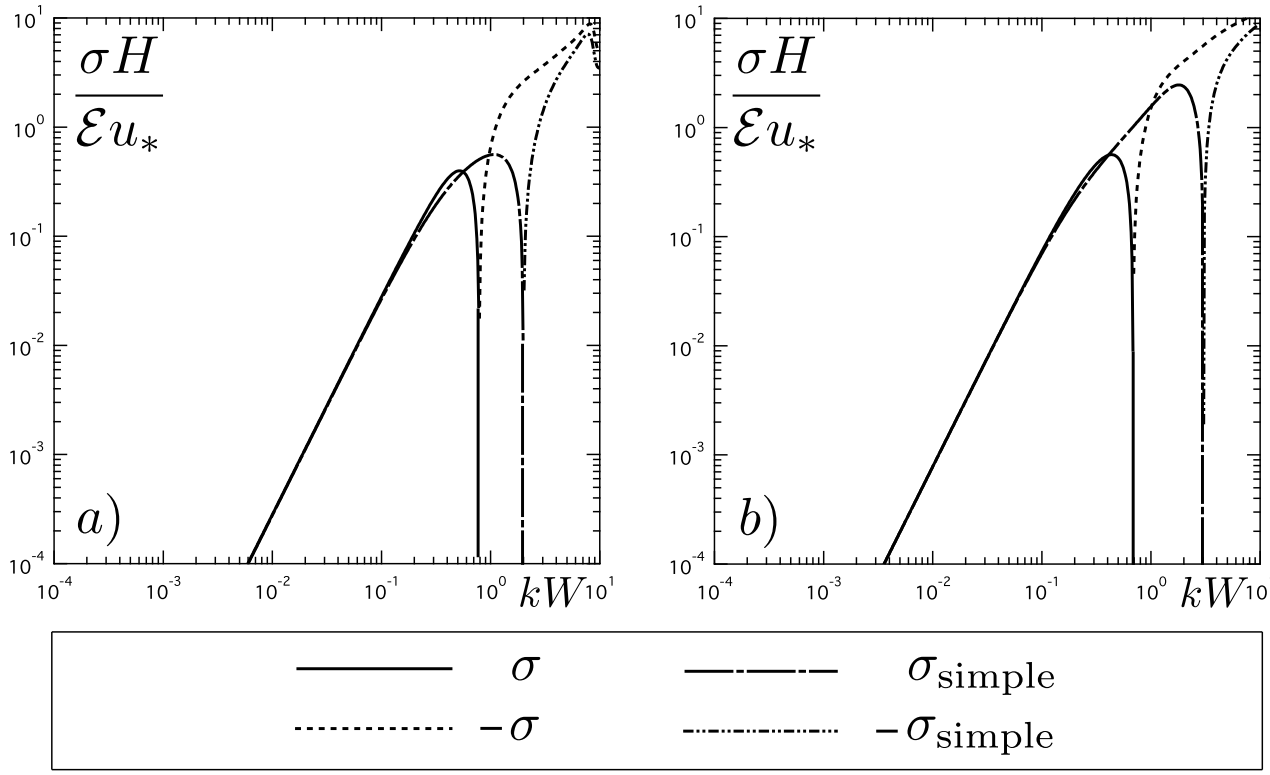


Figure 8.15: Growth rate computed with the complete expression of Z_n^{eq}/Υ (Eq. 8.13) and with the simplified formula (Eq. 8.25). (a) Computation with the parameters corresponding to the laboratory experiments ($\mathcal{F} = 0.77$, $\beta = 4$, $C = 0.1$, $u_*/u_{\text{th}} = 1.6$ and $\mu = 0.45$) and (b) corresponding to the Leyre river ($\mathcal{F} = 0.29$, $\beta = 4$, $C = 0.04$, $u_*/u_{\text{th}} = 2$ and $\mu = 0.5$). σ has been computed as a sum over the first three odd modes.

The above expression is in quantitative agreement with the computation of $\bar{U}_n^Z$ by the three dimensional RANS model (see figure 8.14). We also verified that this scaling is kept for the successive modes $\bar{U}_3^Z$, $\bar{U}_5^Z$, ... Interestingly, this $1/k$-behaviour is balanced by the overall factor k in the expression (8.22). As a result, most of the behavior of σ_{bed} effectively comes from the ratio Z_n^{eq}/Υ.

One can also make simplifications to have a better qualitative understanding of the function Z_n^{eq} – see Eq. (8.13) to recall its expression. We find that its behaviour is dominated by the transversal basal stress $\tau_{1,b}^{yz}$ generated by banks perturbation, namely D_y^n, so that we can write a simple approximation:

$$\left.\frac{Z_n^{\text{eq}}}{\Upsilon}\right|_{\text{simple}} = \frac{\mathcal{K}_n\, D_y^n}{\mathcal{J}_n} \tag{8.24}$$

where $\mathcal{K}_n$ and $\mathcal{J}_n$ are respectively explicated in equations (8.14) and (8.15). In figure 8.15, we compare the growth rate computed with the complete expression of Z_n^{eq}/Υ and with this simplified formula

$$\sigma_{\text{simple}} = -\mathcal{E} u_* k \sum_{n=1}^{\infty} \left[\bar{U}_n^{\Upsilon} + \frac{\mathcal{K}_n\, D_y^n}{\mathcal{J}_n} \cdot \bar{U}_n^Z \right] . \tag{8.25}$$

We see that the curves remain qualitatively the same, despite a shift of the most unstable mode towards larger wavenumbers.

8.4.3 The origin of the instability

Figure 8.16 illustrates the direct effect of the modulated banks on the flow velocity. The displayed data have been computed for a value of kW close to the maximum of instability. We clearly see a large transverse secondary vortex with centrifugal velocities close to the surface and centripetal velocities close to the bottom. The velocity correction in the longitudinal flow direction is, for these parameters, negative at the outside channel bend.

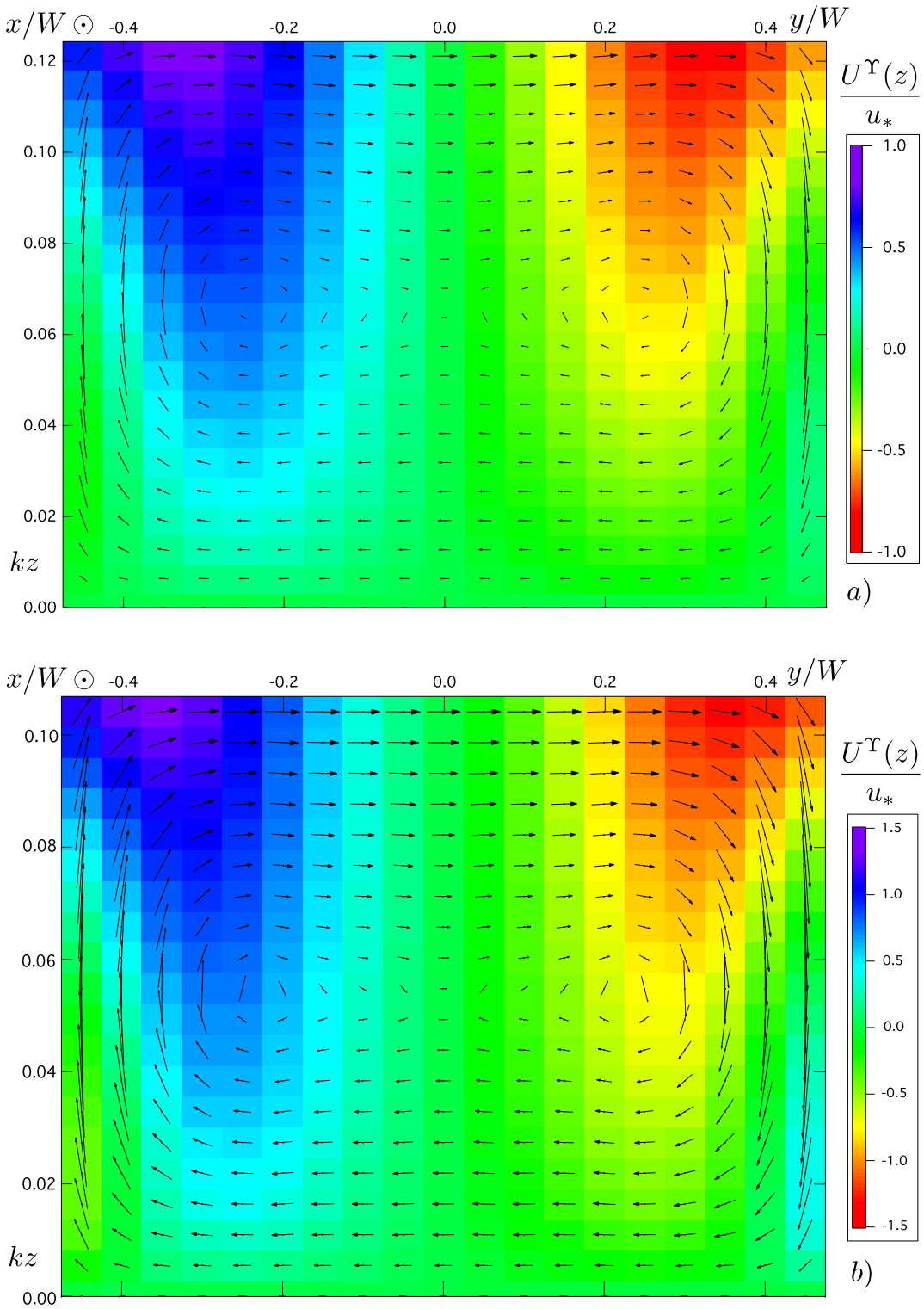


Figure 8.16: Velocity field in response to the modulated banks (flat bed) in the (y, z) plane at the channel bend (see schematics). Color scale: out of plane x-component. Arrows: in plane velocity. The main flow comes out of the plane, i.e. the left (outside) bank is on the right and vice-versa, see schematics. Panel (a): computation $kW = 0.51$ and with parameters corresponding to the experimental set-up ($\mathcal{F} = 0.77$, $\beta = 4$, $C = 0.1$). Panel (b): computation for $kW = 0.51$ and with parameters corresponding to the Leyre river ($\mathcal{F} = 0.29$, $\beta = 4$, $C = 0.04$). Modes up to $n = 11$ have been summed up for this picture.

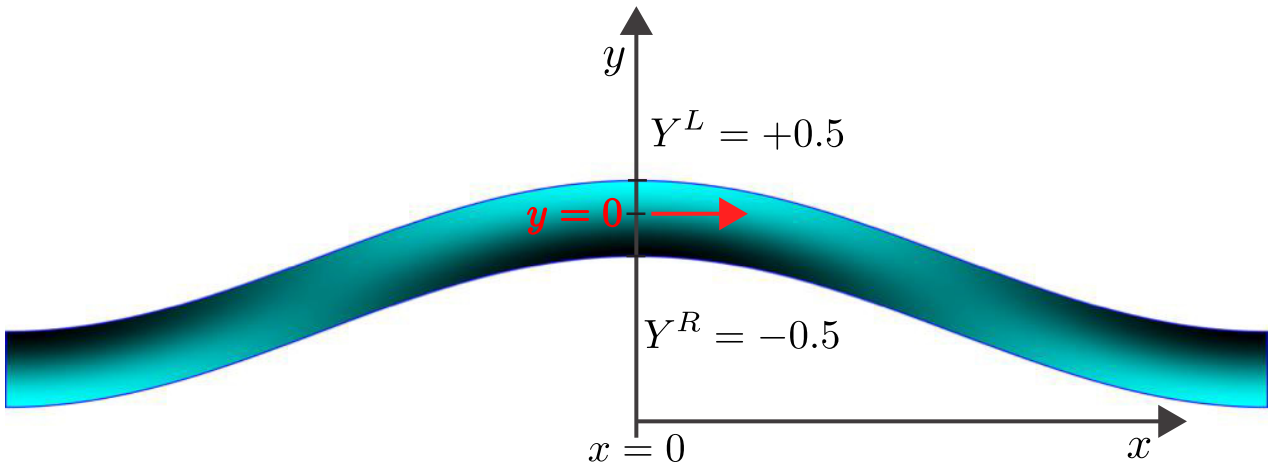


Figure 8.17: Schematic of meander bend taken for figure 8.16. Right bank has negative y and left bank positive. The red arrow gives the direction of the flow.

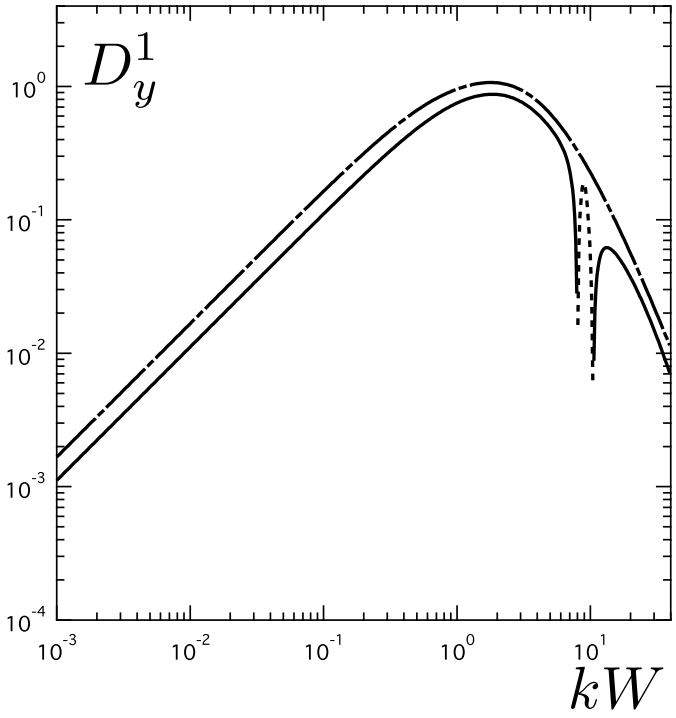


Figure 8.18: Stress coefficient D_y^1 computed from RANS equations, with the parameters corresponding to the laboratory experiments (solid line, $\mathcal{F} = 0.77$, $\beta = 4$, $C = 0.1$) and corresponding to the Leyre river (dashed line, $\mathcal{F} = 0.29$, $\beta = 4$, $C = 0.04$). Negative values in this log-log representation are displayed following graphical convention in chapters 3 and 4.

As we have defined it, the coefficient D_y quantifies the amplitude of the basal shear stress at the channel bend in response to modulated banks – whereas C_y is that at the infection point between two successive bends. Its value for the first mode $n = 1$ is displayed in figure 8.18. On can see that it is positive in all of the relevant range of kW. In particular, it behaves as $D_y^1 \sim kH$ at small wavenumbers and $D_y^1 \sim 1/kW$ at large wavenumbers. Positive values of D_y precisely correspond to a centripetal transverse shear stress, in accordance with the velocity correction.

Following the analysis of the previous paragraphs, the origin of the instability is then pretty clear. The direct effect of the modulated banks on the average velocity is negligible, and can even be stabilizing, i.e. producing a reduced velocity at the outside of the channel bend. The direct effect of the modulated banks on the bed is to induce some transverse centripetal component of the sediment flux, which creates higher/deeper regions at the inside/outside of the channel bend. The effect of that bank-induced modulated bed on the flow velocity is to generate an excess average velocity in deeper regions, i.e. at the outside of the channel bend. This excess velocity generates further erosion of the outside bank, thus leading to an unstable dynamics.

The qualitative explanation for the selection of the most unstable mode $k_{\max}W$ is then related to the existence of a maximum in the curve $D_y(kW)$. This wavenumber corresponding to this maximum can be understood as a crossover value which separates two asymptotic regimes. The river flow is vertically limited by the length scale H, transversally by W and longitudinally by λ. At small wavenumbers, the flow is limited by the smallest of the three dimensions: H. The transversal velocity at the river bend consequently depends on both the curvature $1/R \sim k$ and the water depth H as $v \sim u_* kH/C$. The basal stress is defined as $\tau_{1,b}^{yz} \sim Cu_* v$ and, by with its definition (8.7), this leads to the scaling $D_y \sim kH$. On the contrary, for large wavenumber, the dominating (i.e. the smallest) length scale is λ. Because of inertial effects, the flow disturbance penetrates over a length scale comparable to the wavelength. Two vortices localized close to river banks of relative size λ/W form and generate a traversal basal stress $\tau_{1,b}^{yz} \sim Cu_* v\lambda/W \sim u_*^2/kW$ at the bed. The traversal velocity at the river bend is $v \sim u_* k\lambda/C \sim u_*/C$, which, combined to this basal stress leads to $D_y \sim 1/kW$. The crossover value is obtained when these two scaling are equal, i.e. for $kW \sim \sqrt{W/H} = \sqrt{\beta}$.

8.4.4 The Saint-Venant predictions

It is interesting to compare the prediction of the theory we built with those obtained when hydrodynamics is computed with Saint-Venant shallow water (SVSW) equa-

tions. More precisely, we keep the overall structure of the modeling identical, but take the results on basal coefficients and velocities either from RANS or from SVSW equations, as detailed in chapters 3 and 4.

The result of such a comparison is shown in figure 8.19. We clearly see that SVSW equations are not qualitatively able to reproduce the instability (σ is always negative). The reason can be attributed to the inability of the depth-averaged model to describe secondary flow induced by the banks on hydrodynamics. In particular, SVSW equations predict a bank-induced basal stress coefficient D_y with the wrong sign, as shown in figure 8.20.

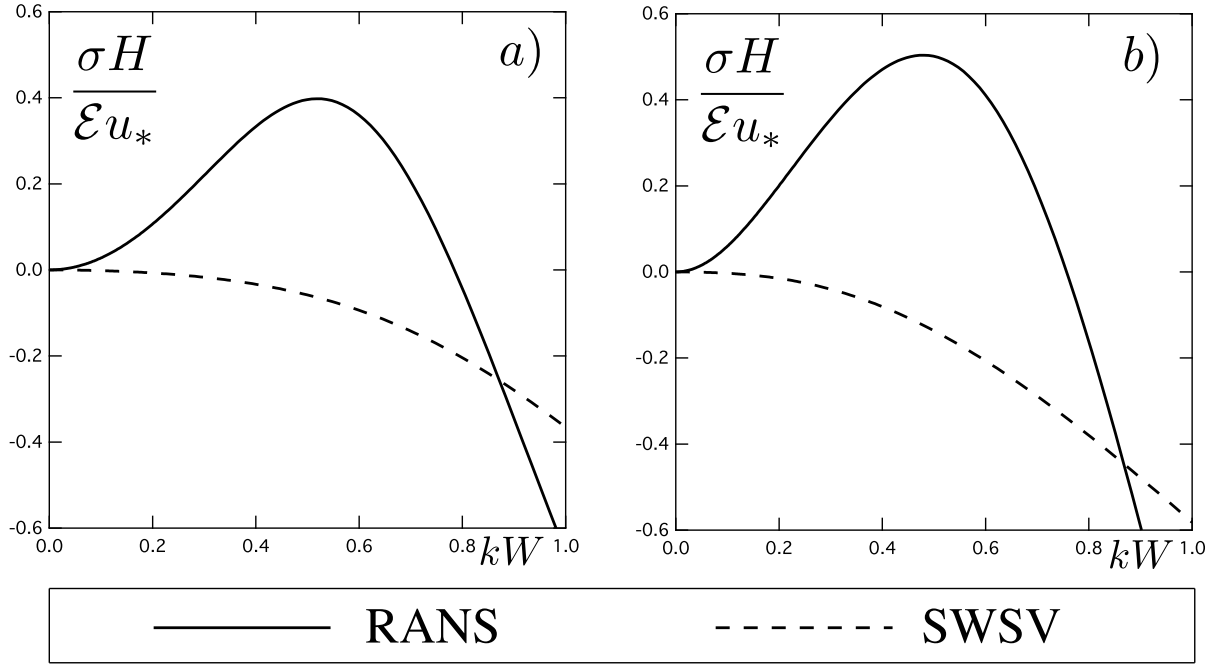


Figure 8.19: Dispersion relation computed with RANS and SVSW equations. (a) Computation with $\mathcal{F} = 0.77$, $\beta = 4$, $C = 0.1$, $u_*/u_{\rm th} = 1.6$ and $\mu = 0.45$ and (b) $\mathcal{F} = 0.29$, $\beta = 4$, $C = 0.04$, $u_*/u_{\rm th} = 2$ and $\mu = 0.5$. σ has been computed as a sum over the first three odd modes.

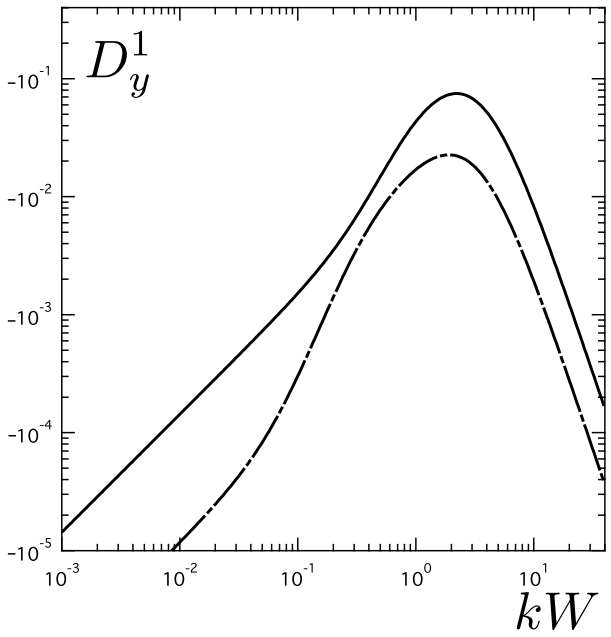


Figure 8.20: Coefficient D_y^1 predicted by SVSW equations. Computation for parameters corresponding to the laboratory experiments in solid line ($\mathcal{F} = 0.77$, $\beta = 4$, $C = 0.1$) and to the Leyre river in dashed line ($\mathcal{F} = 0.29$, $\beta = 4$, $C = 0.04$). We invite the reader to be careful and notice the negative axis.

8.4.5 The resonance-theory predictions

Finally, we compare our results to the predictions of the resonance theory. This theory (Blondeaux & Seminara 1985) has been developed from the idea that the instability of alternate bars can be coupled to an instability of the banks under a particular condition of *resonance*. This condition corresponds to value of the aspect ratio β_c for which the growth rate and the migration velocity of the bars vanish. In that case, the growth rate of the banks can be very large. This is effectively what we recover in our framework, see figure 8.8. However, neither our experiment set-up, nor the field conditions of the Leyre river correspond to this situation. For instance, β is typically smaller than β_c. In fact, a condition to get this resonance is to be in a situation where alternate bars are effectively unstable. In figure 8.21 we show the dispersion relation corresponding to bars prediction for the parameters of our laboratory experiments and the Leyre river: in both the cases the growth rate is negative.

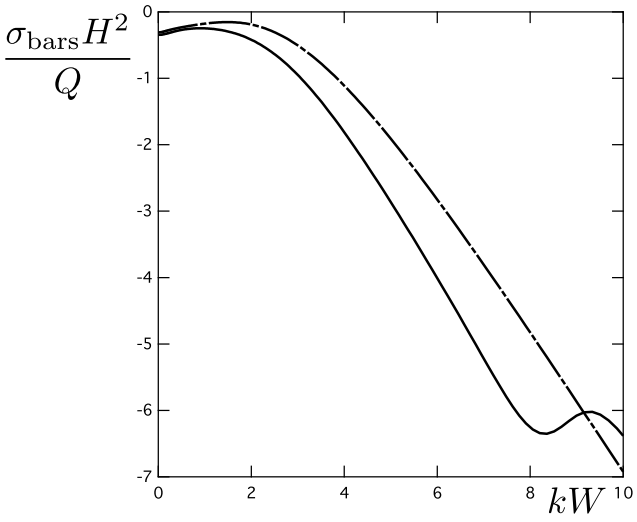


Figure 8.21: Dispersion relation of alternate bars. Solid line: parameters of the laboratory experiments ($\mathcal{F} = 0.77$, $\beta = 4$, $C = 0.1$, $u_*/u_{\text{th}} = 1.6$ and $\mu = 0.45$). Dashed line: parameters of the river Leyre ($\mathcal{F} = 0.29$, $\beta = 4$, $C = 0.04$, $u_*/u_{\text{th}} = 2$ and $\mu = 0.5$).

Chapter 9

Meanders in the lab

In the previous chapter, we have seen how we have gathered hydrodynamics and sediment transport ingredients to perform the linear stability analysis of a rectangular straight channel, taking into account both bed and bank perturbations. The main result was the computation of the dispersion relation, which quantifies the growth rate σ of a perturbation of wavenumber k. In particular, we could identify a most unstable mode, which is expected to emerge during the meander instability. In this chapter, we would like to present experiments where we have measured this dispersion relation for a meandering channel.

9.1 Introduction

Reproducing and managing the river dynamics at laboratory scale raises a great importance since one can easily extrapolate quantitative data and compare them to theoretical predictions. Moreover, it has been demonstrated (Malverti *et al.* 2008) that the evolution of turbulent and laminar flows in a channel are governed by identical dimensionless equations of natural rivers and therefore they follow the same dynamics. The bibliography on the subject shows that meanders are very difficult to produce in the laboratory. In most of the experiments, channels develop bars and braids (e.g. Federici & Paola 2003). The first report of meanders in a flume is that of Smith (1998), using for the bed and the banks various cohesive mixtures (e.g. rock flour and kaolinite). Another experiment is that of Braudrik *et al.* (2009), were the undulating channel has been stabilized by vegetation (Tal & Paola 2009). Both f these works remain very qualitative and do not provide a physical explanation of the meander instability. In this chapter we describe how we are able to generate, in a controlled and reproducible way, meanders of given wavelength λ, which keep their

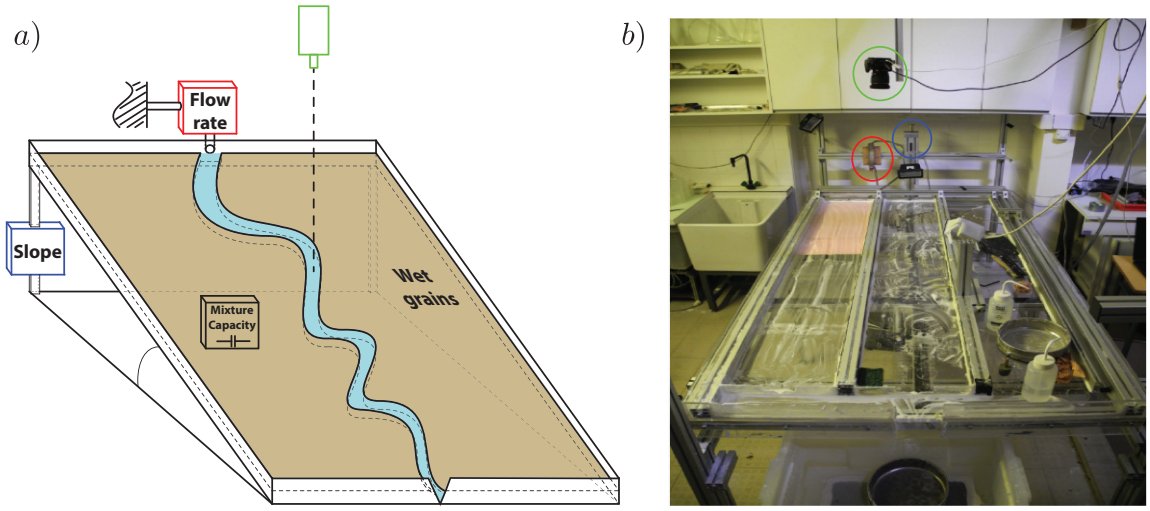


Figure 9.1: a) Scheme of experimental setup. The control and measurement devices are displayed in different colors. b) Photo of the flume. The whole flume length, width and depth dimensions are $2 \times 1 \times 0.05$ in meters. Most of the experiments have actually been performed in the left side (width 0.3 m).

sinusoidal shape for some time, while increasing their amplitude and propagating downstream.

We first describe all details of the experimental setup, the protocol and the the measurement technique. We then present the results, and a dispersion relation in particular. The comparison of these experimental data with the theory is presented at the end of this chapter.

9.2 Experimental setup

Our experimental goal is to reproduce the meandering instability at the laboratory scale. Of course, it is not possible to keep constant all dimensionless numbers of a real river in the downscaling process. A first important point is to work at relatively small slopes θ. We have an inclined plane, made of Plexiglas, whose slope is adjusted through a mechanical gear (blue box in Fig. 9.1). Its value is measured with an electronic inclinometer, with a precision of $0.05°$. On this plane, a layer of humid grains is deposited, and over which the water can flow.

The grains we have used are spheres made of polystyrene, whose density is $\rho_p = 1010$ kg/m^3. We have used mono-dispersed grains, of different diameters: 20, 40,

80, and 140 μm, and also a mixture of grains with diameters of 140 and 250 μm. There are a main reason for using such light grains: as we wish to observe sediment transport at small slopes, and for a water depth on the order of few millimeters, the transport shear stress threshold must be low. This condition is then favored with polystyrene beads. In order to ensure reproducibility of the preparation and the cohesion of the granular bed, we indirectly control the degree of humidity and its uniformity through the measure of the electrical capacity C and resistance R associated to the resistivity ρ_E and the relative permeability ε_r of the mixture. The typical precision of such measures is 0.01 nF and 10 Ω.

The injection of the water on the plane is regulated by a damper (red in Fig. 9.1) connected to the water pipe of the laboratory building. The damper measures flow rates in the range from 1 to 10 ℓ/h, with a error on the measurements of 0.25 ℓ/h. For this water at ambient temperature derived from the plumbing system of the laboratory, the kinematic viscosity is $\nu = 10^{-6}$ m$^2/s$ and the density is $\rho = 10^3$ kg/m^3.

We take pictures of the plane with a reflex camera (green in Fig. 9.1), from which we measure the channel characteristics and follow their evolution with time. We have also used two video cameras to measure the average and instant velocities of the flow. One of them was a fast camera able to save up to 3000 images per second. All these devices are placed above the system, at a vertical distance of around 1 m with respect of the plane. A laptop computer provides the backup space of recorded data and it was also used as a triggering device for the cameras. In order to get well contrasted images and to be able to measure the thickness of the flow, we made use a backlighting system: this was composed of some thin lightning papers, that were sticked on the bottom of the plexiglass plane (see rose papers below the plexiglass in the figure) with the light orientation towards the cameras. At the down end of the plane, the mixture of water and grains directly falls into a filter that collects the humid grains and leave the water flow into the drain system.

9.2.1 Technical aspects and calibration

Reflex camera

The typical focal of the camera was in the range 24–35 mm, which produced negligible image distortion. The aperture was quite closed, in the range $f/5.6$–$f/7.1$, in order to capture many details. The film-equivalent ISO number of the digital sensor speed was kept at 300 in order to avoid noise and, as a consequence, the shutter time was fixed at 1/5–1/6 s. Pictures were shot every 2–5 s thanks to the computer triggering and recordered under JPEG and NEF (Nikon RAW) formats.

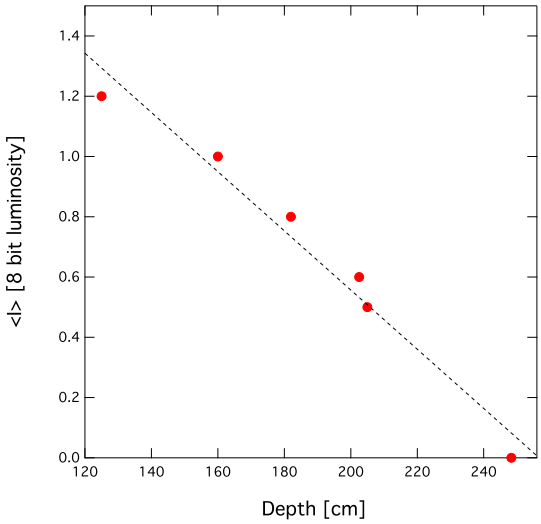


Figure 9.2: Calibration curve to relate thickness of the bed to the greyscale level on the picture taken by the camera.

High frequency video camera

The fast camera was set to record 500 frame per second. The triggering was provided from the camera software installed on the computer. The exposition time was of 1/500 s but it could be set to a quicker time while the device worked at 12 bit of depth resolution.

Back lightning

The back lighting papers were sticked on the bottom of the plexiglass plane. Light transmission through the the grains can be used as a measure of the bed thickness. We have computed a calibration curve to relate grain layer depth and luminosity. For this purpose, different homogeneous water and grains layers of different thickness have been prepared. For each of them, a photo was taken with the reflex camera. The equation we used for the conversion from greyscale GS level to the bed thickness D is:

$$D\,(\mathrm{cm}) = -9.6\,10^{-3} \cdot GS \,+\, 2.5\,. \tag{9.1}$$

These numbers correspond to a given setting of the camera that was not changed afterwards. The absorption by the water alone was found to be negligible.

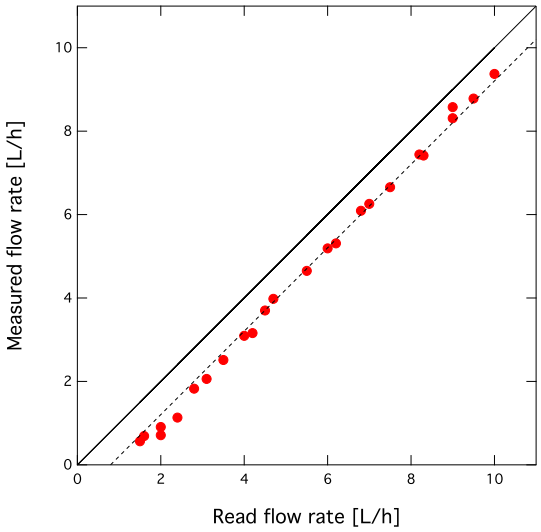


Figure 9.3: Damper calibration curve.

Water damper

The flow rate was measured at the outlet of the plane (Q_m), and compared to the value read on the screen of the damper (Q_r). The comparison between the two is displayed in Fig 9.3, showing a systematic shift:

$$Q_m = Q_r - 0.8 \quad \text{L/h}. \tag{9.2}$$

The precision of the instrument given by the constructor is around 0.5 L/h. This value is on the same order as the shift, though a bit smaller. In fact, we expect the presence of air bubbles trapped inside the damper to affect the measurement and the actual precision is more likely to be around 1 L/h.

9.2.2 Experimental procedure

Our experimental goal is to observe, study and describe the meandering instability of a channelized flow. We are especially interested in the early linear response of the channel to a given initial, small, perturbation. This initial stage was a sinusoidal channel of controlled amplitude Υ and wavelength λ. Following the time evolution of the channel, we could measure the growth rate of the perturbation as well as its migration velocity. Varying λ we have then access to the dispersion relation of the system.



Figure 9.4: Leveling of the granular bed



Figure 9.5: Sinusoidal guide for the future channel incision. The ruler gives an idea of the typical amplitude and wavelength we have worked with. Here $\Upsilon = 0.8$ cm and $\lambda = 11$ cm respectively.



Figure 9.6: Incision of the initial channel



Figure 9.7: Cleaning the borderlines from scratch and irregularities.



Figure 9.8: a) Measure of capacity and resistance of the granular paste. b) Wetting of the bed in order to obtain the correct proportion between water and grains.

The preparation of the experiment is divided into different steps that have to be followed accurately in order to obtain reproducible results.

1. The grains are washed with a dish cleaner liquid (i.e. with surfactants) and the foam is removed. The presence of foam can in fact disturb the measurements, as it hides the boundaries of the channel and interacts with the flow.

2. The mixture composed of water and grains is then filtered and dried until the correct proportion between water and grains (a verification is provided later), approximately 1 volume part of water for 6 volume parts of grains. The total volume of the paste used in our experiments is typically around 1 dm^3. This step is crucial for the reproducibility and the run of the experiment since the humidity plays an important role in the stability of the banks. If the water content of the paste is too small or too large, a flow rate through the banks makes them melt. This phenomenon is equivalent to what happens in nature where rivers develops at the elevation to the phreatic aquifer.

3. The paste so obtained is spread on the plane homogeneously and the chosen thickness is reach by slowly scrubbing a thin layer of paste after an other (see Fig 9.4).

4. We choose of the amplitude and the wavelength of initial sinusoidal channel, and make a metallic guide that covers a whole sinus wavelength.

5. With the help of a ruler placed in the middle of the plane, we use the sinusoidal guide to mark the path of the future channel (see Fig 9.5). After a certain number of undulations (at least four), the path is kept straight until the outlet of the plane.

6. This initial path is enlarged to the definitive width and depth of the channel by means of a simple metallic cylinder. This process results in a channel with approximate width and depth of $W = 1$ cm and $D = 0.5$ cm respectively (see Fig 9.6).

7. The borderlines of banks are cleaned from scratch and irregularities resulting from the carving process (see Fig 9.7).

8. We measure the resistance and the capacity of the mixture with a tester in AC regime at 120 Hz in different places. Two metallic plates of size 4.5×13 cm^2 approximately are inserted into the paste at a distance of $\simeq 1$ cm and we check that we measure each time a capacity that lies in the range of $80 - 200$ nF and a resistance around $1.4 - 2$ kΩ. If values outside these ranges are obtained, the mixture is wetted or dried until a reproducible state is reached (see Fig 9.8).

9. A photo of the initial configuration with the rulers is taken, in order to set the reference system.

10. We start the water flow, and we regulate the flow rate to the desired value with the damper. Refined value of the flow rates (liquid + solid) are later measured: the mixture of water and sediments is collected at the outlet of the plane.

11. During the initial flowing of the water inside the channel, we check that no foam form. In the case some foam appears, we remove it delicately with a spoon-like tool.

12. We turn on the backlighting system at the maximum power.

13. We turn off the general lighting of the room and start to take photos every 2–5 s.

14. If we wish to measure the surface velocity of the flow, we mount the fast camera. We spread some small particles of carbon on the water surface in the upstream part of the system, and start recording for a few seconds.

15. The experiment is stopped when non-linearities or other instabilities start to affect the evolution of the channel.

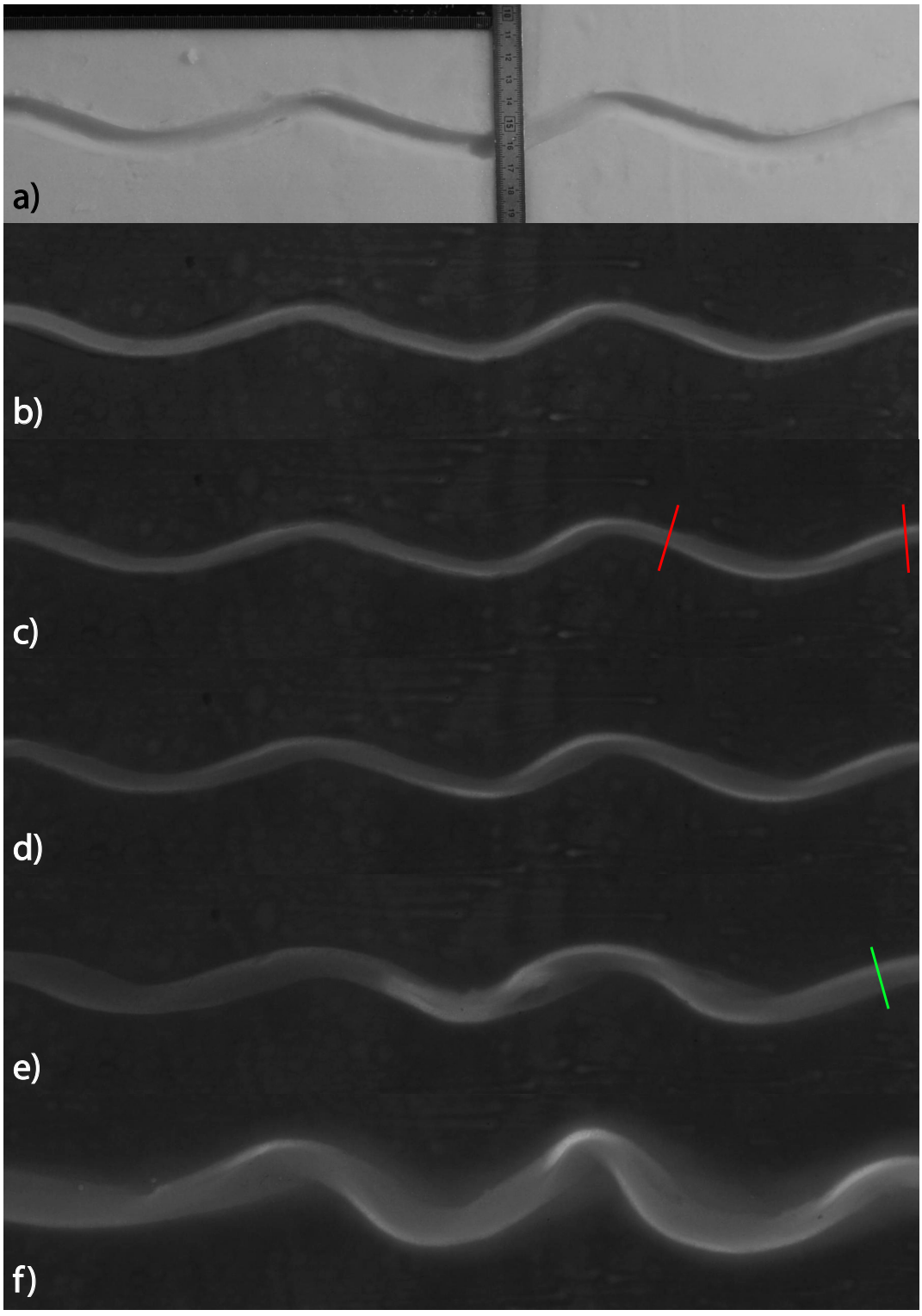


Figure 9.9: Channel evolution. Flow is from right to left. (a) Initial (empty) channel at $t = 0$ s. Channel with flowing water at $t = 60$ s (b), $t = 85$ s (c) and $t = 130$ s (d) in the linear regime. Observation of the first non-linearities at $t = 215$ s (e), and stronger ones at $t = 400$ s (f). For this experiment, the flow rate was $Q \simeq 5.5$ ℓ/h, the slope was $\theta \simeq 0.7°$, the grain diameter was $d = 140$ μm, and the initial wavelength and amplitude of channel were: $\lambda = 14$ cm and $\Upsilon = 0.8$ cm. Red and green lines: location of the cross profiles shown in Fig. 9.13 and 9.14.

9.3 Experimental data

The photos and videos of the experiment allow us to follow the time evolution of the channel. As shown in Fig 9.9, one can distinguish a first regime where the amplitude of the meanders grows, while the sinusoidal shape, and the wavelength in particular, is maintained. After some time, non-linearities appears, which affect the sinusoidal shape of the channel. We are mainly interested in the first regime, and willing to measure the growth rate and propagation velocity of the meanders. We have also recorded the transverse geometry of the channel, as well as hydrodynamical properties of the flow in the channel.

9.3.1 Measurement of the meander evolution

We follow the channel shape and evolution by image analysis. As illustrated in Fig. 9.10, we can fit a sinus function to the left and right banks of the channel. In the linear regime we are mostly interested in, we fix the wavelength at its initial imposed value and record the meander amplitude Υ *versus* time. We also measure the phase of the sinus at instant t, with respect to the initial profile at $t = 0$, which corresponds to the propagation of the meander. When we enter the non-linear regime, the fit starts to be of poor quality and this analysis is stopped – nonetheless we see a change of the wavelength, but the whole channel shape is not sinusoidal any more.

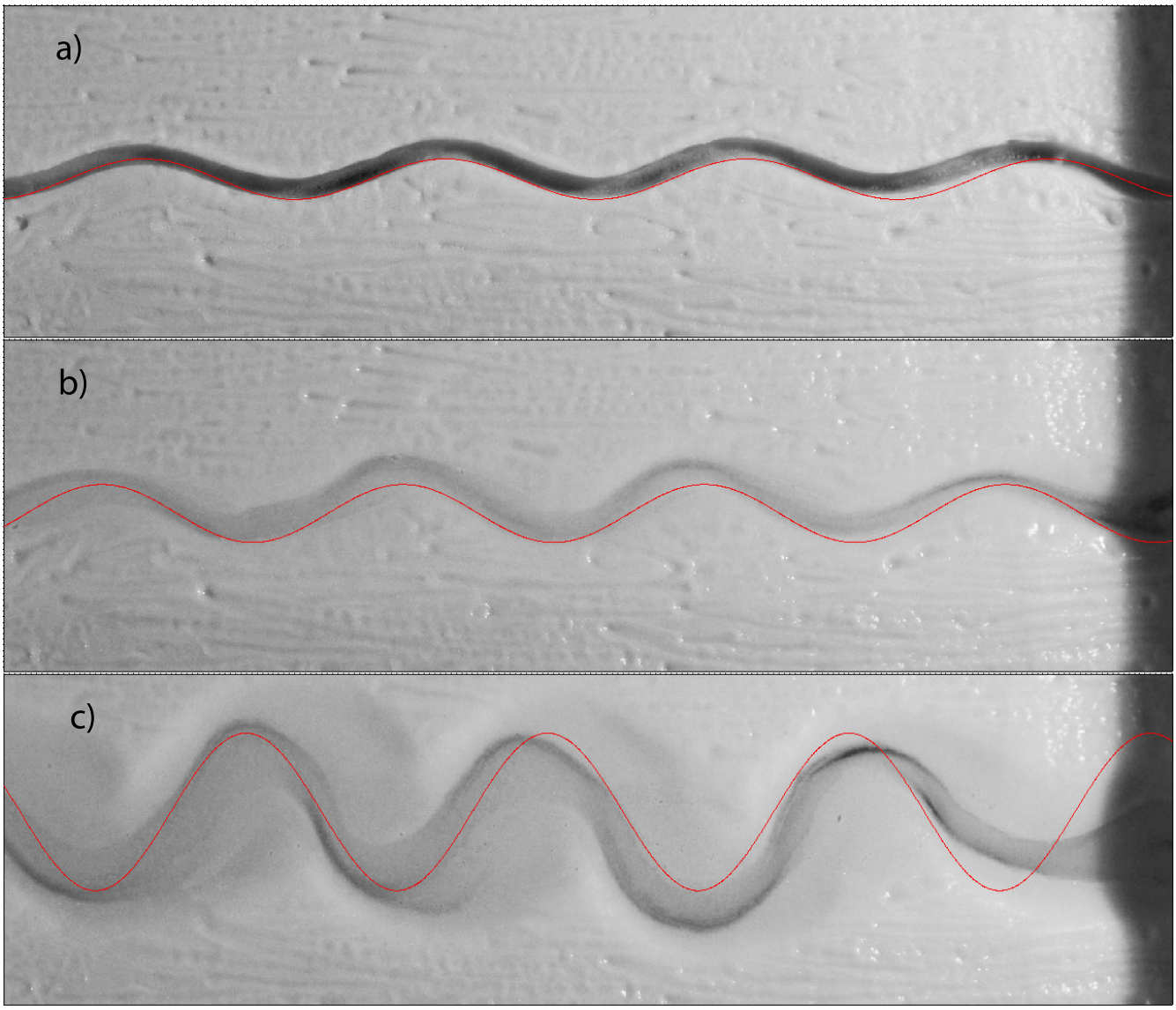


Figure 9.10: Superposition of experimental images and fitted sinus curves: (a) Channel at $t = 0$ s. (b) Channel at $t = 175$ s. (c) Channel at $t = 540$ s. Parameters for this experiment: grains diameter $d = 140$ μm, flow rate $Q \simeq 5.5$ ℓ/h, slope $\theta \simeq 0.7°$. Initial wavelength and amplitude: $\lambda = 13$ cm, $\Upsilon = 0.8$ cm. The meander amplitude grows in time, whereas its wavelength stays approximately constants. The meanders also propagates downwards. Flow is from right to left.

Meanders amplitude and position

As discussed in the previous theoretical chapter, the amplitude is expected to vary exponentially with time in the linear regime:

$$\Upsilon(t) = \Upsilon(0)\, e^{\sigma t}\,, \tag{9.3}$$

where σ is the growth rate. In Fig 9.11 – **a** is displayed an example of the measure of $\Upsilon(t)$. We can see that the exponential behavior is verified over approximatively the first 200 s and after one enters in the non-linear regime. The fit of these data with Eq. 9.3 gives a direct measure of the growth rate, which is a function of the wavelength, or the wavenumber k. As a matter of fact, for some values of k, σ is positive, which indicates that the meanders develop, whereas $\sigma < 0$ means that the channel gets straighter with time – the meanders disappear (Fig. 9.12).

One can similarly determinate the angular and migration velocities of meanders, respectively $\omega(k)$ and $c(k)$. We measure the phase shift φ of the sinusoidal channel with respect to its initial position *versus* time. In the linear regime, we expect this shift to vary linearly with t:

$$\varphi(t) \sim \omega t = ckt. \tag{9.4}$$

In Figs. 9.11 and 9.12, we see data corresponding to unstable and stable meanders. They both have well defined positive (downwind) velocities.

9.3.2 Geometry of the channel

Thanks to the back lightning system we are able to record the bathymetry of the channel (see calibration curve in Fig. 9.2) and understand how it develops with time. A cross-section of the channel at two different locations is shown in Fig. 9.13: panel **a** corresponds to a profile derived at the inflection point of the meanders, the shape is symmetric with respect the left and right banks. By contrast, panel **b** corresponds to the meander bend and shows an asymmetric profile of the bed typical of meandering channel. As shown below, the bank and bed modulations are *not in phase*.

In figure 9.14 we show the bed elevation at the channel bend again, but at time $t = 215$ s (green line in figure 9.9). We see an increase of the channel width from $W \simeq 1$ cm to $W \simeq 1.5$ cm. The corresponding average flow depth changes from $H \simeq 0.3$ cm to $H \simeq 0.15$ cm. The aspect ratio then varies from $\beta \simeq 3$ to $\beta \simeq 10$. These are typical ranges during the linear regime of the instability (see Fig. 9.9).

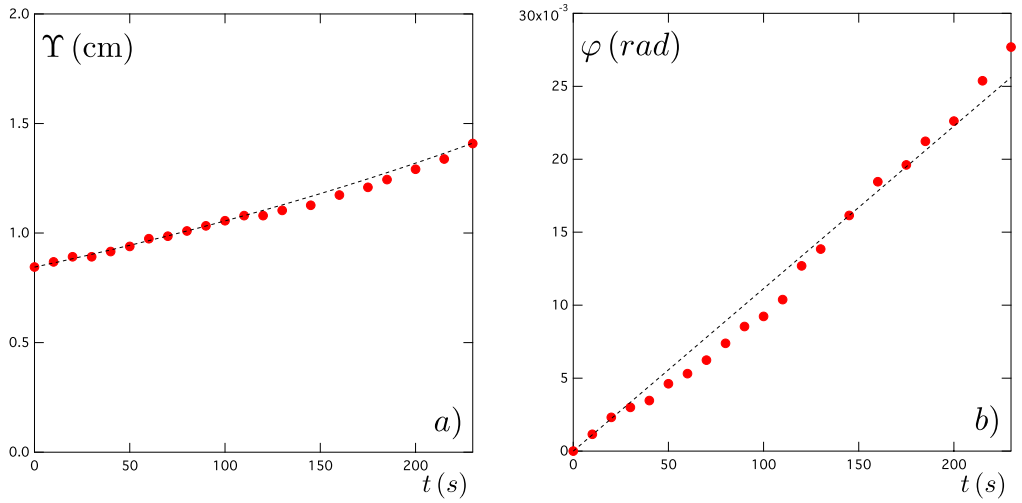


Figure 9.11: Time evolution of the amplitude and phase of an unstable meandering channel. The initial sinusoidal channel has been prepared with $\lambda = 13$ cm, $\Upsilon = 0.8$ cm. The other experimental parameters are: grain diameter $d = 140$ μm, slope $\theta = 0.7°$, flow rate $Q = 5.4$ ℓ/h. (a) Amplitude Υ *versus* time. Dotted line: exponential fit (Eq. 9.3), leading to $\sigma = 0.0022$ s^{-1}. (b) Phase shift φ of the sinusoidal channel with respect to its initial position *versus* time. Dotted line: linear fit (Eq. 9.4), with $k = 2\pi/\lambda = 0.48$ cm^{-1}, leading to $c = 0.1$ cm/s.

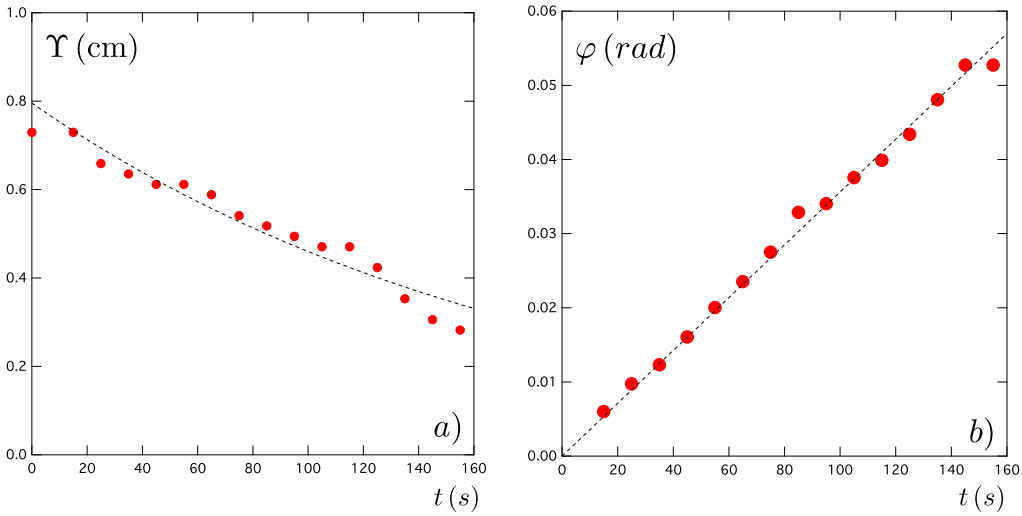


Figure 9.12: Time evolution of the amplitude and phase of a stable meandering channel. Same as Fig. 9.11, but with an initial sinusoidal channel of wavelength $\lambda = 7$ cm. (a) Growth rate $\sigma = -0.006$ s^{-1}. (b) Propagation velocity $c = 0.51$ cm/s.

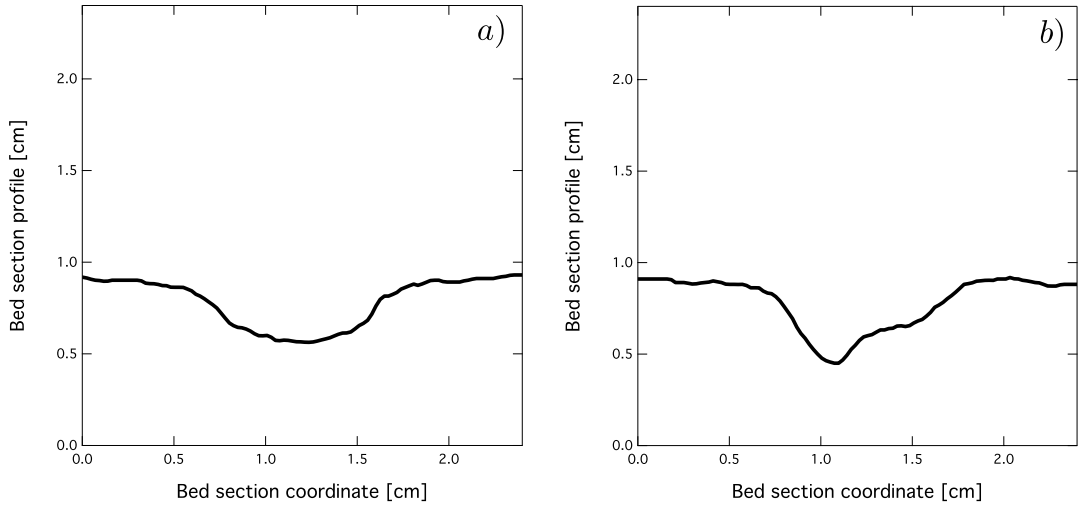


Figure 9.13: Cross-section of the channel at $t = 60$ s, located (a) at the inflection point and (b) in the bend of the meanders (see red lines in Fig. 9.9). The right bank is on the right of the pictures.

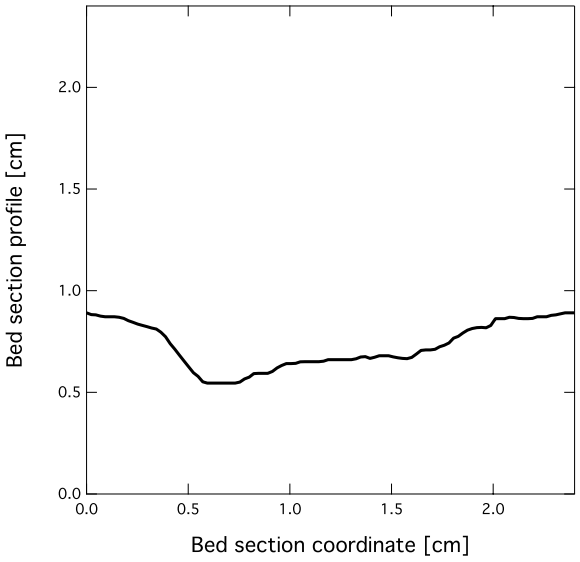


Figure 9.14: Cross-section of the channel at $t = 215$ s, located in the bend of the meanders (see green line in Fig. 9.9). The right bank is on the right of the picture.

In order to better investigate the bed profile of the channel, we show in figure 9.15 – **a** the contour plot of the experimental bed elevation divided by the amplitude of banks undulation Υ. The x and y coordinates have been made dimensionless by the channel width W. Interestingly, one can reproduce all main features of the bathymetry with an expression corresponding to the first bed mode discussed in chapter 8:

$$Z(x,y) = |Z_1|\cos(kx+\varphi_1^Z)|c_1\rangle = |Z_1|\cos(kx+\varphi_1^Z)\,\cos\left[\pi\left(\frac{y}{2y_0}+\frac{1}{2}\right)\right], \qquad (9.5)$$

where the definition and the properties of $|c_1\rangle$ are detailed in chapter 2. The resulting contour plot is showed in figure 9.15 – **b**. For this plot, the values of $|Z_1|$ and φ_1^Z in this expression have been computed from the prediction of equation 8.13 at the kW (and the other parameters) corresponding to that of the experiment: $|Z_1|/\Upsilon \simeq 0.15$ and $\varphi_1^Z \simeq -68°$.

The experimental and theoretical images quantitatively show similar behaviours. In particular low and high regions ('beaches' and 'pools') alternate with the same phase. The intensity of bed perturbation is, averaged of several experiments on the order of

$$\left.\frac{|Z_1|}{\Upsilon}\right|_{\text{average}} \simeq 0.16, \qquad (9.6)$$

in quantitative agreement with the theoretical prediction, while in the specific case shown in figure 9.15 – **a**, it is more around 0.2.

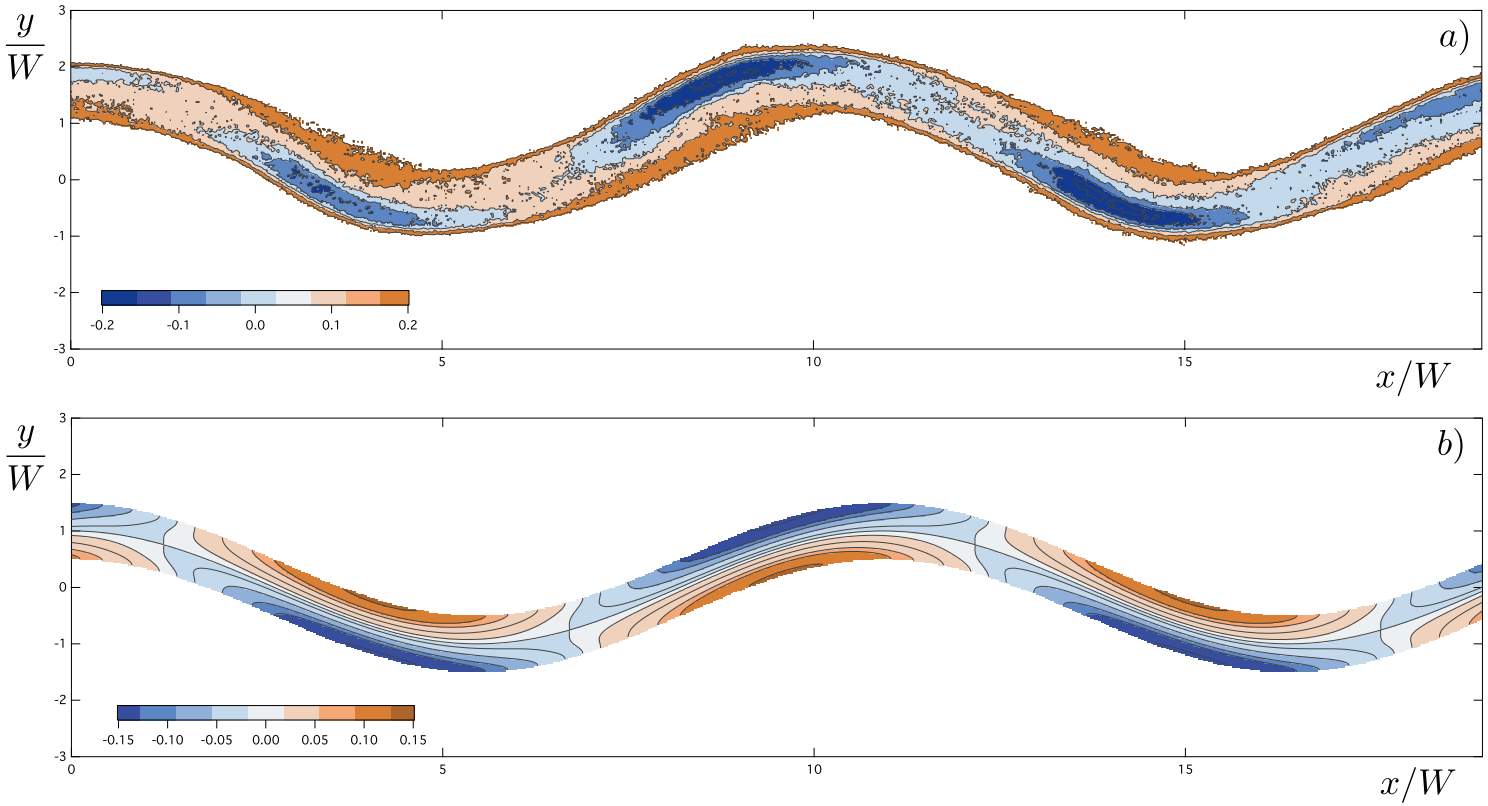


Figure 9.15: Experimental (a) and theoretical (b) contour plots of the bed elevation. The experimental dimensions are $\lambda \simeq 13$ cm, $W \simeq 1.1$ cm, $\Upsilon \simeq 0.85$ cm ($kW \simeq 0.54$). The theoretical prediction has been computed with $C = 0.1$, $\beta = 4$, $\mathcal{F} = 0.77$, $\mu = 0.45$, $u_*/u_{\rm th} = 1.6$ and $kW = 0.54$.

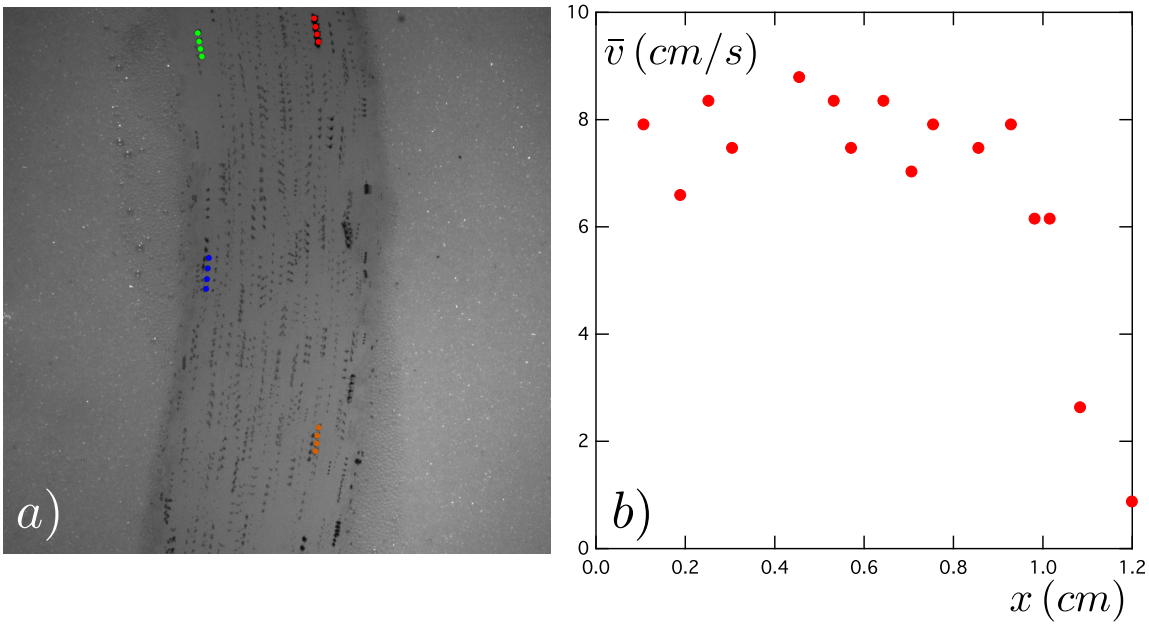


Figure 9.16: Flow velocity measurement by particle tracking. (a) Here we superimpose four photos at different time intervals: $\delta t = 0$, $\delta t = 14$, $\delta t = 30$ and $\delta t = 42$ ms. The flow is from top to bottom. Channel width: $W \simeq 1.2$ cm. Water flow rate: $Q = 7.5\ \ell/\mathrm{h}$. (b) Measurements of velocity along the channel width, we see that the average (vertically) value is around $\bar{v} \simeq 8$ cm/s.

9.3.3 Velocity of the flow and hydrodynamical dimensionless numbers

We have measured the surface flow velocity in the channel by the tracking of carbon particles (diameter 0.5–1 mm) initially spread at the upstream part of the channel. As shown in Fig. 9.16, the frame rate of the fast camera was enough to follow the particle trajectories, and to compute their velocity. Assuming that these particles act as passive tracers, we get, for this picture, an average velocity in the central region of the channel on the order of $\bar{v} = 8 \pm 0.5$ cm/s from which we derived a surface velocity of $v_{\mathrm{surf}} = 13.4 \pm 0.5$ cm/s. The whole transverse velocity profile can be qualitatively deducted thanks to the colored spot in the above figure: its shape can be reasonably fitted by a constant in the central layer (since we do not see any substantial variation along the transversal direction) and we also distinguish on the right and on the left the two bank layers in which the velocity progressively pass from

the constant value to zero. If we assume that the velocity profile is parabolic over the vertical direction, then the flow rate Q is related to the central surface velocity, the width and the depth of channel as

$$Q = \frac{2}{3} W H v_{\text{surf}} . \tag{9.7}$$

This relationship provides another way to determine the effective H, knowing the three other quantities. For the case of the channel of Fig. 9.16, it gives $H \simeq 2.3$ mm. This is consistent with estimates of the previous paragraph. Note that, these velocity measurements have been taken at the beginning of the sinusoidal channel destabilization, i.e. a similar situation of the case displayed in Fig. 9.13.

Let us now discuss the value of hydrodynamical dimensionless numbers. With velocities on the order of 0.1 m/s and a water depth on the order of a few mm, the Reynolds number is Reynolds number:

$$\mathcal{R} \simeq 300 . \tag{9.8}$$

This value is typical of a transitional regime between laminar and turbulent. As for the Froude number, with the above values we get

$$\mathcal{F} \simeq 0.5 . \tag{9.9}$$

This shows that these experiments are indeed run in fluvial regime ($\mathcal{F} < 1$).

Location	θ (°)	W (m)	H (m)	β	$\mathcal{F}$	λ (m)	Υ (m)	kW
Les Trestas	0.11	1.2	0.5	2.4	0.2	11.3	5.8	0.7
Vieux Lugo	0.11	3	1.3	2.3	0.1	19	–	1
Grande Leyre (point triple)	0.06	12	3	4	0.26	200	50	0.37
Leyre (Graoux)	0.05	17	1.7	10	0.27	167	21	0.64

Table 9.1: Field data for meanders of various places in the Leyre bassin: river slope θ, bankfull width W and H, corresponding aspect ration β, Froude number, meander wavelength λ and amplitude Υ, corresponding value of kW. These values are averaged over several measurements.

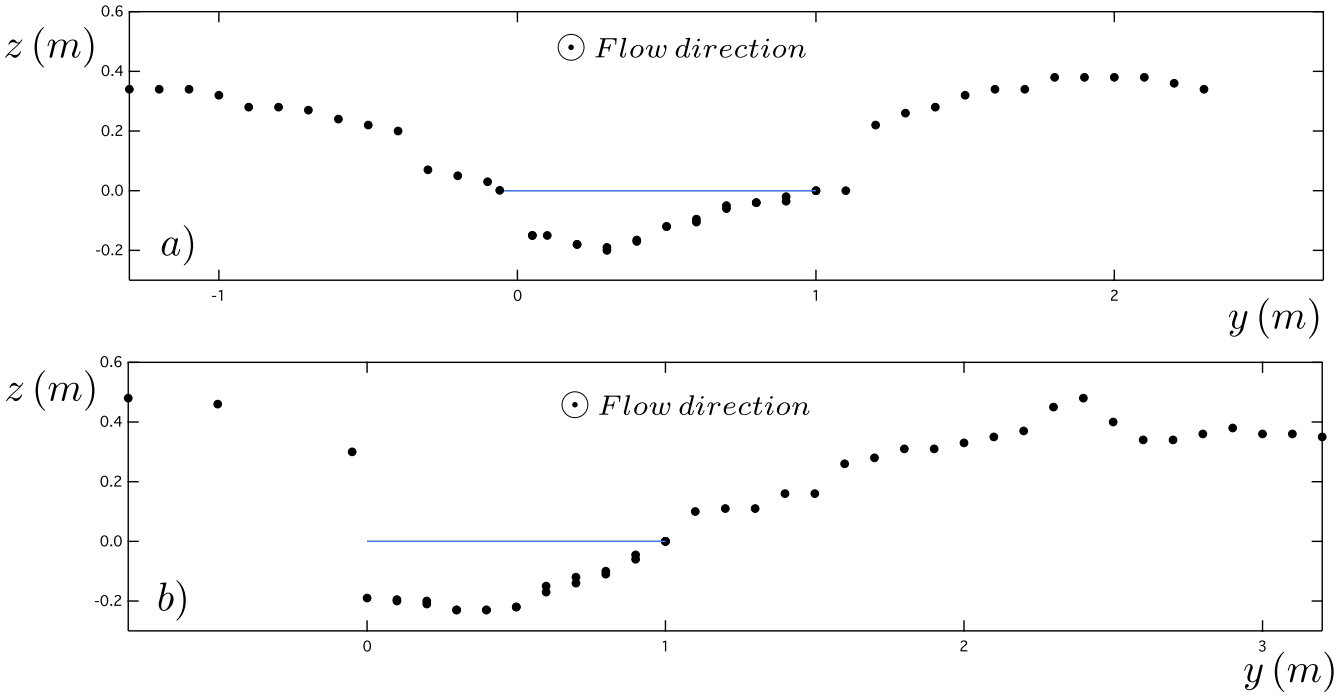


Figure 9.17: Bed transverse profile of a small meandering tributary of the Leyre river – we refer to this location as the "Les Trestas" meanders, see table 9.1. Panel (a): profile at the inflection point between to successive bends. Panel (b): profile at the bend. The right bank is on the left in these graphs. The blue line corresponds to the water surface at the time of the data collection (october 2012).

9.4 Field data

We have collected field data on the meandering channels of the Leyre river and some of its tributaries. The Leyre basin is located South west of France in the region called 'Landes de Gascogne' (44°32'N, 0°52'W). The ground there is remarkably homogeneous and composed of sand (typical diameter 330 μm). We have measured or estimated geometrical and hydrodynamical characteristics of different channels, ranging from width on the order of a meter to ten meters, see table 9.1. Interestingly, they typical values of the aspect ratio β and the rescaled meander wavenumber kW are similar to those in the experiment: respectively a few units and a bit less than 1.

We have measured transverse profiles of the topography on two locations of the 'déchetterie' meanders. They are displayed in figure 9.17 and show in particular the typical asymmetry of the bed in the bend. These profiles also allow us to estimate a typical value of the amplitude of the bed modulation: $|Z_1| \simeq 0.3$ m. With Υ on the order of 3 m at that place, we get a ratio $|Z_1|/\Upsilon \simeq 0.1$. This value has a good agreement with our theoretical predictions ($|Z_1|/\Upsilon \simeq 0.12$) and falls into a reasonable 20% of measure error. It is also of the same order of magnitude of the values we found in laboratory experiments ($|Z_1|/\Upsilon \simeq 0.16$) in confirmation of the their goodness to be able to reproduce natural processes. Furthermore, the slight difference can be attributed to non linear effects that we ignored up to now.



Figure 9.18: Leyre river just before the confluence with the Vieux Lugo stream (44° 30′ N, 0° 49′ W).

9.5 Dispersion relation

Following the procedure described above, we have measured the growth rate and the migration velocity of meanders for initial sinusoidal channels of different wavelengths and amplitudes. We also varied the grain diameter of the bed with beads of 80 and 140 μm, the slope between 0.5 and 0.8 degrees and the flow rate in the range 5–7 ℓ/h. In this section, we shall focus on the most complete series we have performed, i.e. for grains of size 140 μm, at a slope of 0.7° and with a flow rate of $6.5 \sim 7\ell$/h.

The measurements of growth rate have been gathered in Fig. 9.19, and they are compared to the theoretical predictions derived in chapter 8. The agreement is good. In particular, the value of the most unstable mode $k_{\max}W \simeq 0.51$ is well predicted. The comparison of the angular velocity ω to the predictions is also correct, though less quantitative (Fig. 9.20 – **a**). Note that the phenomenological erosion coefficient $\mathcal{E}$ has not been measured independently, and the matching of experimental and theoretical maximum growth rates give $\mathcal{E} \simeq 10^{-3}$, which is consistent with the assumption that banks evolve more slowly than the bed. Finally, Fig. 9.20 – **b** shows the dispersion relation plotted for parameters corresponding to the Leyre river. Again, the range of observed kW (see table 9.1) is in the region where σ reaches its maximum.

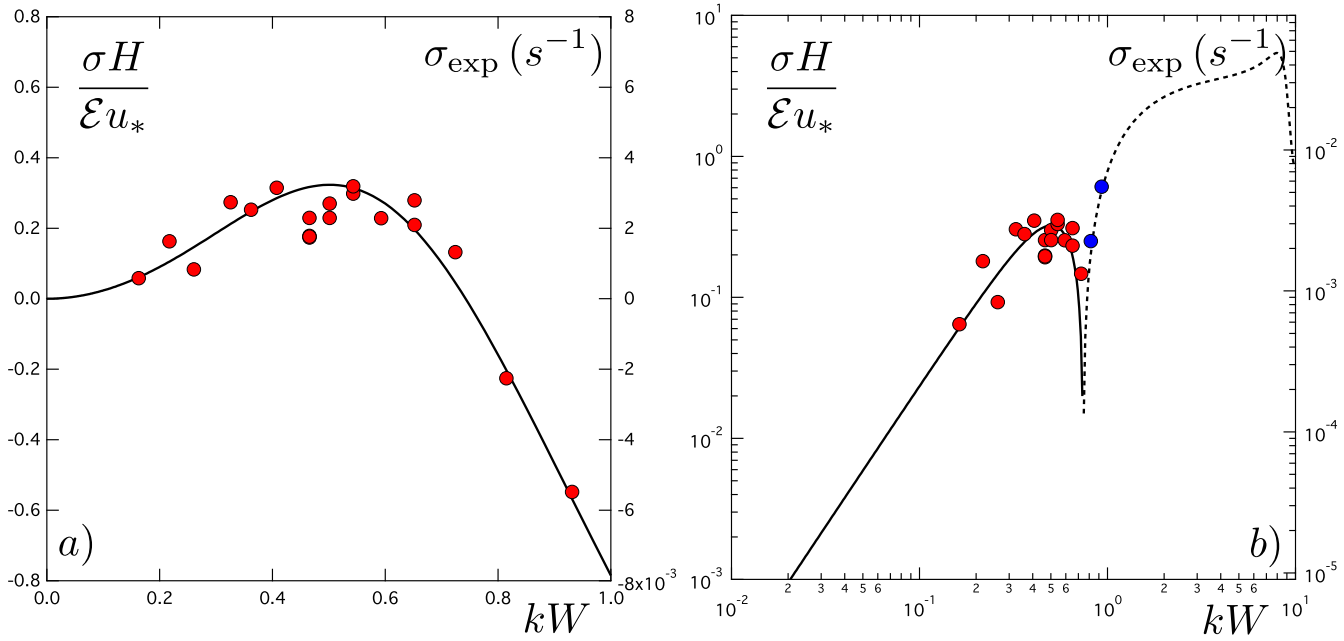


Figure 9.19: Experimental (points, right y-axis) and theoretical (lines, left y-axis) growth rate shown in linear (a) and logarithmic scales (b). NB: in this last case, blue points and dashed lines are used for negative values. The lines have been computed for $C = 0.1$, $\beta = 4$, $\mathcal{F} = 0.77$, $\mu = 0.45$ and $u_*/u_{\rm th} = 1.6$.

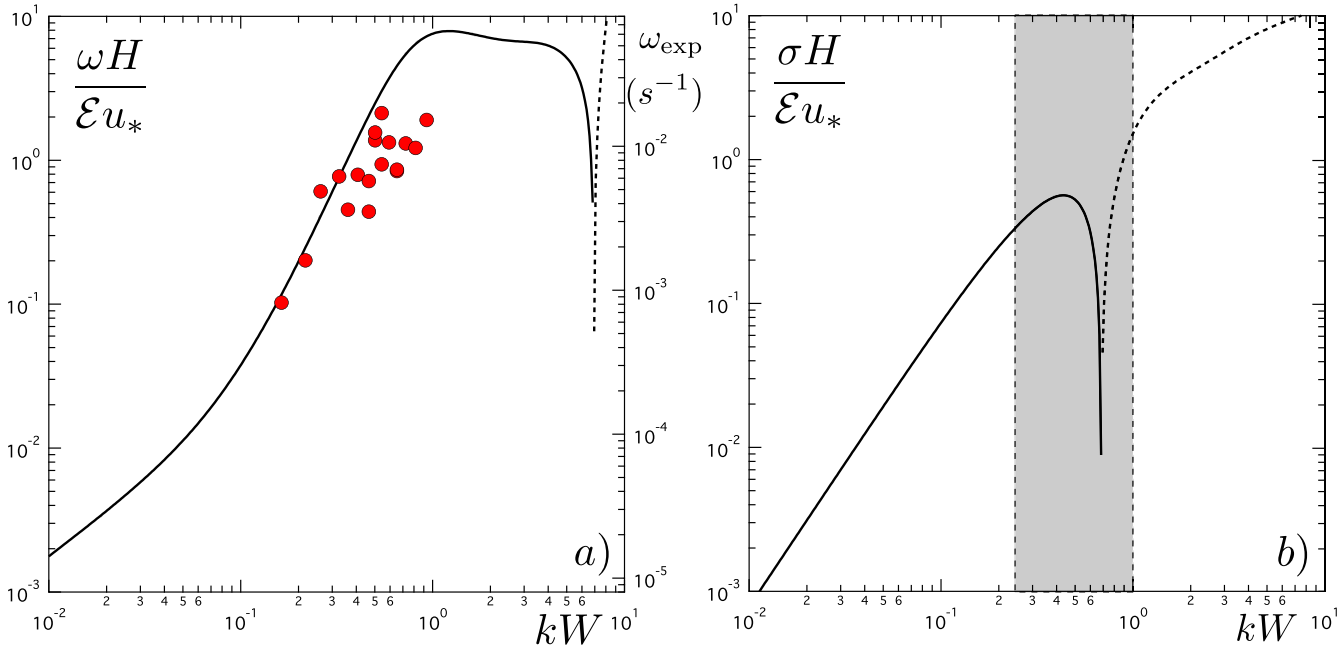


Figure 9.20: (a) Same as in Fig. 9.19, but for the angular velocity ω. (b) Theoretical predictions for parameters corresponding to the Leyre river: $C = 0.04$, $\beta = 4$, $\mathcal{F} = 0.29$, $\mu = 0.5$ and $u_*/u_{\rm th} = 2$. Grey zone: range of kW observed in the field, see table 9.1.

Conclusion

This thesis has been devoted to three different problems related to the morphodynamics of rivers. The first of them concerns sediment transport, for which a two-phase flow model has been proposed, valid in both viscous and turbulent regimes. An important novelty is the account for the diffusion of particles induced by non-affine motion. As a main result, this model describes the transition from bed load to suspended load when the Shields number is increased. The second subject was the formation of bars. We revisited the linear stability analysis of these bedforms in order to emphasise the role played by the ratio of the saturation length characterising the response length scale of transport to the water depth. We have shown that this 'saturation number' $L_{\rm sat}/H$ controls the transition from transverse bedforms (ripples, eventually coarsening in dunes) when $L_{\rm sat}/H$ is small, to bars when $L_{\rm sat}/H$ is large. Interestingly, this ratio itself is expected to jump by several orders of magnitude when the mode of sediment transport changes from bed-load to suspension.

The third and most developed aspect of this PhD work was dedicated to the formation of meanders. By means of 3D RANS equations, we have performed a detailed description of hydrodynamics in a channel with both modulated bed and undulating banks. Coupled to sediment transport and under the assumption that the bed evolves more rapidly than the banks, the linear stability analysis of the problem gives predictions for the growth rate, the migration velocity and the shape of the bed for given meandering banks of wavenumber k. These predictions are in quantitative agreement with experimental data we obtained in a small flume: nonetheless the entire dispersion relation is well fitted with reasonable parameters of the modelling, but also the bed modulation (amplitude and phase) is correctly reproduced. In particular, the most unstable mode follows the approximate scaling law kW equals a constant (of order one), in agreement with data recorded on many natural meandering rivers.

On the qualitative side, we have identify the mechanism responsible for this instability. The direct effect of the modulated banks on the bed is to induce some transverse centripetal component of the sediment flux, which creates higher/deeper

regions at the inside/outside of the channel bend. The effect of that bank-induced modulated bed on the flow velocity is to generate an excess average velocity in deeper regions, i.e. at the outside of the channel bend. This excess velocity generates further erosion of the outside bank, thus leading to an unstable dynamics. This mechanism is different to that proposed by Einstein (1926), where the excess velocity at the outside of the bend is a direct effect of the banks. It is also different to the resonance proposed by Blondeaux & Seminara (1985), where the dynamics of meanders and bars are coupled. Finally, we have shown that depth-averaged (Saint-Venant) equations are not able to reproduce the instability.

Different perspectives of this work can be drawn. First, the variation of the saturation number, in relation to the change of transport mode, should be systematically measured in dedicated experiments and its role in the emergence of bedforms should be further investigated. For instance, the interpretation of the 'upper plane regime' (Southard 1991) could be revisited in light of this point of view. As for meanders, this first successful attempt to reproduce meanders at the laboratory scale – with no vegetation or other experimental tricks – should be consolidated by additional experiments. In particular, a better control of later times, with a clear evolution of the channel to non-linear meanders is desired. Also, the reproduction and the modeling of tidal meanders is another way to investigate further the dynamical mechanisms at work. Finally, more field data should be analysed or reanalysed, having this new point of view in mind. For example, the meanders on the Loire river (see $46^\circ\,49'$ N, $3^\circ\,21'$ E), for which some precise data are available (Dreal Centre data), offer promising possibilities.

Bibliography

[Abbott *et al.* 1977] Abbott, J.E. & Francis, J.R.D. 1977 Saltation and suspension trajectories of solid grains in a water stream. *Phil. Trans. R. Soc. London* **284**, 225-254.

[Allen 1985] Allen, J.R.L. 1985 Principles of Physical Sedimentology, The Blackburn Press, Caldwell USA.

[Andreotti *et al.* 2002] Andreotti, B., Claudin, P. & Douady, S. 2002 Selection of dune shapes and velocities. Part 2: A two-dimensional modelling. *Eur. Phys. J. B* **28**, 341-352.

[Andreotti 2004] Andreotti, B. 2004 A two species model of aeolian sand transport. *J. Fluid Mech.* **510**, 47–50.

[Andreotti *et al.* 2008] Andreotti, B., Claudin, C. & Pouliquen, O. 2008 Measurements of the aeolian sand transport saturation length, submitted to *Geomorphology.*

[Andreotti *et al.* 2012] Andreotti, B., Claudin, P., Devauchelle, O. Durán, O. & Fourrière, A. 2012 Bedforms in a turbulent stream: ripples, chevrons and antidunes. *J. Fluid Mech.* **690**, 94-128.

[Andreotti & Claudin] Andreotti, B., and Claudin, P. 2012 Chapter 7: Physics of sediment and aeolian transport. *Erosion of geomaterial* (S.Bonelli Editor), ISTE/Wiley.

[Andreotti *et al.* 2013] Andreotti, B., Forterre, Y., and Pouliquen, O. 2013 *Granular media: Between Fluid and Solid*, Cambridge University Press.

[Ayotte *et al.* 1994] Ayotte, K. W., Xu, D. & Taylor, P. A. 1994 The impact of turbulence closure schemes on predictions of the mixed spectral finite-difference model for flow over topography. *Boundary-Layer Met.* **68**, 1-33.

[Bagnold 1941] Bagnold, R.A. 1941 *The physics of blown sand and desert dunes*, Chapmann and Hall, Methuen, London.

[Bagnold 1956] Bagnold, R.A., 1956. The flow of cohesionless grains in fluids, *Phil. Trans. R. Soc. Lond.* **249**, 235-297.

[Berlcher & Hunt 1998] Berlcher, S.E., and Hunt, J.C.R. 1998 Turbulent flow over hills and waves. *Ann. Rev. Fluid Mech.* **30**, 507 –538.

[Blondeaux & Seminara 1985] Blondeaux, P. & Seminara, G. 1985 A unified bar-bend theory of river meanders. *J. Fluid Mech.* **157**, 449-470.

[Bunte *et al.* 2010] Bunte, K., Abt, R. S., Swingle, W. K., Potyondy, J. P. 2010 Bankfull mobile particle size and its prediction from a Shields-type approach. *Proceedings of 2nd Joint Federal Interangecy Conference, Las Vegas*

[Buckles *et al.* 1984] Buckles, J., Hanratty, T.J., Adrian, R.J. 1984 Turbulent flow over large-amplitude wavy surfaces. *J. Fluid Mech.* **140**, 27Ð44.

[Callander 1969] Callander, R.A. 1969 Instability and river channels. *J. Fluid Mech.* **36**, 465-480.

[Celik & Rodi 1988] Celik, I. & Rodi, W. (1988), Modeling suspended sediment transport in nonequilibrium situations, *J. Hydr. Engrg.* **114**, 1157–1191.

[Chang & Simons 1970] Chang, H.Y. & Simons, D.B. 1970 The bed configuration of straight sand-bed channels when flow is nearly critical. *J. Fluid Mech.* **42**, 491-495.

[Chang *et al.* 1971)] Chang, H.Y., Simons, D.B. & Woolhiser, D.A. 1971 Flume experiments on alternate bar formation. *J. Waterways Harbors Costal Eng. Div.* **97**, 155-165.

[Charru *et al.* 2004] Charru, F., Mouilleron-Arnould, H. & Eiff O. 2004 Erosion and deposition of particles on a bed sheared by a viscous flow. *J. Fluid Mech.* **519**, 55-80.

[Charru 2006] Charru, F. 2006 Selection of the ripple length on a granular bed sheared by a liquid flow. *Phys. Fluids* **18**, 121508.

[Charru *et al.* 2008] Charru, F., Larrieu, E., Dupont, J.-B. & Zenith, R. 2008 Motion of a particle near a rough wall in a viscous shear flow. *J. Fluid Mech.* **570**, 431-453.

[Charru *et al.* 2013] Charru, F., Andreotti, B. & Claudin, P. 2013 Sand ripples and dunes. *Annu. Rev. Fluid Mech.*, accepted.

[Cherukat *et al.* 1998] Cherukat, P., Na, Y., Hanratty, T.J., McLaughlin, J.B. 1998 Direct numerical simulation of a fully developed turbulent flow over a wavy wall. *Theoret. Comput. Fluid Dyn.* **11**, 109 –34.

[Chiodi *et al.* 2012] Chiodi, F., Andreotti, B. & Claudin, P. 2012 The bar instability revisited. `ArXiv:1210.3223`.

[Chomaz 2005] Chomaz, J.-M. 2005 Global instabilities in spatially developping flows: non-normality and nonlinearity. *Annu. Rev. Fluid Mech.* **37**, 357-392.

[Claudin & Andreotti 2006] Claudin, P. & Andreotti, B. 2006 A scaling law for aeolian dunes on Mars, Venus, Earth, and for sub-aqueous ripples. *Earth Pla. Sci. Lett.* **252**, 30-44.

[Claudin *et al.* 2011] Claudin, P., Charru, F. & Andreotti, B. 2011 Transport relaxation time and length scales in turbulent suspensions. *J. Fluid Mech.* **671**, 491-506.

[Claudin *et al.* 2012] Claudin, P., Wiggs, G.F.S. & Andreotti, B. 2012 Field evidence for the upwind velocity shift at the crest of low dunes. Submitted to Boundary-Layer Meteorology, `ArXiv:1205.4411`.

[Coleman 1970] Coleman, N. L. 1970 Flume studies of the sediment transfer coefficient. *Water Resour. Res.* **6**, 801–809.

[Colombini *et al.* 1987] Colombini, M. Seminara, G. & Tubino, M. 1987 Finite-Amplitude Alternate Bars. *J. Fluid Mech.* **181**, 213-232.

[Colombini & Stocchino 2005] Colombini, M. & Stocchino, A. 2005 Coupling or decoupling bed and flow dynamics: fast and slow sediment waves at high Froude numbers. *Phys. Fluids* **17**, 036602.

[Crosato & Musselman 2009] Crosato, A., & Mosselman, E. 2009 Simple physics-based predictor for the number of river bars and the transition between meandering and braiding. *Water Ressources Res.* **45**, W03424.

[Crosato *et al.* 2011] Crosato, A., Mosselman, E., Desta, F.B. & Uijttewaal, W.S.J. 2011 Experimental and numerical evidence for intrinsic nonmigrating bars in alluvial channels. *Water Ressources Res.* **47**, W03511.

[Davy & Lague 2009] Davy, Ph. & Lague, D. 2009 Fluvial erosion/transport equation of landscape evolution models revisited *J. Geophys. Res.* **114**, F03007 (16 pages).

[deAngelis *et al.* 1997] de Angelis, V., Lombardi, P., Banerjeeb, S. 1997 Direct numerical simulation of turbulent flow over a wavy wall *Phys. Fluids* **9**, 2429Ð2442.

[Devauchelle *et al.* 2010 a] Devauchelle, O., Malverti, L., Lajeunesse, E., Josserand, C., Lagrée, P.-Y., & Métivier, F. 2010 Rhomboid beach pattern: a laboratory investigation. *J. Geophys. Res.* **115**, F02017.

[Devauchelle *et al.* 2010 b)] Devauchelle, O., Malverti, L., Lajeunesse, E., Lagrée, P.-Y., Josserand, C. & Nguyen Thu-Lam, K.-D. 2010 Stability of bedforms in laminar flows with free surface: from bars to ripples. *J. Fluid Mech.* **642**, 329-348.

[Dey 2003] Dey, S., 2003 Threshold of sediment motion on combined transverse and longitudinal sloping beds. *J. Hydraul. Res.* **41**, 405-415.

[Dreal Centre data] Website: www2.centre.ecologie.gouv.fr/SIEL/index-0.html

[Durán *et al.* 2011] Durán, O., Claudin, P. & Andreotti B. 2011 On aeolian transport: grain-scale interactions, dynamical mechanisms and scaling laws. Review Article. Aeolian Research **3**, 243-270.

[Durán *et al.* 2012] Durán, O., Andreotti B. & Claudin, P. 2012 Numerical simulation of turbulent sediment transport, from bed load to saltation. To appear in *Phys. Fluids*, `ArXiv:1111.6898`.

[Einstein 1926] Einstein, H.A. 1926 The Cause of the Formation of Meanders in the Courses of Rivers and of the So-Called BaerÕs Law. *Die Naturwissenschaften*, **14**.

[Einstein 1950] Einstein, H. A. 1950 The bedload function for sediment transportation in open channel flow. *Techn. Bull. 1026, U.S. Dept of Agriculture, Washington D.C.*, 1–71.

[Elbelrhiti *et al.* 2005] Elbelrhiti, H., Claudin, C. & Andreotti, B. 2005 Field evidence for surface wave induced instability of sand dunes. *Nature* **437**, 720-723.

[Engelund 1970] Engelund, F. 1970 Instability of erodible beds. *J. Fluid Mech.* **42**, 225–244.

[Engelund & Skovgaard 1973] Engelund, F. & Skovgaard, O. 1973 On the origin of meandering and braiding in alluvial streams. *J. Fluid Mech.* **57**, 289-302.

[Ferguson *et al.* 2004] Ferguson, R.I., Church, M., 2004. A simple universal equation for grain settling velocity. *J. Sedim. Res.* **74**, 933-937.

[Fernandez Luque & van Beek 1976] Fernandez Luque, R. & van Beek, R. 1976 Erosion and transport of bed-load sediment. *J. Hydraul. Res.* **14**, 127-144.

[Fourrière *et al.* 2010] Fourrière, A., Claudin P. & Andreotti, B. 2010 Bedforms in a turbulent stream: formation of ripples by primary linear instability and of dunes by non-linear pattern coarsening. *J. Fluid Mech.* **649**, 287-328.

[Frederick & Hanratty 1988] Frederick, K.A., Hanratty, T.J. 1988 Velocity measurements for a turbulent non-separated flow over solid waves. *Exp. Fluids* **6**, 477-486.

[Fredsøe & Deigaard 1992] Fredsøe, J. & Deigaard, R. 1992 Mechanics of coastal sediment transport. World Scientific, Singapore.

[Fredsøe 1978] Fredsøe, J. 1978 Meandering and braiding of rivers. *J. Fluid Mech.* **84**, 609-624.

[Fujita & Muramoto 1982] Fujita, Y. & Muramoto, Y. 1982 Experimental study on stream channel processes in alluvial rivers. *Bull. Disas. Prev. Res. Inst.* (Kyoto Univ.) **32**, 49-96.

[Fujita & Muramoto 1985] Fujita, Y. & Muramoto, Y. 1985 Studies on the process of development of alternate bars. *Bull. Disas. Prev. Res. Inst.* (Kyoto Univ.) **35**, 55-86.

[Fukuoka 1989] Fukuoka, S., 1989 Finite amplitude development of alternate bars. in *River Meandering*, edited by S.Ikeda and G.Parker, Water Res. Monogr. **12**, AGU, Washington, D.C., 237-265.

[García & Niño 1993] García, M. & Niño, Y. 1993 Dynamics of sediment bars in straight and meandering channels: experiments on the resonance phenomenon. *J. Hydraul. Res.* **31**, 739-761.

[Henn & Sykes 1999] Henn, D.S., Sykes, R.I. 1999 Large-eddy simulation of slow over wavy surfaces *J. Fluid Mech.* **383**, 75 –112.

[Hunt *et al.* 1988] Hunt, J.C.R., Leibovich, S. & Richards, K.J. 1988 Turbulent shear flows over low hills. *Q. J. R. Meteorol. Soc.* **114**, 1435–1470.

[Hunt *et al.* 2007] Hunt, J.C.R., Delfos, R., Eames, I. & Perkins, R. 2007 Vortices, Complex Flows and Inertial Particles. *Flow, Turbulence and Combustion* **79**, 207–234.

[Ikeda *et al.* 1981] Ikeda, S., Parker, G., and Sawai, K. 1981 Bend theory of river meanders. Part 1. Linear development. *J. Fluid Mech.* **112**, 363Ð377.

[Ikeda 1983] Ikeda, H. 1983 Experiments on bedload transport, bedforms, and sedimentary structures using fine gravel in the 4-meter-wide flume. *Environ. Res. Center pap.* (Tsukuba Univ.) **2**, 1-78.

[Inversen *et al.* 1994] Iversen, J.D., Rasmussen, K.R., 1994. The effect of surface slope on saltation threshold. *Sedimentology* **41**, 721-728.

[Jackson & Hunt 1975] Jackson, P. S. & Hunt, J. C. R. 1975 Turbulent wind flow over a low hill. *Q. J. R. Meteorol. Soc.* **101**, 929-955.

[Julien 1998] Julien, P.Y. 1998 Erosion and sedimentation. *Cambridge University Press.*

[Jobson & Sayre 1970] Jobson, A. E. & Sayre, W. W. (1970), Vertical transfer in open channel flow. *J. Hydr. Div., ASCE* **96**, 703–724.

[Kamphuis 1974] Kamphuis, J.W. 1974 Determination of Sand Roughness for Fixed Beds. *J. Hydraul. Res.* **12**, 193–207.

[Kennedy 1963] Kennedy, J.F. 1963 The mechanics of dunes and antidunes in erodible bed channels. *J. Fluid Mech.* **16**, 521-544.

[Kroy *et al.* 2002] Kroy, K., Sauermann, G. & Herrmann, H.J. 2002 Minimal model for aeolian sand dunes. *Phys. Rev. E* **66**, 031302.

[Lagrée 2003] Lagrée, P.-Y. 2003 A triple deck model of ripple formation and evolution. *Phys. Fluids* **15**, 2355.

[Lajeunesse *et al.* 2010] Lajeunesse, E., Malverti, L. & Charru, F. 2010 Bedload transport in turbulent flow at the grain scale: experiments and modeling. *J. Geophys. Res.* **115**, F04001.

[Lanzoni 2000 a] Lanzoni, S. 2000 Experiments on bar formation in a straight flume. 1. Graded sediment. *Water Resources Res.* **36**, 3337-3349.

[Lanzoni 2000 b] Lanzoni, S. 2000 Experiments on bar formation in a straight flume. 2. Uniform sediment. *Water Resources Res.* **36**, 3351-3363.

[Leopold & Wolman 1957] Leopold, L.B., and Wolman, M.G. 1957 River Channel Patterns: Braided, Meandering and Straight *Geo. Sruvey Professional Paper* **282 - B**, 39-85.

[Lisle *et al.* 1991] Lisle, T.E., Ikeda, H. & Iseya, F. 1991 Formation of stationary alternate bars in a steep channel with mixed-size sediment: a flume experiment. *Earth Surf. Proc. Landforms* **16**, 463-469.

[Lisle *et al.* 1997] Lisle, T.E., Pizzuto, J.E., Ikeda, H., Iseya, F. & Kodama, Y. 1997 Evolution of a sediment wave in an experimental channel. *Water Resources Res.* **33**, 1971-1981.

[Luchini & Charru 2010] Luchini, P. & Charru, F. 2010 Consistent section-averaged equations of quasi-one-dimensional laminar flow. *J. Fluid Mech.* **656**, 337-341.

[Malverti *et al.* 2008] Malverti, L., E. Lajeunesse, and F. Métivier 2008 Small is beautiful: Upscaling from microscale laminar to natural turbulent rivers *J. Geophys. Res.* **113**, F04004

[Meyer-Peter & Müller 1948] Meyer-Peter, E. & Müller, R. 1948 Formulas for bed load transport. Proc., 2nd Meeting, IAHR, Stockholm, Sweden, 39-64.

[Nezu & Rodi 1986] Nezu, I. & Rodi, W. (1986), Open-channel flow measurements with a laser doppler anemometer, *J. Hydr. Engrg.* **112**, 335–355.

[Nielsen 1992] Nielsen, P. 1992 Coastal bottom boundary layers and sediment transport. World Scientific, Singapore.

[Odgaard 1987] Odgaard A. Jacob 1987 Streambank erosion along two rivers in Iowa *Water Resour. Res.* **23**, 1225 –1236.

[Parker 1975] Parker, G. 1975 Sediment inertia as cause of river anti-dunes. *J. Hydraul. Div.* **101**, 211Ð221.

[Parker 1976] Parker, G. 1976 On the cause of characteristic scales of meandering and braiding in rivers. *J. Fluid Mech.* **76**, 457-480.

[Parker 1978] Parker, G. 1978 Self-formed straight rivers with equilibrium banks and mobile bed. Part 1. The sand-silt river. *J. Fluid Mech.* **89**, 109–125.

[Parker & Andrews 1986] Parker, G., and Andrews, E. D. 1986 On time development of meanders bends. *J. Fluid Mech.* **162**, 139Ð156.

[Pizzuto & Meckelnburg 1989] Pizzuto, J.E., and Meckelnburg, T.S. 1989 Evaluation of a linear bank erosion equation *Water Resour. Res.* **25**, 1005 –1013.

[Poggi *et al.* 2007] Poggi, D. , Katul, G. G., Albertson, J. D. & Ridolfi, L. 2007 An experimental investigation of turbulent flows over a hilly surface. *Phys. Fluids* **19**, 036601.

[Raudkivi 1966] Raudkivi, A. J. 1966 Bedforms in alluvial channels. *J. Fluid Mech.* **26**, 507 –514.

[Raudkivi 1998] Raudkivi A. J. 1998 Loose Boundary Hydraulics. A.A. Balkema, Rotterdam.

[Rasmussen *et al.* 1996] Rasmussen, K.R., Iversen, J.D., Rautaheimo, P., 1996. Saltation and wind flow interaction in a variable slope wind tunnel. *Geomorphology* **17**, 19-28.

[Richards 1980] Richards, K.J. 1980 The formation of ripples and dunes on an erodible bed. *J. Fluid Mech.* **99**, 597–618.

[van Rijn 1984] van Rijn, L. C. 1984 Sediment transport, Part II: Suspended load transport. *J. Hydr. Engrg.* **110**, 1613–1641.

[van Rijn 1986] van Rijn, L. C. 1986 Application of sediment pickup function. *J. Hydr. Engrg.* **112**, 867–874.

[Rinaldo *et al.* 1993] Rinaldo, A., Rodriguez-Iturbe, I., Rigon, I., Bras, R.L., Ijjasz-Vasquez, E. 1993 Self-organized fractal river networks *Phys. Rev. Lett.* **70**, 1222-1226.

[Ross *et al.* 2004] Ross, A.N., Arnold, S., Vosper, S.B., Mobbs, S.D., Dixon, N., Robins, A.G. 2004 A comparison of wind-tunnel experiments and numerical simulations of neutral and stratified flow over a hill. *Bound.-Layer Meteorol.* **113**,427Ð459.

[Ruyer-Quil & Manneville 1998] Ruyer-Quil, C. & Manneville, P. 1998 Modeling film flows down inclined planes. *Eur. Phys. J. B* **6**, 277-292.

[Ruyer-Quil & Manneville 2000] Ruyer-Quil, C. & Manneville, P. 2000 Improved modeling film flows down inlined planes. *Eur. Phys. J. B* **15**, 357-369.

[Schielen *et al.* 1993] Schielen, R., Doelman, A. & de Swart, H.E. 1993 On the nonlinear dynamics of free bars in straight channels. *J. Fluid Mech.* **252**, 325-356.

[Schlichting & Gersten 2000] Schlichting, H. & Gersten, K. 2000 Boundary layer theory. 8^{th} edition. Springer-Verlag, Berlin.

[Schumm & Khan 1972] Schumm, S.A. & Khan, H.R. 1972 Experimental study of channel patterns. *Geol. Soc. Am. Bull.* **83**, 1755-1770.

[Seminara & Tubino 1989] Seminara, G. & Tubino, M., 1989 Alternate bars and meandering: free, forced a mixed interactions. in *River Meandering*, edited by S.Ikeda and G.Parker, Water Res. Monogr. **12**, AGU, Washington, D.C., 267-320.

[Seminara & Tubino 2001] Seminara, G., and Tubino, M. 2001 Sand bars in tidal channels Part 1. Free bars. *J. Fluid Mech.* **440**, 49 –74

[Seminara 2006] Seminara, G. 2006 Meanders. *J. Fluid Mech.* **554**, 271–297.

[Seminara 2010] Seminara, G. 2010 Fluvial sedimentary patterns. *Annu. Rev. Fluid Mech.* **42**, 43-66.

[Smith 1998] Smith, C.E. 1998 Modeling high sinuosity meanders in a small flume *Geomorphology* **25**, 19 –30.

[Solari *et al.* 2002] Solari, L., Seminara, G., Lanzoni, S., Marani, and Rinaldo, A. 2002 Sand bars in tidal channels Part2. Tidal meanders. *J. Fluid Mech.* **451**, 203 –238.

[Southard 1991] Southard JB. 1991. Experimental determination of bed-form stability. Annu. Rev. Earth Planet. Sci. 19:423Ð55

[Sykes 1980] Sykes, RI. 1980 An asymptotic theory of incompressible turbulent boundary-layer flow over a small bump. *J. Fluid Mech.* **101**, 647 –670

[Tubino *et al.* 1999] Tubino, M., Repetto, R. & Zolezzi, G. 1999 Free bars in rivers. *J. Hydraul. Res.* **37**, 759-775.

[Tubino & Seminara 1990] Tubino, M., Seminara, G., 1990. Free-forced interactions in developing meanders and suppression of free bars. *J. Fluid Mech.* **214**, 131-159.

[Valance 2005] Valance, A. 2005 Formation of ripples over a sand bed submitted to a turbulent shear flow. *Eur. Phys. J. B* **45**, 433-442.

[Valance & Langlois 2005] Valance, A. & Langlois, V. 2005 Ripple formation over a sand bed submitted to a laminar shear flow. *Eur. Phys. J. B* **43**, 283-294.

[van Boxel *et al.* 1999] van Boxel, J.H., Arens, A.M., van Dijk, P.M. 1999 Aeolian processes across transverse dunes. I: Modelling the air flow. *Earth Surf. Process. Landf.* **24**, 255Ð70.

[Yalin et al. 1979] Yalin, M.S., Karahan, E.J., 1979. Inception of sediment transport. *J. Hydraul. Div.* **105**, 1433-1443.

[Zilker *et al.* 1977] Zilker, D.P., Cook, G.W., Hanratty, T.J. 1977 Influence of the amplitude of a solid wavy wall on a turbulent flow.Part 1.Non-separated flows. *J. Fluid Mech.* **82**, 29-51.

[Zilker & Hanratty 1979] Zilker, D.P., Hanratty, T.J. 1979 *Influence of the amplitude of a solid wavy wall on a turbulent flow. Part 2. Separated flows. J. Fluid Mech.* **90**, 257 –271.

[Zolezzi & Seminara 2001] Zolezzi, G., and Seminara, G. 2001 Downstream and upstream influence in river meandering. Part 1. General theory and application to overdeepening. *J. Fluid Mech.* **438**, 183 –211